# DISSECTING THE CELLULAR AND MOLECULAR MECHANISMS MEDIATING NEUROFIBROMATOSIS TYPE 1 RELATED BONE DEFECTS

Steven David Rhodes

Submitted to the faculty of the University Graduate School
in partial fulfillment of the requirements
for the degree
Doctor of Philosophy
in the Department of Anatomy and Cell Biology
Indiana University

June 2013

Accepted by the Faculty of Indiana University, in partial
fulfillment of the requirements for the degree of Doctor of Philosophy.

_____

Feng-Chun Yang, M.D., Ph.D., Chair

_____

D. Wade Clapp, M.D.

Doctoral Committee

_____

Alexander G. Robling, Ph.D.

April 15, 2013

_____

Joseph P. Bidwell, Ph.D.

ACKNOWLEDGEMENTS

I would like to thank my mentor, Dr. Feng-Chun Yang for her guidance and support throughout my training. Working with Dr. Yang has had a profound impact on my growth and development as a scientist. Mental toughness is one of the most important qualities Dr. Yang has instilled in me during my training – to remain confident, patient, and persistent when facing challenges or the unexpected. Dr. Yang, you have so generously invested your time, talent, and personal experience in me over the past four years. You have truly gone above and beyond to support me in my training process, encouraging me to pursue every opportunity available to enable my future success as an aspiring physician scientist. ‘Thank you’ cannot express my deepest appreciation for all that you have given.

In addition to Dr. Yang, I would like to thank each member of my research committee: Dr. D. Wade Clapp, Dr. Alexander Robling, and Dr. Joseph Bidwell. Dr. Clapp first introduced me to Dr. Yang during my second year of medical school and has also been my co-mentor throughout the past four years. Dr. Clapp, thank you for guiding me towards this truly outstanding training experience. Dr. Robling and Dr. Bidwell, your expertise in bone biomechanics and skeletal biology have been indispensable for the advancement of my thesis project. Thank you for generously investing your time and effort to mentor me, not only during my committee meetings, but also for working one-on-one with me, to teach me experimental techniques and to give insightful research advice.

I would like to thank the Indiana University Medical Scientist Training Program (MSTP). Dr. Clapp and Dr. Maureen Harrington recruited me into the program six years ago. Among many worthy applicants, thank you for considering my potential as a future physician scientist. Were it not for your vision, I certainly would not be here today. I also would like to extend a special thanks to Jan Receveur and Kelly Forestal in the MSTP office. Thank you for the many times you have gone out of your way to help me resolve issues ranging from stipends to insurance and beyond, enabling me to stay focused on my training.

Thank you to all members of the Yang, Clapp and Xu labs who have selflessly helped me to complete this work. Dr. Shi Chen, Dr. Xiaohua Wu, Dr. Yongzheng He, Hao Yang, Ruizhi Dong, Richa Sharma, Xianlin Yang, Xiaohong Li, Jin Yuan, Li Jiang, Dr. Karl Staser, Keshav Menon, and Jeff Gehlhausen, you have all invested your time, talent, and experience to help move this project forward, giving special meaning to the phrase, “Many hands make light work.”

I would also like to thank Dr. Theresa Guise and Dr. Khalid Mohammad for the privilege of collaborating with you both over the past several years. Thank you for providing the SD-208 compound, which has been instrumental in validating the biological significance of aberrant TGF-β signaling in our neurofibromatosis type 1 mouse model. You generously opened your lab to me, making key resources available including x-ray, μCT, and the Bioquant imaging system, which have been essential in the skeletal phenotyping of our mice. In particular, I am grateful to Dr. Mohammad, for the many hours you have spent

with me, sharing your personal experience and teaching me many of the fundamental techniques in bone biology.

Thank you to my parents, David and Judy Rhodes, for being a constant source of love and support throughout my life. Having been through graduate school yourselves, you knew the training process wouldn't be easy, but you encouraged me to work hard, believe in myself, and keep pushing forward. Thank you for always being there for me as my mom and dad. I love you both so much.

To my wife, Carrie, I am grateful beyond words for your love and companionship. Since the day we first met in Anatomy class, you have stayed by my side through the highs and the lows, encouraging me and caring for me. You are the love of my life, my sweetheart, and my best friend. I am blessed beyond measure to share my life with you. I treasure our time together and with your family – I am truly grateful for all of their love, prayers, and support as well.

I give thanks to God, Jesus Christ, and the Holy Spirit for my salvation, good health, my loving wife and family, close friends, and the outstanding mentors who have supported me in this training process. I pray that He will use my talents and abilities in mighty ways to serve and love others.

ABSTRACT

Steven David Rhodes

DISSECTING THE CELLULAR AND MOLECULAR MECHANISMS UNDERLYING BONE DEFECTS IN NEUROFIBROMATOSIS TYPE 1

Skeletal manifestations including short stature, osteoporosis, kyphoscoliosis, and tibial dysplasia cumulatively affect approximately 70% of patients with neurofibromatosis type 1 (NF1). Tibial pseudarthrosis, the chronic non-union of a spontaneous fracture, is a debilitating skeletal malady affecting young children with NF1. These non-healing fractures respond poorly to treatment and often require amputation of the affected limb due to limited understanding of the causative mechanisms.

To better understand the cellular and molecular pathogenesis of these osseous defects, we have established a new mouse model which recapitulates a spectrum of skeletal pathologies frequently observed in patients with NF1. *Nf1*$^{flox/-}$*;Col2.3Cre* mice, harboring *Nf1* nullizygous osteoblasts on a *Nf1*$^{+/-}$ background, exhibit multiple osseous defects which are closely reminiscent of those found in NF1 patients, including runting (short stature), bone mass deficits, spinal deformities, and tibial fracture non-union.

Through adoptive bone marrow transfer studies, we have demonstrated that the *Nf1* haploinsufficient hematopoietic system pivotally mediates the pathogenesis of bone loss and fracture non-union in *Nf1*$^{flox/-}$*;Col2.3Cre* mice. By

genetic ablation of a single *Nf1* allele in early myeloid development, under the control of LysMCre, we have further delineated that *Nf1* haploinsufficient myeloid progenitors and osteoclasts are the culprit lineages mediating accelerated bone loss. Interestingly, conditional *Nf1* haploinsufficiency in mature osteoclasts, induced by CtskCre, was insufficient to trigger enhanced lytic activity. These data provide direct genetic evidence for *Nf1's* temporal significance as a gatekeeper of the osteoclast progenitor pool in primitive myelopoiesis.

On the molecular level, we found that transforming growth factor-beta1 (TGF-β1), a primary mediator in the spatiotemporal coupling of bone remodeling, is pathologically overexpressed by five- to six- fold in both NF1 patients and in mice. *Nf1* deficient osteoblasts, the principal source of TGF-β1 in the bone matrix, overexpress TGF-β1 in a gene dosage dependent fashion. Moreover, p21Ras dependent hyperactivation of the Smad pathway accentuates responses to pathological TGF-β1 signals in *Nf1* deficient bone cells. As a proof of concept, we demonstrate that pharmacologic TβRI kinase inhibition can rescue bone mass defects and prevent tibial fracture non-union in $Nf1^{flox/-}$;*Col2.3Cre* mice, suggesting that targeting TGF-β1 signaling in myeloid lineages may provide therapeutic benefit for treating NF1 skeletal defects.

Feng-Chun Yang, M.D., Ph.D., Chair

TABLE OF CONTENTS

# ABBREVIATIONS

| | |
|---|---|
| α-MEM | Alpha-Minimum Essential Medium |
| $\Delta C_T$ | Delta cycles to threshold |
| μCT | Micro-computed tomography |
| Abl | Abelson murine leukemia protein |
| AdCre | Cre-expressing adenovirus |
| Akt | Protein Kinase B |
| ALP | Alkaline phosphatase |
| ANOVA | Analysis of Variance |
| APC | Allophycocyanin |
| BFR | Bone formation rate |
| BM | Bone marrow |
| BMD | Bone mineral density |
| BMMNCs | Bone marrow mononuclear cells |
| BMP | Bone morphogenetic protein |
| BS | Bone surface |
| BV/TV | Bone volume fraction |
| CD | Cluster of differentiation |
| CFU | Colony forming unit |
| cGy | Centigray |
| Col1a1 | Collagen type 1, alpha 1 |
| Col2.3 | 2.3 kb segment of Col1a1 promoter |
| Conn.D | Connectivity density |
| CMV | Cytomegalovirus |
| CPT | Congenital pseudarthrosis of the tibia |
| Cre | Cre recombinase |
| Ctsk | Cathepsin K |
| CTX | C-terminal cross-linking telopeptide of type I collagen |
| C/V ratio | Spinal canal area (C)/ vertebral body area (V) ratio |
| Cy | Cyanin |
| dLS | Double label surface |
| DMEM | Dulbecco's Modified Eagle Media |
| Dpd/Pyd | Deoxypyridinoline/pyridinoline ratio |
| ECL | Enhanced chemiluminescence |
| EDTA | Ethylene diamine tetraacetic acid |
| ERK | Extracellular regulated kinase |
| FBS | Fetal bovine serum |
| FITC | Fluorescein isothiocyanate |
| Flox | Flanked by loxP sites |
| G | Gauge |
| GAP | GTPase activating protein |
| GAPDH | Glyceraldehyde-3-phosphate dehydrogenase |
| GDP | Guanosine diphosphate |

| | |
|---|---|
| GFP | Green fluorescent protein |
| GMP | Granulocyte-macrophage progenitor |
| Gr1 | Granulocyte differentiation antigen 1 |
| GRD | GAP-related domain |
| GTP | Guanosine triphosphate |
| H&E | Hematoxylin and eosin |
| HPF | High power field |
| HSC | Hematopoietic stem cell |
| IACUC | Institutional Animal Care and Use Committee |
| IMDM | Iscove's Modified Dulbecco's Medium |
| Ir.L.Wi | Interlabel width |
| JMML | Juvenile myelomonocytic leukemia |
| L | Lumbar |
| LacZ | Gene encoding β-galactosidase protein |
| LAP | Latency associated peptide |
| LARC | Laboratory Animal Research Center |
| LOH | Loss of heterozygosity |
| LysM | Lysozyme M |
| Mac1 | Macrophage 1 antigen |
| MAPK | Mitogen activated protein kinase |
| MAR | Mineral apposition rate |
| M-CSF | Macrophage-colony stimulating factor |
| MEK | MAPK/ERK kinase |
| MMP | Matrix metalloproteinase |
| MNCs | Mononuclear cells |
| MPD | Myeloproliferative disease |
| MPNST | Malignant peripheral nerve sheath tumor |
| mRNA | Messenger RNA |
| MS | Mineralizing surface |
| MSC | Mesenchymal stem cell |
| MSCV | Murine stem cell virus |
| MSPC | Mesenchymal stem progenitor cell |
| NF1 | Neurofibromatosis type1 |
| NFκB | Nuclear factor-kappaB |
| N.Ob | Osteoblast number |
| N.Oc | Osteoclast number |
| Ob | Osteoblast |
| OBL | Osteoblast |
| OC | Osteoclast |
| OPG | Osteoprotegerin |
| OPN | Osteopontin |
| OVX | Ovariectomy |
| PBS | Phosphate buffered saline |
| PCR | Polymerase chain reaction |
| pDEXA | Peripheral dual-energy X-ray absorptiometry |
| PE | R-Phycoerythrin |

| | |
|---|---|
| Peri | 3.9 kb fragment of Periostin promoter |
| PGK | Phosphoglycerate kinase |
| PI-3K | Phosphatidylinositol 3-kinase |
| PTH | Parathyroid hormone |
| pQCT | Peripheral quantitative computed tomography |
| Prx1 | Paired related homeobox 1 |
| PVDF | Polyvinylidene fluoride |
| Rac1 | Ras-related C3 botulinum toxin substrate 1 |
| Raf | Rapidly accelerated fibrosarcoma protein |
| RANKL | Receptor activator of nuclear factor kappa-B ligand |
| Ras | Rat sarcoma protein |
| RNA | Ribonucleic acid |
| ROI | Region of interest |
| RT | Room temperature |
| Sca1 | Stem cell antigen 1 |
| SDS | Sodium dodecyl sulfate |
| sLS | Single labeled surface |
| Smad | Sma/Mad (Mothers against decapentaplegic) homology protein |
| T | Thoracic |
| TAK1 | TGF-β activated kinase 1 |
| Tb.N | Trabecular number |
| Tb.Sp | Trabecular spacing |
| Tb.Th | Trabecular thickness |
| TGF-β1 | Transforming growth factor-beta1 |
| TβRI | TGF-β receptor, type 1 |
| TβRII | TGF-β receptor, type 2 |
| TRACP | Tartrate resistant acid phosphatase |
| UV | Ultraviolet |
| vBMD | Volumetric bone mineral density |
| VOI | Voxel of interest |
| WT | Wild-type |

# CHAPTER 1. INTRODUCTION

## Neurofibromatosis type 1

Neurofibromatosis type 1 (NF1) is a common autosomal dominant genetic disorder affecting one in 3,500 persons worldwide [1]. NF1 results from mutations in the *NF1* tumor suppressor gene located on the long arm of chromosome 17 at 17q11.2 [2, 3]. Containing 60 exons and spanning greater than 300kb of genomic DNA, the *NF1* gene encodes the Ras-GTPase activating protein neurofibromin, which negatively regulates the activity of $p21^{ras}$ (Ras) by accelerating the conversion of active Ras-guanosine triphosphate (GTP) to inactive Ras-guanosine diphosphate (GDP) [2, 3]. Ras proteins lie upstream of multiple signaling pathways regulating cell growth, survival, differentiation and cytoskeletal function. Active Ras-GTP recruits the serine-threonine kinase Raf-1 to the plasma membrane, which subsequently activates a series of downstream targets such as extracellular signal-regulated kinases (ERKs) (p44/p42 MAPK) and phosphatidylinositol 3-kinase (PI-3K) [4, 5]. Loss of one or both functional copies of the *NF1* allele results in Ras hyperactivation in response to external stimuli. This dysregulation of Ras signaling gives rise to the genetic disorder neurofibromatosis type I (NF1).

In 1882, the German pathologist Freidrich von Recklinghausen first published his seminal case report documenting “innumerable” cutaneous tumors composed of both neurons and fibroblasts, which he called neurofibromas [6]. Beyond the pathognomonic cutaneous and plexiform neurofibromas, extensive

epidemiological study [1, 7, 8] now shows that NF1 patients suffer a range of malignant and non-malignant manifestations including café au lait macules, axillary or inguinal freckling, optic gliomas [9, 10], Lisch nodules [11], cognitive impairment [12], and cardiovascular disease [13-18]. Children with NF1 have a 500-fold increased risk of developing juvenile myelomonocytic leukemia (JMML) due to loss of heterozygosity (LOH) of the normal *NF1* allele [19-21].

**Skeletal manifestations of NF1**

Aside from the aforementioned features, NF1 patients develop a range of characteristic skeletal manifestations including osteoporosis [22-27], kyphoscoliosis [28-30], short stature [31-33], macrocephaly [32], chest wall deformities [34], sphenoid wing dysplasia [8], and pseudarthrosis of the tibia [35-39]. Osseous defects in NF1 can be subclassified as either generalized or focal in nature. Generalized deficits, including reduced bone mineralization and short stature, affect greater than half of all NF1 patients collectively. Focal deficits, such as dystrophic scoliosis, sphenoid wing dysplasia, and tibial pseudarthrosis, occur at a lower frequency, yet carry significant morbidity.

Osteoporosis

Although osteoporosis is recognized as a major source of morbidity in the aging population, it is quite rare among children and adolescents and was previously unrecognized as a significant complication of NF1. In 2001, Illes and colleagues were the first to document reduced bone mineral density (BMD) in NF1 patients with scoliosis requiring surgical correction, noting “very soft

vertebral bone" upon intraoperative assessment [30]. Measurement of lumbar spine BMD by peripheral dual energy x-ray absorptiometry (pDEXA) revealed a mean z-score of -2.5. Moreover, patients with the most pronounced reductions in BMD tended to have increased severity of scoliosis [30], a finding which was later corroborated in a larger cross-sectional study of 104 NF1 patients [22]. A consensus of published literature suggests that BMD may be significantly reduced in up to 50% of children and adolescents with NF1 [22, 24-26].

Consistent with these findings, children and adolescents with NF1 also exhibit significantly increased deoxypyridinoline (Dpd)/pyridinoline (Pyd) ratios [40], an established biomarker of bone resorption that is often increased in patients with a variety of high bone turnover states including osteoporosis, Paget's disease, and hyperparathyroidism [41-43]. While the consequences of low BMD in the pediatrics NF1 population remain unclear, it has been hypothesized that increased bone resorption and reduced BMD could lead to the accumulation of clinically undetected microfractures in patients with NF1, compromising the mechanical integrity of the bone later in life. Indeed, Tucker and colleagues found that the risk of fracture among adults with NF1 was markedly increased as compared to their unaffected siblings and spouses [27]. 41 fractures were documented among 24 out of 72 NF1 patients, as compared to just six fractures among six individuals out of 73 unaffected siblings. Moreover, among the NF1 patient cohort, 24 pathological fractures (associated with minimal trauma) were documented in 14 individuals, whereas no pathological fractures were reported in the unaffected cohort [27]. More recently, a controlled study of

460 neurofibromatosis patients conducted in Finland [44] confirmed that adults with NF1 ages 41 years and older had a 5.2-fold increased risk of fracture versus age-matched controls without NF1. Children with NF1 ages 17 and under had a 3.4-fold increased risk ratio for fractures [44].

Although NF1 associated osteopenia and osteoporosis commonly present during childhood, there are currently no clinical trials which support the use of traditional osteoporotic drugs (bisphosphonates, PTH, etc.) in this population [36]. Despite evidence of reduced Vitamin D levels in a subset of NF1 patients [45], supplementation with calcium and Vitamin D did not significantly improve BMD z-scores after 2 years follow-up [46]. Collectively, these findings are suggestive of a generalized metabolic bone defect due to functional inactivation of neurofibromin.

Vertebral defects

Gould and Weiss first called attention to the high incidence of spinal deformities in patients with NF1 in the early 1900s [47, 48]. Vertebral defects are observed in between 10-77% of NF1 patients according to varying clinical reports [49-51] and approximately 2% of all pediatric scoliosis cases are associated with NF1[52]. Scoliosis is sub-classified as either non-dystrophic or dystrophic, based on the absence or presence of various radiographic findings [53]. Non-dystrophic scoliosis in NF1 mimics idiopathic scoliosis in the general population, but presents earlier and is associated with a higher risk of pseudarthrosis after spinal fusion [54]. Dystrophic scoliosis refers to dysplastic osseous changes with rapid onset and progression. Studies have identified characteristic radiographic

features associated with dystrophic scoliosis in NF1 which include rib penciling, short-segment sharply angulated curves involving four to six vertebrae, vertebral rotation, scalloping of the vertebral margins, spindling of the transverse processes, pedicle defects, and widening of the spinal canal [53, 55]. Dystrophic scoliosis can be a debilitating condition for children and adolescents with NF1, with the potential to degenerate rapidly to neurological impairment. Orthopedic manipulation is also associated with a risk of pseudarthrosis in the affected vertebrae following surgical intervention [28, 56].

Congenital pseudarthrosis of the tibia (CPT)

Congenital pseudarthrosis, first described by James Paget in 1891, is a rare orthopedic condition characterized by anterolateral bowing of the tibia with tapering at the defective site [57]. While the overall incidence is only 1:140,000-1:250,000 live births [58], remarkably, 50-80% of all congenital tibial pseudarthrosis cases have been reported to involve mutations in the *NF1* gene [59-62]. Fractures can occur spontaneously or following minimal trauma. Bone healing is insufficient, resulting in persistent fibrous non-union even after multiple surgeries. Faced with limited and ineffective treatment options, elective limb amputation is often required to restore mobility.

Fibrous hamartoma tissues surgically excised from pseudarthrosis lesions associated with NF1 maintain a mesenchymal lineage phenotype, expressing the cell surface markers CD44 and CD105, but are negative for CD45 and CD14 [63]. Although they express BMP receptors, they do not undergo osteoblastic differentiation *ex vivo* in response to BMP [63]. In addition to defective

osteogenesis, osteoclasts are abundant in pseudarthrosis tissue [62, 64, 65]. Furthermore, Cho and colleagues reported that fibrous hamartoma cells harvested from pseudarthrosis tissue expressed a significantly increased levels of receptor activator of nuclear factor kappa-B ligand (RANKL) and lower levels of osteoprotegerin (OPG) as compared to control tibial periosteal cells, enhancing osteoclast differentiation in co-culture with Raw264.7 cells [63]. Collectively, these findings suggest that the pathogenesis of NF1 tibial pseudarthrosis is likely complex, involving the heterotypic interaction of dysfunctional mesenchymal stem cells (MSCs) and/or osteoblasts as well as excessive osteoclast bone resorption. Yet fully dissecting the cellular and molecular mechanisms of pseudarthrosis and other NF1 osseous deficits will require the generation of new mouse models which accurately recapitulate multiple skeletal phenotypes seen in the human disease.

**Modeling NF1 osseous defects in the mouse**

Mouse models have been critical in facilitating key insights into the role of *Nf1* in bone biology and as a platform for preclinical testing of potential pharmacologic therapies (Table 1). *Nf1*$^{-/-}$ mice die *in utero* before day 13 of gestation due to heart developmental abnormalities associated with excessive proliferation and premature apoptosis of the endocardium [66]. Additionally, adoptive transfer experiments with *Nf1*$^{-/-}$ fetal liver cells have been shown to consistently induce a myeloproliferative disease (MPD) similar to JMML seen in

NF1 patients [67, 68]. For these reasons, *Nf1*$^{-/-}$ mice are not suitable for bone studies.

*Nf1*$^{+/-}$ mice exhibit cytokine hypersensitivity in multiple myeloid lineages including myeloid progenitors, mast cells, and osteoclasts. Osteoclasts derived from both human NF1 patients and *Nf1*$^{+/-}$ mice display multiple gain-in-functions including increased proliferation, survival, and bone resorption, which are associated with more severe osteoporotic bone loss in *Nf1*$^{+/-}$ mice induced by ovariectomy (OVX) pro-resorptive stress [69-71]. These phenotypes are associated with elevated p21$^{ras}$-GTP and Akt phosphorylation in response to M-CSF stimulation. Intriguingly, genetic intercross with mice deficient in class 1a PI-3K (p85α) attenuated Akt phosphorylation and restored aberrant *Nf1*$^{+/-}$ osteoclast functions to WT levels [69]. Collectively, these findings provided seminal evidence that hyperactivity of p21ras and PI3K cooperate to alter *Nf1* haploinsufficient osteoclast functions.

Downstream of hyperactivated Ras, Rho GTPases act as molecular gatekeepers, cycling between inactive-GDP and active-GTP-bound forms to modulate osteoclast cytoskeletal functions. We previously demonstrated that the Rho-GTPase Rac1 is a crucial Ras effector mediating aberrant osteoclast migration and f-actin rearrangement within the podosomes of *Nf1*$^{+/-}$ osteoclasts [72]. Genetic disruption of *Rac1* in *Nf1*$^{+/-}$ mice attenuated elevated levels of phosphorylated extracellular signal-regulated kinases (Erk1/2) while normalizing *Nf1* haploinsufficient cytoskeletal phenotypes and bone resorptive activity. Analogous results were achieved after application of a pharmacologic MEK

inhibitor (PD98059), suggesting that Rac1-GTPase hyperactivation contributes in turn to excessive activation of the Ras-PI3K-Erk signaling axis in *Nf1*$^{+/-}$ osteoclasts [72].

Recent studies also show that neurofibromin plays a critical role in osteoblast differentiation from mesenchymal stem cells (MSCs). MSCs from *Nf1*$^{+/-}$ mice have increased proliferation and colony forming unit-fibroblast (CFU-F), but impaired osteoblast differentiation as confirmed by alkaline phosphatase staining, and reduced mRNA levels of osteoblast specific markers such as osteocalcin and osteonectin [73]. Retroviral transduction of *Nf1*$^{+/-}$ MSPCs with *NF1* GTPase activating related domain (NF1 GRD) was sufficient to rescue the impaired osteoblast differentiation in these cells [73].

While osteoclasts and osteoblasts cultured *ex vivo* from *Nf1*$^{+/-}$ mice exhibit aberrant differentiation and function, surprisingly, bone mineral density and peripheral quantitative computed tomography (pQCT) analysis show no difference in bone mass or microarchitecture as compared to WT controls [74]. This finding suggests that *Nf1* heterozygosity alone may be insufficient to spontaneously recapitulate the full spectrum of skeletal manifestations observed in the human disease. In an effort to more accurately recapitulate the full spectrum of osseous defects observed in the human disease, Cre-lox technology has been utilized by various laboratories to achieve conditionally *Nf1* nullizygosity in select lineages within the mesenchymal hierarchy.

Elefteriou and colleagues utilized a genetic approach to delete *Nf1* in the osteoblast lineage by intercrossing *Nf1*$^{flox/flox}$ mice with α1(I) Collagen Cre

transgenic mice and paradoxically found that *Nf1* inactivation in osteoblasts led to increased bone mass in the vertebral spine [75]. These results are difficult to interpret since they represent the antithesis of the osteoporotic phenotype observed in human NF1 patients. Moreover, the same authors later reported recalcitrant bone healing in the same mice due to deficiencies in osteoblast differentiation [76]. For reasons which are still unclear, we have been unable to recapitulate the results described by Elefteriou and colleagues in *Nf1*$^{flox/flox}$*;Col2.3Cre* mice [77, 78].

Kolanczyk and colleagues observed tibial bowing and runting in *Nf1*$^{flox/flox}$ mice with conditional *Nf1* nullizygosity in undifferentiated limb bud mesenchyme driven by *Prx1Cre* [79]. While informative, this model remains limited as it does not spontaneously recapitulate the osteoporotic manifestations of NF1 patients. Clinically, bone mass defects tend to be localized to the load-bearing anatomical sites, such as the tibia and spine, where dystrophic deformities most often occur [23]. These findings suggest a strong association between the osteoporotic and the dystrophic skeletal phenotypes of NF1 which warrants further investigation.

Regardless of these discrepancies, the inability of various single lineage conditional knockout models to recapitulate the full spectrum of NF1 skeletal defects suggests that certain manifestations, particularly pseudarthrosis, may require the heterotypic interaction of multiple cell lineages with varying gene dose. In support of this paradigm, Stevenson and colleagues first demonstrated two cases of biallelic *NF1* inactivation in the bone tissue by microdissection, while patients remained *NF1* haploinsufficient in the peripheral blood [80]. More

recent case series since corroborated these findings, in which loss of NF1 heterozygosity (LOH) was documented in four out of 16 patients tested [81]. Collectively, these data suggest that localized biallelic *NF1* inactivation in either osteoblasts or mesenchymal progenitor cells, interacting with other NF1 haploinsufficient lineages in the bone microenvironment, may pivotally underpin the pathological bone repair process in at least a subset of patients with pseudarthrosis.

To model this complex genetic framework, we generated two novel murine models (*Nf1$^{flox/-}$;PeriCre* and *Nf1$^{flox/-}$;Col2.3Cre* mice ), harboring *Nf1* nullizygous MSCs and osteoblasts, respectively, on a *Nf1* heterozygous background. In the third chapter of this thesis, we show that *Nf1$^{flox/-}$;PeriCre* and *Nf1$^{flox/-}$;Col2.3Cre* mice closely recapitulate multiple skeletal phenotypes observed in NF1 patients, including osteoporosis [78], non-dystrophic and dystrophic vertebral deficits [77], and tibial fracture non-union (pseudarthrosis) [78]. Collectively, these findings provide strong evidence of a non-cell autonomous mechanism for NF1 osseous defects and serve as our platform for investigations of the cellular and molecular mechanisms mediating aberrant NF1 bone homeostasis *in vivo* as described in detail in later chapters of this thesis.

| Species | Disease/ Model | Conclusion | Authors, Date |
|---|---|---|---|
| Mouse | *Nf1*$^{+/-}$ mice | ***In vitro:*** Reduced osteoblast differentiation. Multiple osteoclast gain-in-functions. ***In vivo:*** Increased bone loss after ovariectomy stress. Deficient tibial fracture repair. | (Yu et al., 2005) (Yang et al., 2006) (Schindeler et al., 2008) |
| Mouse | Conditional KO: *Nf1*$^{OB-/-}$ (*Prx1Cre*, *Col2.3Cre*) | ***In vitro:*** Reduced osteoblast differentiation (*Prx1Cre* model). ***In vivo:*** Runting and tibial bowing (*Prx1Cre* model). Paradoxically, increased bone mass but with bone healing defects (*Col2.3Cre* model). | (Elefteriou et al., 2006) (Kolanczyk et al., 2007) (Wang et al., 2010) |
| Human | Pseudarthrosis | *NF1* loss of heterozygosity (LOH) in pseudarthrosis tissue. | (Stevenson et al., 2006) |
| Human | Osteoporosis | Osteoclasts derived from the peripheral blood of NF1 patients show multiple gain-in-functions. Decreased bone mineral density and content in the load-carrying anatomical regions. | (Kuorilehto et al., 2005) (Yang et al., 2006) (Heervä et al., 2010) |
| Mouse | Conditional KO w/ *Nf1*$^{+/-}$ Background: *Nf1+/-*$^{OB-/-}$ (*Col2.3Cre*) | Decreased bone mass in the vertebrae and long bones. Severe fracture repair deficits compared to *Nf1*$^{OB-/-}$ and *Nf1*$^{+/-}$ mice. Transplantation of WT bone marrow rescues phenotype. | (Zhang, Rhodes et al., 2011) (Wu et al., 2011) |

Table 1

**Table 1.** Mouse models of NF1 skeletal defects.

### *Nf1* haploinsufficient hematopoietic cells: critical mediators in the pathogenesis of bone defects

Neurofibromas, the pathognomonic tumors of NF1, are unique with respect to their cellular heterogeneity, containing Schwann cells, fibroblasts, mast cells, and vasculature [82, 83]. Genetic studies indicate that biallelic loss of *Nf1* in Schwann cells is necessary but not sufficient for tumor formation. Indeed, Yang and colleagues demonstrated that heterozygosity of bone marrow-derived cells in the tumor microenvironment is required for neurofibroma genesis in mice harboring *Nf1* nullizygous Schwann cells [84].

Analogously, $Nf1^{flox/flox}$*;Col2.3Cre* mice (harboring conditional nullizygous osteoblasts on a WT background) do not exhibit osseous defects [78], implying that *Nf1* deficiency in osteoblasts alone is insufficient for the full penetrance of NF1 skeletal deficits. By contrast, $Nf1^{flox/-}$*;Col2.3Cre* mice recapitulate a spectrum of boney defects observed in the human disease [77, 78], including runting (short stature), low bone mass, vertebral defects, and tibial fracture non-union, suggesting that *Nf1* haploinsufficiency in at least a subset of lineages within the bone microenvironment must be critical to the pathogenesis of these osseous features. To establish whether the hematopoietic microenvironment plays a key role in recalcitrant fracture healing in $Nf1^{flox/-}$*;Col2.3Cre* mice, Wu and colleagues transplanted bone marrow mononuclear cells (BMMNCs) from either WT or $Nf1^{+/-}$ donor mice into lethally irradiated $Nf1^{flox/-}$*;Col2.3Cre* or $Nf1^{flox/flox}$*;Col2.3Cre* recipients [78]. After four months of hematopoietic reconstitution, the recipient

mice underwent three-point bending fracture. The fracture healing process was monitored for a duration of four weeks.

Fracture healing in *Nf1$^{flox/flox}$;Col2.3Cre* mice reconstituted with *Nf1$^{+/-}$* marrow was significantly impaired relative to those receiving WT bone marrow cells as confirmed by radiographic and histological analysis. μCT revealed significantly reductions in BV/TV fraction in *Nf1$^{flox/flox}$;Col2.3Cre* recipients transplanted with *Nf1$^{+/-}$* bone marrow cells as compared to WT bone marrow. Conversely, transplantation of WT bone marrow prevented tibial fracture non-union normally observed in *Nf1$^{flox/-}$;Col2.3Cre* mice (Figure 1). Collectively, these data provide rigorous evidence that at least some component of the *Nf1* haploinsufficient bone marrow microenvironment plays an essential role in the skeletal manifestations of NF1, particularly in fracture non-union. Still, the specific lineage(s) in the hematopoietic system that is(are) critical for the pathological bone repair process remains unclear.

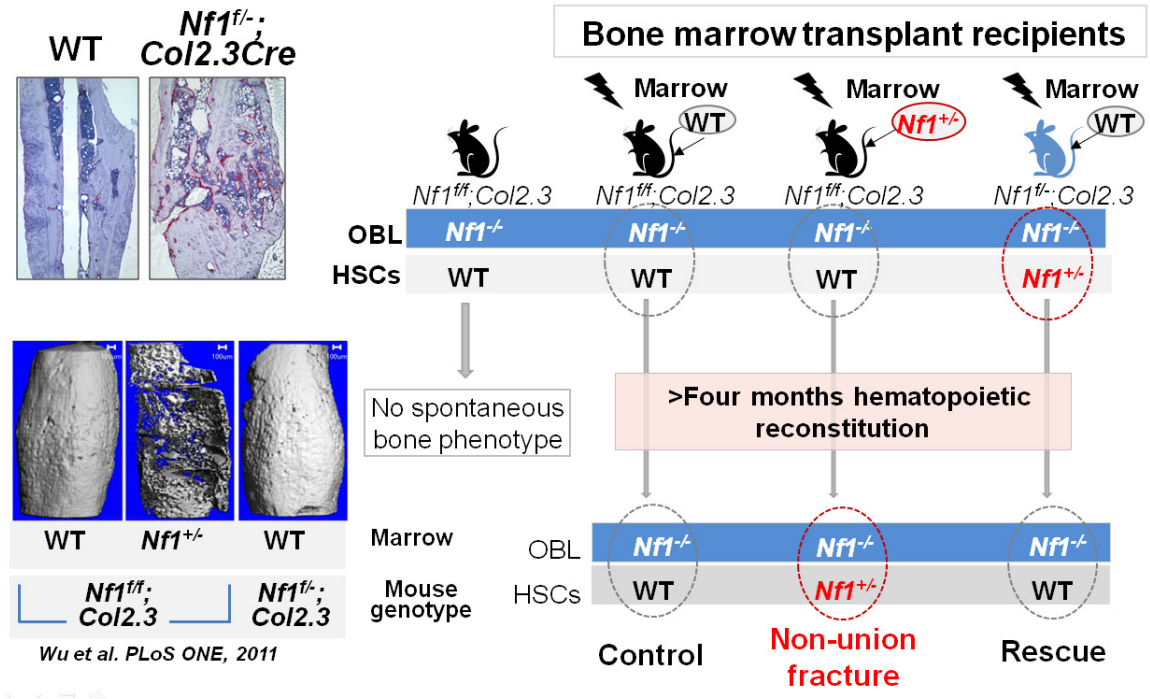
WT
Nf1f/-; Col2.3Cre
Bone marrow transplant recipients
Marrow
WT
Marrow
Nf1+/-
Marrow
WT
Nf1f/f;Col2.3
Nf1f/f;Col2.3
Nf1f/f;Col2.3
Nf1f/-;Col2.3
OBL
HSCs
Nf1-/-
WT
Nf1-/-
WT
Nf1-/-
WT
Nf1-/-
Nf1+/-
No spontaneous bone phenotype
>Four months hematopoietic reconstitution
WT
Nf1+/-
WT
Marrow
Mouse genotype
Nf1f/f; Col2.3
Nf1f/-; Col2.3
OBL
HSCs
Nf1-/-
WT
Nf1-/-
Nf1+/-
Nf1-/-
WT
Control
Non-union fracture
Rescue
Wu et al. PLoS ONE, 2011

Figure 1

**Figure 1. The *Nf1* status of the hematopoietic microenvironment significantly alters tibial fracture healing in *Nf1*$^{flox/flox}$ and *Nf1*$^{flox/-}$*;Col2.3Cre* mice.** Adoptive transfer of *Nf1*$^{+/-}$ hematopoietic cells to *Nf1*$^{flox/flox}$*;Col2.3Cre* mice results in tibial fracture non-union as compared to isogenic controls transplanted with WT bone marrow cells. Conversely, adoptive transfer of WT hematopoietic cells to *Nf1*$^{flox/-}$*;Col2.3Cre* mice rescues fracture healing deficits in these animals.

**Transforming growth factor-beta (TGF-β), decoupled bone remodeling, and osteoblast/osteoclast dysfunction**

Exacerbating intrinsic imbalances in osteoclast and osteoblast function in the context of *Nf1* inactivation is the dysregulated secretion of paracrine factors including receptor activator of nuclear factor kappa-B ligand (RANKL), osteoprotegerin (OPG), and osteopontin (OPN), which further promote excessive osteoclastogenesis and osteoclast bone lytic activity [75, 85, 86]. As such, the identification and characterization of hyperactive Ras-dependent paracrine effector pathways that can be interrupted with currently existing monoclonal antibodies or small molecule inhibitors holds strong potential for improving skeletal health in the NF1 population.

Transforming growth factor-beta (TGF-β) is known to be a key regulator of bone mass, matrix, and mechanical properties, which in turn impacts the ability of bone to resist fracture [87, 88]. Previously, our laboratory established that hypersecretion of TGF-β by $Nf1^{+/-}$ mast cells induces neurofibroma phenotypes by enhancing $Nf1^{+/-}$ fibroblast proliferation and collagen synthesis via hyperactivation of the Ras-c-abl pathway [89]. Although the pivotal role of TGF-β in physiological bone turnover has been previously characterized, genetic and pharmacologic studies characterizing the potential consequences of hyperactive TGF-β signaling with respect to NF1 pathological bone remodeling are lacking.

Recently, a study by Wang et al. examining tibial fracture healing in transgenic mice carrying *Nf1* nullizygous osteoblasts ($Nf1^{ob-/-}$ mice) demonstrated an increase in TGF-β mRNA expression in $Nf1^{ob-/-}$ calluses compared with WT

controls [76]. Intriguingly, local delivery of low-dose lovastatin improved deficits in callus strength and maturation in *Nf1*$^{ob-/-}$ mice [76]. Although lovastatin reduced callus TGF-β mRNA expression, its effects are not restricted to TGF-β signaling. By inhibiting the biosynthesis of mevalonate and its metabolites, lovastatin is recognized to exert a number of off-target effects by disrupting the post-translational modification of a wide variety of proteins including the Ras, Rab, and Rho families [90, 91]. Still, direct genetic and pharmacologic studies assessing the potential role of dysregulated TGF-β signaling in NF1 associated bone defects remain lacking.

The complex role of TGF-β in bone remodeling

Three distinct yet structurally similar isoforms of TGF-β (TGF-β1 to -β3) exist in mammals [92]. These are differentially expressed in various tissues and induce different biological effects. Considerable evidence suggests that TGF-β1 (the predominant isoform in bone) plays a critical role in coordinating the formation, function, and cell-cell interactions of osteoblasts and osteoclasts to modulate bone mass and remodeling [87, 93-95]. TGF-β is secreted as a latent precursor, which is sequestered abundantly in the bone matrix. Following release from the bone matrix and proteolytic activation, TGF-β binds type II receptors which complex with and activate type I receptors, leading to the phosphorylation of Smad2 and Smad3 among other effector pathways (Figure 2). Phosphorylated Smad2/3 bind with Smad4 and together translocate to the nucleus to regulate the transcription of TGF-β target genes [96, 97].

Studies across multiple laboratories suggest a complex regulatory system in which TGF-β induces biphasic effects on bone cells. *In vitro* studies reveal that at early stages of osteoblast differentiation, TGF-β1 increases bone formation by stimulating the recruitment and proliferation of osteoblast progenitors [87]. Consistent with these observations, TGF-β1 knockout mice exhibit reduced bone mineral density and bone elasticity [98, 99]. Contrastingly, at later stages, TGF-β1 has been show to potently inhibit terminal osteoblast differentiation, suppressing mineralization and osteocalcin expression [100, 101]. *In vivo*, the attenuation of TGF-β signaling in osteoblasts by overexpression of a truncated, dominant negative TGF-β type II receptor in transgenic mice enhanced trabecular bone mass and resistance to fracture [102]; mice with conditional knockout of the TGF-β type II receptor show a similar phenotype [103]. Reduction of TGF-β signaling through its effector Smad3 can also promote anabolic bone remodeling; *Smad3*$^{+/-}$ mice show increased bone mass, matrix, and mechanical properties as compared to controls [95].

As with osteoblasts, TGF-β has also been shown to exert differential effects on osteoclasts. Several *in vitro* studies contend that TGF-β inhibits osteoclastogenesis both directly and indirectly by increasing the ratio of OPG/RANKL production by osteoblasts [104-106]. On the opposing end of the spectrum, however, other groups have reported increased osteoclast formation in cultures from spleen, bone marrow, and peripheral blood mononuclear cells following exposure to TGF-β [107-110]. Recently, Gingery et al. concluded that TGF-β coordinately activates the TAK1/MEK/AKT/NFκB and SMAD pathways to

promote osteoclast survival [111]. Futakuchi et al. also found that TGF-β increased osteoclastogenesis and bone resorptive activity in RANKL stimulated RAW 264.7 macrophage-like cells [112]. Yet despite conflicting *in vitro* data, *in vivo* data generated from transgenic mouse models consistently suggest that TGF-β positively regulates osteoclast differentiation and function [94, 95]. Although osteoclasts derived from *Nf1*$^{+/-}$ mice and the peripheral blood of human NF1 patients exhibit multiple gain-in-functions [69, 70], the potential contribution of excessive TGF-β signaling to the enhanced bone resorptive capacity of *Nf1*$^{+/-}$ osteoclasts remains unknown.

TGF-β antagonism as a novel strategy in bone formation therapy

The concept that attenuation of TGF-β signaling can produce both anabolic as well as anti-catabolic effects on bone is further supported by recent studies utilizing small molecule inhibitors of TGF-β receptors and TGF-β neutralizing antibodies. Mohammad and colleagues demonstrated that pharmacologic TGF-β blockade with SD-208, a small molecule inhibitor of TGF-β type I receptor (TβRI) kinase activity, increased bone mass and quality [113]. SD-208 treated mice showed enhanced osteoblast differentiation and bone formation, while osteoclast formation and bone resorption were reduced [113]. Similar results were achieved utilizing 1D11, a neutralizing antibody directed against all three TGF-β isoforms [114].

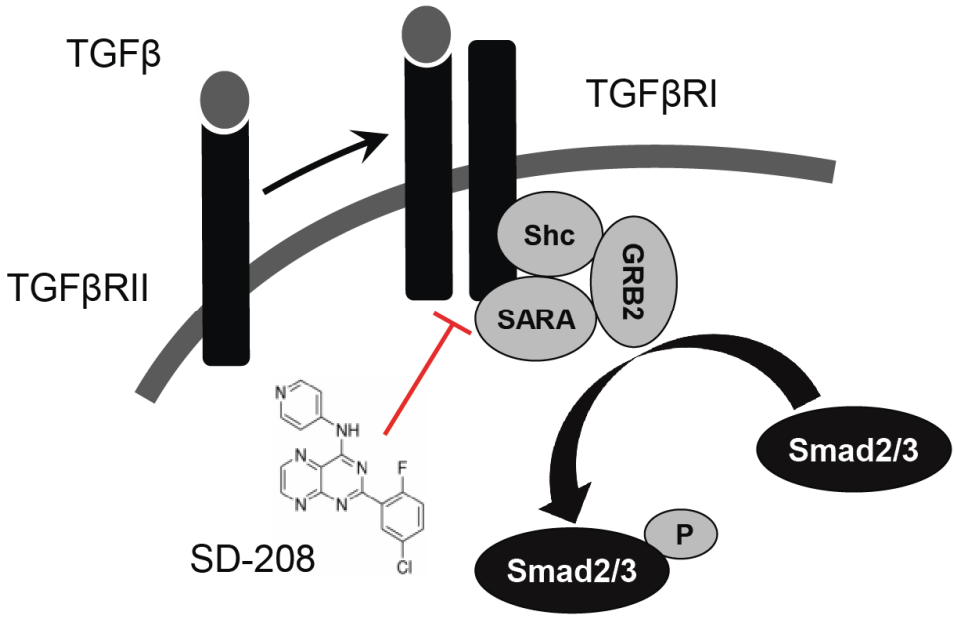


Figure 2

**Figure 2. Cartoon schematic of TGF-β signaling.** TGF-β binds type II receptors (TβRII), which complex with and activate type I receptors (TβRI), leading to activation of the canonical Smad pathway. The pharmacologic agent SD-208 blocks TGF-β signaling by inhibiting TβRI kinase activity.

**Thesis overview**

Establishing animal models which accurately recapitulate the full spectrum of osseous features seen in NF1 patients is critical to improving our understanding of the cellular and molecular etiology of these anomalies. Here we describe the generation and phenotypic characterization of a novel NF1 murine model: *Nf1*$^{flox/-}$*;Col2.3Cre* mice, which exhibits multiple osseous deficits including runting (short stature), low bone mass, vertebral defects, and tibial fracture non-union as described herein. These features are closely reminiscent of those observed in the human disease, thus rendering the *Nf1*$^{flox/-}$*;Col2.3Cre* model a viable platform from which to interrogate the cellular and molecular mechanisms underpinning the pathogenesis NF1 associated skeletal deficits.

We have further demonstrated through a series of adoptive bone marrow transfer experiments, that the *Nf1* haploinsufficient hematopoietic microenvironment is critical to the pathogenesis of bone mass deficits and tibial fracture non-union in *Nf1*$^{flox/-}$*;Col2.3Cre* mice. However, which specific hematopoietic lineage(s) play a pivotal role in this process remains unclear. Given that *Nf1* haploinsufficiency leads to Ras mediated cytokine hypersensitivity in multiple myeloid lineages, we reasoned that *Nf1* haploinsufficiency in osteoclasts and their precursors within the myeloid lineage may be required for the genesis of the observed osseous phenotypes.

To test this hypothesis, we generated *Nf1*$^{flox/+}$*;LysMCre* mice harboring conditional inactivation of a single *Nf1* allele in myeloid cells. Indeed *Nf1*$^{flox/flox}$*;Col2.3Cre* mice stably reconstituted with *Nf1*$^{flox/+}$*;LysMCre*

hematopoietic cells exhibited significant defects in tibial fracture healing as compared to controls reconstituted with WT bone marrow. Compared to WT BM cells, mice reconstituted with *Nf1$^{flox/+}$;LysMCre* BM cells exhibited deficient cortical bridging and significantly reduced callus bone volume fraction (BV/TV) as determined by micro-computed tomography (μCT), indicating substantial deficits in fracture repair. Histological analysis revealed fibrous infiltrates and excessive osteoclast numbers within the fracture callus.

To further dissect the stage of myeloid development at which *Nf1* haploinsufficiency is permissive of osteoclast gain-in functions, we compared the phenotype of *Nf1$^{flox/+}$;LysMCre* mice to *Nf1$^{flox/+}$;CtskCre* mice, where conditional inactivation of a single *Nf1* allele is restricted to mature osteoclasts. While *Nf1$^{flox/+}$;LysMCre* mice exhibit increased osteoclast progenitor frequency (CFU-M), enhanced osteoclastogenesis, and accelerated bone loss following ovariectomy induced resorptive challenge, *Nf1$^{flox/+}$;CtskCre* mice did not recapitulate these phenotypes in analogous experiments. These data provide direct genetic evidence that haploinsufficiency of *Nf1* in myeloid progenitors, but not terminally differentiated OCs alone, is required to expand the pool of OC progenitors, thereby enabling increased bone resorption *in vivo*.

Collectively, these findings suggest that the cellular mechanisms of *Nf1* osseous dysplasia are complex and may require the cooperative interaction of *Nf1* nullizygous osteoblasts and/or progenitors, as well as *Nf1* heterozygous osteoclasts and their myeloid precursors. On the molecular level, transforming growth factor-beta1 (TGF-β1) has become increasingly recognized as a master

regulator in the spatiotemporal coupling of osteoblast and osteoclast activity [94]. Dysregulated TGF-β signaling is associated with a spectrum of osseous defects seen in Loeys-Dietz syndrome [115-118], Marfan syndrome [119-123], and Camurati-Engelmann disease [124]. Intriguingly, neurofibromatosis type 1 (NF1) patients recapitulate many of these characteristic skeletal features; however, the molecular mechanisms underlying these phenotypes remain unclear. Having previously established that *Nf1* haploinsufficient myeloid cells potentiate neurofibroma phenotypes through secreted TGF-β signaling [89], we reasoned that analogous dysregulated paracrine signaling may be integral to the pathogenesis of NF1 skeletal defects.

Here, we provide genetic and pharmacologic evidence that hyperactive TGF-β1 signaling pivotally underpins osseous defects in *Nf1*$^{flox/-}$*;Col2.3Cre* mice. Compared to controls, we show that serum TGF-β1 levels are five- to six- fold increased both in *Nf1*$^{flox/-}$*;Col2.3Cre* mice and in a cohort of NF1 patients. *Nf1* deficient osteoblasts, the principal source of TGF-β1 in bone, overexpress TGF-β1 in a gene dosage dependent fashion. Moreover, *Nf1* deficient osteoblasts and osteoclasts are hyperresponsive to TGF-β1 stimulation, potentiating osteoclast bone resorptive activity while inhibiting osteoblast differentiation. These cellular phenotypes are further accompanied by p21-Ras dependent hyperactivation of the canonical TGF-β1-Smad pathway. Re-expression of the human, full-length neurofibromin GTPase-activating protein (GAP) related domain (*NF1* GRD) in primary *Nf1* deficient osteoblast progenitors, attenuated TGF-β1 expression levels and reduced Smad phosphorylation in response to TGF-β1 stimulation. As

an *in vivo* proof of principle, we demonstrate that administration of the TβRI kinase inhibitor, SD-208, can rescue bone mass deficits and prevent tibial fracture non-union in *Nf1*$^{flox/-}$*;Col2.3Cre* mice. In sum, these data demonstrate a pivotal role for hyperactive TGF-β1 signaling in the pathogenesis of NF1 associated osteoporosis and pseudarthrosis, thus implicating the TGF-β signaling pathway as a potential therapeutic target in the treatment of NF1 osseous defects which are refractory to current therapies.

## CHAPTER 2. MATERIALS AND METHODS

### Animals

*Nf1*$^{+/-}$ mice [125] were obtained from Tyler Jacks of the Massachusetts Institute of Technology (Cambridge, Massachusetts, USA). *Nf1*$^{flox/flox}$ mice [126], provided by Dr. Luis Parada at the University of Texas Southwestern Medical Center, were intercrossed with *Nf1*$^{+/-}$ and 2.3kb α1 (I) collagen Cre (*Col2.3Cre*) mice [127] to selectively drive expression of Cre recombinase in the osteoblast lineage. Four genotypes of mice were generated from the intercross (Figure 3). (1) *Nf1*$^{flox/flox}$*;Col2.3Cre*$^{-}$ mice (wild-type (WT) background); (2) *Nf1*$^{flox/-}$*;Col2.3Cre*$^{-}$ mice (*Nf1*$^{+/-}$ background); (3) *Nf1*$^{flox/flox}$*;Col2.3Cre*$^{+}$ mice (WT background and *Nf1*$^{-/-}$ osteoblasts); and (4) *Nf1*$^{flox/-}$*;Col2.3Cre*$^{+}$ mice (*Nf1*$^{+/-}$ background and *Nf1*$^{-/-}$ osteoblasts) as published previously [77, 78].

As further validation of this model, *Col2.3Cre* transgenic mice were intercrossed with *ROSA26* $^{flox/flox}$ reporter mice. LacZ staining was performed to assess Cre recombination in skeletal tissues. Abundant β-galactosidase expression was observed in the long bones and vertebrae of *ROSA26* $^{flox/flox}$*;Col2.3Cre*$^{+}$ mice, but was absent in *ROSA26* $^{flox/flox}$*;Col2.3Cre*$^{-}$ controls (Figure 4). Efficient deletion of neurofibromin in osteoblasts was further confirmed by western blot (Figure 5).

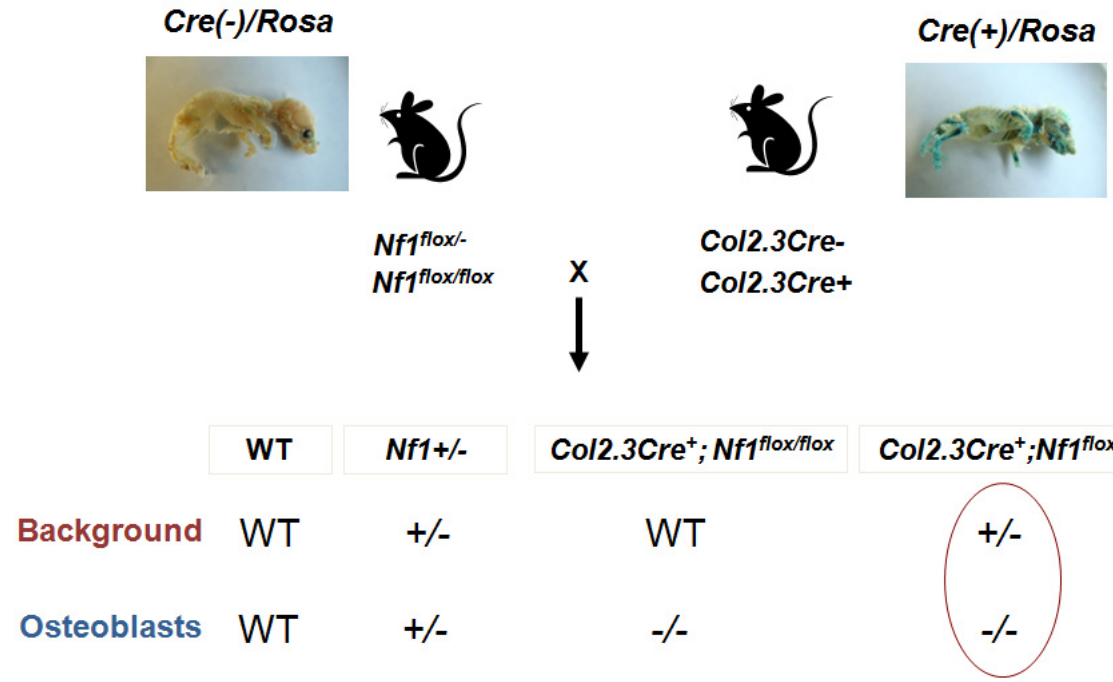
Cre(-)/Rosa
Cre(+)/Rosa
Nf1flox/-
Nf1flox/flox
X
Col2.3Cre-
Col2.3Cre+
WT
Nf1+/-
Col2.3Cre+; Nf1flox/flox
Col2.3Cre+;Nf1flox/-
Background
WT
+/-
WT
+/-
Osteoblasts
WT
+/-
-/-
-/-

Figure 3

**Figure 3. Breeding schema.** *Nf1*$^{+/-}$, *Nf1*$^{flox/flox}$, and *Col2.3Cre*$^{+}$ mice were intercrossed to yield four resulting genotypes of mice. (1) *Nf1*$^{flox/flox}$*;Col2.3Cre*$^{-}$ mice (WT); (2) *Nf1*$^{flox/-}$*;Col2.3Cre*$^{-}$ mice (*Nf1*$^{+/-}$); (3) *Nf1*$^{flox/flox}$*;Col2.3Cre*$^{+}$ mice (WT background with *Nf1*$^{-/-}$ osteoblasts); and (4) *Nf1*$^{flox/-}$*;Col2.3Cre*$^{+}$ mice (*Nf1*$^{+/-}$ background with *Nf1*$^{-/-}$ osteoblasts).

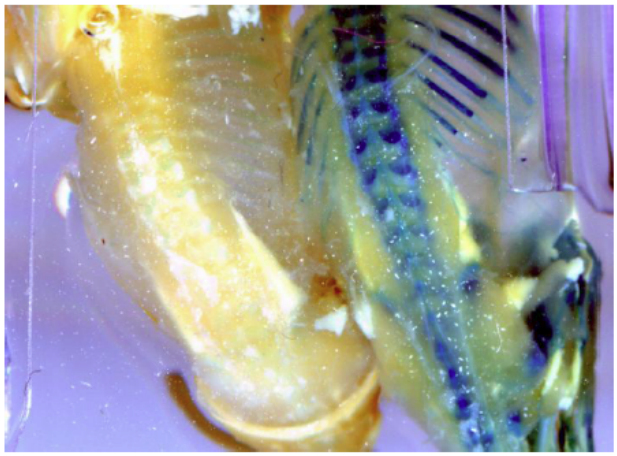

*Rosa26* $^{flox/flox}$; *Col2.3Cre*$^{-}$ *Rosa26* $^{flox/flox}$; *Col2.3Cre*$^{+}$

Figure 4

**Figure 4.** LacZ staining was performed to assess Cre recombination in the long bones and vertebral spine. β-galactosidase was abundantly expressed in the long bones and vertebrae of *ROSA26*$^{flox/flox}$*;Col2.3Cre*$^{+}$ mice, but not present in *ROSA26*$^{flox/flox}$*;Col2.3Cre*$^{-}$ controls.

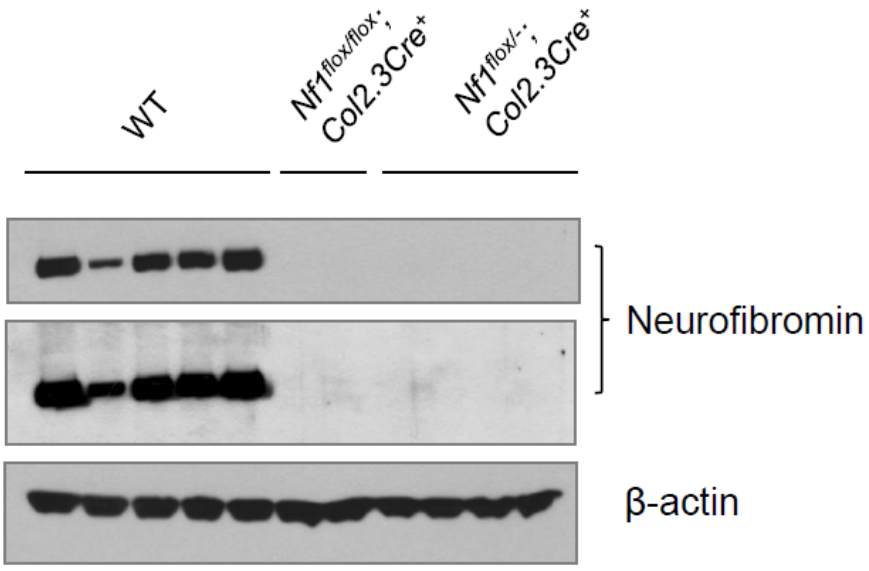
WT
Nf1flox/flox; Col2.3Cre+
Nf1flox/-; Col2.3Cre+
Neurofibromin
β-actin

Figure 5

**Figure 5.** Western blot showing the relative neurofibromin expression level in osteoblasts cultured from WT, *Nf1*$^{flox/flox}$*;Col2.3Cre*, and *Nf1*$^{flox/-}$*;Col2.3Cre* mice. Neurofibromin expression was undetectable in osteoblasts cultured from both *Nf1*$^{flox/flox}$*;Col2.3Cre* and *Nf1*$^{flox/-}$*;Col2.3Cre* mice, indicating that phenotypic differences between these strains are not attributable to differential Cre recombination of *Nf1* in the osteoblast lineage.

Conditional *Nf1* haploinsufficiency in myeloid progenitors and osteoclasts was achieved by placing Cre recombinase under the control of either the Lysozyme M (*LysM*) or Cathepsin K (*Ctsk*) promoter. *LysMCre* mice [128], generated by Dr. Irmgard Forster (University of Dusseldorf), and *CtskCre* mice[129], generated by Dr. R.A. Davey (University of Melbourne, Australia) were purchased from the Jackson Laboratory and intercrossed with $Nf1^{flox/flox}$ mice to yield $Nf1^{flox/+}$;$LysMCre^{+}$ and $Nf1^{flox/+}$;$CtskCre^{+}$ mice. $Nf1^{flox/+}$;$LysMCre^{-}$ and $Nf1^{flox/+}$;$CtskCre^{-}$ mice were used respectively as WT controls. Cre mediated recombination of the floxed *Nf1* allele was validated by PCR and western blot (Figure 6A-C). Experimental animals were maintained at the Indiana University Laboratory Animal Research Center (LARC) in accordance with the Institutional Animal Care and Use Committee (IACUC) guidelines.

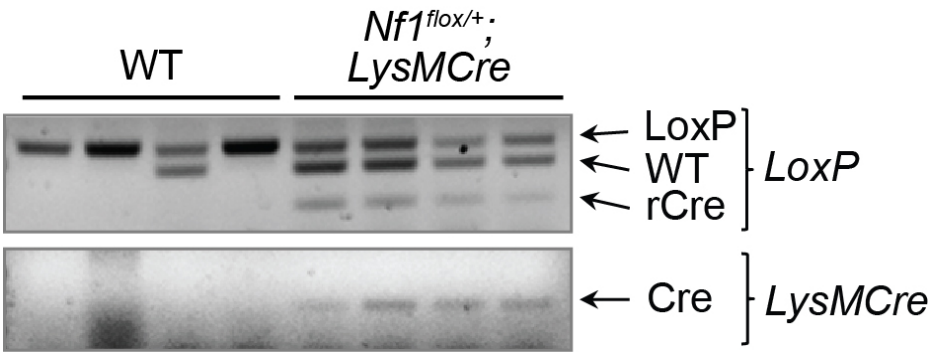


Figure 6A

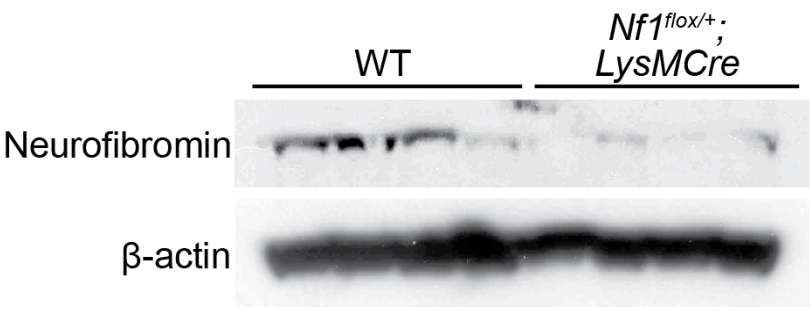


Figure 6B

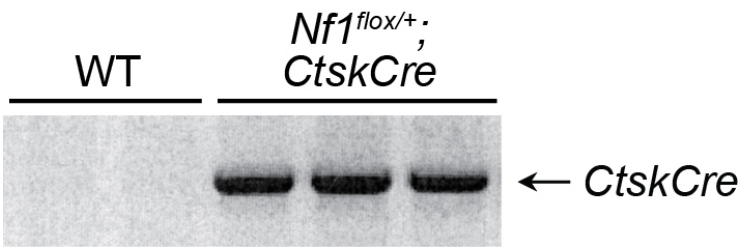


Figure 6C

**Figure 6.** Validation of *Nf1*$^{flox/+}$*;LysMCre* and *Nf1*$^{flox/+;}$*CtskCre* mouse models. (A) PCR genotyping was performed on tail genomic DNA from WT and *Nf1*$^{flox/+}$*;LysMCre* mice as shown. Bands representing the WT, *Nf1*-floxed, and *LysMCre* alleles are labeled accordingly. The Cre recombination band, labeled rCre, demonstrates efficient Cre mediated excision of the floxed *Nf1* allele. (B) Neurofibromin expression levels were detected by western blot in macrophages cultured from WT and *Nf1*$^{flox/+}$*;LysMCre* mice. (C) PCR genotyping of WT and *Nf1*$^{flox/+;}$*CtskCre* mice was performed on tail genomic DNA. Bands demonstrating the presence or absence of *CtskCre* are shown.

**Isolation of bone marrow**

Bone marrow was flushed from the femur, tibia, and iliac crest in a 5 mL volume of Alpha-Minimum Essential Medium (α-MEM, Gibco/Invitrogen), supplemented with 10% fetal bovine serum (FBS) using a 1.5 inch 23-guage needle. Low density bone marrow mononuclear cells (BMMNCs) were isolated by density gradient centrifugation for 30 min at 1750 rpm (gh-3.8 rotor, Beckman Coulter) on a 3.5 mL volume of Histopaque (Sigma). The buffy coat layer was collected and washed with α-MEM or other media prior to further assays.

**Osteoclast culture**

Murine osteoclasts

5 x$10^4$ BMMNCs from *Nf1*$^{+/-}$ and WT mice were cultured in 96-well plates in α-MEM supplemented with 10% FBS in the presence of murine recombinant RANKL (20 ng/mL; PeproTech), murine recombinant M-CSF (30 ng/mL; PeproTech), and in some instances, TGF-β1 (1 ng/mL; R&D Systems). After three days, the medium was changed to M-CSF (30 ng/mL), RANKL (60 ng/mL), and for certain experiments, TGF-β1 (1 ng/mL) for an additional three days of culture. To identify osteoclasts at the end of culture, adherent cells were fixed with and stained for tartrate resistant acid phosphatase (TRACP) using a commercially available kit (Sigma) according to the manufacturer's instructions. Images were acquired on a Nikon TE2000-S microscope using a QImaging camera and QCapture Pro software. Multinucleated, TRACP positive staining cells containing more than three nuclei were scored as mature osteoclasts.

Number of nuclei per osteoclast, mean osteoclast size, and TRACP positive multinucleated osteoclast area per high power field (HPF) were scored quantitatively using Image J software.

Human osteoclasts

Peripheral blood mononuclear cells (MNCs) were separated from heparinized peripheral blood by Histopaque (Sigma) centrifugation. MNCs were plated at a density of 5 x $10^4$ MNCs per well in 96-well plates and cultured in α-MEM supplemented with 10% FBS, human recombinant RANKL (50 ng/mL; PeproTech), and human recombinant M-CSF (30 ng/mL; PeproTech) for seven days with media replacement on day four as previously described [71]. Adherent cells were fixed in 10% formaldehyde in PBS, treated with ethanol–acetone (50:50), and stained for TRACP (Sigma). Images were acquired and analyzed in the same manner described above for murine osteoclast cultures.

**Osteoclast "pit" formation assays**

Bone marrow mononuclear cells were seeded on dentine slices (ALPCO Diagnostic, Windham, NH) and cultured in the presence of M-CSF and RANK-L at 37°C, 5% $CO_2$. Following seven days culture, dentine slices were rinsed with PBS and immersed overnight in 1 M ammonium hydroxide. After staining with a 1% crystal violet solution, the number and area of resorptive "pits" were quantified using NIH Image J Software on low-power fields (100x magnification).

**Mesenchymal stem cell culture**

BMMNCs flushed from the femora, tibiae, and iliac crests were suspended in 10 mL MesenCult® Mesenchymal Stem Cell (MSC) Basal Medium (Mouse) plus MSC Stimulatory Supplements (Stem Cell Technologies) and plated in a 10-cm tissue culture dish at 37°C, 5% $CO_2$ for continuous culture as described previously [73]. Once the cultures were 80–90% confluent, adherent cells were trypsinized and replated. MSCs at passage five to passage 10 were used for experiments.

**Osteoblast culture**

Osteoblast differentiation from MSCs

5 x $10^4$ MSCs were plated in 12-well tissue culture dishes and supplemented with osteogenic differentiation medium (MesenCult® MSC Basal Medium plus MSC Stimulatory Supplements, $10^{-8}$ M dexamethasone, 5 mg/mL ascorbic acid 2-phosphate and 10 mM β-glycerophosphate). The medium was changed every other day for one week of continuous culture as described previously [73]. Some MSCs were also supplemented with TGF-β1 (1 ng/mL) and SD-208 (1 μM) (Tocris Bioscience). Alkaline phosphatase (ALP) activity was subsequently assessed using an ALP staining kit (Sigma) according to the manufacturer's instructions. Photomicrographs of the stained cells were acquired with a Nikon TE2000-S microscope. ALP positive staining was quantified using Image J software.

Vertebral osteoblast cultures

Osteoblast-like cells were cultured from vertebrae as previously reported with minor modifications [130, 131]. Briefly, one-month-old mice were sacrificed and vertebrae were isolated by removing the surrounding muscle and connective tissue. Individual vertebrae (L1–L5) were collected and minced. Marrow cells were harvested by digestion of the minced tissue in a solution of type III collagenase (0.1 mg/mL) and 2.5% trypsin, while shaking in a hot water bath at 37°C for 40 min. The reaction was stopped by addition of 10 volumes of Dulbecco's Modified Eagle Media (DMEM; Gibco/Invitrogen) supplemented with 10% fetal bovine serum (FBS). The cells were then washed once with DMEM, and aggregates were removed from the cell suspension by sieving through a 70 μm strainer. Cell number was determined by counting trypan blue negative cells.

To examine the frequency of osteoblast progenitors in the marrow of *Nf1*$^{flox/-}$*;Col2.3Cre* lumbar vertebrae, colony forming units of osteoblasts (CFU-OBL) were assessed following ALP staining as previously described [73]. In brief, mononuclear cells from lumbar vertebrae were cultured at $2\times10^6$/mL in osteogenic differentiation medium (MesenCult® MSC Basal Medium plus MSC Stimulatory Supplements with $10^{-8}$ mol/L dexamethasone, 5 μg/mL ascorbic acid 2-phosphate, and 10 mmol/L β-glycerophosphate). After two weeks of culture, cells were washed with PBS and stained with 2% Alizarin Red S solution (pH = 4.2) for one hour. The cells were then washed with distilled water and incubated with 500 μL of 1% hydrochloric acid in 70% ethanol and shaken on a plate rotator for 30 min. The extracted supernatant was collected and the optical density was

measured at a wavelength of 450 nm. For each sample, measurements were performed in triplicate.

Von Kossa staining was also used to evaluate the osteogenic differentiation of marrow cells from the vertebrae. After four weeks culture in osteoblast differentiation media in 6-well tissue culture plates, the cells were fixed with 10% neutral formalin. Freshly prepared 5% silver nitrate (2 mL) was added to each well, and then incubated under UV light for 60 min. The dishes were then rinsed with distilled water and fixed with 5% sodium thiosulfate for 2 min. The wells were photographed using a phase-contrast microscope, and the number of mineralized bone nodules was recorded.

**Quantitative real-time PCR**

*Tgfb1* gene expression in WT and *Nf1* deficient MSCs was determined using quantitative real-time PCR. Primers used for *Tgfb1* were CAGTGGCTGAACCAAGGA (forward) and AGCAGTGAGCGCTGAATCG (reverse) and for *Gapdh* TGCACCACCAACTGCTTAG (forward) and GGATGCAGGGATGATGTTC (reverse). Total RNA was extracted using an RNeasy Plus mini kit (Qiagen). Reverse transcription was performed, and real-time PCR was carried out on an ABI 7500 system with SYBR® Green reagents (Applied Biosystems). Relative *Tgfb1* gene expression levels were determined with respect to the *Gapdh* control using the $\Delta C_T$ method [132].

**Serum TGF-β1 measurement**

250 μL of peripheral blood was collected by tail vein bleeding into EDTA-coated tubes (Beckton Dickinson). Serum was obtained following centrifugation at 3000 rpm in a microcentrifuge for 10 min. Total serum TGF-β1 levels were determined using a mouse TGF-β1 DuoSet ELISA Development kit (R&D systems). Since the assay is designed to detect only active TGF-β1, total TGF-β1 levels were measured by acid activation of latent TGF-β1 with 1 N HCL for 10 min, followed by neutralization with a 1.2 N NaOH/0.5 M HEPES solution per the manufacturer's protocol.

**Western blotting**

Following stimulation with TGF-β1 and/or various inhibitors, cells were lysed in a RIPA lysis buffer containing inhibitors for proteases and phosphatases. Isolated proteins were fractionated using NuPAGE 4-12% Bis-Tris Gels (Invitrogen) and electro-transferred to PVDF membranes. Callus proteins were harvested 14 days after tibial fracture using a mortar and pestle to grind the callus in proteolysis buffer. Immunoblots were carried out using antibodies specific to p-Smad2 (Cell Signaling), total Smad2 (Cell Signaling), active TGF-β1 (R&D Systems), latent (LAP)TGF-β1 (R&D Systems), and β-actin (Sigma). After incubation with anti-rabbit IgG or anti-mouse IgG (GE Healthcare) antibodies conjugated with HRP, signals were detected using ECL chemiluminescence substrate (Amersham). Densitometry was performed using Image J software.

**Smad dual-luciferase reporter assays**

Osteoprogenitors were transfected with Smad reporter, negative, and positive control dual-luciferase constructs (Cignal Reporter Assay, Qiagen) [133]. The Smad reporter construct contains a mixture of an inducible Smad responsive firefly luciferase reporter and a constitutively expressed *Renilla* construct in a 40:1 ratio. The *Renilla* construct constitutively expresses the *Renilla* luciferase reporter gene under the control of a CMV promoter element and functions as an internal control for normalizing transfection efficiencies. The negative control construct contains a mixture of non-inducible firefly luciferase reporter together with the constitutively expressed *Renilla* construct in a 40:1 ratio. The positive control construct contains a mixture of a constitutively expressing GFP, firefly luciferase, and *Renilla* luciferase constructs in a 40:1:1: ratio. Transfection was performed by incubating constructs in a 3:1 FuGENE® HD Transfection Reagent:DNA ratio according to the manufacturer's instructions (Promega). 24 hours following transfection, the culture medium was changed and supplemented with either recombinant active TGF-β1 (1 ng/mL) or 100 times the concentration of latent, LAP-TGF-β1 (100 ng/mL) for an additional 18 hours. Firefly and *Renilla* luciferase activities were measured on a 96-well microtiter plate luminometer (Thermo Labsystems) with LAR II and Stop&Glo reagents from the dual luciferase assay kit (Promega).

**Retroviral expression of *NF1* GRD**

Recombinant retrovirus constructs were used to re-express the human, full-length *NF1* GTPase activation (GAP) related domain (*NF1* GRD) in *Nf1* deficient MSCs under the transcriptional control of the murine stem cell virus (MSCV) promoter as described previously [73, 134]. A puromycin resistance gene, *pac*, is also placed under the control of the phosphoglycerate kinase (PGK) promoter as a selectable marker. 72 hours after transduction, puromycin (4 μg/mL) was used for selection.

**Gelatin zymography**

Gelatinolytic activities of murine myeloid cell conditioned media and human serum samples were assessed using sodium dodecyl sulfate (SDS) – polyacrylamide gel electrophoresis under non-reducing conditions as described previously [135]. Myeloid cell conditioned media (15 μL) was mixed with 5 μL of loading buffer (0.16 M Tris-HCl, 50% glycerol, 8% SDS, and 0.08% bromophenol blue) and loaded onto a 10% polyacrylamide gel copolymerized with 2 mg/mL gelatin (Sigma). Electrophoresis was performed at 120 V for 2-3 hours at 4°C. Gels were washed three times for 20 minutes each by immersion in 2.5% Triton X-100 (Sigma) with gentle shaking to remove residual SDS. Renaturation of the electrophoresed enzymes was achieved by incubation in zymography buffer (0.15 M NaCl, 5 mM $CaCl_2$, 0.05% $NaN_3$, 50 mM Tris-HCl, pH 7.5) for 48 hours at room temperature. Zones of lytic activity were revealed by staining with 0.05%

Coomassie brilliant blue G-250 (Sigma) in 2.5:1:7 ethanol-acetic acid-water followed by destaining with 2:1:7 isopropanol-acetic acid-water.

**Flow cytometry**

Marrow cells were incubated for 45 min at 4°C with saturating concentrations of anti-mouse antibodies in 100 µL 3% FBS/0.09% $NaN_3$ in PBS with 0.25 µg anti-mouse CD16/CD32 ("Fc Block"). For the myeloid progenitor analysis, the following antibodies from BD Biosciences were used: FITC-conjugated anti-lineage markers (CD3, CD4, CD8, B220, Mac1, Gr1, Ter119), anti-CD16/32-PE, anti-CD34-PacificBlue, anti-Sca1-APC-Cy7, and anti-c-Kit-PerCP-Cy5.5. For the mature lineage analysis, the following antibodies from BD Biosciences were used: anti-CD3-FITC, anti-CD8-PacBlue, anti-B220-V500, anti-Mac1-PE, anti-Gr1-PECy7, anti-CD4-APC-Cy7, anti-CD45.2-PerCP-Cy5.5. Cells were analyzed on an LSR II 407 flow cytometer, and single color compensation controls were acquired using polystyrene microbeads (BD Biosciences). All post-acquisition analyses were performed with FlowJo 7.6.3 software (TreeStar) with gating parameters determined by fluorescence minus-one controls. The following gating definitions were used: granulocyte-monocyte progenitors (GMPs): Lin–Sca1–c-Kit+CD34+FcγRII/ II+; myeloid cells: CD3-B220-; and monocytes: CD3-B220-Gr1-Mac1+ as described elsewhere [136].

**Bone marrow transplantation**

3 x $10^6$ syngeneic WT or *Nf1*$^{flox/+}$;*LysMCre* bone marrow cells were injected intravenously into the tail vein of lethally irradiated (1100 cGy, split dose) *Nf1*$^{flox/flox}$;*Col2.3Cre* recipient mice [84]. After waiting four months to allow stable engraftment of the donor hematopoietic cells, tibial fractures were induced as described below.

**Ovariectomy surgery**

12-week old mice underwent either ovariectomy or sham surgery. Mice were anesthetized using a mixture of ketamine (150 mg/kg) and xylazine (10 mg/kg) administered IP. A 2-cm midline dorsal skin incision was made, followed by incision of the peritoneal cavity to identify and excise the ovaries. pDEXA scans were acquired prior to surgery and again six weeks post-operatively to assess the percent change in BMD as described below. At the experimental endpoint of six weeks, the long-bones were excised for post-mortem analysis. Uterine weights of ovariectomized and sham operated mice were compared to validate the surgical method (Figure 7A, B).

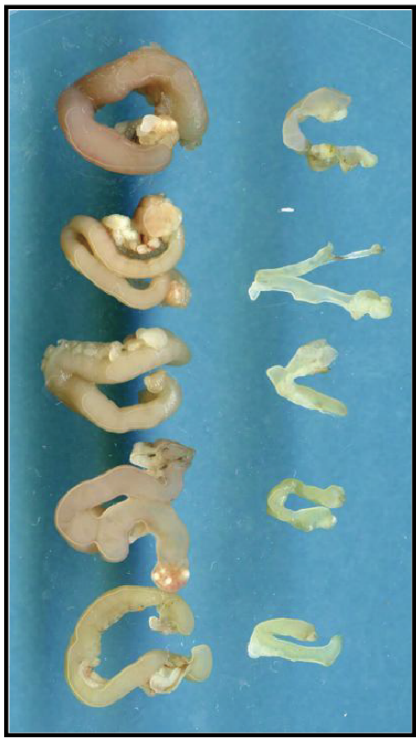


Figure 7A

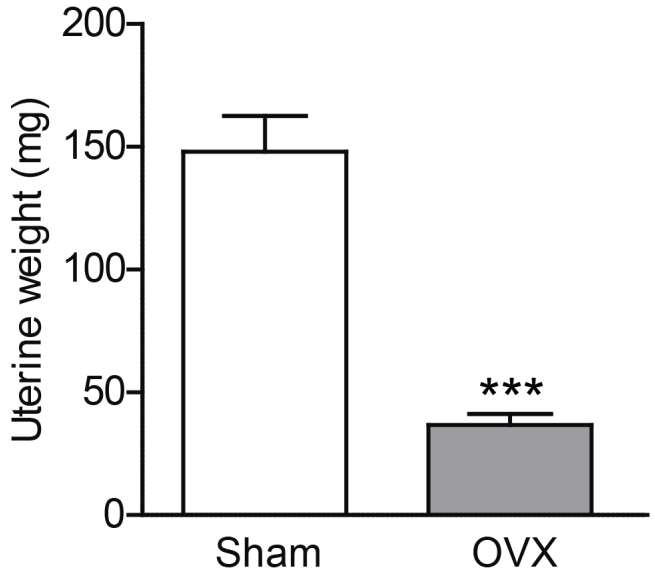


Figure 7B

**Figure 7. Uterine weights of ovariectomized (OVX) and sham operated mice were compared to validate the surgical method.** (A) Representative photographs illustrate the uterine size of sham versus OVX mice. (B) The uterine weight (mg) was measured on an analytic balance as shown in the bar graph above. $n$ = 20 per group. ***$P$ < 0.001, comparing the mean uterine weight of OVX mice to sham operated controls.

**Tibial fracture**

Open tibial fractures were induced by a three-point method in 12-week old *Nf1$^{flox/-}$;Col2.3Cre* mice under ketamine anesthesia as described previously [78, 137]. Prior to fracture, an intramedullary stabilizing rod (27-G needle) was inserted into the tibia to permit load-bearing. A 200-gram weight was dropped from a height of 30-cm to fracture the tibia. Proper fracture position between the middle to distal 1/3 of the tibia below the fibular junction was confirmed by x-ray (pixRay-100, Bioptics). Weekly radiographs were acquired to monitor fracture healing. Mice were euthanized with carbon dioxide at the experimental endpoint of four weeks. The long bones were harvested for further evaluation by μCT and histology as described below.

**TβRI inhibitor treatment**

The TβRI kinase inhibitor, SD-208, was reconstituted in a vehicle solution of 1% methylcellulose in sterile water. SD-208 was administered by gavage at a dose of 60 mg/kg/day. Some cohorts received the vehicle treatment (1% methylcellulose) as a control. Treatments were delivered once daily, beginning at the time of tibial fracture surgery for a duration of four weeks. For ovariectomy studies, SD-208 or vehicle was administered daily for six weeks.

**Biomechanical testing**

Vertebral compression tests

To evaluate the structural integrity of L5 vertebrae, biomechanical testing was conducted utilizing an R Series PC Controlled Test System: R 1.4.2 (TestResources Inc.). L5 vertebral bodies were isolated by removing the surrounding soft tissue and the adjacent intervertebral discs to expose the cranial and caudal bone surfaces. After equilibration to room temperature, L5 vertebral bodies were subjected to mechanical testing in compression at a rate of 20 mm/min. Peak load was defined as the maximum load that the specimen can withstand before fracturing. The cross sectional area of each vertebral body was measured in the medial and lateral (transverse) planes. Peak stress was calculated by the equation: peak stress = peak load/vertebral cross sectional area.

Three-point bending

Following euthanasia, the left tibia was dissected to remove the surrounding soft tissue, wrapped in saline-soaked gauze, and stored at -20°C. At the time of testing, all samples were equilibrated to RT in a saline bath. Tibias were positioned with the posterior side facing upwards across the two lower supports of an Electroforce 3200 three-point bending apparatus (Bose). The bones were loaded to failure under monotonic compression at a crosshead speed of 0.2 mms/s. Force-displacement measurements were acquired at 0.005 s intervals at a force resolution of 0.01 N. Ultimate force (N), yield force (N),

stiffness (N/mm), energy to failure (mJ), failure (breaking) force (N), and energy to yield (mJ) were computed from the force versus displacement curves.

**X-ray**

X-rays were acquired using a piXarray 100 DSR System (Bioptics). Whole spine anterior–posterior radiographs were taken. The height (mm) of the L5 vertebral body was measured between the cranial and caudal ends. In other experiments, lateral radiographs of fractured tibiae were obtained weekly under ketamine anesthesia. Fracture healing was monitored for a duration of four weeks until the experimental endpoint was reached.

**Peripheral dual-energy X-ray absorptiometry (pDEXA)**

BMD was measured using a PIXImus mouse densitometer (GE Lunar II, Faxitron Corp., Wheeling, IL). The mice were placed in the prone position on a specimen tray and scanned. The skull was excluded from total body scans. Regions of interest (ROI) included the lumbar spine (20 x 50 pixels) and distal femur immediately proximal to the growth plate (12 x 12 pixels). For certain experiments, the percent change in BMD was determined by comparing a baseline scan, acquired prior to the initiation of ovariectomy surgery or drug treatment, with an endpoint scan acquired prior to euthanasia.

**Peripheral quantitative computed tomography (pQCT)**

The whole axial spine was placed in the gantry of a XCT Research SA+ pQCT scanner (Stratec Medizintechnik GmbH, Pforzheim, Germany) with Software Version 5.50. A voxel size of 70 μm was used for analysis. A scout view was obtained and the anatomical reference line was positioned at the midpoint of the rostral/caudal margin of the L5 pedicle. Individual slices were obtained from each vertebra. The centrum of the vertebra was selected as the ROI. Volumetric bone mineral density (vBMD; $mg/cm^3$) of the cortical and trabecular bone was measured. The ratio of spinal canal area/vertebral body area was derived by measuring the area of the L5 vertebral body and the spinal intervertebral canal from the pQCT images.

**Micro-computed tomography (μCT)**

Formalin fixed femora were placed in the gantry of a micro-computed tomographer (VivaCT 40, SCANCO Medical). Images were acquired at a voxel size of 10.5 μm. The voxel of interest (VOI) comprised 100 transverse CT slices beginning 250 μm away from the femoral growth plate and extending proximally. Fractional bone volume (BV/TV, fraction) and microarchitectural properties of trabecular reconstructions, including trabecular thickness (Tb.Th., mm), trabecular number (Tb.N., $mm^{-1}$), trabecular spacing (Tb.Sp., mm), and connectivity density (Conn.D., $mm^{-3}$) were calculated using standard algorithms. For quantitative evaluation of tibial fracture calluses, contouring was performed for 100 transverse CT slices extending in both directions from the fracture

midline. Callus fractional bone volume (BV/TV) and volumetric bone mineral density (vBMD) were measured within the callus, excluding the cortical bone comprising the original tibial shaft.

**Histology**

Femur

Tissues were fixed in 10% formalin for 48 hours, demineralized for two weeks in 10% EDTA, and embedded in paraffin. 3.5 μm thick longitudinal sections were cut using a rotary microtome (Leica). Trabecular BV/TV of the secondary spongiosa and osteoblast numbers (N.Ob/BS) normalized to the bone surface were quantified on H&E stained sections of the distal femur at 200x magnification using BIOQUANT OSTEO v11.2 software (BIOQUANT Image Analysis Corporation). In a similar fashion, osteoclast numbers normalized to the bone surface (N.Oc/BS) were quantified on TRACP stained sections at 200x magnification.

Lumbar vertebrae

Lumbar vertebrae were harvested and fixed in 4% formaldehyde at RT. The vertebrae were then decalcified in 10% EDTA, 4% formaldehyde for four days. The tissues were then dehydrated in graded alcohols and embedded in paraffin. 5-μm thick longitudinal sections of L5 were obtained and processed for TRACP staining and MacNeal staining. N.Oc/BS and N.Ob/BS were quantified

by manual cell counting at 200x magnification on TRACP and MacNeal-stained sections, respectively.

**Immunohistochemistry**

For p-Smad2 immunohistochemical staining, sections were incubated in DeCal Retrieval Solution (Biogenex Laboratories, San Ramon, CA) for 30 min at RT. Primary antibody to p-Smad2 (Cell Signaling, diluted 1:100) was applied overnight at 4°C. Vectastain ABC kit containing biotinylated secondary antibody (diluted 1:2000) and 3,3'-diaminobenzidine (DAB) substrate kit (Vector Laboratories) were used for detection. Quantification of p-Smad2 staining in fracture calluses was performed with Aperio ImageScope v11.1.2.760 software using the Positive Pixel Count v9 algorithm under default settings.

**Dynamic histomorphometry**

Two doses of the fluorochrome label calcein (30 mg/kg) were administered by intraperitoneal injection 11 and three days prior to euthanasia. Femurs were fixed in 10% neutral-buffered formalin for 48 hours, dehydrated in graded ethanols, and embedded without decalcification in methylmethacrylate. 6-μm thick sections were analyzed at 100x magnification on four independent fields beginning 100 μm distal to the growth plate and excluding cortical bone. The bone surface (BS), single labeled surface (sLS), double label surface (dLS), and interlabel width (Ir.L.Wi) were determined by manually tracing the perimeter of interest in BIOQUANT OSTEO v11.2 software (BIOQUANT Image Analysis

Corporation). The mineralizing surface (MS/BS; %), mineral apposition rate (MAR, μm/day), and bone formation rate (BFR; $\mu m^3/\mu m^2$/year) were derived using standard formulas.

**Statistical analysis**

Differences between experimental groups were interrogated using the Student's t-test or either one- or two-factor analysis of variance (ANOVA) statistical tests as appropriate. In the instances where the ANOVA was significant, post-hoc testing was performed between individual groups using the Newman-Keuls multiple comparison test. An alpha level of 5% was set as the type I error rate for all studies, with $p$ values $< 0.05$ required to reject the null-hypothesis.

# CHAPTER 3. MODELING NF1 SKELETAL DEFECTS IN THE MOUSE

## Introduction

The development of effective targeted therapies for the treatment of NF1 associated skeletal manifestations has been hampered by the lack of appropriate animal models which accurately recapitulate the cardinal features of NF1 osseous disease. As described in Chapter 1, genetic studies in *Nf1*$^{+/-}$ and *Nf1*$^{OB-/-}$ (harboring *Nf1* nullizygous osteoblasts) mice have implicated *Nf1* deficient osteoblasts and/or their progenitors as critical mediators in the recalcitrant bone repair process [76, 79, 138]. These models are limited, however, in that they do not spontaneously recapitulate many of the hallmark skeletal manifestations of NF1 patients including osteoporosis, spinal deformities, and pseudarthrosis which cumulatively affect up to 70 percent of the NF1 patient population. Here, we demonstrate that *Nf1*$^{flox/-}$*;Col2.3Cre* mice, harboring *Nf1* nullizygous osteoblasts on a systemic *Nf1*$^{+/-}$ background, exhibit multiple osseous features that are closely reminiscent of those seen in the human disease, including bone mass deficits (osteoporosis), spinal deformities, and tibial fracture non-union (pseudarthrosis). This chapter will characterize the various skeletal phenotypes observed in the *Nf1*$^{flox/-}$*;Col2.3Cre* mouse model, correlating these findings with the clinical features of human patients with NF1.

**Bone mass deficits (osteoporosis) in *Nf1$^{flox/-}$;Col2.3Cre* mice**

Reduced BMD, cortical, and trabecular bone mass in the lumbar spine of *Nf1$^{flox/-}$;Col2.3Cre* mice

Kuorilehto and colleagues previously documented that the lowest local BMD values in NF1 patients tended to be clustered to the load-carrying anatomical regions including the spine and lower limbs [23]. Within the spine, the lumbar region contains the primary load-bearing vertebrae, L1-L5. Recent clinical reports have confirmed that reduced BMD in the lumbar spine is a prominent feature of NF1 patients with bone involvement [25], and moreover, tends to correlate with the severity of scoliosis in such patients [30]. Here, we show that *Nf1$^{flox/-}$;Col2.3Cre* mice (harboring *Nf1* nullizygous osteoblasts on a *Nf1$^{+/-}$* background) exhibit a phenotype which is analogous to the human disease. When we used pDEXA to compare the BMD of the lumbar spine (L1-L5) between *Nf1$^{flox/-}$;Col2.3Cre* mice and various controls, we observed a significant reduction in L1-L5 BMD within the *Nf1$^{flox/-}$;Col2.3Cre* mice versus controls (Figure 8A, B). In contrast, we observed no significant differences when we compared the BMD of the whole axial spine in *Nf1$^{flox/-}$;Col2.3Cre* mice versus controls (Figure 8C). Consistent with these findings, clinical studies which report reduced BMD in site-specific regions, such as the spine or femur of NF1 patients, often do not observe statistically significant differences when comparing total body BMD between NF1 patients and healthy age/sex matched controls [25].

To further dissect whether reductions in L1-L5 BMD in *Nf1$^{flox/-}$;Col2.3Cre* mice were primarily due to loss of cortical or trabecular bone, we analyzed the L5 vertebral bodies of *Nf1$^{flox/-}$;Col2.3Cre* mice by peripheral quantitative computed tomography (pQCT) and compared the results to WT controls (Figure 9A). Cortical volumetric BMD (vBMD) (Figure 9B), cortical bone area (Figure 9C), and trabecular vBMD (Figure 9D) were significantly reduced in the L5 vertebrae of *Nf1$^{flox/-}$;Col2.3Cre* mice. These data imply that reductions in L1-L5 BMD in *Nf1$^{flox/-}$;Col2.3Cre* mice are likely due to deficiencies in both the cortical and trabecular bone compartments.

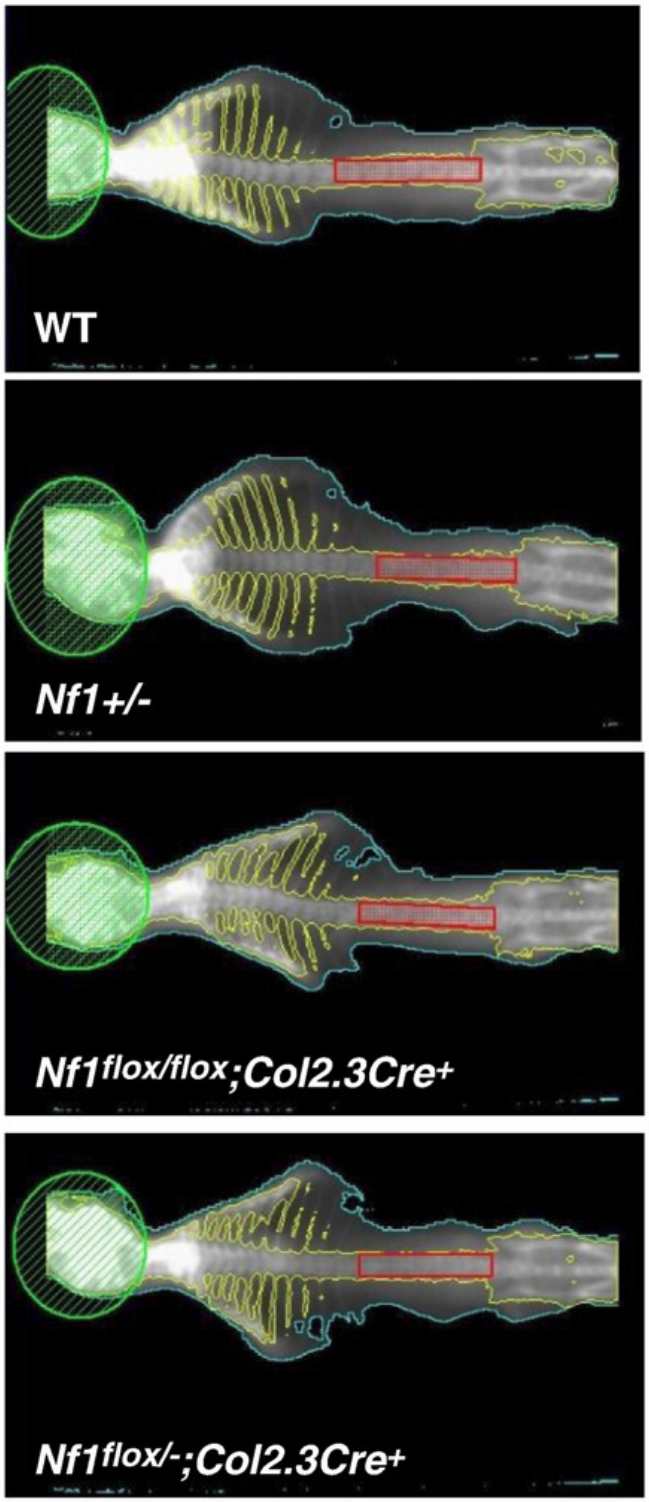


Figure 8A

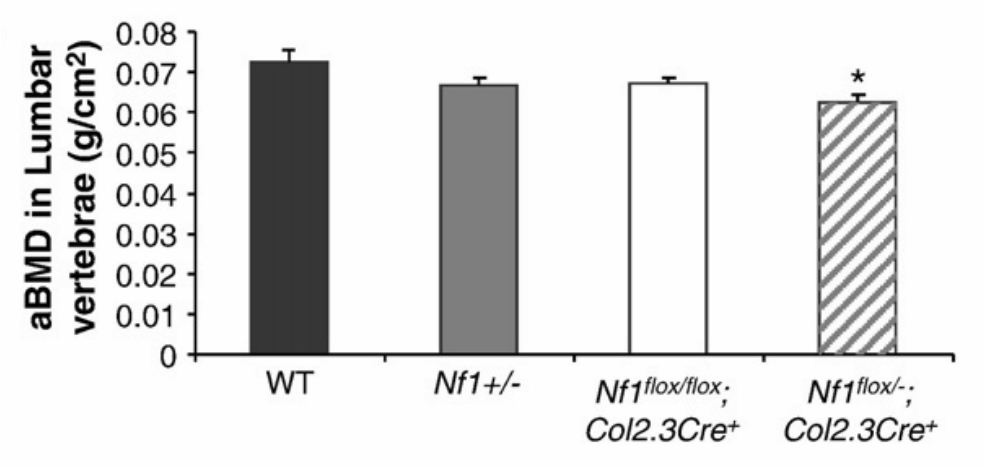
aBMD in Lumbar vertebrae (g/cm²)
0.08
0.07
0.06
0.05
0.04
0.03
0.02
0.01
0
*
WT
Nf1+/-
Nf1flox/flox; Col2.3Cre+
Nf1flox/-; Col2.3Cre+

Figure 8B

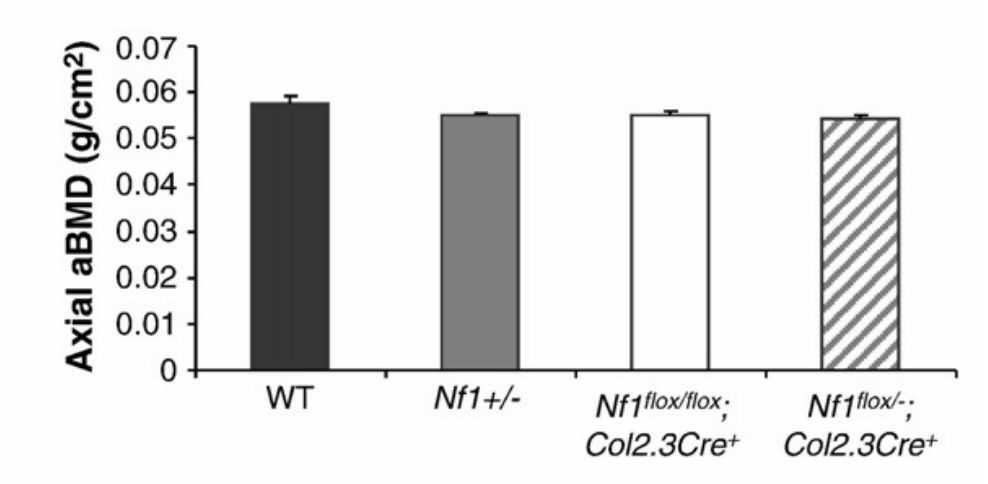
Axial aBMD (g/cm²)
0.07
0.06
0.05
0.04
0.03
0.02
0.01
0
WT
Nf1+/-
Nf1flox/flox; Col2.3Cre+
Nf1flox/-; Col2.3Cre+

Figure 8C

**Figure 8. Reduced bone mineral density (BMD) in the L1–L5 vertebrae of *Nf1$^{flox/-}$;Col2.3Cre* mice.** (A) Representative pDEXA scans. The calvarium was excluded from the measurement of total axial BMD. The region of interest enclosed by the red rectangle includes the L1–L5 vertebrae. (B) L1-L5 BMD (g/cm$^2$) was quantified by pDEXA as shown. Data represent the mean ± SEM of nine mice in each genotype group. *$P$ < 0.05 for *Nf1$^{flox/-}$;Col2.3Cre* mice vs. WT controls as determined by ANOVA and multiple-comparison post-hoc t-tests. (C) Total axial BMD was quantified by pDEXA and revealed no-significant differences between genotypes.

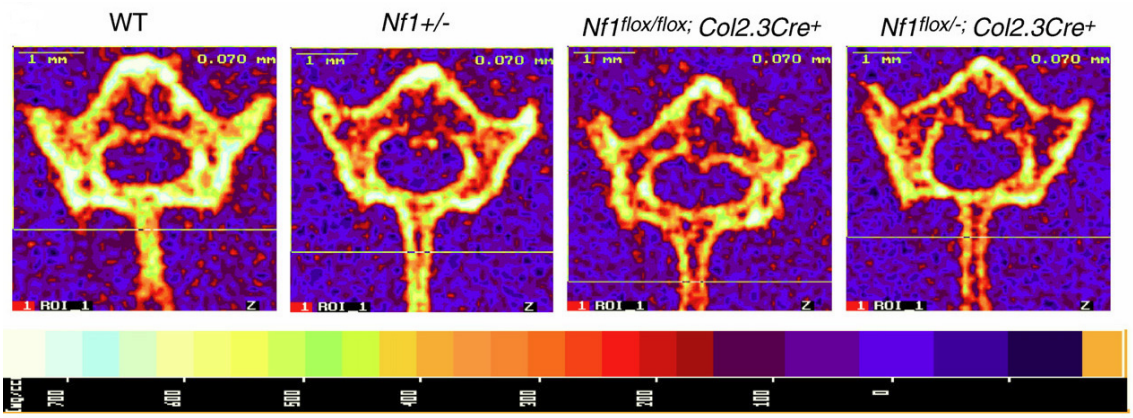
WT
Nf1+/-
Nf1flox/flox; Col2.3Cre+
Nf1flox/-; Col2.3Cre+
1 mm
0.070 mm
1 ROI_1
Z
mg/cc
700
490
560
420
350
280
140
0

Figure 9A

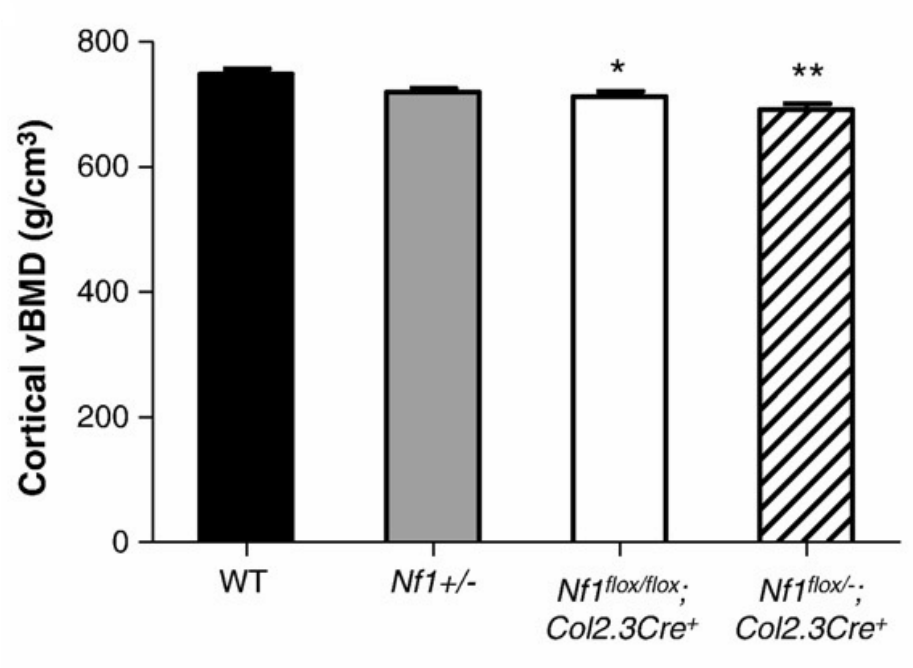
800
600
400
200
0
Cortical vBMD (g/cm³)
*
**
WT
Nf1+/-
Nf1flox/flox; Col2.3Cre+
Nf1flox/-; Col2.3Cre+

Figure 9B

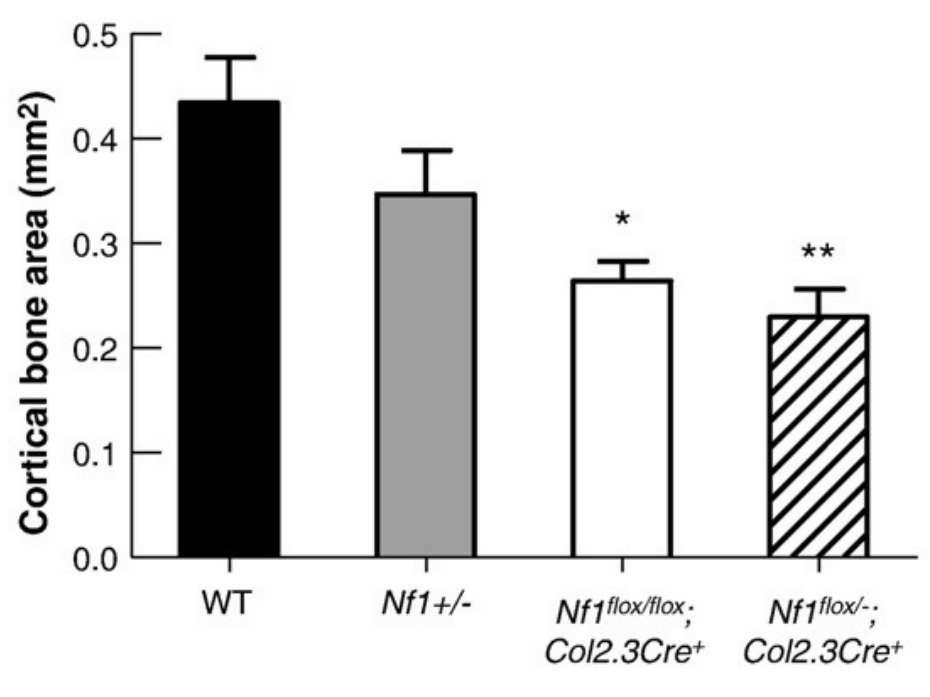
Cortical bone area (mm²)
0.5
0.4
0.3
0.2
0.1
0.0
*
**
WT
Nf1+/-
Nf1flox/flox; Col2.3Cre+
Nf1flox/-; Col2.3Cre+

Figure 9C

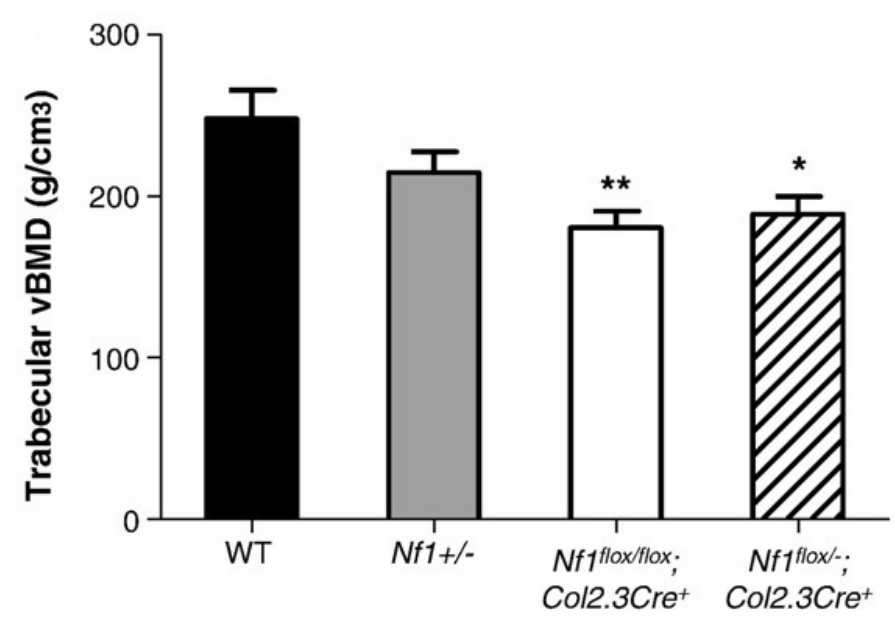
Trabecular vBMD (g/cm3)
300
200
100
0
**
*
WT
Nf1+/-
Nf1flox/flox; Col2.3Cre+
Nf1flox/-; Col2.3Cre+

Figure 9D

**Figure 9. Reduced cortical and trabecular bone mass in the L5 vertebrae of *Nf1$^{flox/-}$;Col2.3Cre* mice.** (A) Representative pQCT cross sections from L5 of four genotypes of mice. The relative intensity of bone is shown in the bottom panel. (B) Cortical vBMD of L5 was assessed at the midpoint between the rostral/caudal margins of the pedicle in four different genotypes of mice as shown. Data represent mean ± SEM of 9–10 mice per genotype. *$P < 0.05$ *Nf1$^{flox/flox}$;Col2.3Cre* vs. WT. ** $P < 0.001$ *Nf1$^{flox/-}$;Col2.3Cre* vs. WT. (C). The cortical bone area in the L5 vertebral body was compared between the four groups of mice. Data represent mean ± SEM of 9–10 mice per genotype. *$P < 0.01$ *Nf1$^{flox/flox}$;Col2.3Cre* vs. WT. **$P < 0.01$ *Nf1$^{flox/-}$;Col2.3Cre* vs. WT. (D) Trabecular vBMD within the L5 vertebral body was compared between the four genotypes of mice. Data represent mean ± SEM of 9–10 mice per group. **$P < 0.01$ *Nf1$^{flox/flox}$;Col2.3Cre* vs. WT. *$P < 0.05$ *Nf1$^{flox/-}$;Col2.3Cre* vs. WT.

Reduced femoral BMD and trabecular bone mass in *Nf1$^{flox/-}$;Col2.3Cre* mice

The lower extremities are another load-bearing anatomical region where BMD is frequently compromised in the NF1 patient population [23]. We observed significant reductions in femoral BMD (Figure 10A) and trabecular bone volume fraction (BV/TV) (Figure 10B) in *Nf1$^{flox/-}$;Col2.3Cre* mice as compared to controls. Corroborating these results, analogous reductions in bone mass were also observed in *Nf1$^{flox/-}$;PeriCre* mice, in which a 3.9kb fragment of the Periostin promoter mediates Cre expression in mesenchymal stem cells (MSCs) and osteoblast precursors [78]. In sum, these studies validate that *Nf1$^{flox/-}$;Col2.3Cre* mice develop bone mass deficits with an anatomical specificity that is analogous to human NF1 patients with osteoporosis.

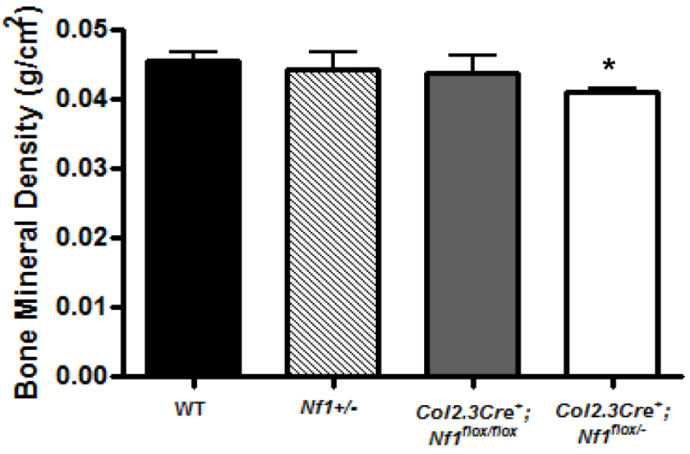
Bone Mineral Density (g/cm2)
0.05
0.04
0.03
0.02
0.01
0.00
*
WT
Nf1+/-
Col2.3Cre+; Nf1flox/flox
Col2.3Cre+; Nf1flox/-

Figure 10A

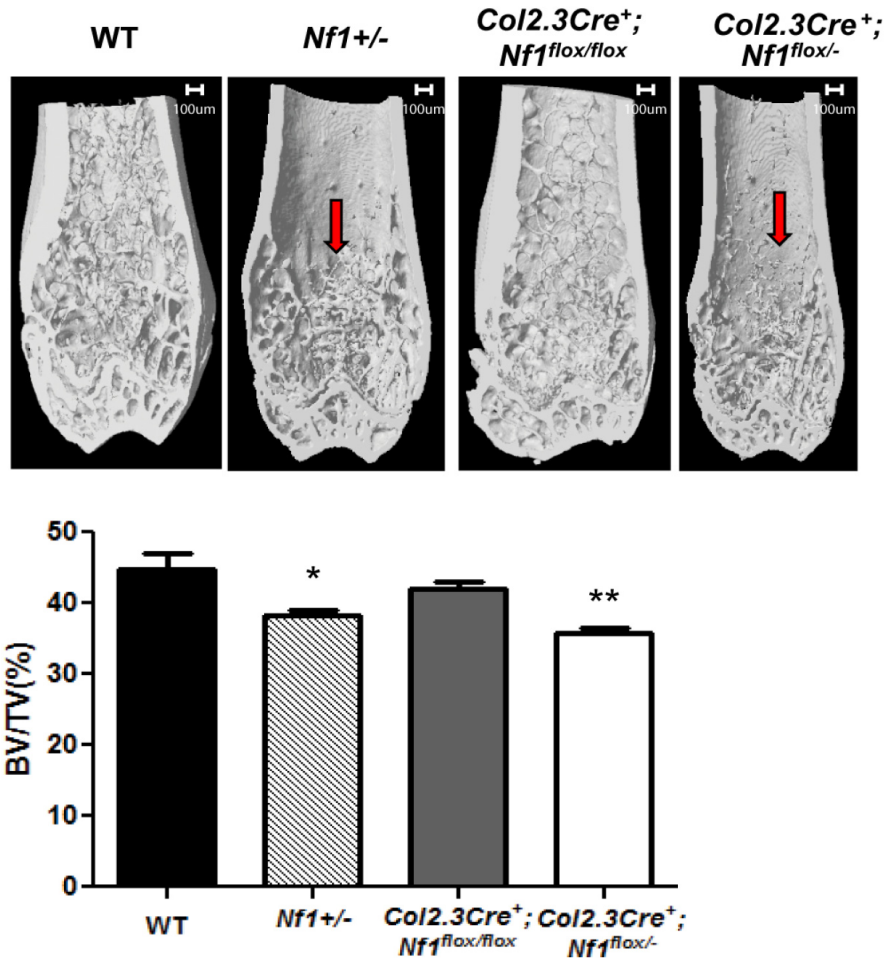
WT
Nf1+/-
Col2.3Cre+; Nf1flox/flox
Col2.3Cre+; Nf1flox/-
100um
BV/TV(%)
50
40
30
20
10
0
*
**
WT
Nf1+/-
Col2.3Cre+; Nf1flox/flox
Col2.3Cre+; Nf1flox/-

Figure 10B

**Figure 10. *Nf1*$^{flox/-}$*;Col2.3Cre* mice have reduced BMD and trabecular bone mass in the distal femur.** (A) BMD was measured by pDEXA scans acquired at eight weeks of age. *n* = 10-12 mice per group. **P* < 0.05 as compared to WT. (B, Top panel) Representative μCT reconstructions of the distal femur in longitudinal cross-section acquired at four months of age are shown. (Bottom panel) Femoral bone volume fraction (BV/TV) was quantified by μCT. n = 5 mice per group. **P* < 0.05, ***P* < 0.01 as compared to WT.

Impaired biomechanical integrity of *Nf1$^{flox/-}$;Col2.3Cre* vertebrae and tibiae

Recent studies have demonstrated the clinical ramifications of osteopenia and osteoporosis within the NF1 patient population in terms of increased fracture risk. NF1 patients were found to exhibit a markedly increased incidence of fracture and pathological fracture (occurring with minimal trauma) as compared to matched, healthy controls [27, 44]. We therefore sought to ascertain whether the bone mass reductions observed in *Nf1$^{flox/-}$;Col2.3Cre* mice were accompanied by similar deficiencies in bone strength. We began by evaluating the load bearing capacity of L5 in mechanical compression. Peak load to failure in the L5 vertebrae of *Nf1$^{+/-}$*, *Nf1$^{flox/flox}$;Col2.3Cre*, and *Nf1$^{flox/-}$;Col2.3Cre* mice was significantly diminished in comparison to WT mice (Figure 11, top panel). Both peak load and peak stress to failure (Figure 11, bottom panel) were lowest in *Nf1$^{flox/-}$;Col2.3Cre* mice as compared to the other experimental genotypes, although these properties were also compromised to a lesser extent in L5 vertebrae from both *Nf1$^{+/-}$* and *Nf1$^{flox/flox}$;Col2.3Cre*. These data are consistent with our previous observations that the most profound reductions in L5 BMD occurred in *Nf1$^{flox/-}$;Col2.3Cre* mice as compared to the other mouse genotypes. Whole tibiae from *Nf1$^{flox/-}$;Col2.3Cre* mice exhibited similar deficiencies in three-point bending, showing significant reductions in multiple mechanical indices including yield force (N), energy to yield (mJ), ultimate force (N), failure (breaking) force (N), and stiffness (N/mm) (Figure 12).

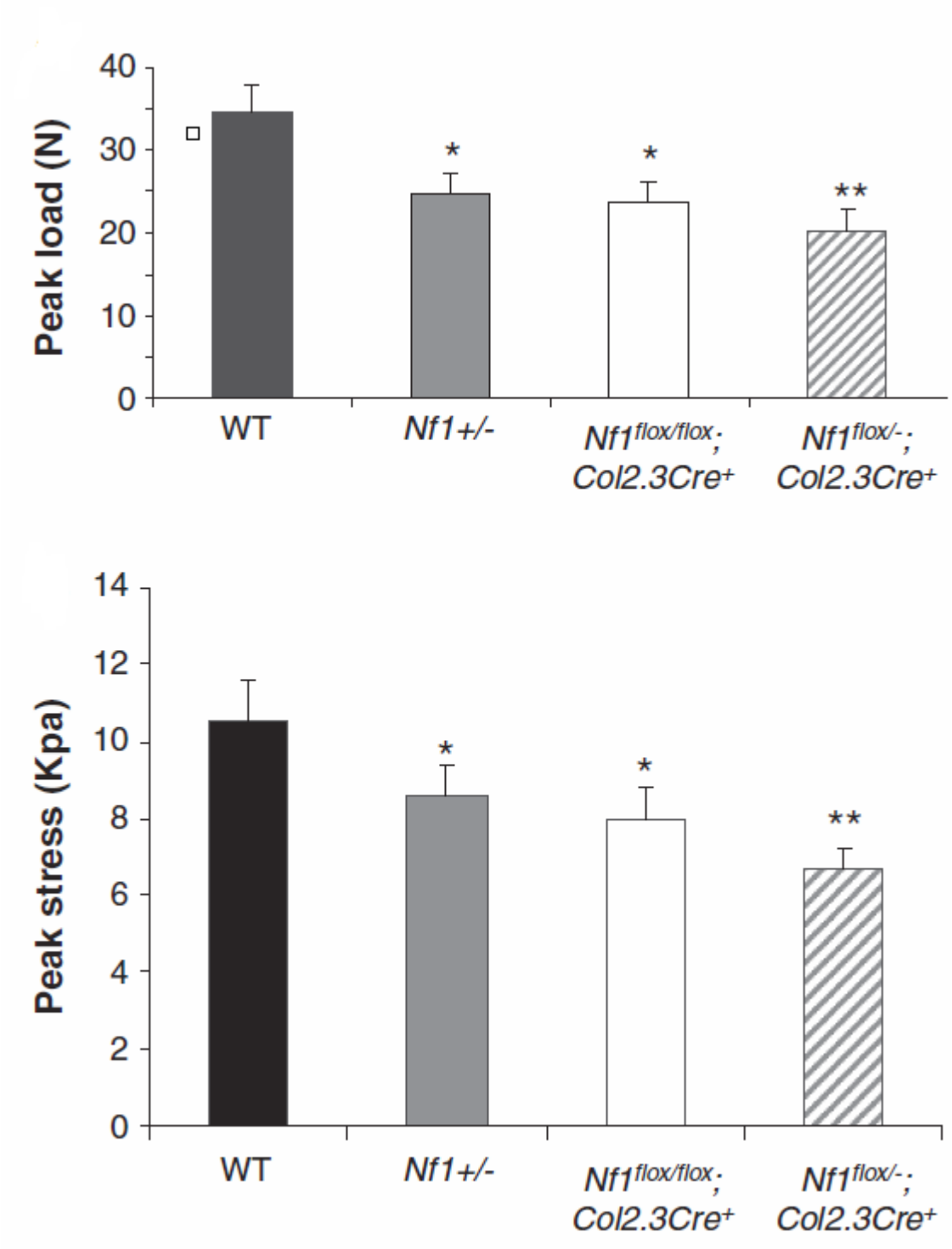
Peak load (N)
40
30
20
10
0
*
*
**
WT
Nf1+/-
Nf1flox/flox; Col2.3Cre+
Nf1flox/-; Col2.3Cre+
Peak stress (Kpa)
14
12
10
8
6
4
2
0
*
*
**
WT
Nf1+/-
Nf1flox/flox; Col2.3Cre+
Nf1flox/-; Col2.3Cre+

Figure 11

**Figure 11. Quantitative evaluation of L5 vertebral peak load.** (Top) The peak load to failure (N) in L5 vertebra was compared between four genotypes. *$P$ < 0.01 for comparing *Nf1*$^{+/-}$ or *Nf1*$^{flox/flox}$*;Col2.3Cre* mice with WT controls. **$P$ < 0.001 for comparing *Nf1*$^{flox/-}$*;Col2.3Cre* mice with WT mice. (Bottom) The peak stress (Kpa) in L5 vertebrae was measured for each genotype. *$P$ < 0.01 for comparing *Nf1*$^{+/-}$ or *Nf1*$^{flox/flox}$*;Col2.3Cre* mice with WT controls. **$P$ < 0.001 for comparing *Nf1*$^{flox/-}$*;Col2.3Cre* mice with WT mice.

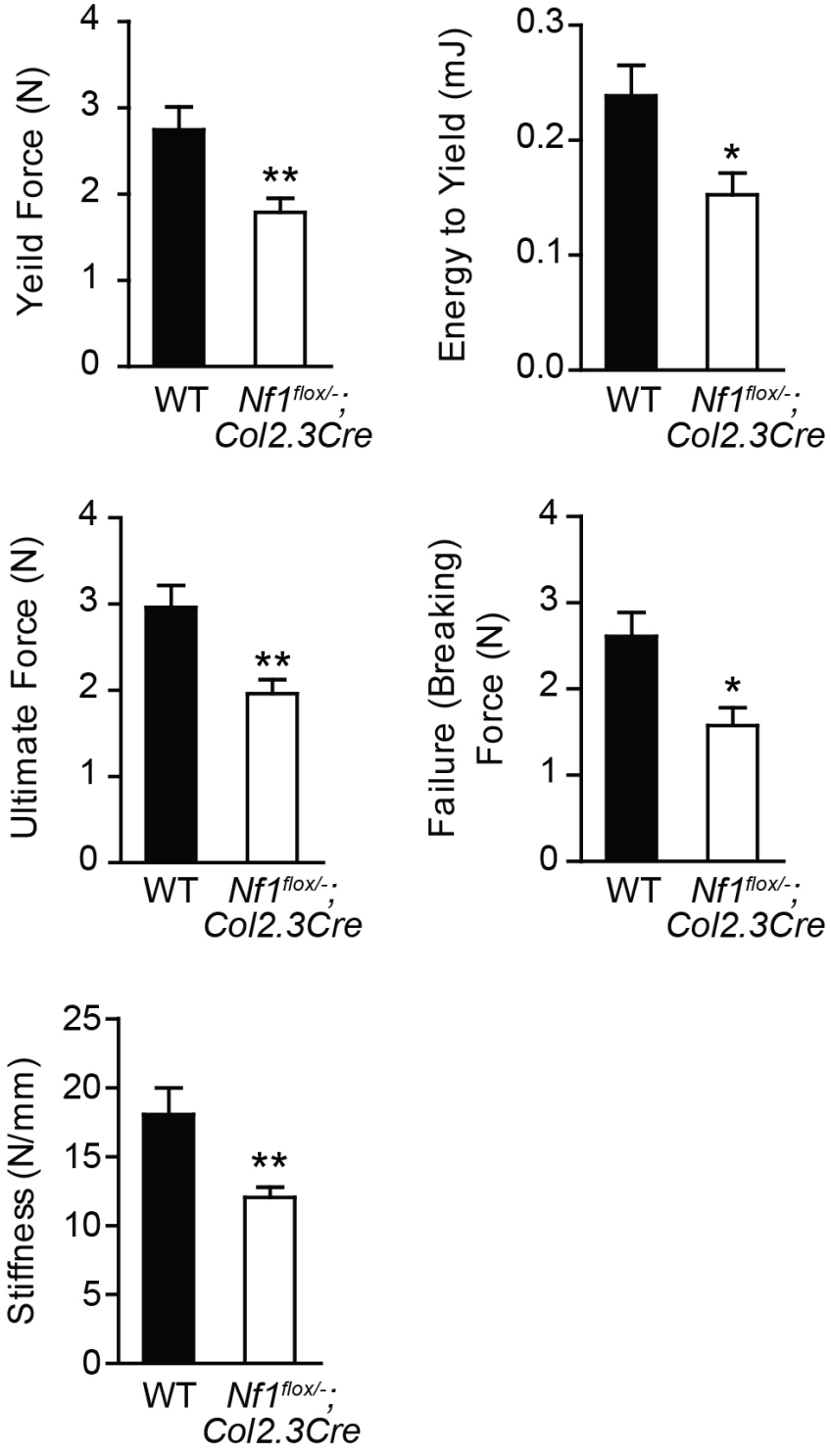
Yeild Force (N)
4
3
2
1
0
**
WT
Nf1flox/-; Col2.3Cre
Energy to Yield (mJ)
0.3
0.2
0.1
0.0
*
WT
Nf1flox/-; Col2.3Cre
Ultimate Force (N)
4
3
2
1
0
**
WT
Nf1flox/-; Col2.3Cre
Failure (Breaking) Force (N)
4
3
2
1
0
*
WT
Nf1flox/-; Col2.3Cre
Stiffness (N/mm)
25
20
15
10
5
0
**
WT
Nf1flox/-; Col2.3Cre

Figure 12

**Figure 12. Reduced fracture toughness in tibias of *Nf1$^{flox/-}$;Col2.3Cre* mice.** The mechanical integrity of tibias from WT and *Nf1$^{flox/-}$;Col2.3Cre* mice were tested under three-point bending. Significant reductions in yield force (N), energy to yield (mJ), ultimate force (N), failure (breaking) force (N), and stiffness (N/mm) are shown in the bar graphs above. $n$ = 5-7. *$P$ < 0.05, **$P$ < 0.01 as compared to WT.

Impaired bone remodeling in *Nf1$^{flox/-}$;Col2.3Cre* L5 vertebrae

Bone remodeling is a constitutive process where mature bone tissue is resorbed by osteoclasts and replaced with new bone matrix by osteoblasts. Uncoupling of this dynamic process can result in metabolic bone diseases, such as osteoporosis, where the resorptive capacity of osteoclasts outstrips the rate at which osteoblasts generate new bone matrix. We therefore tested whether dysregulated bone remodeling may be associated with the low bone mass phenotype of *Nf1$^{flox/-}$;Col2.3Cre* mice. The bone remodeling process was monitored *in vivo* by intraperitoneal injection of two fluorochromes, calcein (green) and alizarin (red), administered eight and three days prior to euthanasia, respectively. Representative photomicrographs illustrate a markedly reduced incorporation of the calcein and alizarin labels into the trabecular bone surface of L5 *Nf1$^{flox/-}$;Col2.3Cre* vertebrae as compared to WT controls (Figure 13A). Statistically significant reductions in the active bone-forming surface, or mineralizing surface (MS/BS, %), and the mineral apposition rate (MAR, μm/day), a measure of the rate of radial expansion of new bone, were observed in the *Nf1$^{flox/-}$;Col2.3Cre* L5 vertebrae versus controls. Moreover, the bone formation rate (BFR, $\mu m^3/\mu m^2$/year), an overall measure of bone formation that combines MS/BS and MAR, was dramatically reduced in *Nf1$^{flox/-}$;Col2.3Cre* mice as compared to WT. Collectively, these data suggest an uncoupling of the bone remodeling process in the *Nf1$^{flox/-}$;Col2.3Cre* mice, in which defective *Nf1* nullizygous osteoblasts are unable to regenerate and mineralize new bone matrix as it is progressively degraded by hyper-resorptive *Nf1$^{+/-}$* osteoclasts.

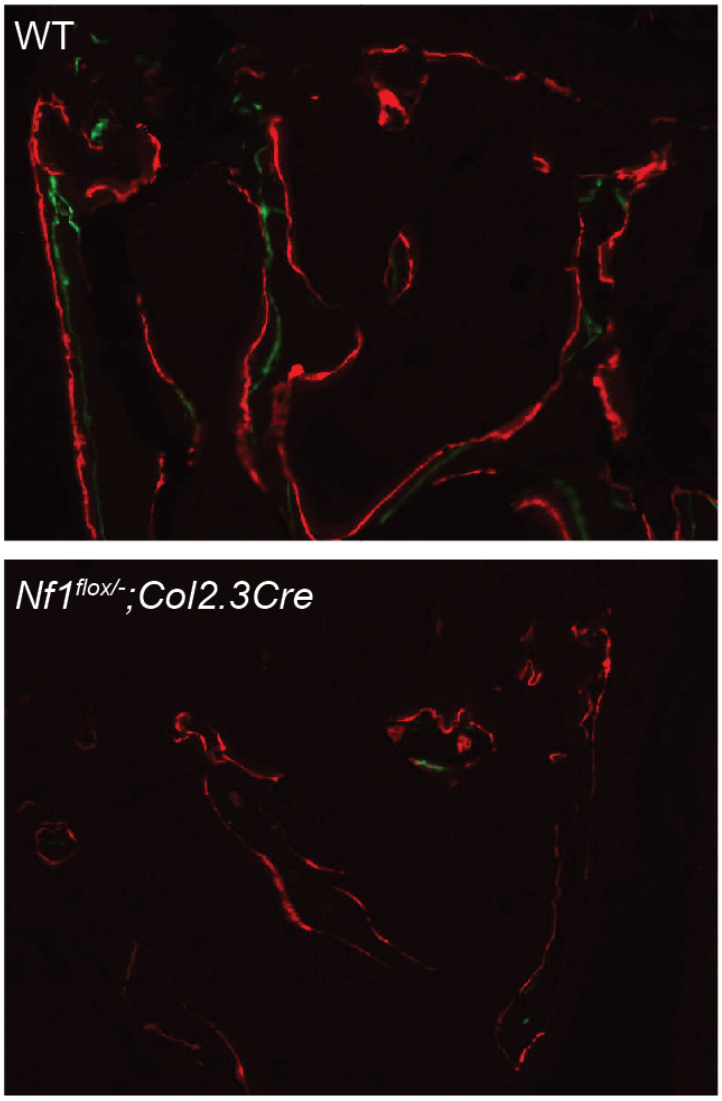


Figure 13A

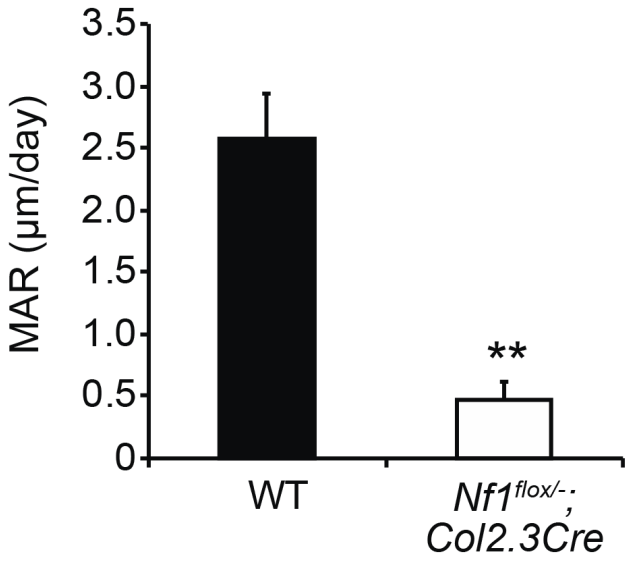


Figure 13B

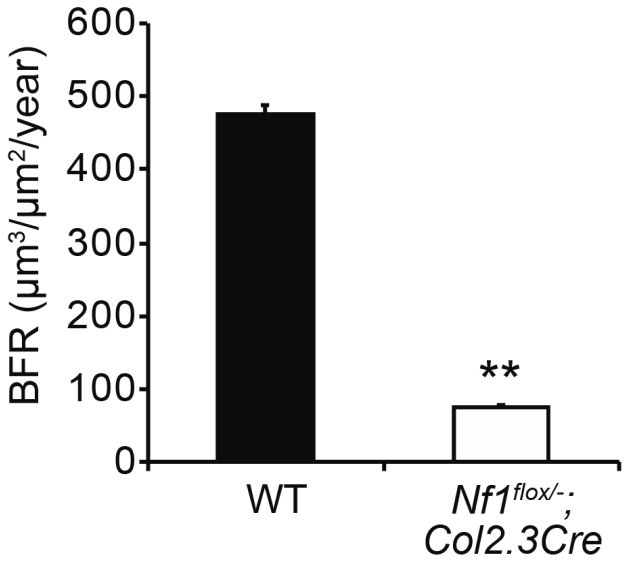


Figure 13C

**Figure 13. Defective bone remodeling in L5 vertebrae of *Nf1$^{flox/-}$;Col2.3Cre* mice.** (A) Representative photomicrographs show calcein and alizarin labeling of L5 vertebrae at 200x magnification (B) The mineral apposition rate (MAR, μm/day) was calculated as shown. $n = 5$. *$P < 0.05$, **$P < 0.01$ as compared to WT. (C) The bone formation rate (BFR, $\mu m^3/\mu m^2$/year) was quantified as shown. $n = 5$. *$P < 0.05$, **$P < 0.01$ as compared to WT.

Altered osteoclast and osteoblast numbers in *Nf1$^{flox/-}$;Col2.3Cre* mice

Osteoclasts and osteoblasts are the two major cell lineages responsible for maintaining skeletal homeostasis. Imbalances in the differentiation and/or activity of these cell types can lead to pathological alterations in bone mass. As quadrupeds, mice bear mechanical loading with the upper facet process of their vertebrae. To determine whether the number or morphology of these lineages might be altered in *Nf1$^{flox/-}$;Col2.3Cre* mice, we quantified osteoclast and osteoblast numbers within histological sections of the upper L5 facet process. Here, we show that osteoclast numbers per mm of bone surface were significantly increased in the upper facet processes of *Nf1$^{+/-}$* and *Nf1$^{flox/-}$;Col2.3Cre* mice as compared WT and *Nf1$^{flox/flox}$;Col2.3Cre* mice (Figure 14A). In addition, significantly reduced osteoblast numbers per mm of bone surface were observed in the upper L5 facet process of *Nf1$^{flox/-}$;Col2.3Cre* mice, even as compared to *Nf1$^{+/-}$* and *Nf1$^{flox/flox}$;Col2.3Cre* mice which exhibited more mild reductions in osteoblast counts (Figure 14B). These histological changes are commensurate with BMD reductions and defective bone remodeling within the lumbar spine of *Nf1$^{flox/-}$;Col2.3Cre* mice as described above. Consistent with these data, we also observed analogous skewing in osteoclast and osteoblast frequencies within the distal femur of *Nf1$^{flox/-}$;Col2.3Cre* mice [78].

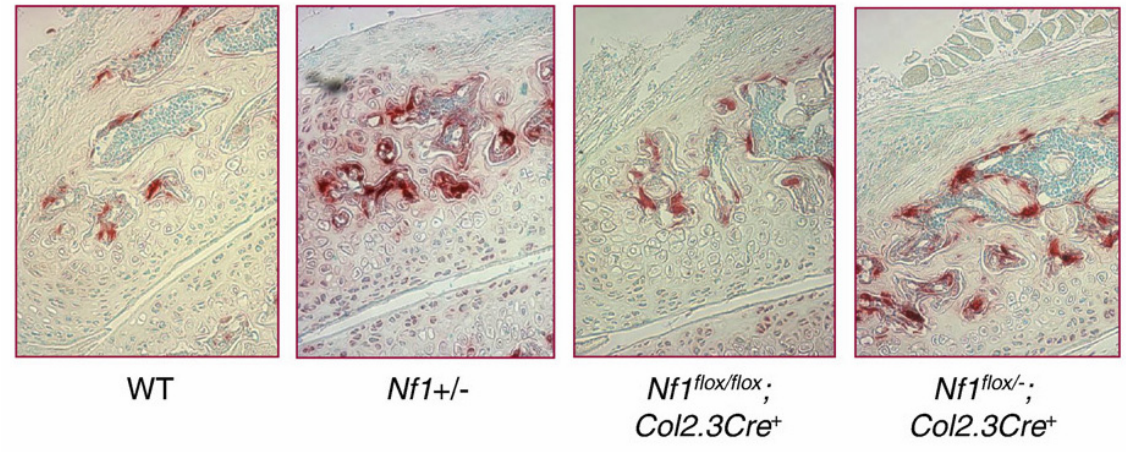
WT
Nf1+/-
Nf1flox/flox; Col2.3Cre+
Nf1flox/-; Col2.3Cre+

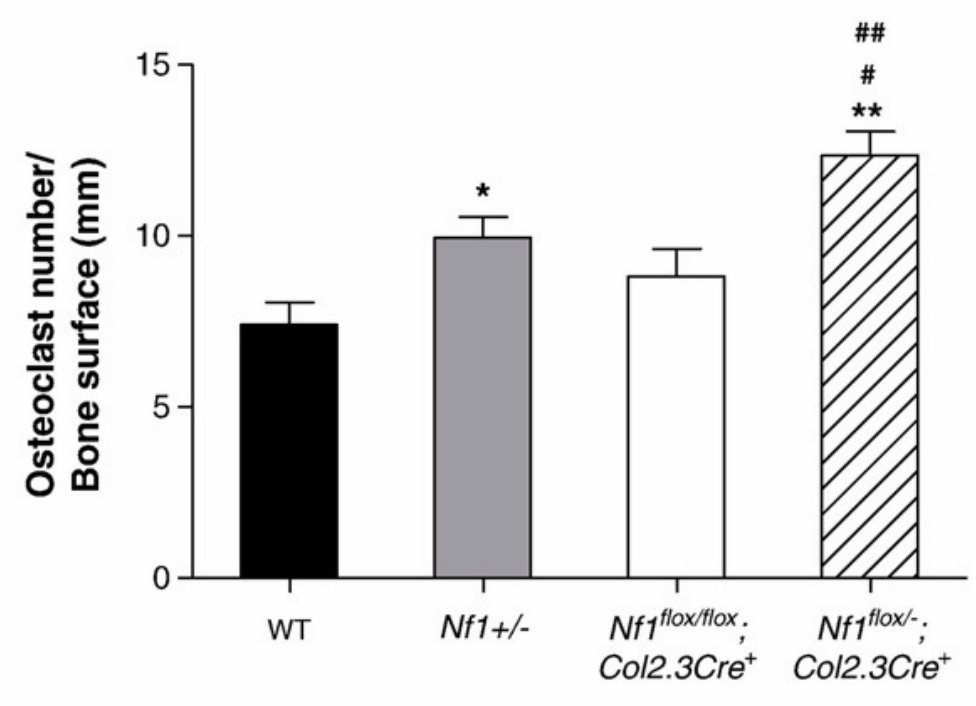
Osteoclast number/ Bone surface (mm)
15
10
5
0
*
##
#
**
WT
Nf1+/-
Nf1flox/flox; Col2.3Cre+
Nf1flox/-; Col2.3Cre+

Figure 14A

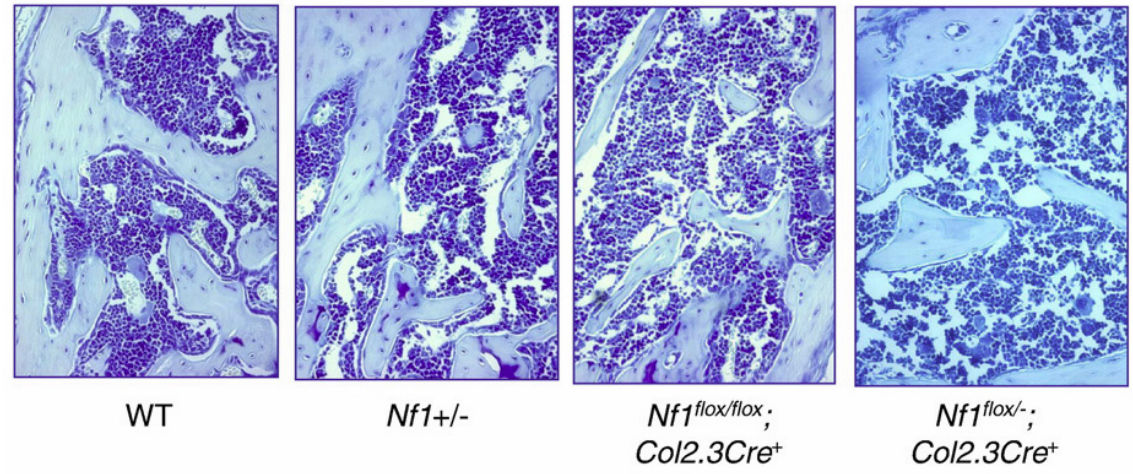
WT
Nf1+/-
Nf1flox/flox; Col2.3Cre+
Nf1flox/-; Col2.3Cre+

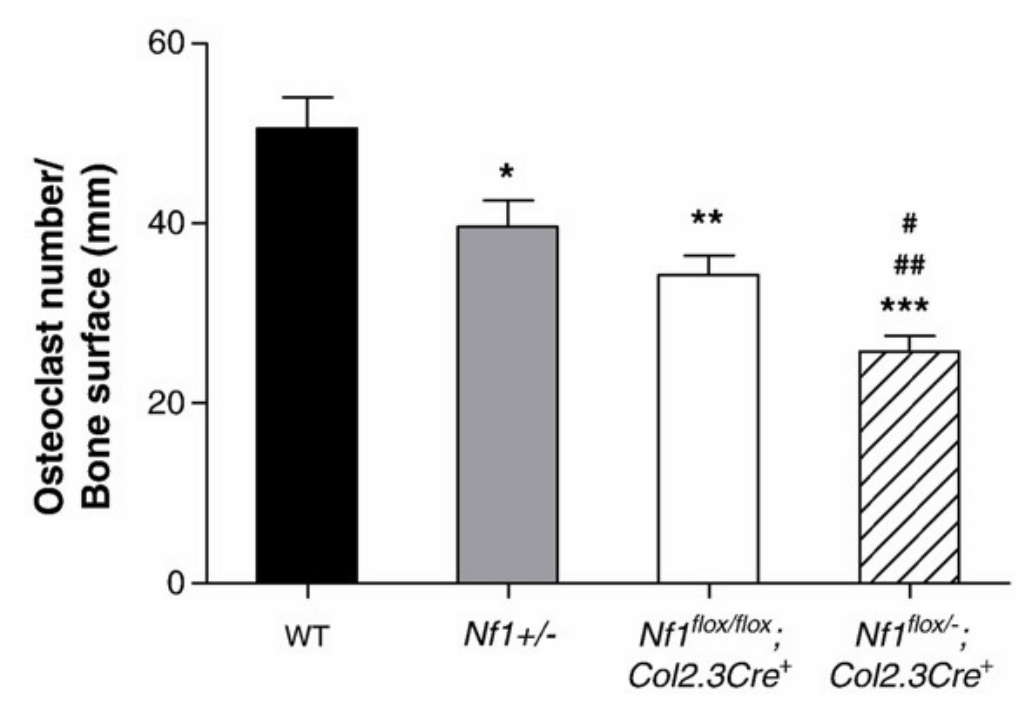
Osteoclast number/ Bone surface (mm)
60
40
20
0
*
**
#
##
***
WT
Nf1+/-
Nf1flox/flox; Col2.3Cre+
Nf1flox/-; Col2.3Cre+

Figure 14B

**Figure 14. *Nf1$^{flox/-}$;Col2.3Cre* mice have increased osteoclast number and reduced osteoblast number per mm of bone surface in the upper facet processes.** (A) (Top panel) Representative photomicrographs (magnification, 200x) of the upper facet processes of four genotypes of mice following TRACP staining. (Bottom panel) Mean osteoclast number per mm of bone surface was quantified per 200x field. Data represent mean ± SEM of five fields for each genotype. Five mice were used for each group. **P* <0.01 *Nf1$^{+/-}$* vs. WT. ***P* < 0.001 *Nf1$^{flox/-}$;Col2.3Cre* vs. WT. $^{\#}$*P* <0.05 *Nf1$^{flox/-}$;Col2.3Cre* vs. *Nf1$^{+/-}$*. $^{\#\#}$*P* < 0.01 *Nf1$^{flox/-}$;Col2.3Cre* vs. *Nf1$^{flox/flox}$;Col2.3Cre*. (B) (Top panel) Representative photomicrographs (magnification, 200x) of the upper facet processes of four genotypes of mice following MacNeal staining. (Bottom panel) Quantitative evaluation of the osteoblast number per mm of bone surface. Data represent mean ± SEM of five high power fields per mouse and five mice were used in each group. **P* <0.01 *Nf1$^{+/-}$* vs. WT. ***P* < 0.01 *Nf1$^{flox/flox}$;Col2.3Cre* vs. WT. ****P* <0.001 *Nf1$^{flox/-}$;Col2.3Cre* vs. WT. $^{\#}$*P* < 0.05 *Nf1$^{flox/flox}$;Col2.3Cre* vs. *Nf1$^{flox/-}$;Col2.3Cre*. $^{\#\#}$*P* < 0.01 *Nf1$^{flox/-}$;Col2.3Cre* vs. *Nf1$^{+/-}$*.

## Dystrophic spinal deformities in *Nf1$^{flox/-}$;Col2.3Cre* mice

Enlargement of the spinal canal

Widening of the spinal canal is one of the characteristic dystrophic features of NF1 related spinal deformities [55]. To screen for this phenotype in *Nf1$^{flox/-}$;Col2.3Cre* mice, the ratio of spinal canal area (C)/vertebral body area (V) (C/V ratio) was measured at L5 by pQCT (Figure 15). An increased C/V ratio indicates a comparatively larger area of the spinal canal. While vertebral body area (V) was unchanged between the four groups of mice (data not shown), significant increases in the C/V ratio were observed in *Nf1$^{+/-}$*, *Nf1$^{flox/flox}$;Col2.3Cre*, and *Nf1$^{flox/-}$;Col2.3Cre* mice as compared with WT mice, with *Nf1$^{flox/-}$;Col2.3Cre* mice exhibiting the highest ratio. We postulate that this phenomenon may be related to compression mediated by the cerebrospinal fluid, whereby outward pressure of the dural sac pushing against the weakened trabecular bone of the *Nf1$^{flox/-}$;Col2.3Cre* vertebral body leads to enlargement of the spinal canal.

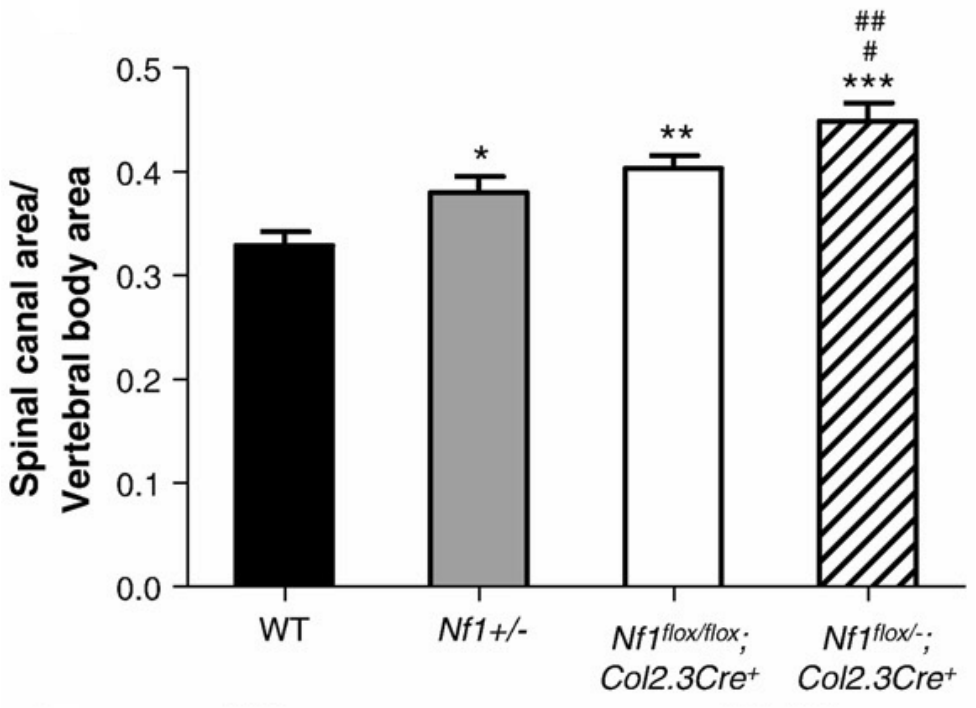
Spinal canal area/
Vertebral body area
0.5
0.4
0.3
0.2
0.1
0.0
*
**
##
#
***
WT
Nf1+/-
Nf1flox/flox;
Col2.3Cre+
Nf1flox/-;
Col2.3Cre+

Figure 15

**Figure 15. Enlargement of the spinal canal in *Nf1$^{flox/-}$;Col2.3Cre* mice.** The ratio of spinal canal area/vertebral body area (C/V) was compared between the four groups of mice. Data represent mean ± SEM of 9–10 mice per genotype. *$P$ < 0.05 *Nf1$^{+/-}$* vs. WT. **$P$ < 0.01 *Nf1$^{flox/flox}$;Col2.3Cre* vs. WT. ***$P$ < 0.001 *Nf1$^{flox/-}$;Col2.3Cre* vs. WT. $^{\#}P$ < 0.05 *Nf1$^{flox/-}$;Col2.3Cre* vs. *Nf1$^{flox/flox}$;Col2.3Cre*. $^{\#\#}P$ < 0.01 *Nf1$^{flox/-}$;Col2.3Cre* vs. *Nf1$^{+/-}$*.

Vertebral dysplasia with interarticular fusion

Dysplastic deformation of the vertebral bodies is one of the hallmark features of dystrophic scoliosis in NF1. Here, we demonstrate progressive dysplastic deformation of the vertebral bodies occurring within focal segments of the *Nf1$^{flox/-}$;Col2.3Cre* axial spine, as shown in plain radiographs (Figure 16A) and by μCT (Figure 16B). Histological sections acquired from mice one, two, six, and 12 months of age further demonstrate the progressive nature of the phenotype, whereby dysplastic bone remodeling within the intervertebral disc space culminates with interarticular fusion of the dystrophic vertebral segments (Figure 16C). While the mechanisms mediating this phenotype are unclear, this anomaly was observed exclusively in *Nf1$^{flox/-}$;Col2.3Cre* mice, suggesting that interactions between *Nf1* nullizygous osteoblasts and other *Nf1* heterozygous lineages within the disc space or elsewhere may play a significant role in the penetrance of the phenotype.

WT


*Nf1$^{flox/-}$;Col2.3Cre*

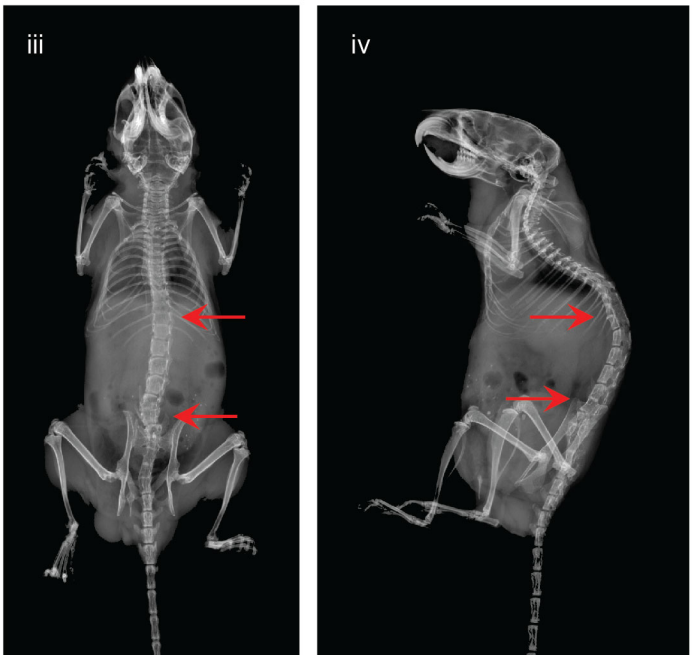


Figure 16A

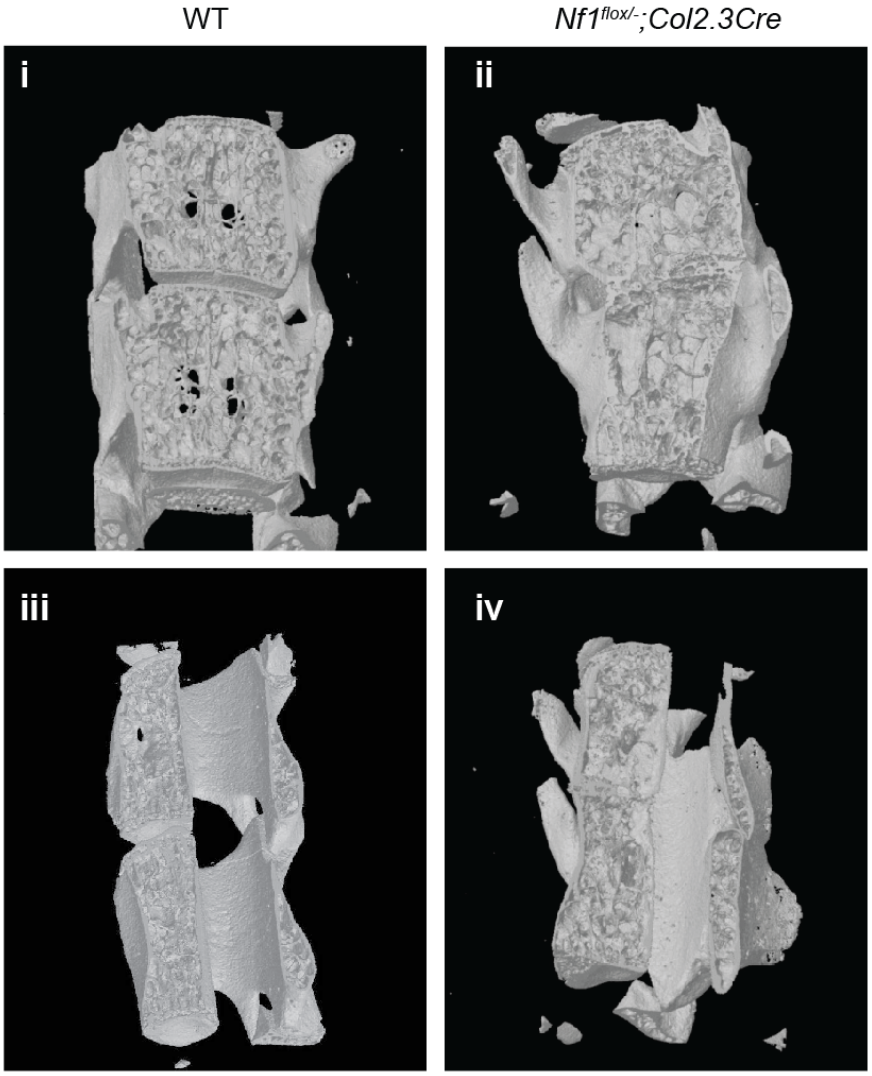


Figure 16B

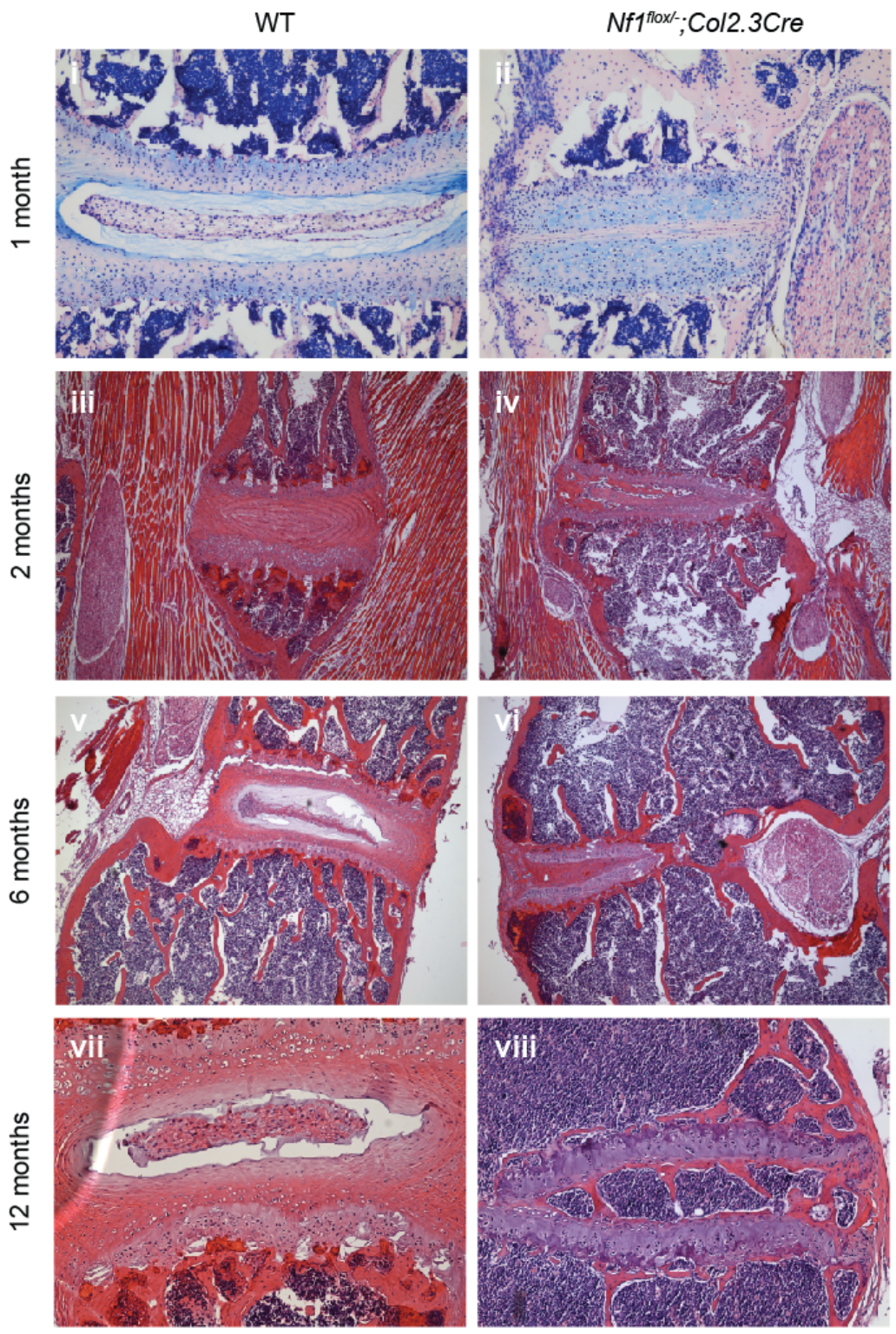
WT
Nf1flox/-;Col2.3Cre
1 month
2 months
6 months
12 months
i
ii
iii
iv
v
vi
vii
viii

Figure 16C

**Figure 16. Vertebral dysplasia with progressive interarticular fusion in *Nf1$^{flox/-}$;Col2.3Cre* mice.** (A) Anterior-posterior (i, iii) and lateral (ii, iv) radiographs demonstrate vertebral dysplasia in *Nf1$^{flox/-}$;Col2.3Cre* mice with interarticular fusion of dystrophic vertebrae. (B) Representative μCT reconstructions of dystrophic vertebral segments in coronal (top, i and ii) or sagittal (bottom, iii and iv) cross-section. Dysplastic bone growth within the intervertebral disc space has led to interarticular fusion of the dystrophic vertebrae. (C) Representative photomicrographs characterize progressive boney dysplasia within the intervertebral disc space of mice at one month (i and ii), two months (iii and iv), six months (v and vi), and 12 months (vii and viii) of age.

Reduced bone volume fraction and disrupted trabecular microarchitecture in dysplastic vertebral bone from *Nf1$^{flox/-}$;Col2.3Cre* mice and in a human NF1 patient with dystrophic scoliosis

To further investigate the pathological changes in bone microarchitecture, μCT scans were performed on dystrophic vertebrae harvested from *Nf1$^{flox/-}$;Col2.3Cre* mice and compared to corresponding segments from age-matched WT animals. Bone microarchitecture parameters including bone volume fraction (BV/TV, %), trabecular number (Tb.N, $mm^{-1}$), and trabecular spacing (Tb.Sp, μm) were significantly altered in dystrophic *Nf1$^{flox/-}$;Col2.3Cre* vertebrae versus controls (Figure 17). As a clinical correlate, we compared the bone mass and trabecular microarchitecture parameters (Figure 18, Table 2) in the T5 facet from a NF1 patient with dystrophic scoliosis and the T7 facet from a matched control with idiopathic scoliosis. These specimens were obtained from our collaborator, Dr. David Stevenson, at the University of Utah. Consistent with the murine data, BV/TV and trabecular microarchitecture parameters were significantly compromised in the NF1 T5 facet as compared to the control. Collectively, these findings suggest that underlying deficits in bone quality may be a contributory factor in the pathogenesis of dystrophic scoliosis in NF1.

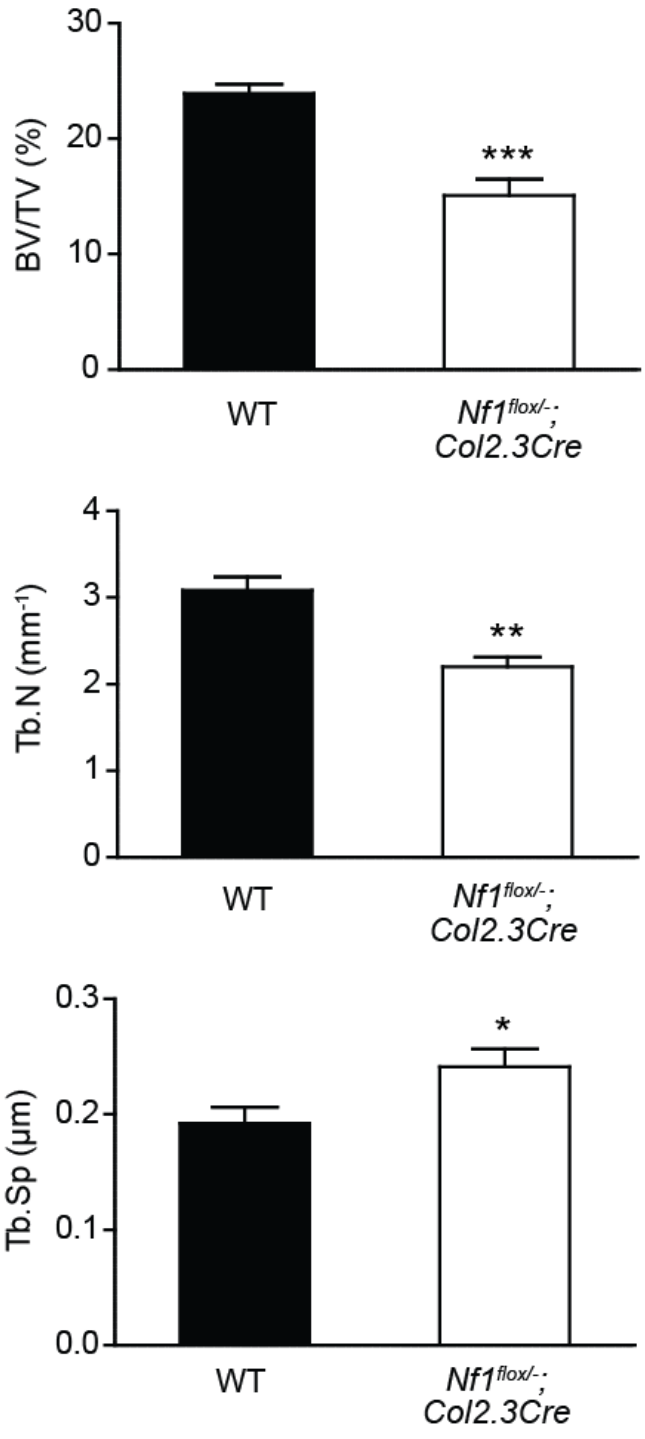
30
20
10
0
BV/TV (%)
***
WT
Nf1flox/-;
Col2.3Cre
4
3
2
1
0
Tb.N (mm-1)
**
WT
Nf1flox/-;
Col2.3Cre
0.3
0.2
0.1
0.0
Tb.Sp (µm)
*
WT
Nf1flox/-;
Col2.3Cre

Figure 17

**Figure 17. Reduced bone mass and altered trabecular microarchitecture in dystrophic *Nf1$^{flox/-}$;Col2.3Cre* vertebrae.** Percent bone volume (BV/TV, %), trabecular number (Tb.N), and trabecular spacing (Tb.Sp) were calculated by μCT as shown above. $n = 5$. *$P < 0.05$, **$P < 0.01$, ***$P < 0.001$ as compared to WT.

Control - T7 Facet

NF1 Patient - T5 Facet

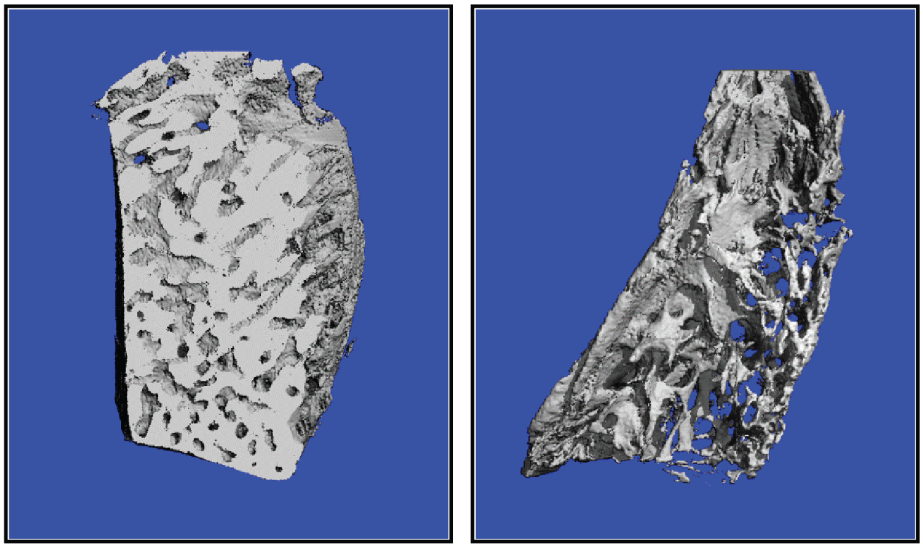

Figure 18

**Figure 18.** Representative μCT reconstructions of the T5 facet from an NF1 patient with dystrophic scoliosis and the T7 facet from an age/sex matched scoliosis patient without NF1.

Table 2

| Microarchitecture Parameters | Control – T7 Facet | NF1 – T5 Facet |
|---|---|---|
| BV/TV | 0.6680 | 0.2992 |
| Conn. D. ($mm^{-3}$) | 146.1781 | 77.1829 |
| Tb.N ($mm^{-1}$) | 6.8418 | 3.0513 |
| Tb.Th (mm) | 0.1999 | 0.1030 |
| Tb.Sp (mm) | 0.0969 | 0.2457 |
| BS/BV ($mm^{-1}$) | 10.4599 | 19.5740 |
| DA | 1.3841 | 1.6518 |

**Table 2.** Quantitative parameters of bone microarchitecture were assessed by μCT in the T5 facet of an NF1 patient with scoliosis versus the T7 facet of a control patient with scoliosis but without NF1.

**Tibial fracture non-union (pseudarthrosis) in *Nf1$^{flox/-}$;Col2.3Cre* mice**

Approximately 3% of young children with NF1 acquire pseudarthrosis, fracture non-union which responds poorly to treatment and often requires amputation of the affected limb. Given that at least a subset of patients exhibit biallelic inactivation of *NF1* in fibrous tissue within the fracture site, while maintaining a single functional *NF1* allele in other tissues [80, 81], we tested whether *Nf1$^{flox/-}$;Col2.3Cre* and *Nf1$^{flox/-}$;PeriCre* mice with an analogous genetic framework might recapitulate the pseudarthrotic phenotype. Tibial fractures were induced by the three-point bending method as first described by Bonnarens and Einhorn [137]. Radiographic assessment of fracture healing at 14 and 28 days post fracture revealed persistent non-union in *Nf1$^{flox/-}$;Col2.3Cre* mice as compared to controls (Figure 19A). Similarly, while 100% of WT mice demonstrated radiographic union of the fracture after four weeks, only 15% of *Nf1$^{flox/-}$;PeriCre* mice showed cortical bridging after four weeks (Figure 19B). This percentage plateaued near 60% after eight weeks of monitoring, such that approximately 40% of *Nf1$^{flox/-}$;PeriCre* mice exhibited persistent radiographic non-union eight weeks post-fracture. By contrast, conditional *Nf1* nullizygosity in MSCs and/or osteoblasts alone in the context of a WT background (*Nf1$^{flox/flox}$;PeriCre* and *Nf1$^{flox/flox}$;Col2.3Cre* mice) was insufficient to cause appreciable deficits in fracture healing (Figure 19A, B). We therefore reasoned that complex interactions between *Nf1$^{-/-}$* MCSs/osteoblasts and at least a subset of other *Nf1* heterozygous lineages must be required for the pathogenesis of fracture non-union in *Nf1$^{flox/-}$;PeriCre* and *Nf1$^{flox/-}$;Col2.3Cre* mice.

To test whether *Nf1* haploinsufficiency within the hematopoietic microenvironment might play a critical role in the pathogenesis of recalcitrant fracture healing in *Nf1$^{flox/-}$;PeriCre* and *Nf1$^{flox/-}$;Col2.3Cre* mice, we transplanted BMMNCs from either WT or *Nf1$^{+/-}$* donor mice into lethally irradiated *Nf1$^{flox/-}$;Col2.3Cre* or *Nf1$^{flox/flox}$;Col2.3Cre* recipients [78]. After four months of hematopoietic reconstitution, the recipient mice underwent three-point bending fracture. The fracture healing process was monitored for four weeks. *Nf1$^{flox/flox}$;Col2.3Cre* mice reconstituted with *Nf1$^{+/-}$* bone marrow cells exhibited severe deficits in fracture repair as compared to controls transplanted with WT hematopoietic cells. μCT revealed defective callus formation and significantly reduced fractional bone volume (BV/TV) within the fracture sites of *Nf1$^{flox/flox}$;Col2.3Cre* mice reconstituted with *Nf1$^{+/-}$* bone marrow cells as compared to WT (Figure 19C). Conversely, adoptive transfer of WT hematopoietic cells to *Nf1$^{flox/-}$;Col2.3Cre* recipient mice rescued fracture healing deficits in these animals. Histologically, mice reconstituted with *Nf1$^{+/-}$* marrow showed significantly increased numbers of TRACP positive staining osteoclasts within areas of recalcitrant fracture healing (Figure 19D), suggesting that perhaps increased osteoclast bone resorptive activity may contribute to persistent non-union in these mice.

In sum, these data provide rigorous evidence that at least some component of the *Nf1* haploinsufficient hematopoietic microenvironment plays a pivotal role in the pathogenesis of tibial fracture non-union in the *Nf1$^{flox/-}$;Col2.3Cre* and *Nf1$^{flox/-}$;PeriCre* murine NF1 pseudarthrosis models. However, the

specific lineage(s) within the hematopoietic system that are critical for the pathological bone repair process remain unclear. Studies undertaken to further investigate this topic are described in Chapter 4.

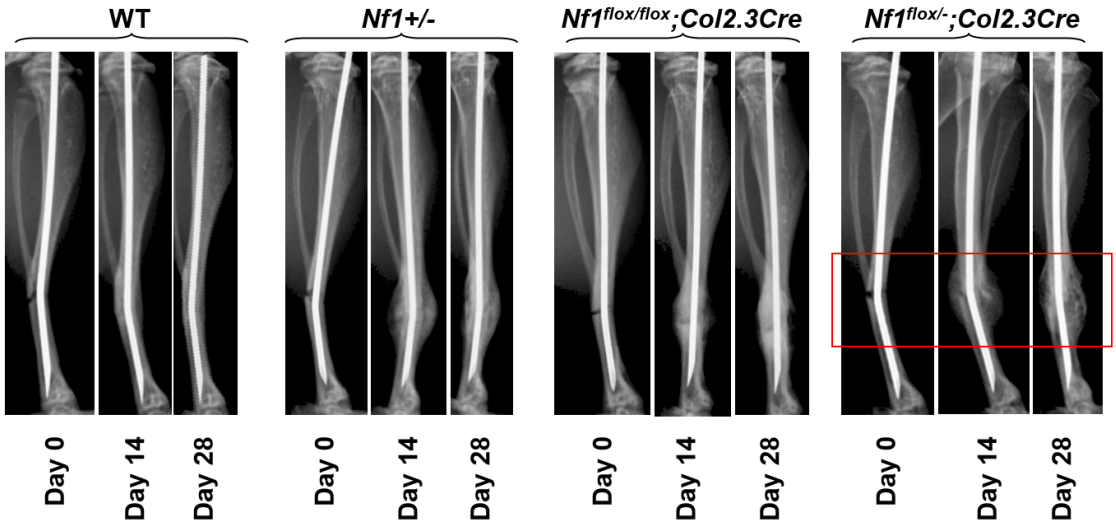
WT
Nf1+/-
Nf1flox/flox;Col2.3Cre
Nf1flox/-;Col2.3Cre
Day 0
Day 14
Day 28
Day 0
Day 14
Day 28
Day 0
Day 14
Day 28
Day 0
Day 14
Day 28

Figure 19A

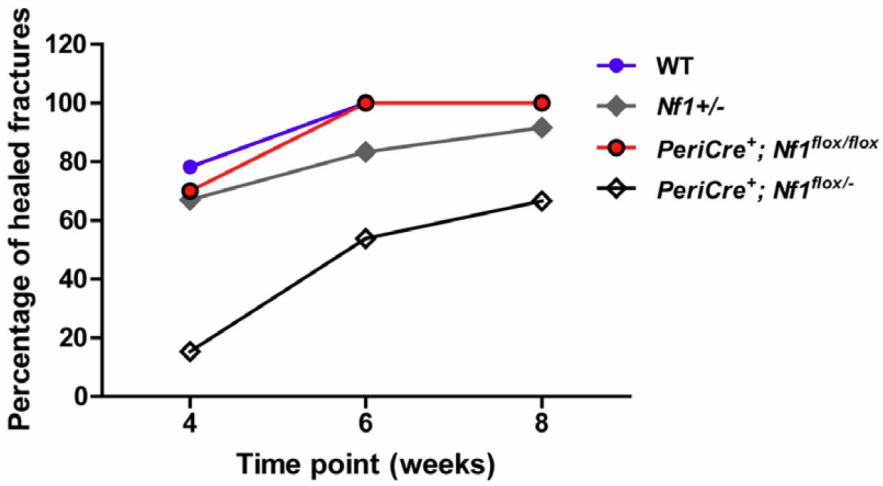
Percentage of healed fractures
120
100
80
60
40
20
0
4
6
8
Time point (weeks)
WT
Nf1+/-
PeriCre+; Nf1flox/flox
PeriCre+; Nf1flox/-

Figure 19B

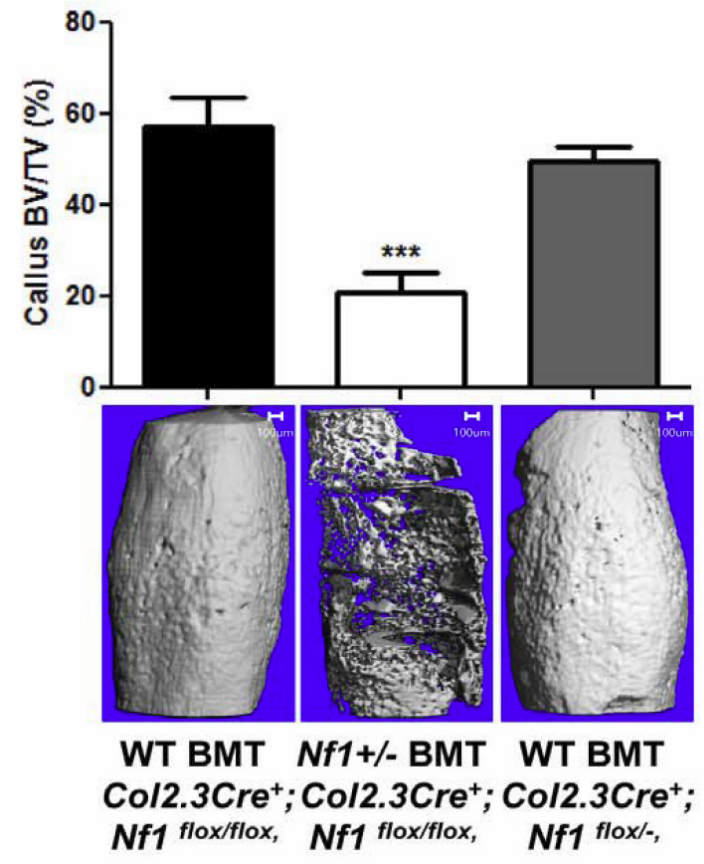
Callus BV/TV (%)
80
60
40
20
0
***
WT BMT
Col2.3Cre+; Nf1 flox/flox,
Nf1+/- BMT
Col2.3Cre+; Nf1 flox/flox,
WT BMT
Col2.3Cre+; Nf1 flox/-,

Figure 19C

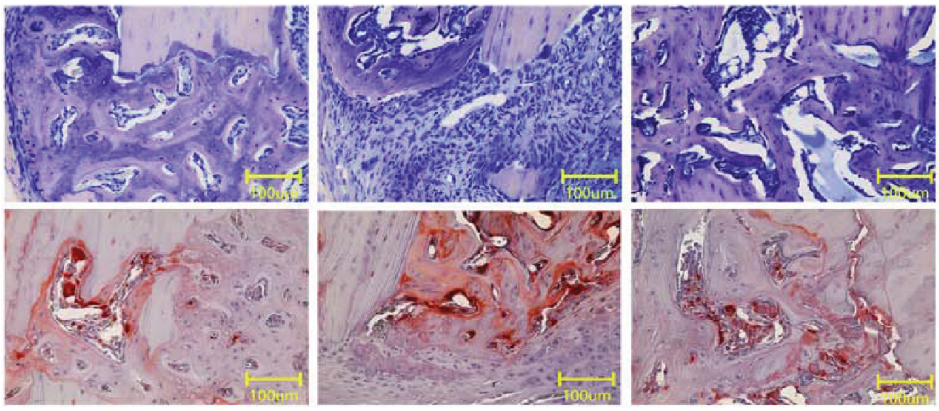


WT BMT
*Nf1*$^{flox/flox}$;
*PeriCre*

*Nf1*$^{+/-}$ BMT
*Nf1*$^{flox/flox}$;
*PeriCre*

WT BMT
*Nf1*$^{flox/-}$;
*PeriCre*

Figure 19D

**Figure 19. *Nf1*$^{+/-}$ hematopoietic cells are necessary for tibial fracture non-union in *Nf1*$^{flox/-}$*;Col2.3Cre* and *Nf1*$^{flox/-}$*;PeriCre* mice.** (A) Representative radiographs of the fracture site were acquired at 14 and 28 days post-fracture to monitor healing. (B) Percent of healed fractures at serial time points as defined radiographically by complete cortical bridging across the fracture site. (C) Fracture healing was monitored in *Nf1*$^{flox/flox}$ and *Nf1*$^{flox/-}$*;Col2.3Cre* mice previously transplanted with either WT or *Nf1*$^{+/-}$ bone marrow. Representative μCT reconstructions with quantification of bone volume fraction (BV/TV) within the callus site are shown. (D) Representative photomicrographs show MacNeal staining (upper panels 200x magnification) and TRACP staining (lower panels, 200x magnification) of fractured tibiae from *Nf1*$^{flox/flox}$ and *Nf1*$^{flox/-}$*;PeriCre* mice reconstituted with either WT or *Nf1*$^{+/-}$ bone marrow.

## Discussion

Skeletal manifestations including osteoporosis, short stature, kyphoscoliosis, and tibia pseudarthrosis cumulatively affect greater than 50% of NF1 patients [36]; however, our cellular and molecular understanding of these osseous defects remains limited due to the lack of animal models which accurately recapitulate these phenotypes. Here we describe the generation and phenotypic characterization of two novel NF1 murine models: *Nf1$^{flox/-}$;Col2.3Cre* and *Nf1$^{flox/-}$;PeriCre* mice, which exhibit multiple skeletal deficits including runting (short stature), low bone mass, spinal deformities, and tibial fracture non-union [77, 78] – features closely reminiscent of the human disease. These models thus serve as a valuable platform for further investigation of the cellular and molecular underpinnings of NF1 osseous manifestations as described in the subsequent chapters of this thesis.

Loss of *Nf1* heterozygosity (LOH) together with *Nf1* haploinsufficiency in the microenvironment has been found to play a critical role in at least two malignant manifestations of NF1, including plexiform neurofibromas and optic gliomas [84, 139, 140]. Our present study provides genetic evidence that a similar paradigm underlies the pathogenesis of NF1-related skeletal defects, particularly tibial pseudarthrosis. Through a series of adoptive bone marrow transfer experiments, we have demonstrated that the *Nf1* haploinsufficient hematopoietic microenvironment is critical to the pathogenesis of tibial fracture non-union in *Nf1$^{flox/-}$;Col2.3Cre* and *Nf1$^{flox/-}$;PeriCre* mice [78]. These data are consistent with recent clinical data suggesting that at least a subset of NF1

pseudarthrosis patients exhibit biallelic NF1 inactivation within tissue microdissected from the fracture site, while retaining a single functional NF1 allele in the peripheral blood [80, 81]. However, which specific *Nf1*$^{+/-}$ hematopoietic lineage(s) play a pivotal role in this process remains unclear. Given that *Nf1*$^{+/-}$ osteoclasts exhibit multiple gain-in-functions [69-72] and are abundantly present in pseudarthrosis tissue from human NF1 patients [62, 64, 65] and mouse models [76, 78, 79, 138, 141], we postulate that hyperactive bone resorbing *Nf1*$^{+/-}$ osteoclasts may be the culprit hematopoietic mediators of tibial fracture non-union in *Nf1*$^{flox/-}$*;Col2.3Cre* mice. Studies undertaken to test this hypothesis are described in Chapter 4 of this thesis.

Beyond generalized bone mass deficits in the femur and lumber spine, we further demonstrate that *Nf1*$^{flox/-}$*;Col2.3Cre* mice recapitulate many of the characteristic dysplastic boney features of NF1 patients with dystrophic scoliosis including widening of the spinal canal and dysplastic deformation of the vertebral bodies with progressive destruction of the intervertebral disc space and fusion of adjacent vertebral segments. While the mechanisms of dystrophic scoliosis in NF1 remain unclear, it is has been debated whether these spinal deformities are primary osseous defects or occur secondary to the pressure of an adjacent paraspinal tumor [52, 142]. Casselman and colleagues speculated that NF1 bone is intrinsically more susceptible to the distorting effects of an adjacent tumor [143]. In 1986, Sartoris et al. published the first case report documenting the fusion of vertebral segments in an NF1 patient [144]. In this case, the patient presented with destruction of the L1-L2 vertebral bodies and intervertebral disk

space. A presumptive diagnosis of neuropathic arthropathy was made, whereby destruction of the bone and articular cartilage is thought to occur secondary to loss of neurosensory feedback from the affected joint. In this patient, a retroperitoneal neurofibroma was identified anterior to the L1-L2 interspace; however, no neurofibromatosis tissue was found within the disk space itself. Thus, questions remain as to whether this lesion was primarily neuropathic or osteopathic in nature.

Intriguingly, a recent genetic study of mice harboring conditional *Nf1* nullizygous osteochondroprogenitor cells driven by the Col2α1-Cre (collagen, type II, alpha 1) promoter demonstrated congenital intervertebral disc formation defects, with improper segmentation of the notochord and impaired proliferation of the nucleus pulposus accompanied by interarticular vertebral fusion across multiple levels of the spine [141]. In the present study, we utilized the 2.3kb segment of the α(I)-Collagen promoter to achieve a more restricted biallelic ablation of *Nf1* in the osteoblast lineage. In this model, dystrophic vertebral features including fusion were observed only when conditional *Nf1* nullizygous osteoblasts were superimposed on a $Nf1^{+/-}$ background, suggesting that *Nf1* heterozygosity in surrounding tissues and cell lineages may play a critical role in the pathogenesis of such osseous defects.

μCT revealed reduced fractional bone volume and disrupted trabecular microarchitecture within dysplastic $Nf1^{flox/-}$*;Col2.3Cre* vertebral segments as well as the T5 facet of a human NF1 patient with dystrophic scoliosis as compared to the T7 facet of an age/sex matched scoliosis patient without NF1. Dynamic

histomorphometric analysis demonstrated disrupted bone remodeling in *Nf1$^{flox/-}$;Col2.3Cre* vertebrae as compared to WT controls, suggesting that intrinsic deficiencies in osteoblast anabolic activity, coupled with enhanced osteoclast catabolic activity, may at least partially underlie the pathogenesis and/or progression of NF1 dystrophic spinal deformities.

The vertebrae in quadrupeds do not receive an axial load to maintain balance of the torso, which is the major loading mechanism in bipeds [145]. The differing mechanical circumstances between bipeds and quadrupeds may explain why *Nf1$^{flox/-}$;Col2.3Cre* mice do not recapitulate the sharp, angulated curves seen in NF1 patients with dystrophic scoliosis. Consistent with this hypothesis, it has been demonstrated that scoliotic deformities can be induced with 100% penetrance in rats attaining bipedal posture after undergoing surgical amputation of the tail and forelimbs [146].

Regardless of this discrepancy, these data support the paradigm that dystrophic vertebral manifestations in NF1 may indeed arise *de novo* from primary defects in bone cell function, rather than merely as a secondary consequence to the paracrine or mass effects of a paraspinal neurofibroma. Moreover, this murine model provides a useful platform for further investigation regarding the basic cellular and molecular mechanism(s) underlying the pathogenesis of dystrophic spinal deformities in NF1.

# CHAPTER 4. *NF1* HAPLOINSUFFICIENT MYELOID PROGENITORS: CRITICAL MEDIATORS OF BONE LOSS AND FRACTURE NON-UNION IN THE NF1 MURINE MODEL

## Introduction

Loss of *NF1* heterozygosity (LOH) in various tissue types has been implicated in multiple neoplastic features of NF1, including juvenile myelomonocytic leukemia (JMML) [67, 68, 147] and malignant peripheral nerve sheath tumor (MPNST) [148, 149]. Clinical studies indicate that at least some NF1 pseudarthrosis patients exhibit *NF1* nullizygosity in the bone tissue by microdissection, suggesting that localized LOH may be a key initiating event promoting the pathogenesis of these lesions [80, 81]. Yet recent data also imply that *Nf1* haploinsufficiency pivotally impacts cell fate and function, contributing to the pathogenesis of a range of non-malignant NF1 phenotypes including plexiform neurofibroma development [84, 89], vascular disease [150], and osteopenia [69, 72, 74, 78, 138].

Through a series of adoptive bone marrow transfer experiments, as outlined in Chapter 3, we have established that haploinsufficiency of *Nf1* in the hematopoietic microenvironment plays a key role in tibial fracture non-union [78]. Transplantation of $Nf1^{+/-}$ bone marrow cells to lethally irradiated $Nf1^{flox/fox}$*;Col2.3Cre* mice (harboring conditional $Nf1^{-/-}$ osteoblasts with a WT background) induced recalcitrant fracture healing as compared to controls reconstituted with WT bone marrow. Conversely, adoptive transfer of WT

hematopoietic cells to *Nf1$^{flox/-}$;Col2.3Cre* mice (harboring *Nf1$^{-/-}$* osteoblasts with a *Nf1$^{+/-}$* background) was sufficient to prevent tibial fracture non-union in these animals. Collectively, these data provide rigorous evidence that at least some component of the *Nf1* haploinsufficient bone marrow microenvironment plays a critical role in NF1 skeletal manifestations such as tibial pseudarthrosis. Yet the culprit cell lineage(s) within the *Nf1$^{+/-}$* hematopoietic system which underlie the pathogenesis of fracture non-union remain unclear.

Hematopoietic-derived osteoclasts are abundantly present in pseudarthrotic tissues of NF1 patients [62, 64, 65] and in mouse models of the disease [76, 78, 79, 138, 141]. Mononuclear cells cultured *ex vivo* from the peripheral blood of NF1 patients [69-71] and the bone marrow of *Nf1$^{+/-}$* mice [69, 72] exhibit enhanced osteoclast differentiation and bone resorptive capacity, driven by Ras-mediated hypersensitivity to limiting doses of M-CSF and RANKL [69]. Yet the stage of myeloid/osteoclast development at which *Nf1* haploinsufficiency is permissive of these gain-in-functions remains unclear. Cell autonomous osteoclast gain-in-functions driven intrinsically through Ras-dependent signaling pathways are difficult to segregate from confounding alterations in extrinsic cytokine levels within the bone microenvironment. It has been postulated that hypersecretion of osteopontin (OPN) by *Nf1* mutant osteoblasts [85] together with alterations in the RANKL/osteoprotegerin (OPG) cytokine ratio [75] may contribute significantly to enhancing osteoclast recruitment and bone catabolic activity *in vivo*. The potential contribution of paracrine effects mediated by other *Nf1* haploinsufficient hematopoietic lineages

including B-cells [151], T-cells [152], and megakaryocytes [153, 154] are equally difficult to ascertain.

To address these unanswered questions and achieve deeper insight into the cell autonomous role of *Nf1* gene dose in regulating myeloid/osteoclast development, we generated *Nf1*$^{flox/+}$*;LysMCre* and *Nf1*$^{flox/+}$*;CtskCre* mice harboring conditional inactivation of a single *Nf1* allele in myeloid osteoclast progenitors and mature osteoclasts, respectively. Here we demonstrate that haploinsufficient loss of *Nf1* in early stage myeloid precursors, not merely in terminally differentiated osteoclasts alone, is required to induce accelerated osteoclast catabolic activity and bone loss *in vivo*. BMMNCs cultured from *Nf1*$^{flox/+}$*;LysMCre* mice, but not *Nf1*$^{flox/+}$*;CtskCre* mice, exhibit increased osteoclast progenitor frequency, M-CSF hypersensitivity in methylcellulose colony formation assays, and increased osteoclast differentiative capacity. Moreover, we provide direct genetic evidence through adoptive bone marrow transfer that cooperative interactions between *Nf1* nullizygous osteoblasts and *Nf1* haploinsufficient osteoclasts within the hematopoietic microenvironment pivotally underlie the pathogenesis of tibial fracture non-union in *Nf1*$^{flox/-}$*;Col2.3Cre* mice. Collectively, these data offer novel insights regarding the differential and reciprocal roles of *Nf1* in terminally differentiated osteoclasts versus early stage hematopoietic/myeloid progenitors while establishing the critical role of this lineage in the pathogenesis of NF1 non-union fracture. This provides important implications for optimizing novel and currently existing targeted therapies.

**Conditional *Nf1* haploinsufficiency in myeloid lineages increases osteoclast progenitor frequency and enhances osteoclast differentiation**

Osteoclastogenesis is a dynamic process requiring the commitment and proliferation of early myeloid progenitors, followed by differentiation to monocytes and ultimately to multinucleated osteoclasts with bone resorptive activity. Mononuclear cells isolated from the bone marrow of $Nf1^{+/-}$ mice [69, 72] and peripheral blood of human NF1 patients [69-71] exhibit an increased capacity for osteoclast differentiation and bone resorption *in vitro*, due to Ras-mediated hypersensitivity to osteoclastogenic cytokines such as M-CSF and RANK-L [69]. Yet no genetic study has directly assessed the stage of myeloid/osteoclast development at which *Nf1* haploinsufficiency is permissive of osteoclast gain-in-functions. To assess the cell autonomous role of *Nf1* in early versus late stage osteoclastogenesis, we began by comparing the commitment and proliferative capacity of myeloid/osteoclast progenitor cells in the bone marrow of $Nf1^{flox/+}$*;LysMCre,* $Nf1^{flox/+}$*;CtskCre,* and wild-type (WT) control mice. BMMNCs were cultured in semisolid methylcellulose media over a range of concentrations of M-CSF. We found that the number of colony forming unit-macrophage (CFU-M) per femur were significantly increased in $Nf1^{flox/+}$*;LysMCre* mice versus WT with increasing doses of M-CSF (Figure 20A). In addition, flow cytometric analysis of the bone marrow revealed a significant increase in the present of myeloid progenitors (Figure 20B). Thus, haploinsufficient loss of *Nf1* induced by

*LysMCre* at the early progenitor stage is sufficient to expand the pool of myeloid precursors that have the potential to mature into fully differentiated osteoclasts.

Given the increase in the number of myeloid/osteoclast progenitors in *Nf1$^{flox/+}$;LysMCre* mice, we next determined the capacity of BMMNCs isolated from these mice to differentiate to mature osteoclasts in tissue culture. When BMMNCs were cultured in the presence of M-CSF and RANK-L, a significant increase in the number of TRACP positive staining multinucleated osteoclasts was observed in the *Nf1$^{flox/+}$;LysMCre* cultures as compared to WT controls (Figure 20C). The number of nuclei per osteoclast was also significantly increased in the *Nf1$^{flox/+}$;LysMCre* cultures (Figure 20C), a phenotype that is characteristic of osteoclasts cultured from the bone marrow of *Nf1$^{+/-}$* mice [69, 72] and the peripheral blood of human NF1 patients [69-71].

A defining morphological feature of mature osteoclasts is the organization of the actin cytoskeleton to form a specialized cell–extracellular matrix that provides the proper microenvironment for degradation of bone matrix. This complex structure is formed by the coalescence of actin cytoskeletal structures termed podosomes that arrange into identifiable patterns such as clusters, rings, and ultimately belts that constitute a functional sealing zone [155]. Here, we show that compared to WT controls, *Nf1$^{flox/+}$;LysMCre* osteoclast cultures exhibit significantly higher levels of belt formation (Figure 20D), a cellular characteristic correlating with bone resorptive activity [72].

By contrast, when we assessed the osteoclast forming potential of BMMNCs flushed from the long bones of *Nf1$^{flox/+}$;CtskCre* mice, we observed no

significant differences in the number of TRACP positive staining multinucleated osteoclasts as compared to WT controls (Figure 20E). Collectively, these findings led us to reason that the enhanced osteoclastogenic potential of *Nf1* haploinsufficient bone marrow cells may in fact require genetic disruption of a single *Nf1* allele in the early stage myeloid progenitor population, before these osteoclast precursors undergo terminal lineage commitment and differentiation.

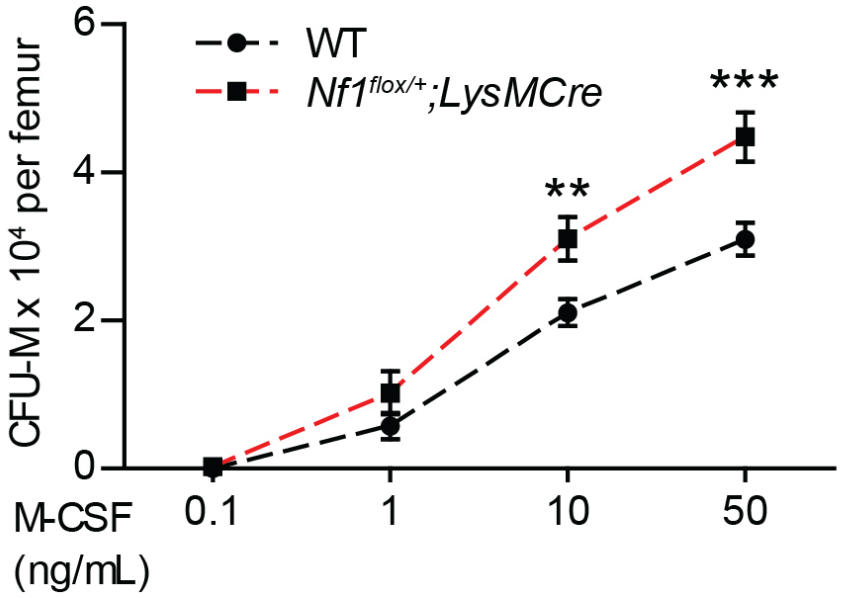
6
4
2
0
CFU-M x 10⁴ per femur
WT
Nf1flox/+;LysMCre
**
***
M-CSF
(ng/mL)
0.1
1
10
50

Figure 20A

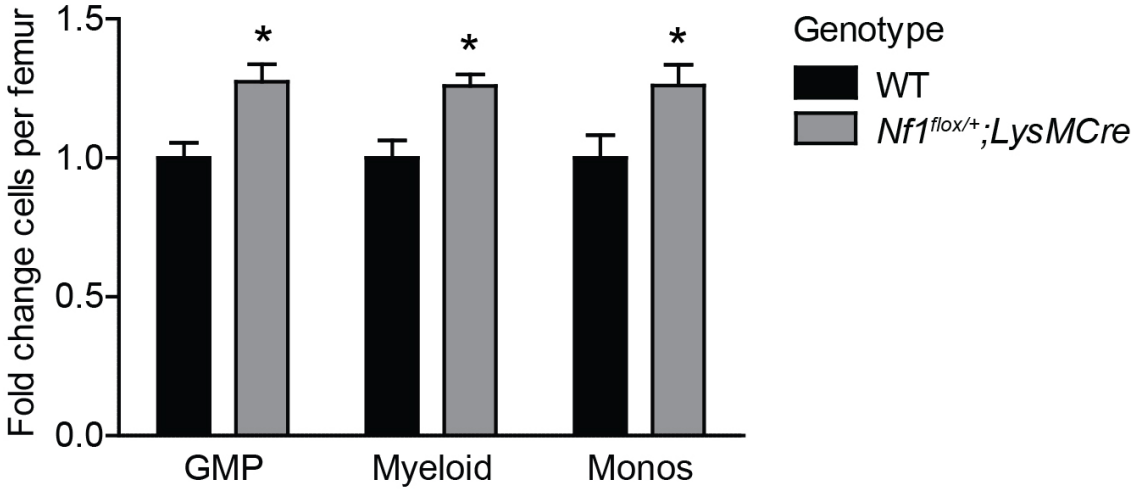
Fold change cells per femur
1.5
1.0
0.5
0.0
*
*
*
GMP
Myeloid
Monos
Genotype
WT
Nf1flox/+;LysMCre

Figure 20B

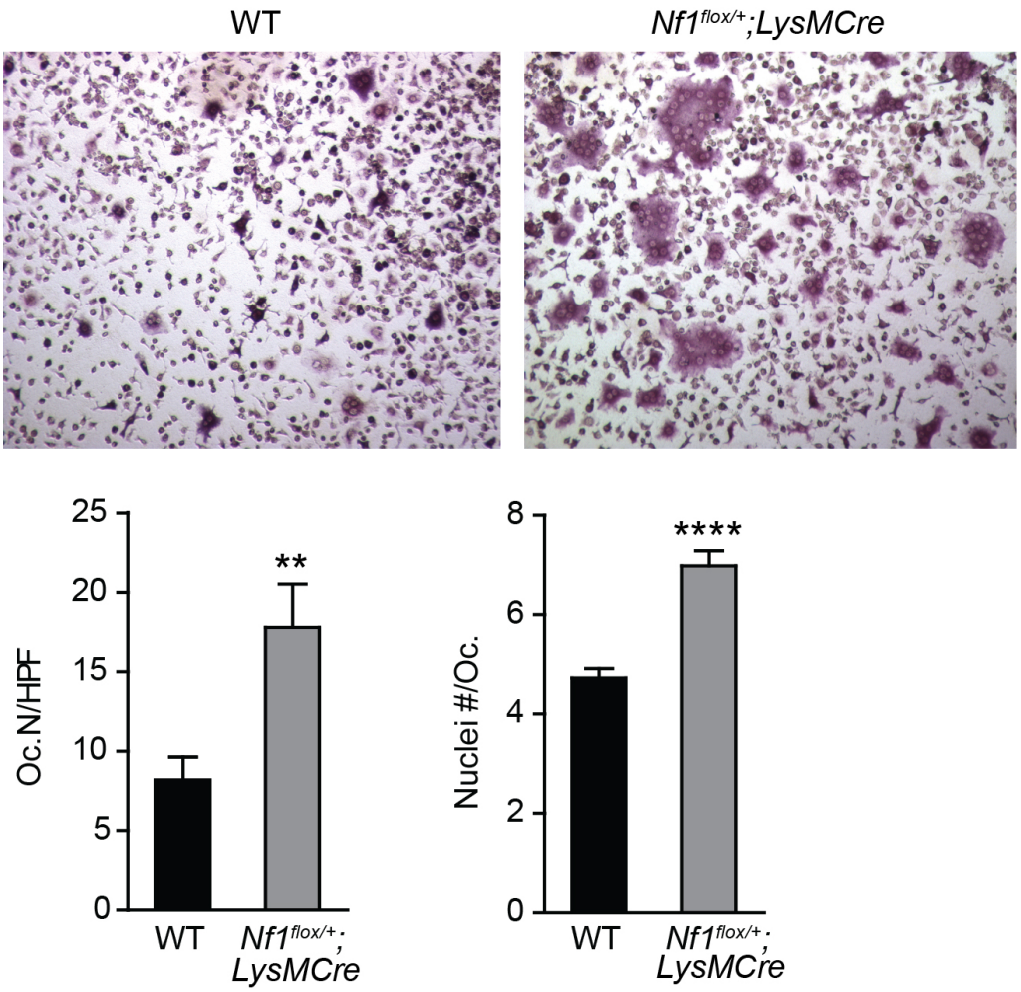
WT
Nf1flox/+;LysMCre
Oc.N/HPF
25
20
15
10
5
0
**
WT
Nf1flox/+; LysMCre
Nuclei #/Oc.
8
6
4
2
0
****
WT
Nf1flox/+; LysMCre

Figure 20C

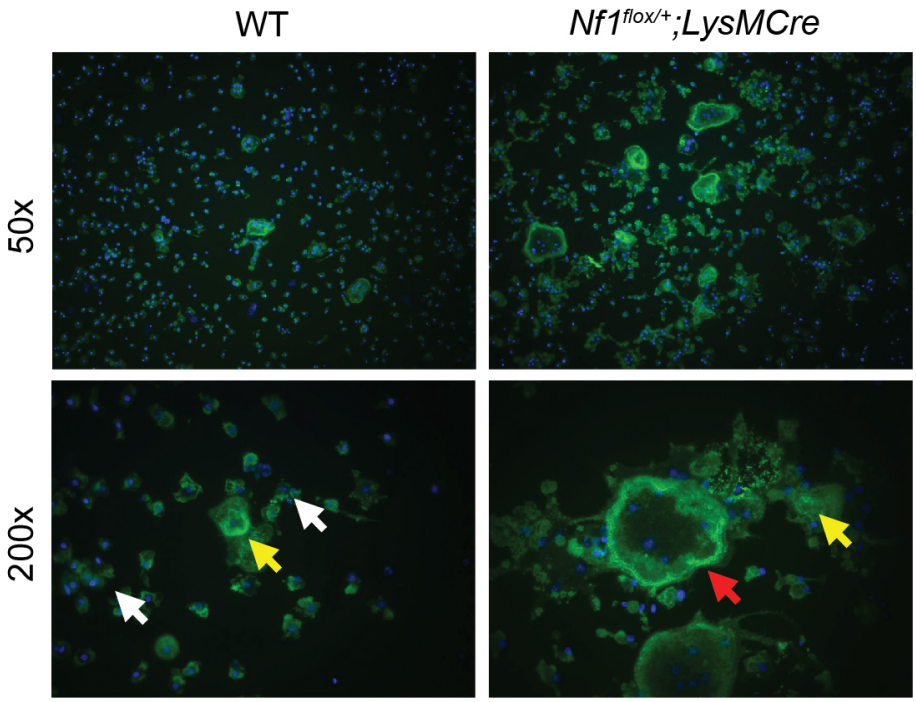
WT
Nf1flox/+;LysMCre
50x
200x

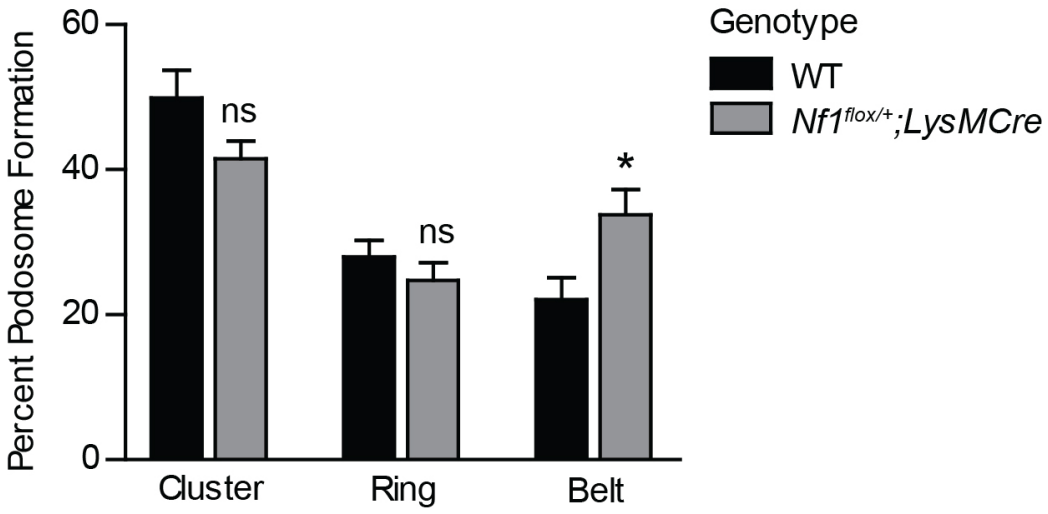
Percent Podosome Formation
60
40
20
0
ns
ns
*
Cluster
Ring
Belt
Genotype
WT
Nf1flox/+;LysMCre

Figure 20D

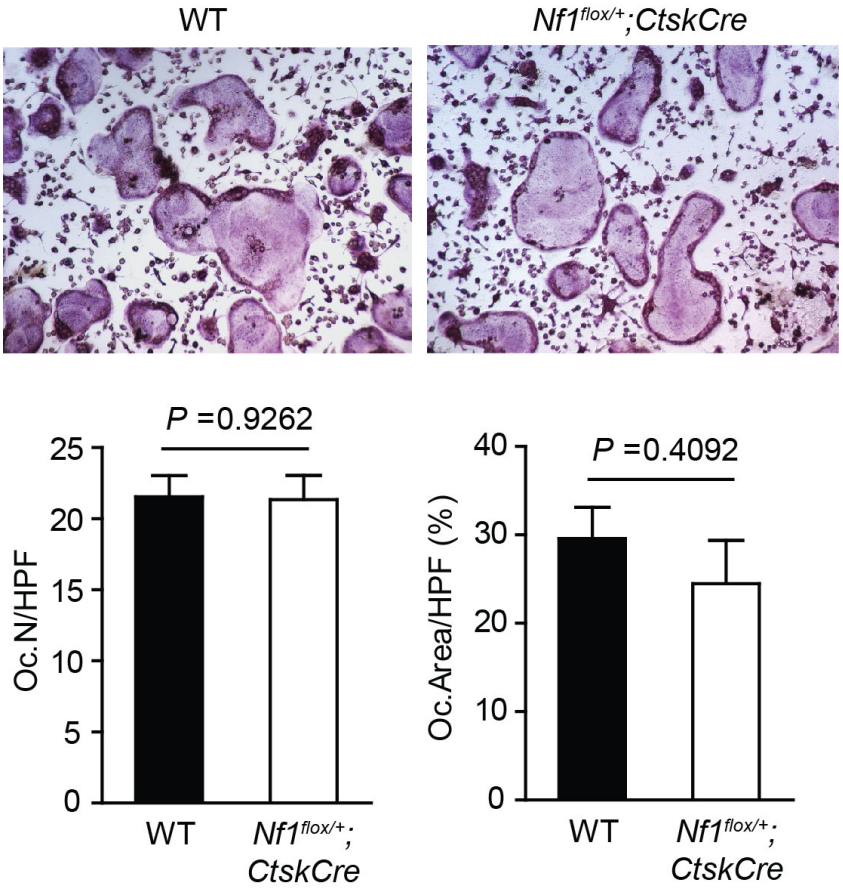
WT
Nf1flox/+;CtskCre
P =0.9262
Oc.N/HPF
25
20
15
10
5
0
WT
Nf1flox/+;
CtskCre
P =0.4092
Oc.Area/HPF (%)
40
30
20
10
0
WT
Nf1flox/+;
CtskCre

Figure 20E

**Figure 20. *Nf1* haploinsufficiency in myeloid progenitors potentiates osteoclast differentiation.** (A) The number of colony forming unit-monocyte/macrophage (CFU-M) per femur were enumerated following seven days culture in semisolid methylcellulose media. $^{**}P < 0.01$, $^{***}P < 0.001$ *Nf1$^{flox/+}$;LysMCre* vs. WT. $n = 8$ mice per genotype. (B) Populations of GMP, myeloid cells, and monocytes in the bone marrow were identified by flow cytometry. Fold changes in the number of cells per femur are reported. $^{*}P < 0.05$ *Nf1$^{flox/+}$;LysMCre* vs. WT. $n = 4$ mice per genotype. (C) Representative photomicrographs show TRACP staining of bone marrow derived osteoclasts cultured from WT and *Nf1$^{flox/+}$;LysMCre* mice in the presence of M-CSF and RANKL for six days (top panel). The number of osteoclasts per high power field (HPF) and the number of nuclei per osteoclast were counted as shown (bottom panel). $^{**}P < 0.01$, $^{***}P < 0.001$ *Nf1$^{flox/+}$;LysMCre* vs. WT. $n = 4$ biological replicates per genotype. (D) Representative photomicrographs show actin ring formation in bone marrow derived osteoclast cultures at 50x and 200x magnification (top panel). Cells were stained with Alexa Fluor® 488 Phalloidin (green) and Hoechst (blue). Podosome formation was evaluated by determining the percent distribution of actin organization into clusters, rings, and belts (bottom panel). $^{*}P < 0.05$ *Nf1$^{flox/+}$;LysMCre* vs. WT. $n = 4$ biological replicates per genotype. (E) Representative photomicrographs show TRACP staining of bone marrow derived osteoclasts cultured from WT and *Nf1$^{flox/+}$;CtskCre* mice in the presence of M-CSF and RANKL for six days (top panel) The number of osteoclasts per HPF and the osteoclast area per HPF were quantified as shown

(bottom panel). *n* = 3 biological replicates per genotype. ns = no significant difference.

**Haploinsufficient *Nf1* deletion in myeloid progenitor cells potentiates bone erosive activity *in vivo***

Although *Nf1*$^{+/-}$ mice exhibit increased osteoclast numbers [69], their bone mass does not differ significantly from WT controls [74]. Likewise, we observed no significant differences in BMD, bone mass, or trabecular architecture between either *Nf1*$^{flox/+}$*;LysMCre* (Figure 21A, B) or *Nf1*$^{flox/+}$*;CtskCre* mice (Figure 22A, B) and their WT counterparts. By contrast, we have previously demonstrated that *Nf1*$^{+/-}$ mice lose significantly more bone mass (by a factor of 2) as compared to WT controls when challenged with ovariectomy induced proresorptive stress [69]. To further characterize the functional consequences of *Nf1* haploinsufficiency in osteoclasts and their progenitors in response to proresorptive challenge, we ovariectomized *Nf1*$^{flox/+}$*;LysMCre* and *Nf1*$^{flox/+}$*;CtskCre* mice and compared the extent of bone loss to WT controls.

As anticipated, the OVX procedure induced bone loss in all genotypes of mice (Figure 23A, B). Notably, the rate of bone loss was markedly accelerated in *Nf1*$^{flox/+}$*;LysMCre*-OVX mice. The percentage reduction in femoral BMD was significantly greater in *Nf1*$^{flox/+}$*;LysMCre*-OVX mice as compared to either ovariectomized WT animals or sham-operated controls during the six week period (Figure 23A). Representative μCT reconstructions show a dramatic loss of trabecular bone in *Nf1*$^{flox/+}$*;LysMCre*-OVX mice as compared to WT-OVX and sham controls (Figure 23B). Quantitative μCT evaluation revealed significant differences in femoral bone volume fraction (Figure 23C) and multiple bone microarchitecture parameters, including trabecular number (Tb.N), trabecular

thickness (Tb.Th), and trabecular spacing (Tb.Sp) (Figure 23D). Intriguingly, however, *Nf1*$^{flox/+}$*;CtskCre* mice did not recapitulate this phenotype. Although bone mass was reduced in both WT- and *Nf1*$^{flox/+}$*;CtskCre*-OVX mice, no significant difference in the percentage reduction in femoral BMD between the two strains was observed (Figure 23E). Representative μCT reconstructions demonstrate equivalent bone loss in the distal femur when comparing WT-OVX and *Nf1*$^{flox/+}$*;CtskCre*-OVX mice. Quantitatively, no significant difference was detected in femoral bone volume fraction (Figure 23F) or trabecular architecture parameters (Figure 23G) between *Nf1*$^{flox/+}$*;CtskCre*-OVX versus WT-OVX mice. Collectively, these data suggest that conditional *Nf1* haploinsufficiency in terminally differentiated osteoclasts is insufficient to trigger increased bone lytic activity in response to proresorptive challenge. Rather, genetic ablation of a single *Nf1* allele in myeloid progenitors may be required to expand the pool of osteoclast precursors, thereby promoting accelerated bone resorption *in vivo*.

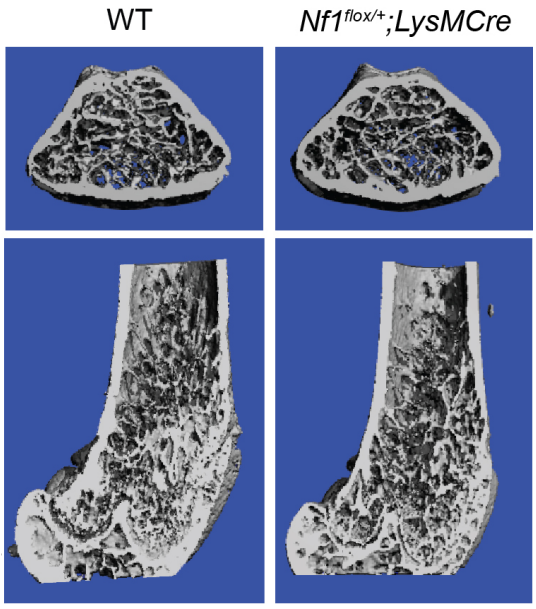


Figure 21A

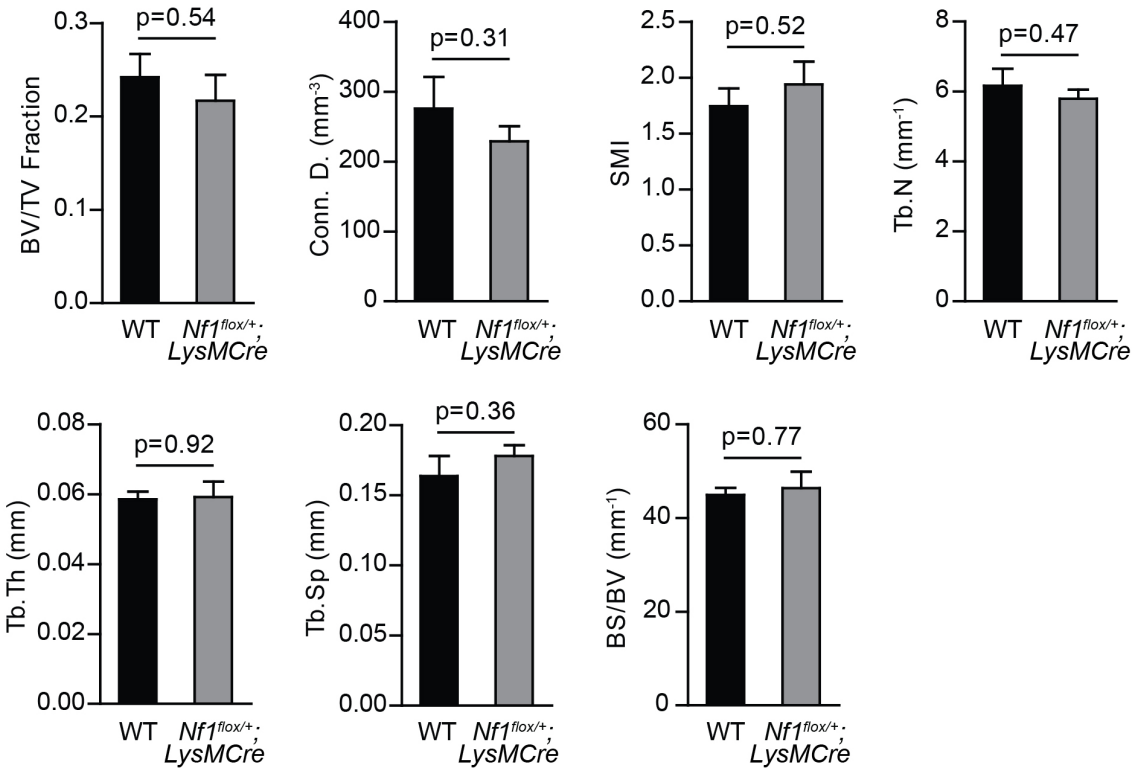
p=0.54
BV/TV Fraction
0.3
0.2
0.1
0.0
WT
Nf1flox/+; LysMCre
p=0.31
Conn. D. (mm-3)
400
300
200
100
0
p=0.52
SMI
2.5
2.0
1.5
1.0
0.5
0.0
p=0.47
Tb.N (mm-1)
8
6
4
2
0
p=0.92
Tb.Th (mm)
0.08
0.06
0.04
0.02
0.00
p=0.36
Tb.Sp (mm)
0.20
0.15
0.10
0.05
0.00
p=0.77
BS/BV (mm-1)
60
40
20
0

Figure 21B

**Figure 21. Haploinsufficient loss of *Nf1* in myeloid lineages does not spontaneously alter bone mass or trabecular microarchitecture *in vivo*.** (A) Representative μCT reconstructed femora of WT and *Nf1*$^{flox/+}$*;LysMCre* mice in transverse (top) and longitudinal (bottom) cross-sections. (B) No significant differences in bone volume fraction (BV/TV), connectivity density (Conn.D.), trabecular number (Tb.N), trabecular spacing (Tb.Sp), and trabecular thickness (Tb.Th), bone surface/bone volume ratio (BS/BV), or structure model index (SMI) were found when comparing WT to *Nf1*$^{flox/+}$*;LysMCre* mice. *n* = 5-8 per group.

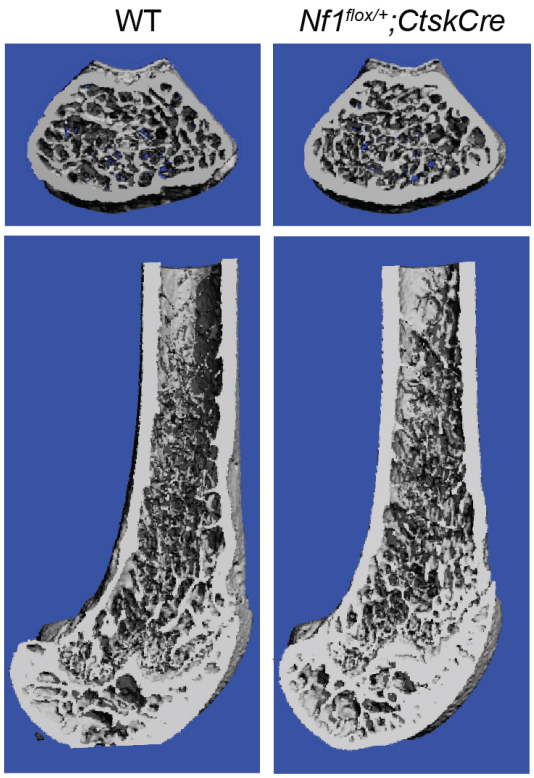


Figure 22A

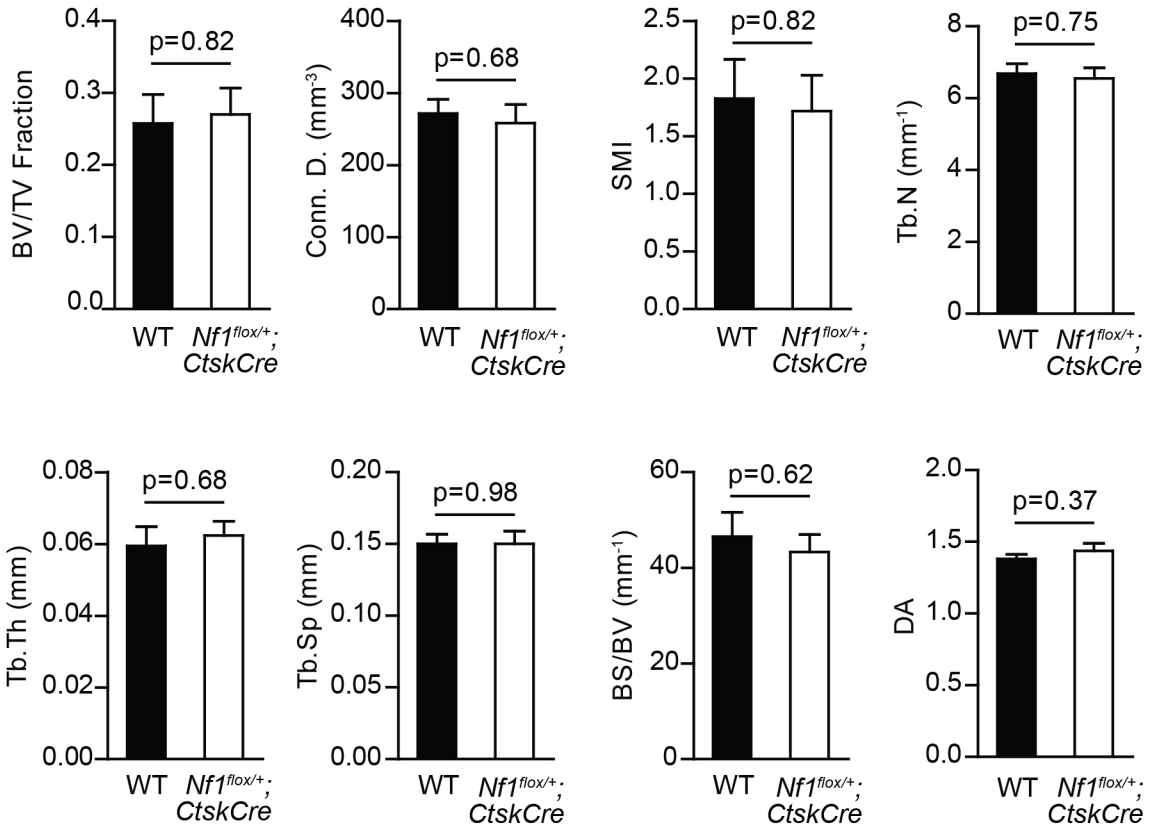
BV/TV Fraction
0.4
0.3
0.2
0.1
0.0
p=0.82
WT
Nf1flox/+; CtskCre
Conn. D. (mm-3)
400
300
200
100
0
p=0.68
WT
Nf1flox/+; CtskCre
SMI
2.5
2.0
1.5
1.0
0.5
0.0
p=0.82
WT
Nf1flox/+; CtskCre
Tb.N (mm-1)
8
6
4
2
0
p=0.75
WT
Nf1flox/+; CtskCre
Tb.Th (mm)
0.08
0.06
0.04
0.02
0.00
p=0.68
WT
Nf1flox/+; CtskCre
Tb.Sp (mm)
0.20
0.15
0.10
0.05
0.00
p=0.98
WT
Nf1flox/+; CtskCre
BS/BV (mm-1)
60
40
20
0
p=0.62
WT
Nf1flox/+; CtskCre
DA
2.0
1.5
1.0
0.5
0.0
p=0.37
WT
Nf1flox/+; CtskCre

Figure 22B

**Figure 22. *Nf1$^{flox/+}$;CtskCre* mice have equivalent bone mass and trabecular architecture parameters to WT controls.** (A) Representative μCT reconstructed femora of WT and *Nf1$^{flox/+}$;CtskCre* mice in transverse (top) and longitudinal (bottom) cross-sections. (B) No significant differences in bone volume fraction (BV/TV), connectivity density (Conn.D.), trabecular number (Tb.N), trabecular spacing (Tb.Sp), trabecular thickness (Tb.Th), bone surface/bone volume ratio (BS/BV), structure model index (SMI), or density anisotropy (DA) were found when comparing WT versus *Nf1$^{flox/+}$;CtskCre* mice. *n* = 6-7 per group.

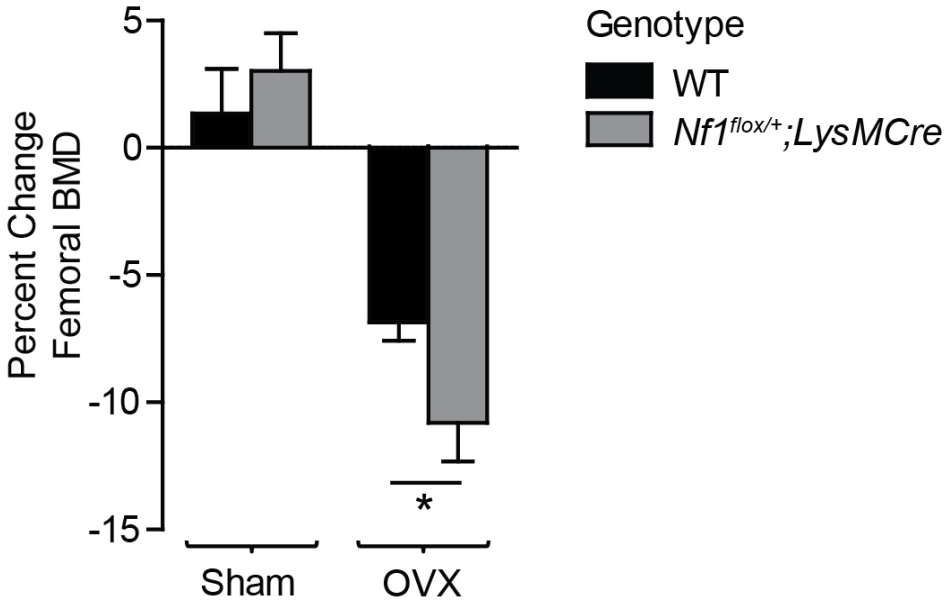
Genotype
WT
Nf1flox/+;LysMCre
Percent Change
Femoral BMD
5
0
-5
-10
-15
*
Sham
OVX

Figure 23A

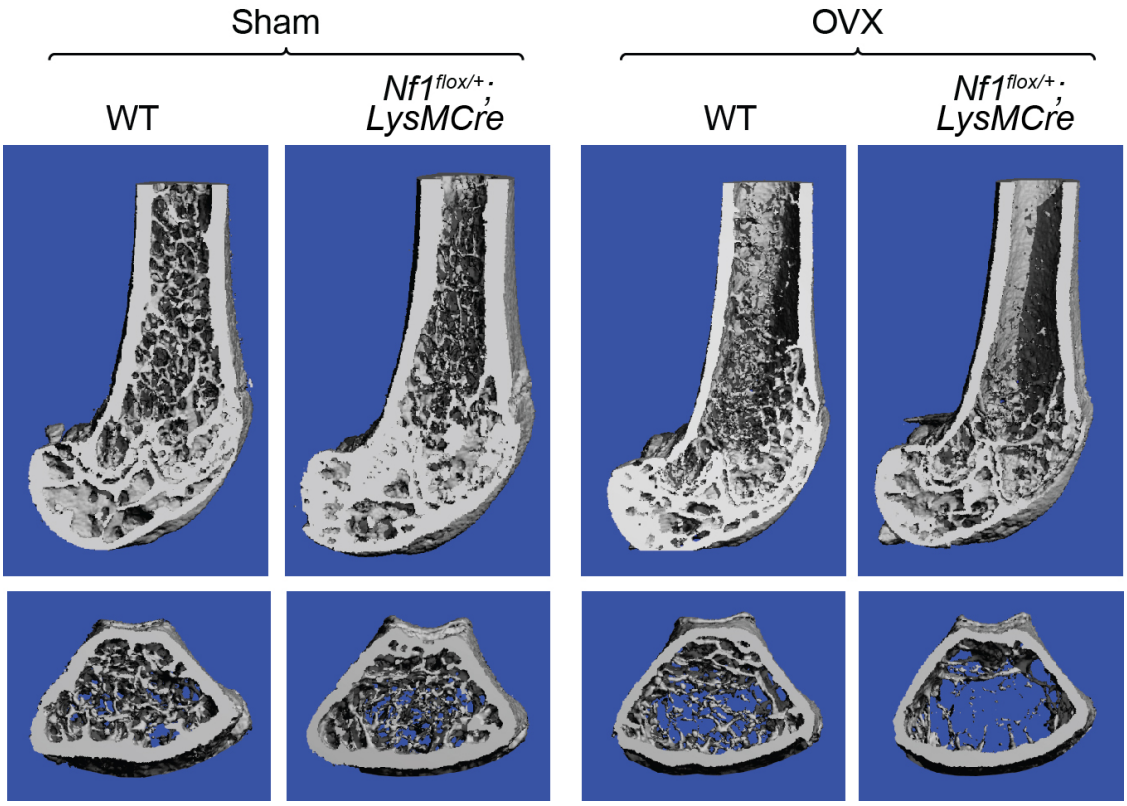


Figure 23B

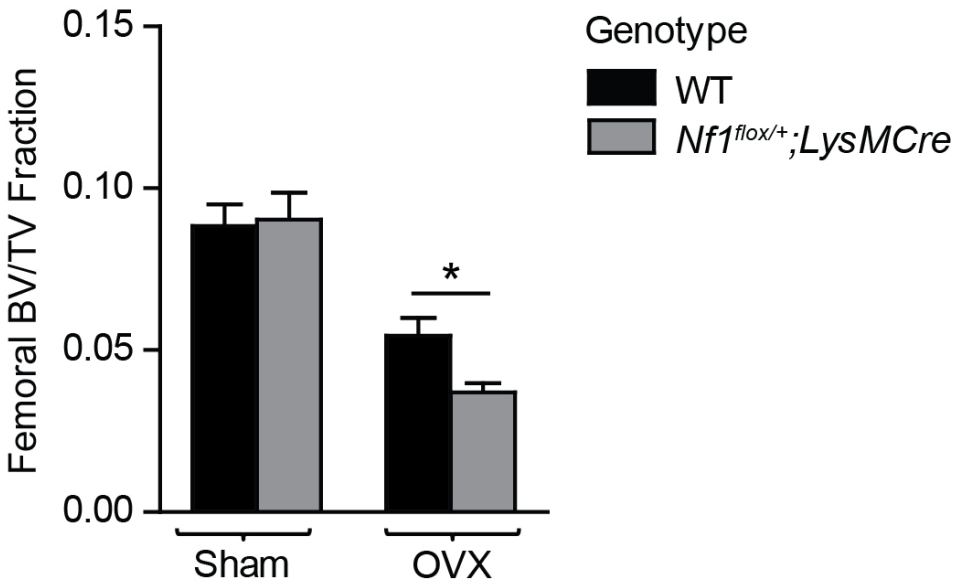
0.15
0.10
0.05
0.00
Femoral BV/TV Fraction
*
Sham
OVX
Genotype
WT
Nf1flox/+;LysMCre

Figure 23C

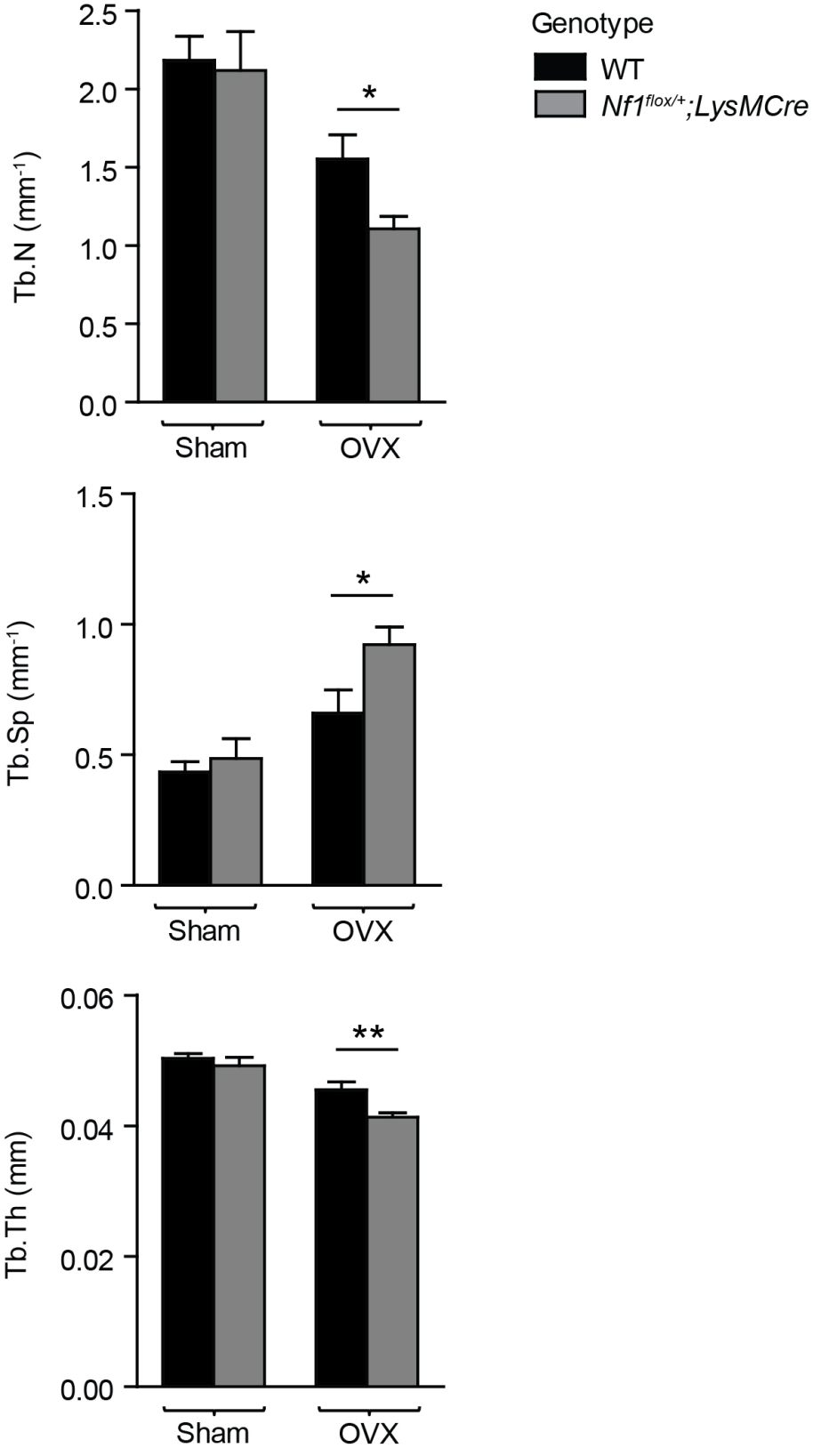
Genotype
WT
Nf1flox/+;LysMCre
Tb.N (mm-1)
2.5
2.0
1.5
1.0
0.5
0.0
*
Sham
OVX
Tb.Sp (mm-1)
1.5
1.0
0.5
0.0
*
Sham
OVX
Tb.Th (mm)
0.06
0.04
0.02
0.00
**
Sham
OVX

Figure 23D

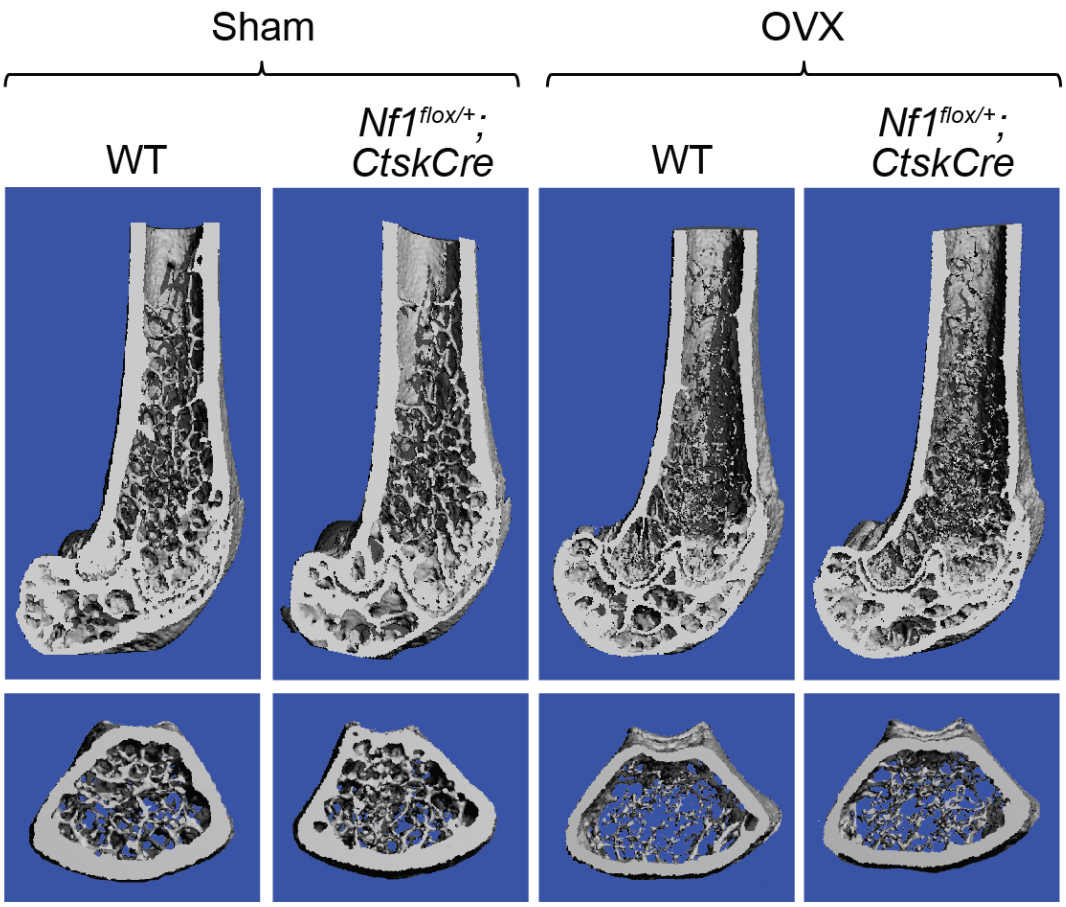


Figure 23E

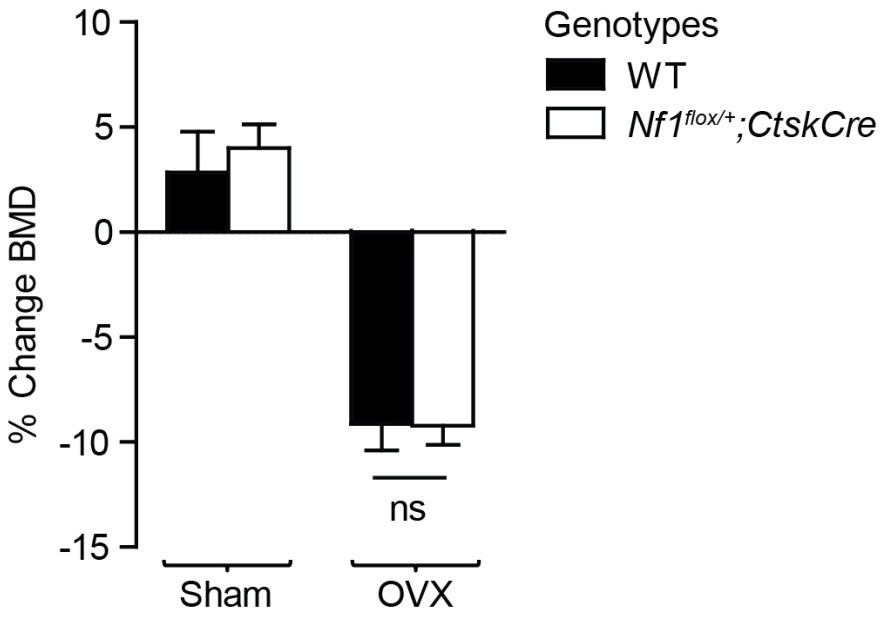
10
5
0
-5
-10
-15
% Change BMD
Genotypes
WT
Nf1flox/+;CtskCre
ns
Sham
OVX

Figure 23F

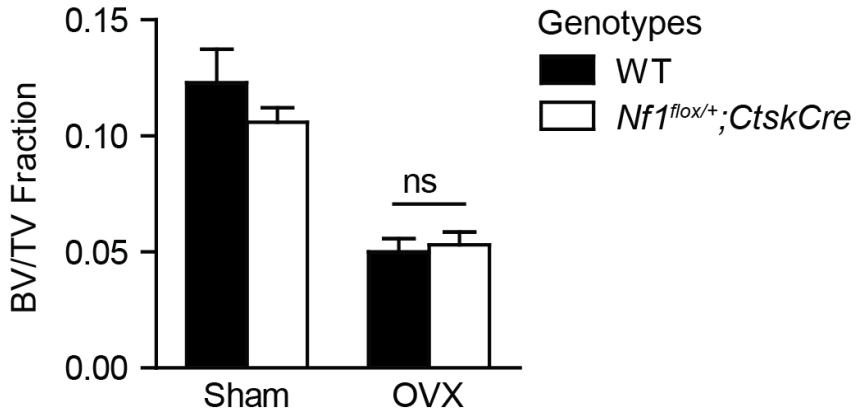
0.15
0.10
0.05
0.00
BV/TV Fraction
ns
Sham
OVX
Genotypes
WT
Nf1flox/+;CtskCre

Figure 23G

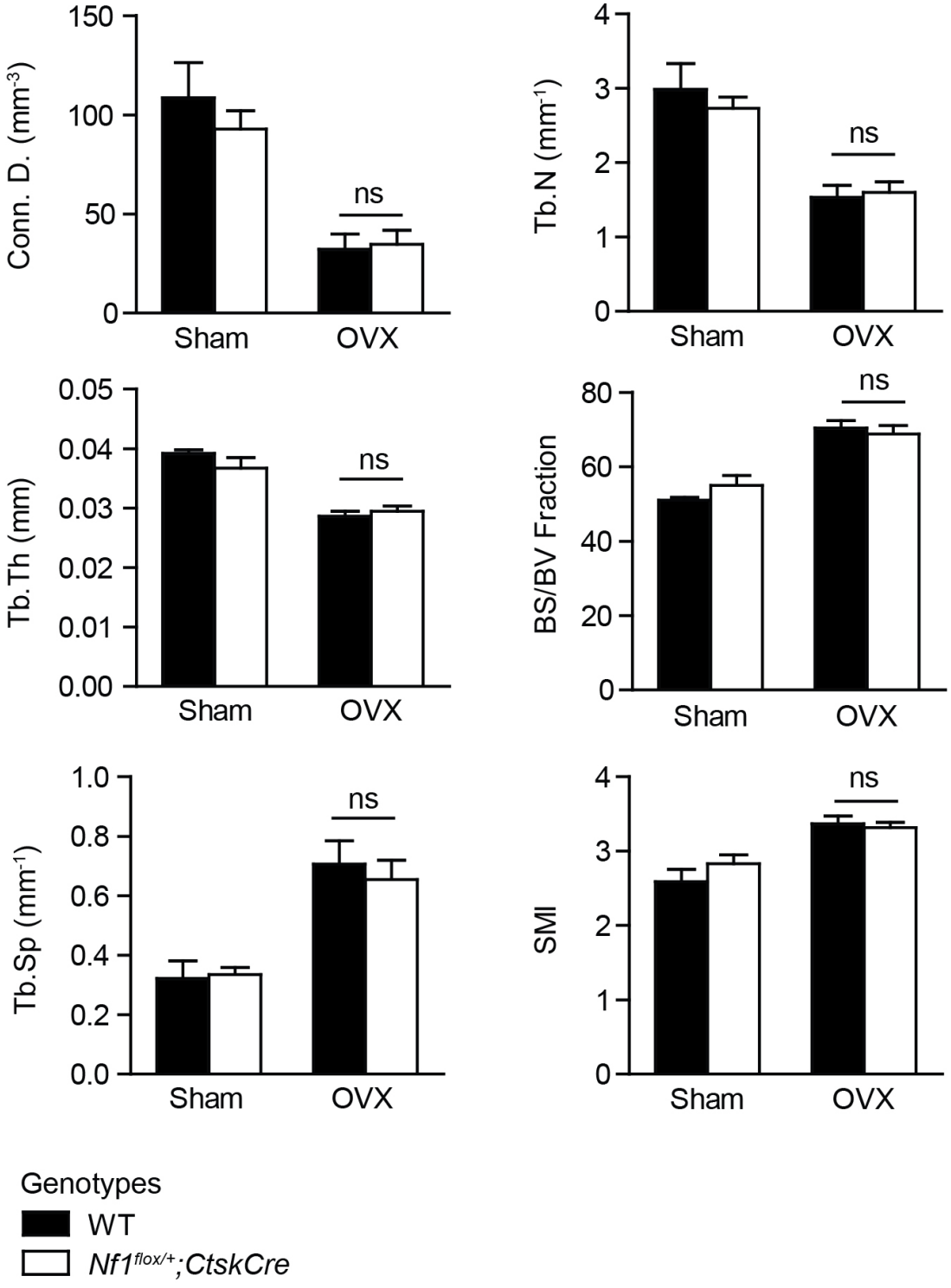
Conn. D. (mm-3)
150
100
50
0
ns
Sham
OVX
Tb.N (mm-1)
4
3
2
1
0
ns
Sham
OVX
Tb.Th (mm)
0.05
0.04
0.03
0.02
0.01
0.00
ns
Sham
OVX
BS/BV Fraction
80
60
40
20
0
ns
Sham
OVX
Tb.Sp (mm-1)
1.0
0.8
0.6
0.4
0.2
0.0
ns
Sham
OVX
SMI
4
3
2
1
0
ns
Sham
OVX
Genotypes
WT
Nf1flox/+;CtskCre

Figure 23H

**Figure 23. *Nf1* haploinsufficiency in myeloid progenitors potentiates bone loss in response to OVX mediated proresorptive challenge.** (A) The percent change in femoral BMD for WT and *Nf1$^{flox/+}$;LysMCre* mice was determined by pDEXA measurements acquired before and six weeks after either sham or OVX surgery. *n* = 5 sham, 8-10 OVX mice per genotype.*$P < 0.05$. (B) Representative μCT reconstructed femora in longitudinal (top) and transverse (bottom) cross-sections for WT versus *Nf1$^{flox/+}$;LysMCre* mice six weeks following either sham or OVX surgery. (C) Trabecular bone volume fraction (BV/TV) was quantified in the distal femur by μCT. *n* = 6 sham, 7-12 OVX mice per genotype. *$P < 0.05$. (D) Parameters of trabecular microarchitecture including trabecular number (Tb.N), trabecular spacing (Tb.Sp), and trabecular thickness (Tb.Th) were quantified as shown. *n* = 6 sham, 7-12 OVX mice per genotype. *$P < 0.05$, **$P < 0.01$. (E) Representative μCT reconstructed femora in longitudinal (top) and transverse (bottom) cross-sections for WT versus *Nf1$^{flox/+}$;CtskCre* mice six weeks following either sham or OVX surgery. (F) No significant difference was observed in the percent change in femoral BMD between WT and *Nf1$^{flox/+}$;CtskCre* six weeks-post OVX surgery. *n* = 6-7 sham, 10-15 OVX mice per genotype. (G) Femoral BV/TV was quantified by μCT as shown and revealed no significant difference between WT and *Nf1$^{flox/+}$;CtskCre* mice. *n* = 5 sham, 12 OVX mice per genotype. (H) No significant differences in trabecular microarchitecture parameters were found when comparing connectivity density (Conn.D.), trabecular number (Tb.N), trabecular spacing (Tb.Sp), and trabecular thickness (Tb.Th), bone surface/bone volume ratio (BS/BV), or structure model index (SMI) between WT and

*Nf1*$^{flox/+}$*;CtskCre* mice undergoing OVX surgery. *n* = 5 sham, 12 OVX mice per genotype.

**Cooperative interactions between *Nf1* haploinsufficient myeloid cells and *Nf1* nullizygous osteoblasts are required to induce tibial fracture non-union in *Nf1$^{flox/-}$;Col2.3Cre* mice**

It has been hypothesized that NF1 osseous defects, in particular pseudarthrosis, may require the heterotypic interaction of multiple cell types with varying *Nf1* gene dosage [86]. Supporting this paradigm, recent clinical data confirms that at least a subset of NF1 pseudarthrosis patients exhibit biallelic inactivation of *NF1* in tissue microdissected from the lesion site [80, 81]. Recently, we established that *Nf1$^{flox/-}$;Col2.3Cre* mice (harboring conditional *Nf1$^{-/-}$* osteoblasts and a *Nf1$^{+/-}$* background) recapitulate characteristic skeletal manifestations found in NF1 patients including tibial fracture non-union [78]. By adoptive transfer of WT and *Nf1$^{+/-}$* bone marrow cells into *Nf1$^{flox/flox}$;Col2.3Cre* recipient mice (harboring conditional *Nf1$^{-/-}$* osteoblasts), we demonstrated that the cooperative interaction between conditional *Nf1$^{-/-}$* osteoblasts and *Nf1$^{+/-}$* hematopoietic cells leads to recalcitrant fracture repair [78]. These data suggest that *Nf1* haploinsufficiency in at least a subset of hematopoietic lineages is integral to the pathogenesis of fracture non-union in this model. Given that *Nf1$^{+/-}$* osteoclasts exhibit multiple gain-in-functions [69, 72], we therefore hypothesized that *Nf1* haploinsufficient osteoclasts and their progenitors are the critical hematopoietic lineage underpinning fracture non-union in the NF1 murine model.

To test this hypothesis, we lethally irradiated *Nf1$^{flox/flox}$;Col2.3Cre* recipient mice and transplanted them with WT and *Nf1$^{flox/+}$;LysMCre* donor bone marrow cells. After waiting four months to achieve stable hematopoietic reconstitution, a

tibial fracture was induced and fracture healing was monitored for three months. *Nf1$^{flox/flox}$;Col2.3Cre* recipients transplanted with WT bone marrow cells healed normally (Figure 24A, B). In contrast, *Nf1$^{flox/flox}$;Col2.3Cre* recipients reconstituted with *Nf1$^{flox/+}$;LysMCre* bone marrow demonstrated persistent tibial fracture non-union (Figure 24A). Representative μCT reconstructions reveal defective cortical bridging across the fracture site (Figure 24B, top panel). Quantitatively, we found that the callus bone volume fraction (BV/TV) was significantly reduced in recipients reconstituted with *Nf1$^{flox/+}$;LysMCre* bone marrow cells as compared to WT (Figure 24B, bottom panel). Histologically, we observed infiltration of fibrous tissue into the lesion site of *Nf1$^{flox/flox}$;Col2.3Cre* mice transplanted with *Nf1$^{flox/+}$;LysMCre* bone marrow, and an abundance of TRACP positive staining osteoclasts (Figure 24C), features which closely recapitulate the human disease [62, 64, 65].

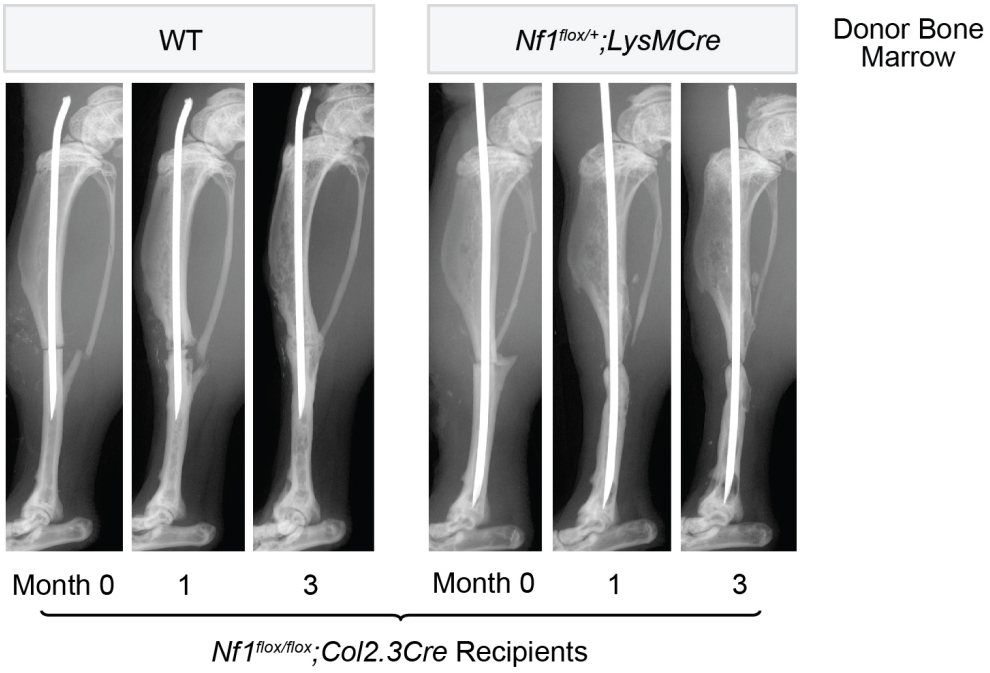
WT
Nf1flox/+;LysMCre
Donor Bone Marrow
Month 0
1
3
Month 0
1
3
Nf1flox/flox;Col2.3Cre Recipients

Figure 24A

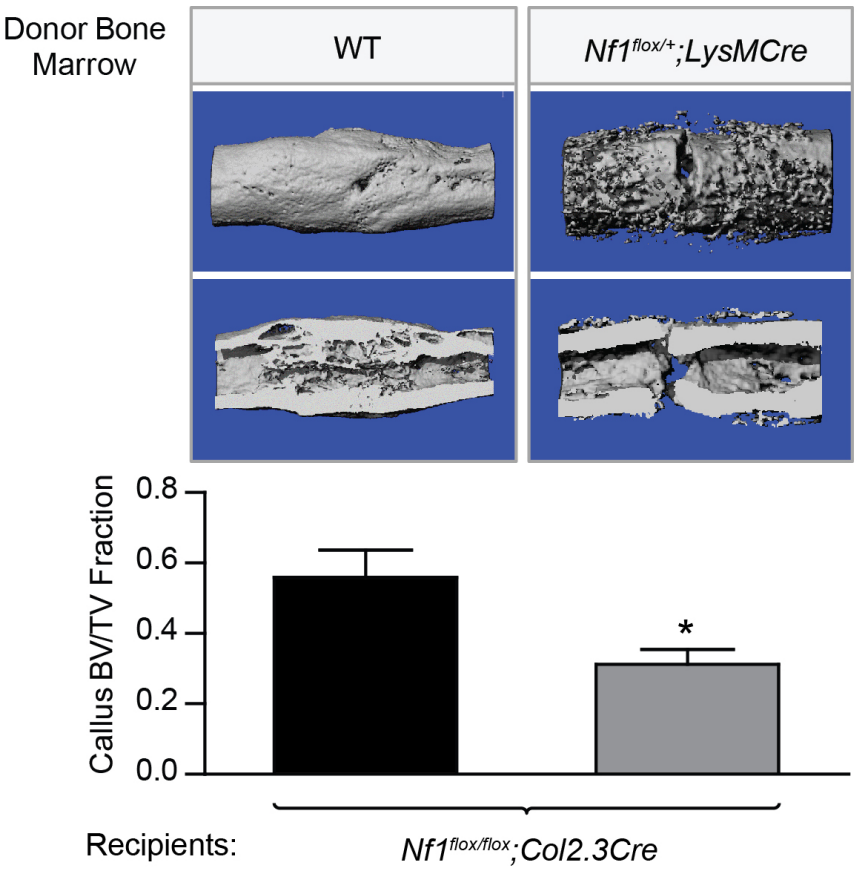
Donor Bone Marrow
WT
Nf1flox/+;LysMCre
Callus BV/TV Fraction
0.8
0.6
0.4
0.2
0.0
*
Recipients:
Nf1flox/flox;Col2.3Cre

Figure 24B

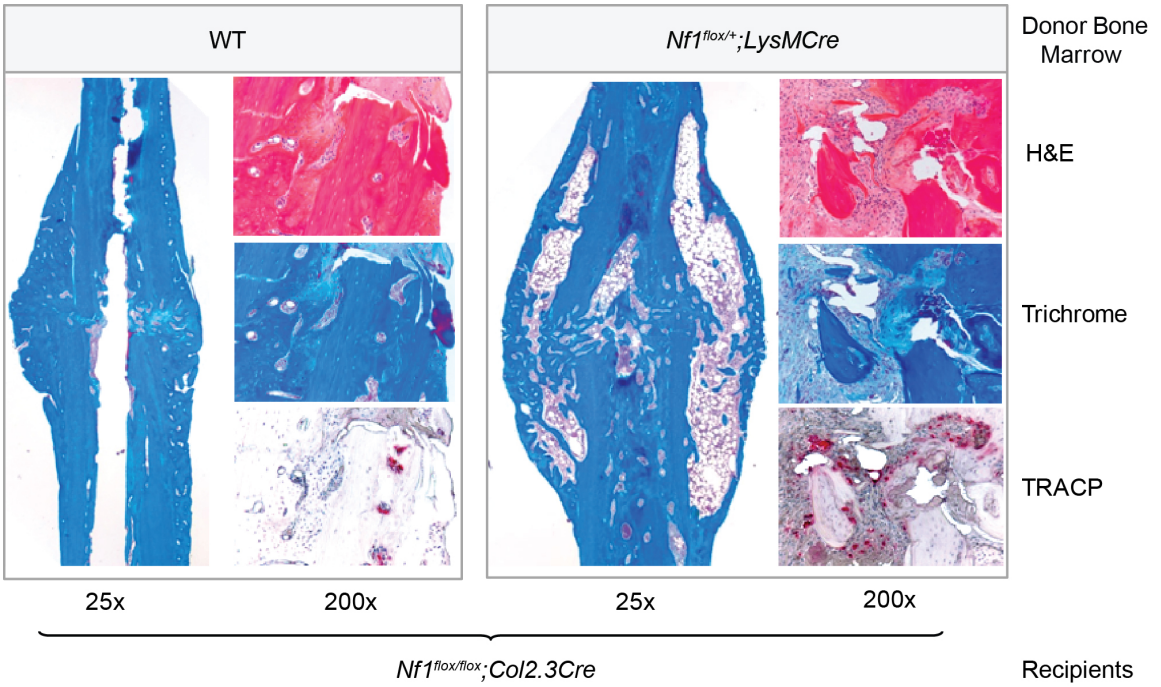
WT
Nf1flox/+;LysMCre
Donor Bone Marrow
H&E
Trichrome
TRACP
25x
200x
25x
200x
Nf1flox/flox;Col2.3Cre
Recipients

Figure 24C

**Figure 24. Transplantation of *Nf1$^{flox/+}$;LysMCre* hematopoietic cells induces tibial fracture non-union in mice harboring *Nf1* nullizygous osteoblasts.** (A) Representative radiographs demonstrate tibial fracture healing in *Nf1$^{flox/flox}$;Col2.3Cre* recipient mice reconstituted with either WT or *Nf1$^{flox/+}$;LysMCre* donor bone marrow cells. X-rays were acquired one and three months post-fracture. (B) Representative μCT reconstructed whole callus (top) and longitudinal cross-sections (bottom) from *Nf1$^{flox/flox}$;Col2.3Cre* mice undergoing bone marrow transplantation and tibial fracture. Callus bone volume fraction (BV/TV) was quantified by μCT as shown in the bar graph below. $n$ = 6-8 mice per group. *$P < 0.05$. (C) Representative tibial fractures in longitudinal cross-section stained with trichrome (25x and 200x magnification), H&E (200x magnification), and TRACP (200x magnification).

## Discussion

Multiple osteoclast gain-in-functions reported in both *Nf1*$^{+/-}$ mice and human *NF1* heterozygous cells are consistent with clinical observations that NF1 patients have reduced bone mineral density [22-26, 30] and are predisposed to increased fracture risk [27, 156]. Yet the precise role of *Nf1* in modulating the step-wise progression of osteoclast development remains unclear. By conditionally inactivating a single *Nf1* allele in early versus late stage osteoclastogenesis, we demonstrate that conditional *Nf1* haploinsufficiency in the early stage of myeloid development potentiates osteoclast differentiation and bone resorption. *Nf1*$^{flox/+}$*;LysMCre* mice exhibit increased frequency of osteoclast progenitors, enhanced osteoclastogenesis, and accelerated bone resorption following ovariectomy induced resorptive stress *in vivo*. Interestingly, recombination of the floxed *Nf1* allele in terminally differentiated osteoclasts, mediated by *CtskCre*, did not recapitulate these phenotypes in analogous experiments. These genetic data implicate haploinsufficient loss of *Nf1* in early stage myeloid progenitors as a pivotal requirement for potentiating osteoclast catabolic activity and bone loss *in vivo*. Given that genetic ablation of a single *Nf1* allele in terminally differentiated osteoclasts alone is insufficient to augment the rate of bone lytic activity, we therefore postulate that proresorptive phenotypes in the context of *Nf1* haploinsufficiency may be primarily mediated through an expansion in the pool of osteoclast precursors and an overall increase in osteoclast numbers, as opposed to the enhanced resorptive activity of individual osteoclasts themselves.

Alanne and colleagues recently reported that transgenic mice harboring conditional *Nf1* nullizygous (*Nf1*$^{-/-}$) osteoclasts driven by *TRAP-Cre*, exhibit increased bone resorptive capacity and aberrant actin ring formation *in vitro* [157]. Despite differences in *Nf1* gene dose (heterozygous versus biallelic *Nf1* inactivation), we postulate that the apparent osteoclast gain-in-functions in this mouse model are likely due to the expression of *TRAP-Cre* in more primitive stages of osteoclast/myeloid development as compared to *Ctsk-Cre*, which is restricted to mature, terminally differentiated osteoclasts [129]. Supporting this concept, the authors report that *Nf1*$^{flox/flox}$*;TRAP-Cre* mice exhibit a number of extra-osseous features including splenomegaly and megakaryocytosis [157]. These findings are reminiscent of the juvenile myelomonocytic leukemia (JMML)-like myeloproliferative disease (MPD) phenotypes seen following *Nf1* loss of heterozygosity (LOH) in the hematopoietic compartment [67, 158-160], and are suggestive of *TRAP-Cre* mediated *Nf1* recombination in relatively primitive myeloid osteoclast precursors as previously characterized [129]. Given the fact that NF1 patients with osteopenia and osteoporosis typically retain a single functional *NF1* allele, we chose to focus our present studies on the physiological consequences of *Nf1* heterozygosity in osteoclast development.

Focal NF1 skeletal abnormalities such as tibial pseudarthrosis occur at a lower rate than generalized bone mass deficits, implying that modifying factors – such as localized *NF1* LOH – may be required to precipitate the pathology. Recent clinical data support this concept, demonstrating that at least a subset of

NF1 pseudarthrosis patients exhibit *NF1* LOH in tissue microdissected from the lesion site [80, 81]. Modeling the heterotypic interaction of multiple cell types with varying *Nf1* gene dosage, we have recently shown that *Nf1$^{flox/-}$;Col2.3Cre* mice (harboring *Nf1$^{-/-}$* osteoblasts on a *Nf1$^{+/-}$* background) recapitulate multiple osseous deficits seen in the human disease, including low bone mass and tibial fracture non-union [77, 78]. Through a series of adoptive bone marrow transfer experiments, we have previously shown that cooperative interactions between conditional *Nf1$^{-/-}$* osteoblasts and *Nf1$^{+/-}$* hematopoietic cells are integral to the pathogenesis of tibial fracture non-union in *Nf1$^{flox/-}$;Col2.3Cre* mice [78]. Still, we had yet to identify the culprit lineage(s) within the hematopoietic system which were critical for inducing the pathological bone repair process.

Although osteoclasts are abundantly present in pseudarthrosis tissue dissected from human NF1 patients [62, 64, 65] as well as in multiple murine models of the disease [76, 78, 79, 138, 141], to date, no study has directly assessed the functional significance of *Nf1* haploinsufficient osteoclasts and their progenitors in the pathogenesis of NF1 fracture non-union. Here, we demonstrate that transplantation of *Nf1$^{flox/+}$;LysMCre* hematopoietic cells can induce tibial fracture non-union in *Nf1$^{flox/flox}$;Col2.3Cre* recipient mice. These data provide direct genetic evidence that inactivation of a single *Nf1* allele in osteoclasts and myeloid progenitors pivotally modulates recalcitrant fracture healing in a murine NF1 pseudarthrosis model.

A recent pseudarthrosis model developed by El-Hoss and colleagues utilizes the injection of a Cre-expressing adenovirus (AdCre) into the tibia to

inactivate floxed *Nf1* alleles within the fracture site [161]. When comparing fractures in *Nf1*$^{flox/flox}$ and *Nf1*$^{flox/-}$ mice following injection of AdCre, there were no significant differences in the rate of fracture healing between the two strains, leading the authors to conclude that the primary deficiency in pseudarthrosis is likely to involve "poor *Nf1*$^{null}$ bone anabolism rather than increased responsiveness of *Nf1*$^{+/-}$ osteoclast precursors [161]." An inherent difficulty associated with this approach, however, is the lack of selectivity associated with AdCre injection, whereby Cre-mediated recombination of the floxed *Nf1* allele(s) will occur non-specifically in any cell types present within the lesion, including both osteoclast and osteoblast progenitors. In effect, AdCre injection renders *Nf1*$^{flox/flox}$ and *Nf1*$^{flox/-}$ strains genetically equivalent within the fracture site, whereby all cells expressing AdCre effectively become *Nf1* nullizygous. This could explain why equivocal results were obtained when comparing the *Nf1*$^{flox/flox}$ and *Nf1*$^{flox/-}$ strains following AdCre injection. By contrast, the results of the present study implicate increased bone lytic activity of *Nf1*$^{+/-}$ osteoclasts as a pivotal factor underlying the pathogenesis of tibial fracture non-union in *Nf1*$^{flox/-}$*;Col2.3Cre* mice. We further contend that a hematopoietic stem cell transplantation approach, as utilized herein, provides a rigorous methodology to segregate and independently assess the functional roles of *Nf1* nullizygous osteoblasts versus *Nf1*$^{+/-}$ osteoclasts and myeloid progenitors in the pathogenesis of tibial fracture non-union.

# CHAPTER 5. HYPERACTIVE TGF-β1 SIGNALING PIVOTALLY UNDERPINS OSSEOUS DEFICITS IN NF1 MICE

## Introduction

The molecular mechanisms responsible for low bone mass and recalcitrant fracture healing in NF1 patients are not clearly defined, yet deregulation of osteoclast and osteoblast function, the principal cellular drivers of bone resorption and bone formation, has been widely reported both in NF1 mouse models [69, 73-75] as well as in osteoblasts and osteoclasts cultured *ex vivo* from human patients with the disease [69-71]. Transforming growth factor-beta1 (TGF-β1) has become increasingly recognized as a critical mediator of physiological and pathological skeletal remodeling. Recently, Tang and colleagues demonstrated the pivotal role of TGF-β1 as a master switch regulating the spatiotemporal coupling of bone resorption and formation [94]. Having previously established that *Nf1* haploinsufficient myeloid cells potentiate neurofibroma phenotypes through secreted TGF-β signaling [89], we hypothesized that analogous paracrine signaling between *Nf1* deficient osteoblasts and osteoclasts may be integral to the pathogenesis of NF1 skeletal defects.

To determine the functional significance of TGF-β signaling in deregulated NF1 bone remodeling, we utilized the *Nf1$^{flox/-}$;Col2.3Cre* mouse model, which recapitulates characteristic skeletal manifestations found in NF1 patients, including low bone mass and tibial non-union fracture [77, 78]. Here, we show

that serum TGF-β1 levels are five- to six- fold increased both in *Nf1*$^{flox/-}$*;Col2.3Cre* mice and in a cohort of NF1 patients. We further delineate a mechanism by which TGF-β1 is hypersecreted from *Nf1* deficient osteoprogenitors and acts to preferentially enhance *Nf1*$^{+/-}$ osteoclast bone resorptive activity, while inhibiting osteoblast differentiation by *Nf1*$^{-/-}$ MSCs. By re-expressing the human, full-length neurofibromin GTPase-activating protein (GAP)-related domain (*NF1* GRD) in *Nf1* deficient osteoprogenitor cells, we demonstrate that p21-Ras-dependent hyperactivation of the canonical TGF-β1-Smad pathway is associated with hyperresponsiveness to TGF-β1 signals by *Nf1* deficient bone cells. Notably, treatment with a pharmacologic inhibitor of TβRI kinase activity (SD-208) rescued bone mass defects and prevented tibial fracture non-union in *Nf1*$^{flox/-}$*;Col2.3Cre* mice. Collectively, these data implicate dysregulated TGF-β1 signaling as a primary factor underlying the pathogenesis of NF1 associated osteoporosis and pseudarthrosis. Moreover, modulation of TGF-β signaling may serve as a potential therapeutic target in the treatment for NF1 osseous defects which are refractory to current modalities.

### *Nf1* regulates TGF-β1 expression

In human disease, alterations in TGF-β signaling occur via several mechanisms, including aberrant ligand expression/activation, receptor mutations, and dysregulation of downstream effectors pathways. We examined the serum TGF-β1 levels in *Nf1*$^{flox/-}$*;Col2.3Cre* mice, which closely recapitulate a spectrum of osseous manifestations seen in NF1 patients. Strikingly, we found that the

serum level of total TGF-β1 in *Nf1$^{flox/-}$;Col2.3Cre* mice was five- to six-fold elevated as compared to WT controls (Figure 25A). To identify the cell type responsible for TGF-β1 overproduction, we examined TGF-β1 expression at the mRNA and protein levels from WT, *Nf1$^{+/-}$*, and *Nf1$^{-/-}$* osteoblast progenitors (MSCs), as this lineage is the principal source of TGF-β1 in bone [87]. *Nf1$^{+/-}$* and *Nf1$^{-/-}$* MSCs, as compared with WT cells, expressed significantly more TGF-β1 mRNA (Figure 25B, top panel) and protein (Figure 25B, bottom panel). Further corroborating neurofibromin's function as a negative regulator of TGF-β1 expression, we observed significantly increased serum TGF-β1 levels in human NF1 patients as compared to healthy controls (Figure 25C). Collectively, these data imply that deletion of *Nf1* leads to pathological TGF-β1 overproduction in a gene dosage-dependent fashion.

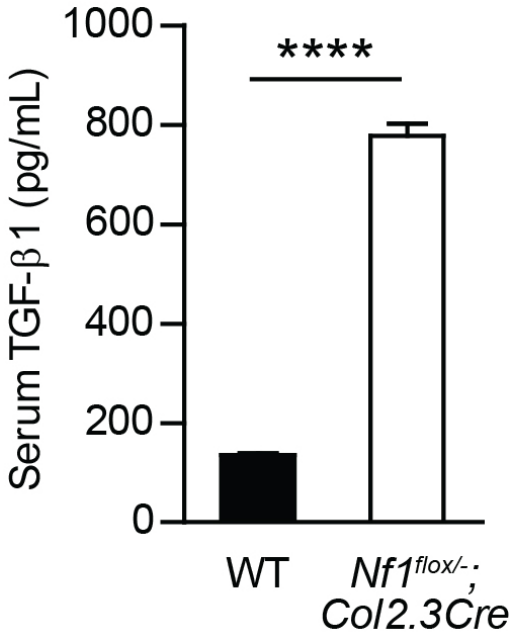


Figure 25A

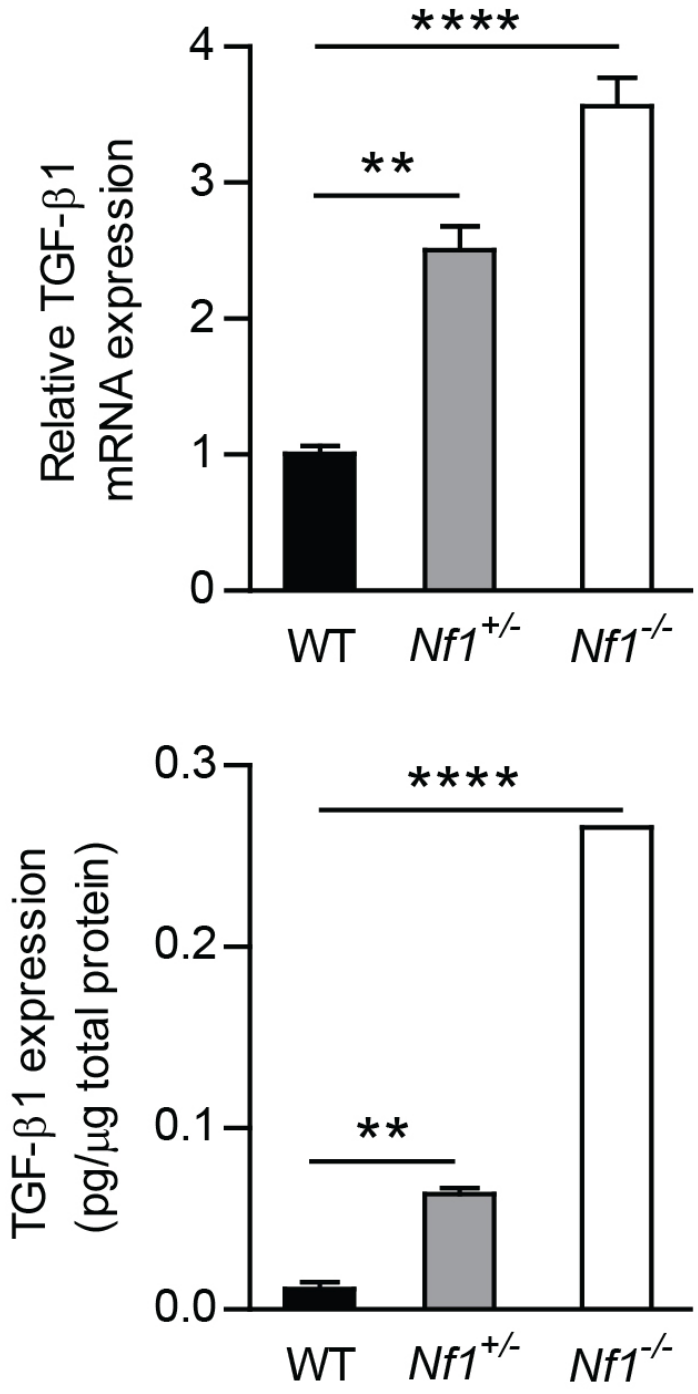
****
**
Relative TGF-β1 mRNA expression
4
3
2
1
0
WT
Nf1+/-
Nf1-/-
****
**
TGF-β1 expression (pg/μg total protein)
0.3
0.2
0.1
0.0
WT
Nf1+/-
Nf1-/-

Figure 25B

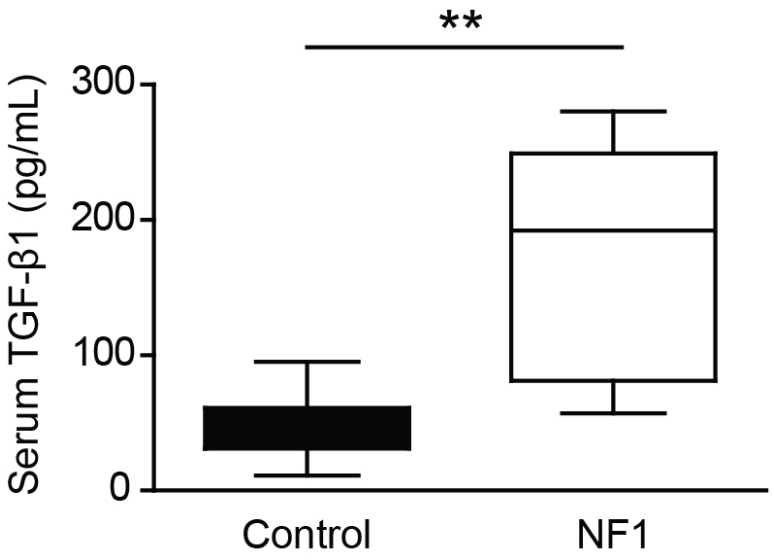


Figure 25C

**Figure 25. *Nf1* gene dose regulates TGF-β1 production by osteoblasts.** (A) Serum TGF-β1 levels were measured by ELISA in WT and *Nf1$^{flox/-}$;Col2.3Cre* mice. $n = 4$. ****$P < 0.0001$. (B) TGF-β1 mRNA expression in WT, *Nf1$^{+/-}$*, *Nf1$^{-/-}$* osteoblast progenitors was examined by real-time quantitative RT-PCR. $n = 3$. **$P < 0.01$, ****$P < 0.0001$ (top panel). Protein extracts were examined by ELISA to determine TGF-β1 protein expression. $n = 3$. **$P < 0.01$, ****$P <$ 0.0001 (bottom panel). (C) Serum TGF-β1 levels were measured by ELISA in human NF1 patients and healthy controls. $n = 7$. **$P < 0.01$.

**Aberrant Smad signaling mediates dysregulated *Nf1* bone cell function**

Loss of *Nf1* leads to p21-Ras-dependent TGF-β1 overexpression and activation of the Smad pathway in MSCs, inhibiting osteoblast differentiation.

Canonical TGF-β signaling involves the phosphorylation of Smad proteins by TβRI [96]. To examine the role of *Nf1* in regulating this pathway, we compared TGF-β1 induced activation of Smad2 in WT, $Nf1^{+/-}$, and $Nf1^{-/-}$ MSCs. We observed an increase in TGF-β1 induced Smad2 phosphorylation in $Nf1^{-/-}$ osteoprogenitors versus WT controls (Figure 26A), while the total protein expression of Smad2 (Figure 26A), TGF-β receptor 1 (TβRI), and TGF-β receptor 2 (TβRII) (Figure 26B) remained constant. To further assess the implications of increased TGF-β1 biochemical activity on osteoblastogenesis, WT and $Nf1^{-/-}$ MSCs were cultured in osteogenic differentiation medium supplemented with TGF-β1. Expression of the osteoblast marker alkaline phosphatase (ALP), which is impaired at the basal level in $Nf1^{-/-}$ osteoblasts, was further reduced by 87% in $Nf1^{-/-}$ cells as compared to just 53% in WT osteoblast cultures stimulated with TGF-β1 (Figure 26C). Application of SD-208, an inhibitor of TβRI activity, was effective in attenuating Smad phosphorylation to basal levels (Figure 26D) and in rescuing ALP expression (Figure 26E). Collectively, these results corroborate neurofibromin's role as a suppressor of canonical TGF-β1 signaling in osteoblasts, whereby haploinsufficient or nullizygous *Nf1* gene ablation amplifies TGF-β1 signaling through the Smad pathway, exacerbating intrinsic deficits in terminal osteoblast differentiation – a critical component of bone anabolism.

To further determine if TGF-β1 overproduction and increased canonical TGF-β1 signaling via the Smad pathway are direct consequences of p21-Ras hyperactivity, *Nf1* deficient MSCs were transduced with a recombinant retrovirus encoding the full length *NF1* GAP-related domain (GRD) and a selectable marker, pac, which confers resistance to puromycin [73]. As compared to *Nf1*$^{-/-}$ MSCs expressing MSCV-pac alone, reconstitution of the full length *NF1* GRD in *Nf1* deficient MSCs attenuated the expression of TGF-β1 mRNA transcripts by nearly 50% (Figure 26F) and suppressed Smad phosphorylation (Figure 26G) following TGF-β1 stimulation. This reduction in TGF-β1 expression and signaling in *Nf1* deficient MSCs is consistent with the normalization of Ras GTP activity following reconstitution with functional *NF1* GRD as we have reported previously [73]. Collectively, these data implicate increased p21-Ras activity as a direct mediator of aberrant TGF-β1 expression and signaling in *Nf1* deficient MSCs.

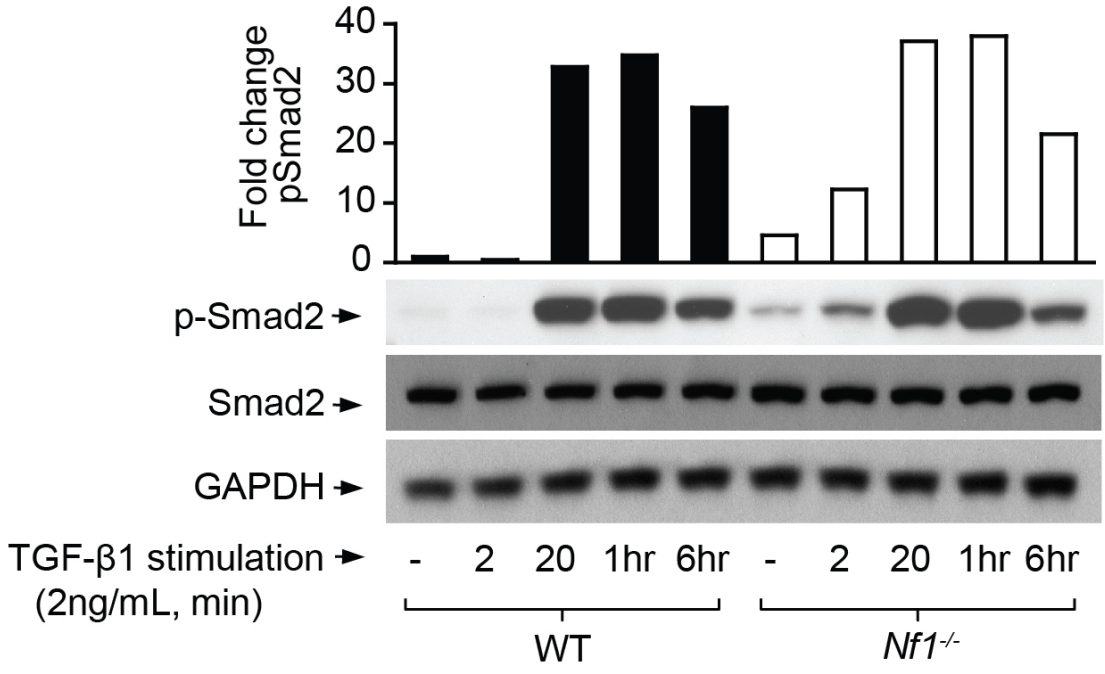
Fold change pSmad2
40
30
20
10
0
p-Smad2
Smad2
GAPDH
TGF-β1 stimulation
(2ng/mL, min)
- 2 20 1hr 6hr - 2 20 1hr 6hr
WT
Nf1-/-

Figure 26A

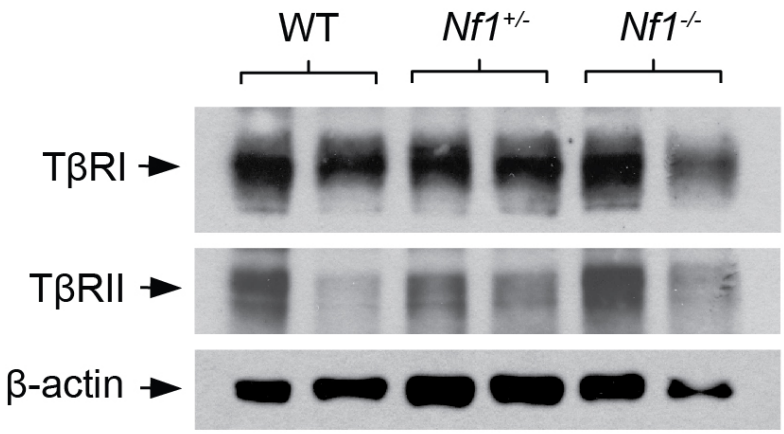


Figure 26B

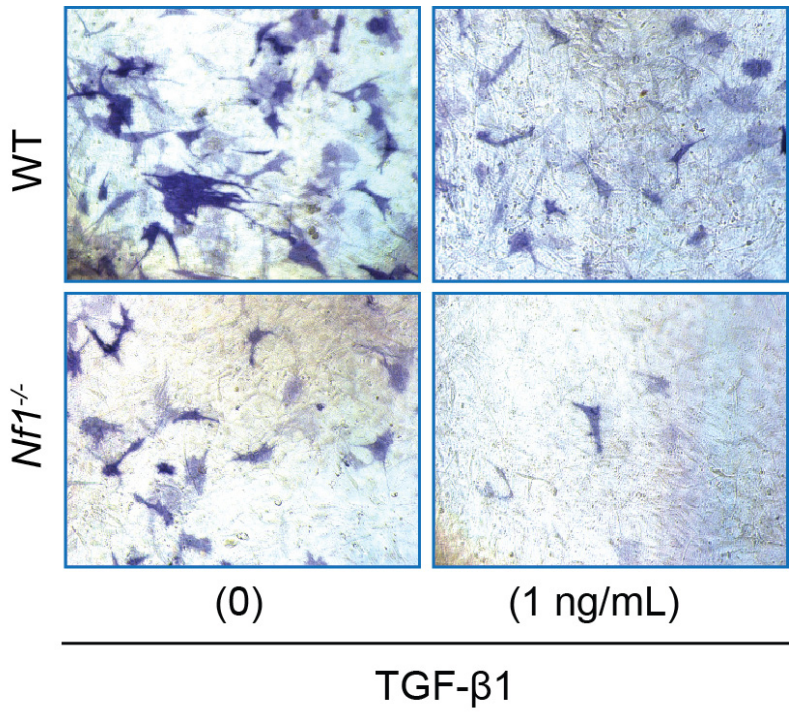
WT
Nf1-/-
(0)
(1 ng/mL)
TGF-β1

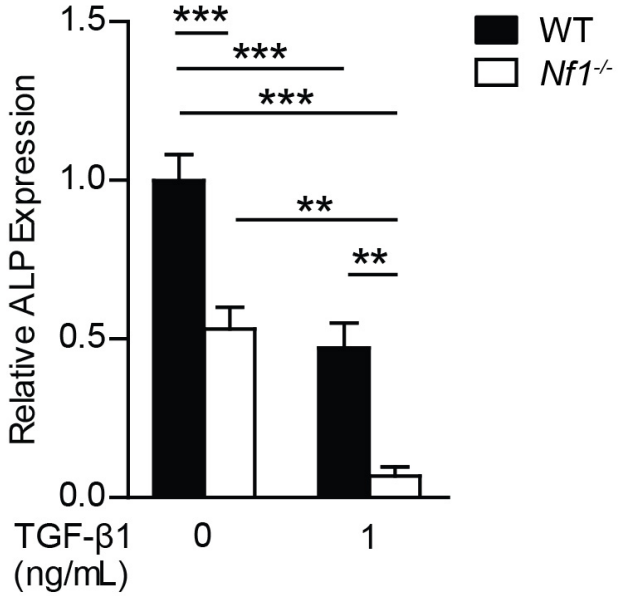
1.5
1.0
0.5
0.0
Relative ALP Expression
***
***
***
**
**
WT
Nf1-/-
TGF-β1
(ng/mL)
0
1

Figure 26C

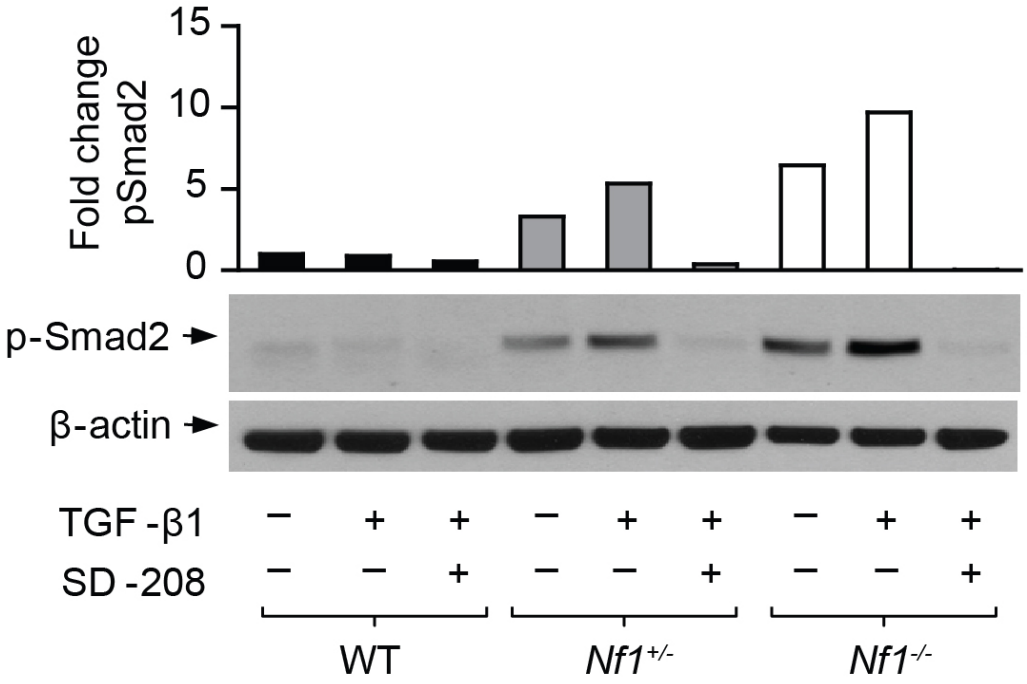
Fold change pSmad2
15
10
5
0
p-Smad2
β-actin
TGF -β1
SD -208
WT
Nf1+/-
Nf1-/-

Figure 26D

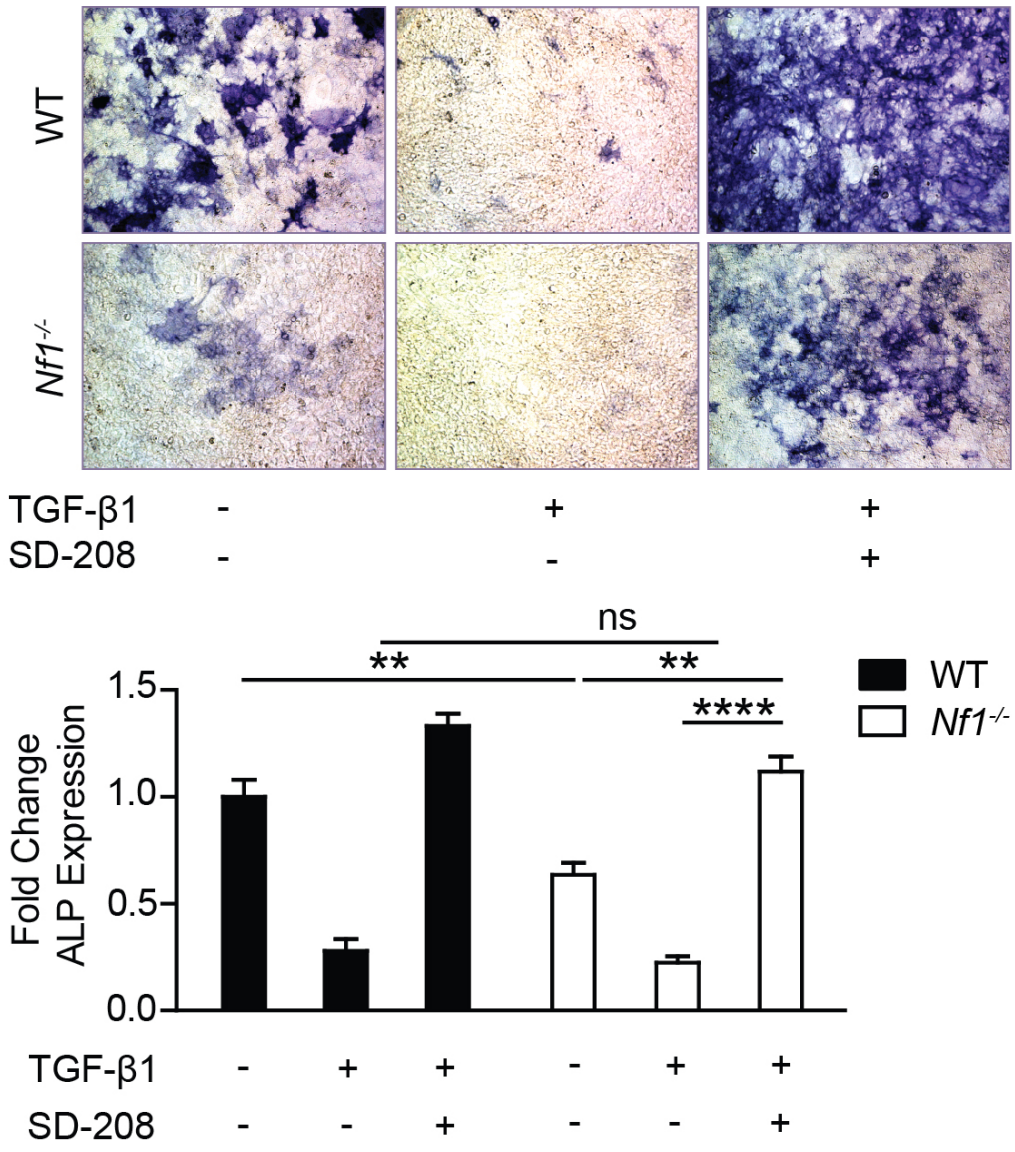
WT
Nf1-/-
TGF-β1 - + +
SD-208 - - +
ns
**
**
****
WT
Nf1-/-
Fold Change ALP Expression
1.5
1.0
0.5
0.0
TGF-β1 - + + - + +
SD-208 - - + - - +

Figure 26E

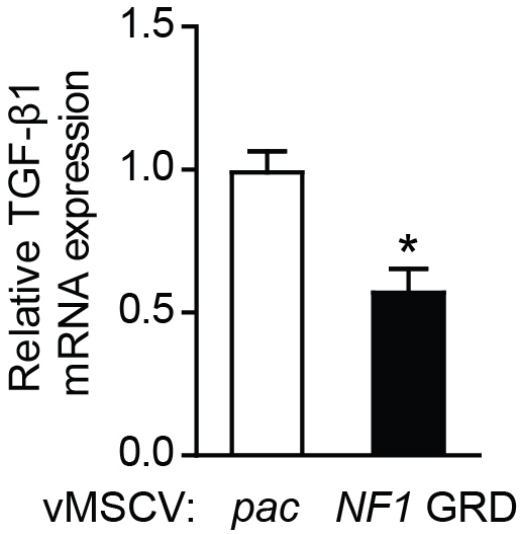


Figure 26F

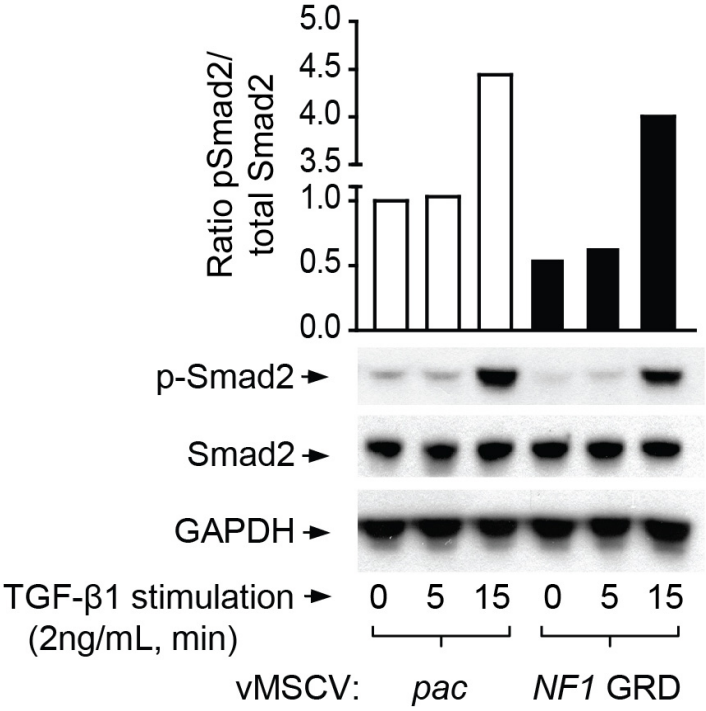
5.0
4.5
4.0
3.5
1.0
0.5
0.0
Ratio pSmad2/
total Smad2
p-Smad2
Smad2
GAPDH
TGF-β1 stimulation
(2ng/mL, min)
0 5 15 0 5 15
vMSCV: pac NF1 GRD

Figure 26G

**Figure 26. *Nf1* deficient MSCs exhibit hyperactivation of the Smad pathway and impaired osteoblast differentiation in response to TGF-β1.** (A) p-Smad2, Smad2, and GAPDH levels were detected by western blot in osteoblast progenitors stimulated with TGF-β1. The quantitative fold change in p-Smad2 was determined relative to the loading control as shown in the bar graph above. (B) Expression levels of TβRI, TβRII, and β-actin were detected by western blot in cell lysates collected from WT, $Nf1^{+/-}$, and $Nf1^{-/-}$ osteoblast progenitors. (C) Osteoblast progenitors were cultured in osteogenic differentiation medium supplemented with TGF-β1. Representative photomicrographs (top panel) show alkaline phosphatase (ALP) positive osteoblasts (magnification, 200x). ALP expression was quantified and normalized to the WT control as shown (bottom panel). $n = 3$. $^{**}P < 0.01$, $^{***}P < 0.001$. (D) Western blot showing p-Smad2 and β-actin expression in osteoprogenitors following treatment with TGF-β1 and SD-208. The bar graph above represents the fold change in p-Smad2 compared to the protein loading control. (E) WT and $Nf1^{-/-}$ osteoblast progenitors were cultured in osteogenic differentiation medium supplemented with TGF-β1 in the presence or absence of SD-208. Representative photomicrographs (top panel) show ALP positive osteoblasts (magnification, 100x). The bar graph (bottom panel) shows the fold change in ALP activity relative to the WT control. $n = 4$. $^{**}P < 0.01$, $^{***}P < 0.0001$. (F) TGF-β1 mRNA expression was measured in $Nf1^{-/-}$ MSCs following retroviral transduction with control vector (MSCV-pac) versus the functional, full-length *NF1* GRD construct. $n = 3$. $^{*}P < 0.05$. (G) p-Smad2, Smad2, and GAPDH levels were detected by western blot in MSCs stimulated with TGF-β1 following

transduction with either MSCV-pac or MSCV-*NF1* GRD retroviral vectors. The quantitative fold change in p-Smad2 was determined relative to the level of total Smad2 protein as shown in the bar graph above.

Hyperactive TGF-β1-Smad signaling potentiates *Nf1*$^{+/-}$ osteoclast catabolic activity

Given that TGF-β1 has a pivotal impact on cellular functions of both osteoblasts and osteoclasts in bone development, we next examined the effects of TGF-β1 on aberrant bone catabolic activity by *Nf1* haploinsufficient osteoclasts. BMMNCs cultured from *Nf1*$^{+/-}$ mice demonstrated a significantly increased capacity to form TRACP positive staining, multinucleated osteoclasts following treatment with TGF-β1 as compared to WT controls (Figure 27A). Application of TβRI kinase inhibitor (SD-208) attenuated osteoclast formation in a dose dependent fashion, with an observable effect beginning at 100 nM in the *Nf1*$^{+/-}$ cultures as compared to 500 nM in the WT cells (Figure 27B). Actin ring formation, a prerequisite for osteoclast bone resorption, was also increased in *Nf1*$^{+/-}$ osteoclasts cultured in the presence of TGF-β1, and suppressed by escalating concentrations of SD-208 (Figure 27C). To directly assess the effects of TGF-β1 on osteoclast function, WT and *Nf1*$^{+/-}$ osteoclasts were cultured on dentine slices in the presence of TGF-β1. *Nf1*$^{+/-}$ osteoclasts generated markedly increased numbers of resorptive “pits” following treatment with TGF-β1 as compared to WT controls (Figure 27D), suggesting that TGF-β1 can preferentially activate osteoclast bone resorptive activity in the context of *Nf1* haploinsufficiency. TβRI kinase inhibition attenuated “pit” formation to basal levels in both WT and *Nf1*$^{+/-}$ osteoclast cultures. We further show that *Nf1*$^{+/-}$ osteoclast hyperresponsiveness to TGF-β1 is correlated with increased biochemical activity of the canonical TGF-β1/Smad pathway. Increased levels of

phosphorylated Smad2 were detected in *Nf1*$^{+/-}$ osteoclasts stimulated with TGF-β1, while total levels of Smad2 protein were equivalent between the two genotypes (Figure 27E). Osteoclasts cultured from the peripheral blood of a human NF1 patient and an age/sex matched healthy control exhibited a similar phenotype when treated with TGF-β1 (Figure 27F). Collectively, these data indicate that neurofibromin functions to negatively regulate Smad-dependent TGF-β1 signaling in osteoclasts, whereby *Nf1* haploinsufficiency promotes excess osteoclast bone lytic activity via hypersensitivity to TGF-β1 stimulation.

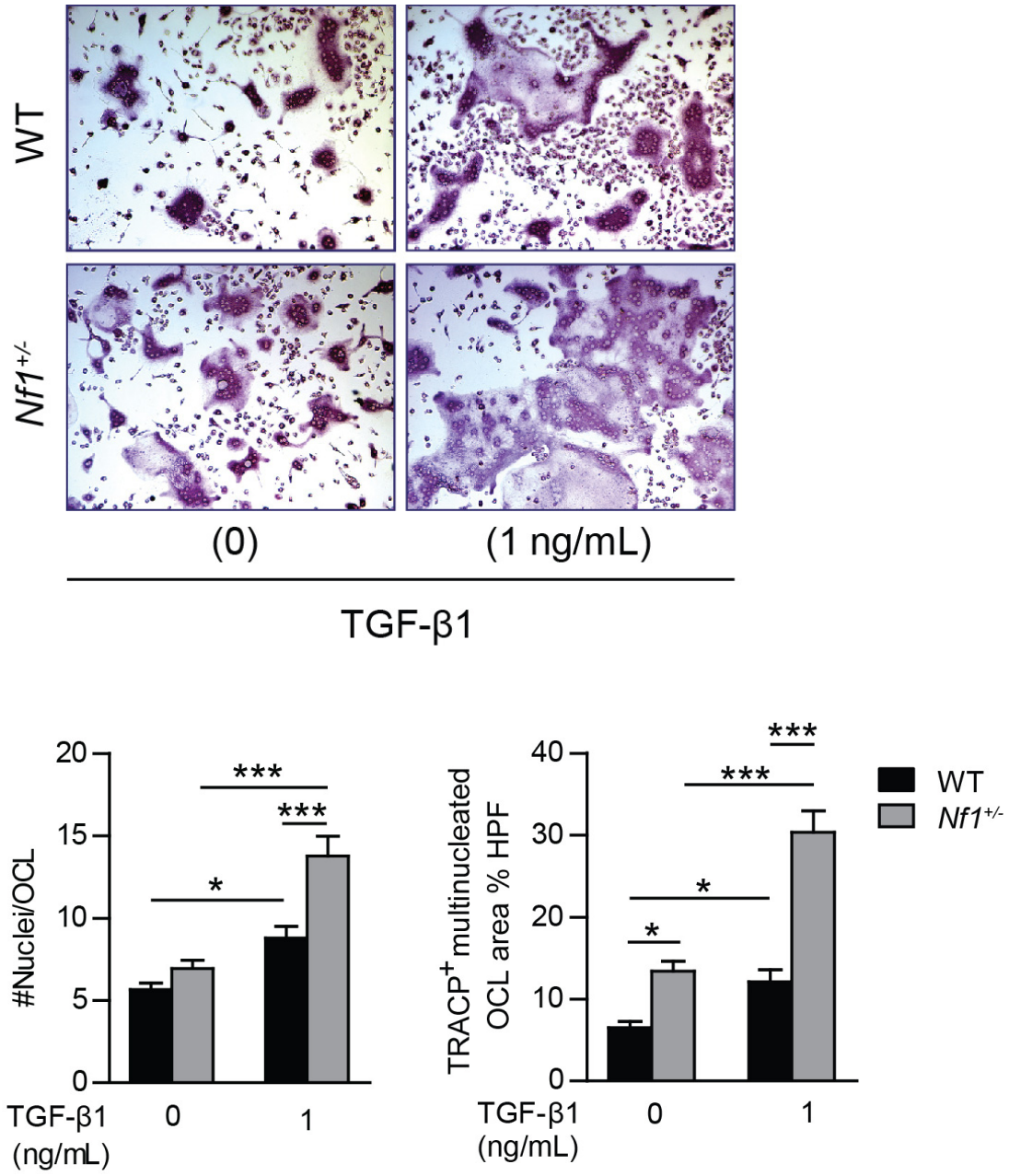
WT
Nf1+/-
(0)
(1 ng/mL)
TGF-β1
#Nuclei/OCL
20
15
10
5
0
***
***
*
TGF-β1
(ng/mL)
0
1
TRACP+ multinucleated
OCL area % HPF
40
30
20
10
0
***
***
*
*
TGF-β1
(ng/mL)
0
1
WT
Nf1+/-

Figure 27A

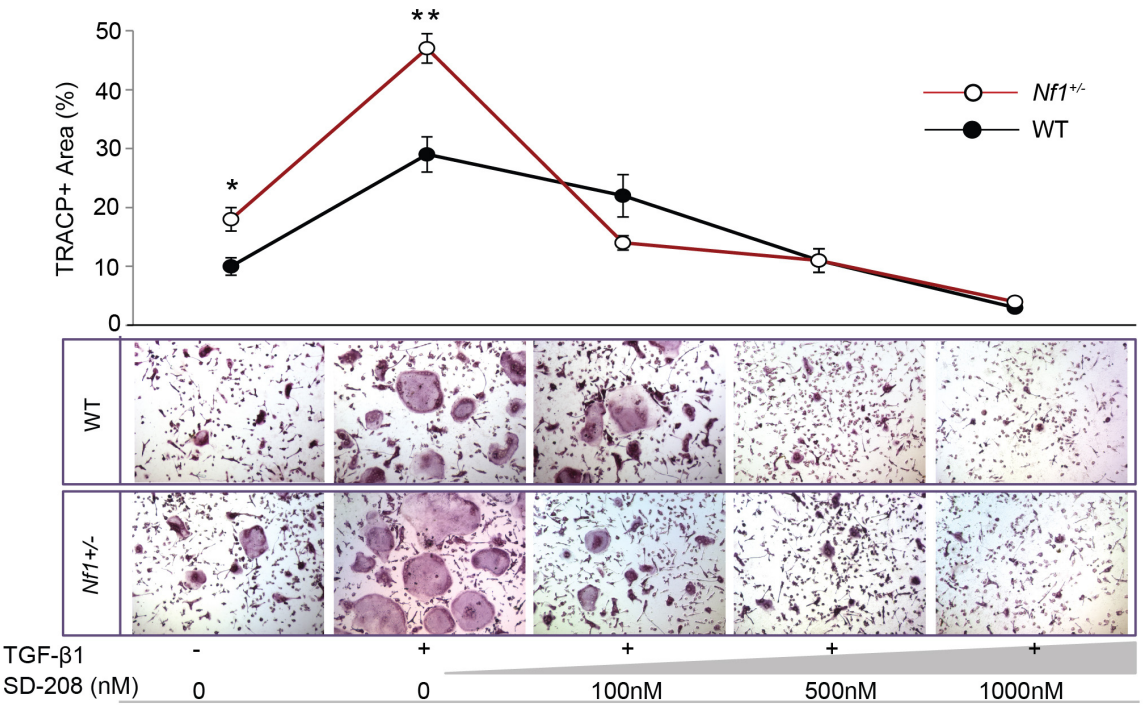
TRACP+ Area (%)
50
40
30
20
10
0
**
*
Nf1+/-
WT
WT
Nf1+/-
TGF-β1
SD-208 (nM)
-
+
+
+
+
0
0
100nM
500nM
1000nM

Figure 27B

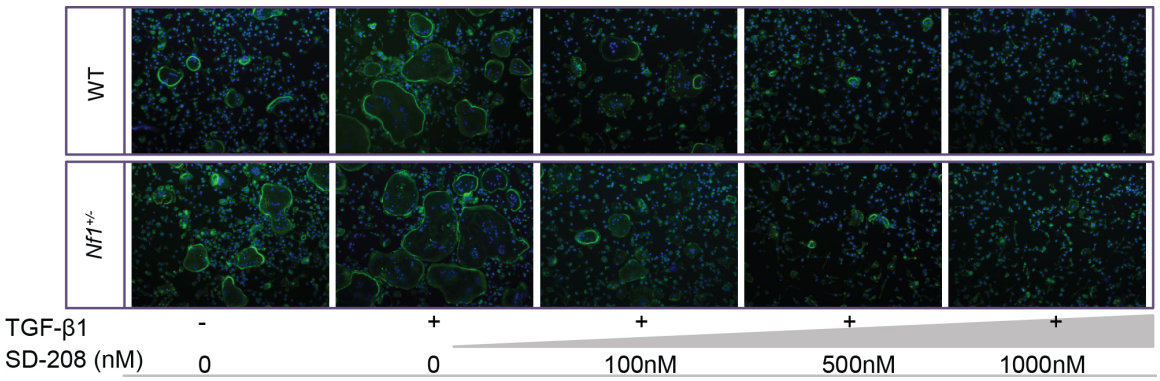


Figure 27C

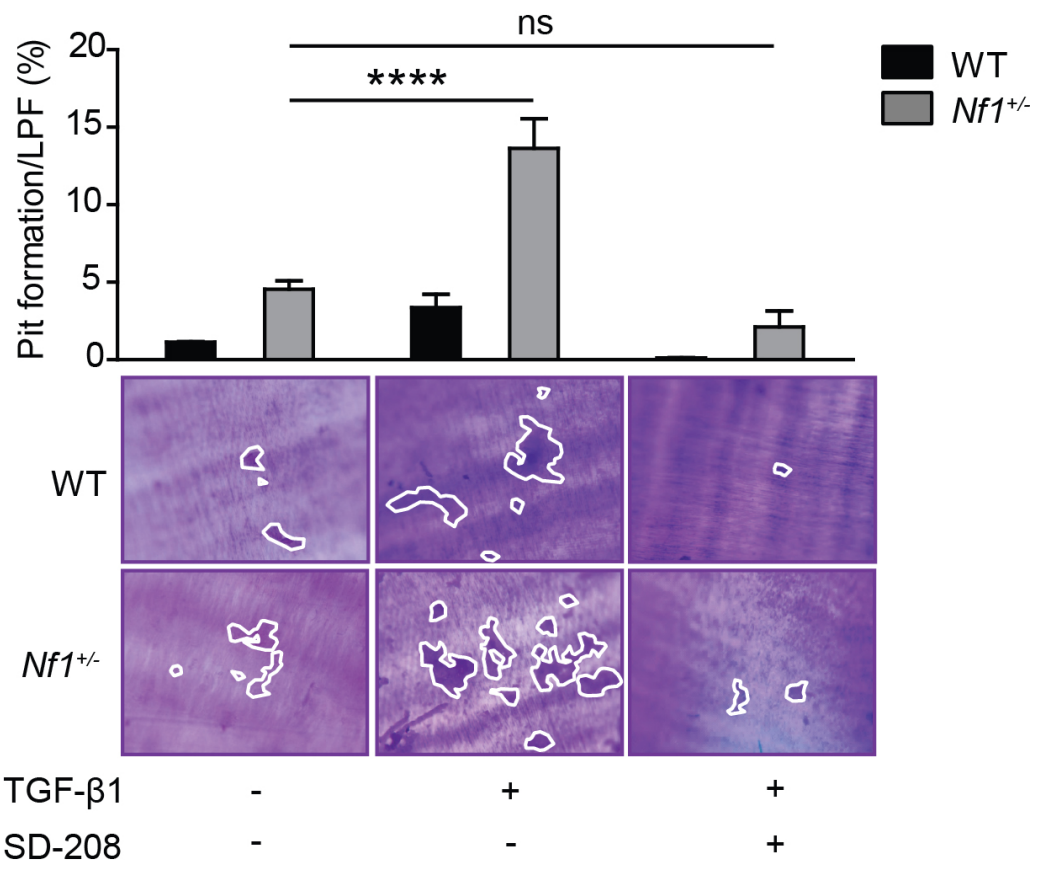


Figure 27D

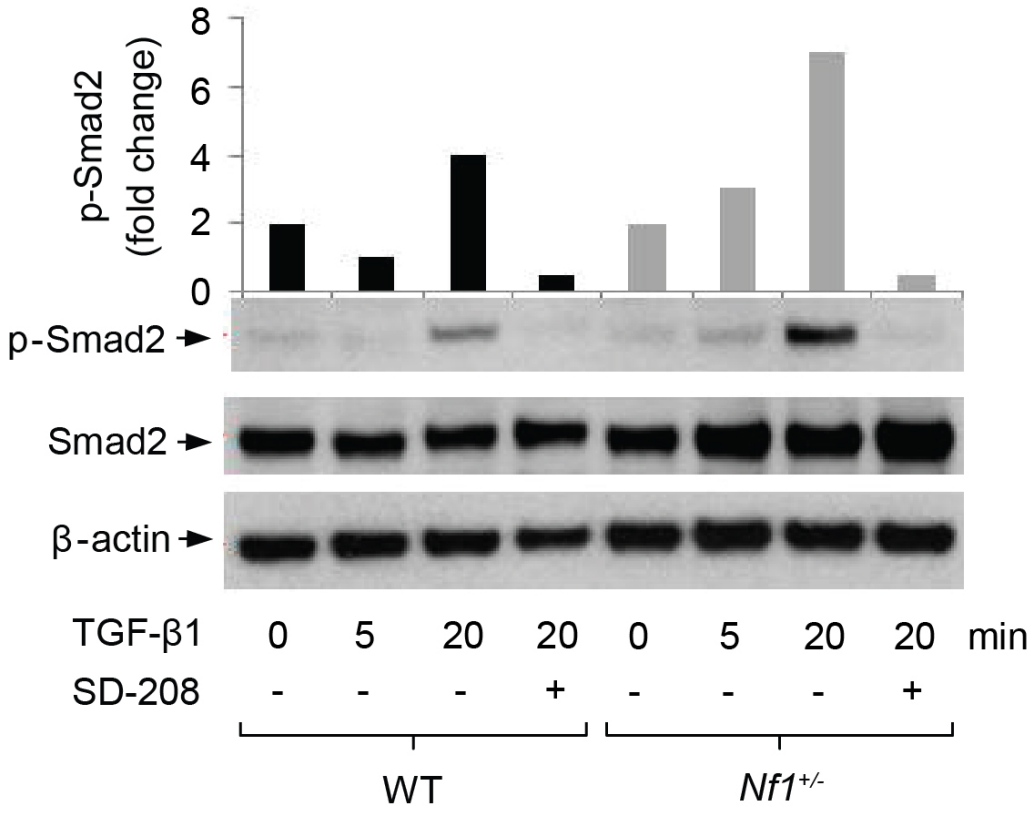
p-Smad2 (fold change)
8
6
4
2
0
p-Smad2
Smad2
β-actin
TGF-β1 0 5 20 20 0 5 20 20 min
SD-208 - - - + - - - +
WT
Nf1+/-

Figure 27E

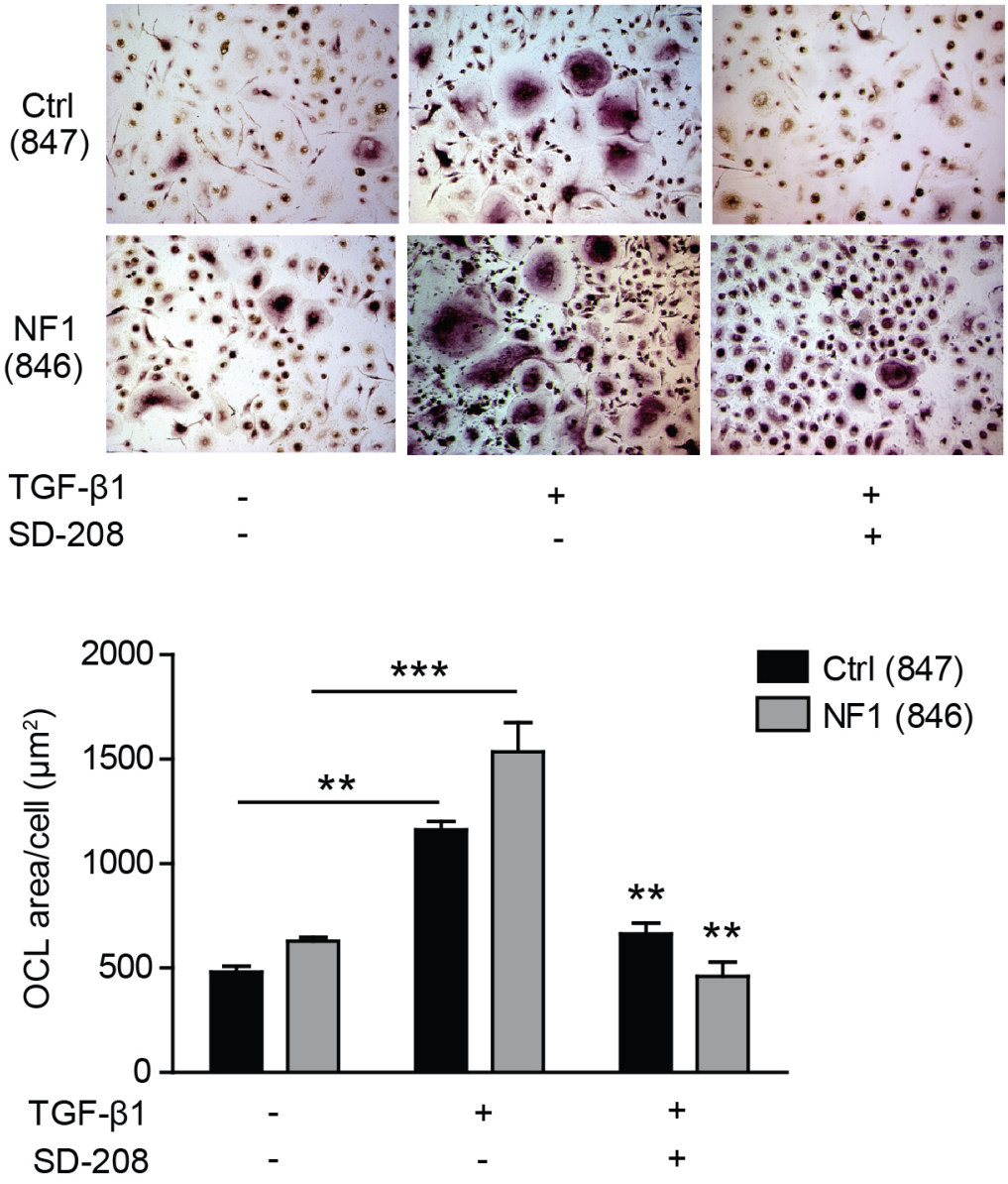
Ctrl
(847)
NF1
(846)
TGF-β1 - + +
SD-208 - - +
2000
1500
1000
500
0
OCL area/cell (μm²)
***
**
**
**
Ctrl (847)
NF1 (846)
TGF-β1 - + +
SD-208 - - +

Figure 27F

**Figure 27. TGF-β1 potentiates *Nf1* haploinsufficient osteoclast gain-in-functions, which are associated with increased activation of the Smad pathway.** (A) Osteoclast formation from bone marrow mononuclear cells was induced by M-CSF and RANKL, in the presence or absence of TGF-β1. Representative photomicrographs show multinucleated osteoclasts (magnification, 200x) following TRACP staining. Bar graphs represent the mean number of nuclei per osteoclast and the area of TRACP positive multinucleated osteoclasts per high power field (HPF), quantified using Image J software. $n = 4$. $^{*}P < 0.05$, $^{***}P < 0.001$. (B) Osteoclast formation was assessed following TGF-β1 stimulation and increasing doses of SD-208. $n = 3$. $^{*}P < 0.05$, $^{**}P < 0.01$ comparing $Nf1^{+/-}$ versus WT. (C) Osteoclast formation from BMMNCs was induced by M-CSF, RANKL, and TGF-β1 with increasing doses of SD-208. Representative photomicrographs showing osteoclast actin rings (magnification, 200x) after staining with phalloidin (green) and Hoechst (blue). (D) Osteoclast bone resorption on dentine slices. Representative photomicrographs show resorptive “pits” (magnification, 100x). “Pit” area was quantified as shown by the bar graph above. $n = 3$. $^{****}P < 0.0001$. (E) Phosphorylated Smad2 (p-Smad2), total Smad2, and β-actin were measured by western blot in pre-osteoclasts stimulated with TGF-β1 (1 ng/mL) in the presence or absence of SD-208 (100 nM). The bar graph shows the fold change in p-Smad2 relative to the loading control. (F) Osteoclasts were cultured from the peripheral blood of a NF1 patient and a matched, healthy control following TGF-β1 stimulation with or without SD-208 inhibitor treatment. $^{**}P < 0.01$, $^{***}P < 0.001$.

Given that osteoclast gain-in-functions lead to increased bone loss in *Nf1*$^{+/-}$ mice following ovariectomy (OVX)-induced resorptive stress [69], we next sought to determine the functional contribution of hyperactive TGF-β1 signaling towards increased osteolytic activity *in vivo,* in the context of *Nf1* haploinsufficiency. WT and *Nf1*$^{+/-}$ mice underwent OVX or sham surgery followed by six weeks treatment with SD-208 (60 mg/kg/day) versus vehicle control. Pharmacologic TβRI kinase inhibition efficiently maintained femoral BMD in OVX mice as compared to vehicle treatment, where bone loss was approximately two-fold greater in the *Nf1*$^{+/-}$ cohort as compared to WT controls (Figure 28A). Three-dimensional μCT further demonstrated preservation of trabecular bone mass in OVX mice treated with SD-208 (Figure 28B, top panel). Trabecular bone volume fraction (BV/TV) (Figure 28B, bottom panel) and trabecular microarchitecture parameters (Figure 28C) including trabecular number (Tb.N), thickness (Tb.Th), spacing (Tb.Sp), and structure model index (SMI) were restored to the level of sham-operated controls following SD-208 administration in OVX mice.

Histological methods corroborated these results (Figure 28D) and provided insights regarding the cellular mechanism of the observed phenotype. Osteoclast numbers, which were markedly increased in vehicle treated *Nf1*$^{+/-}$ OVX mice, returned to baseline levels following SD-208 treatment (Figure 28E, top panel). Serum levels of the C-terminal cross-linking telopeptide of type I collagen (CTX), an established biomarker of osteolytic activity, were significantly increased in vehicle treated *Nf1*$^{+/-}$ OVX mice, but normalized after SD-208 treatment (Figure 28E, bottom panel). Overall, the accentuated response of *Nf1*$^{+/-}$

OVX mice to TβRI kinase inhibition validates the pivotal role of TGF-β in potentiating osteoclast bone erosive activity in the context of *Nf1* haploinsufficiency.

Pharmacologic TGF-β antagonism is known to exert both anabolic and anti-catabolic effects on bone [113, 114]. Although osteoblast numbers were equivalent between WT and $Nf1^{+/-}$ mice, TβRI kinase inhibition significantly increased the number of osteoblasts on the bone surface in both genotypes of mice (Figure 28F). Dynamic histomorphometry performed on $Nf1^{+/-}$ mice confirmed that SD-208 treatment significantly increased the bone formation rate (BFR) and mineral apposition rate (MAR) (Figure 28G), although no significant difference was observed in the mineralizing surface (MS/BS) (Figure 28H). Collectively, these data suggest that, in addition to osteoclast inhibition, an overall increase in osteoblast number and activity is likely to play a key role in the bone sparring effects of TβRI kinase blockade following OVX-induced resorptive stress.

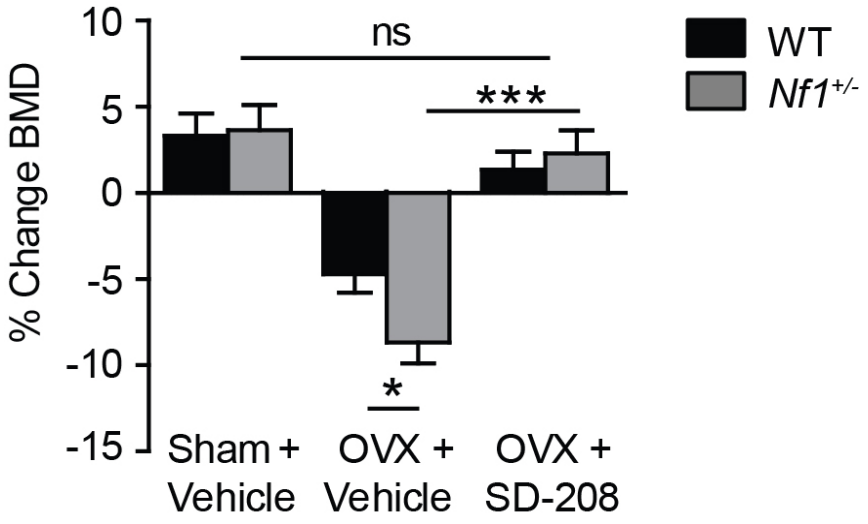
10
5
0
-5
-10
-15
% Change BMD
ns
***
*
WT
Nf1+/-
Sham + Vehicle
OVX + Vehicle
OVX + SD-208

Figure 28A

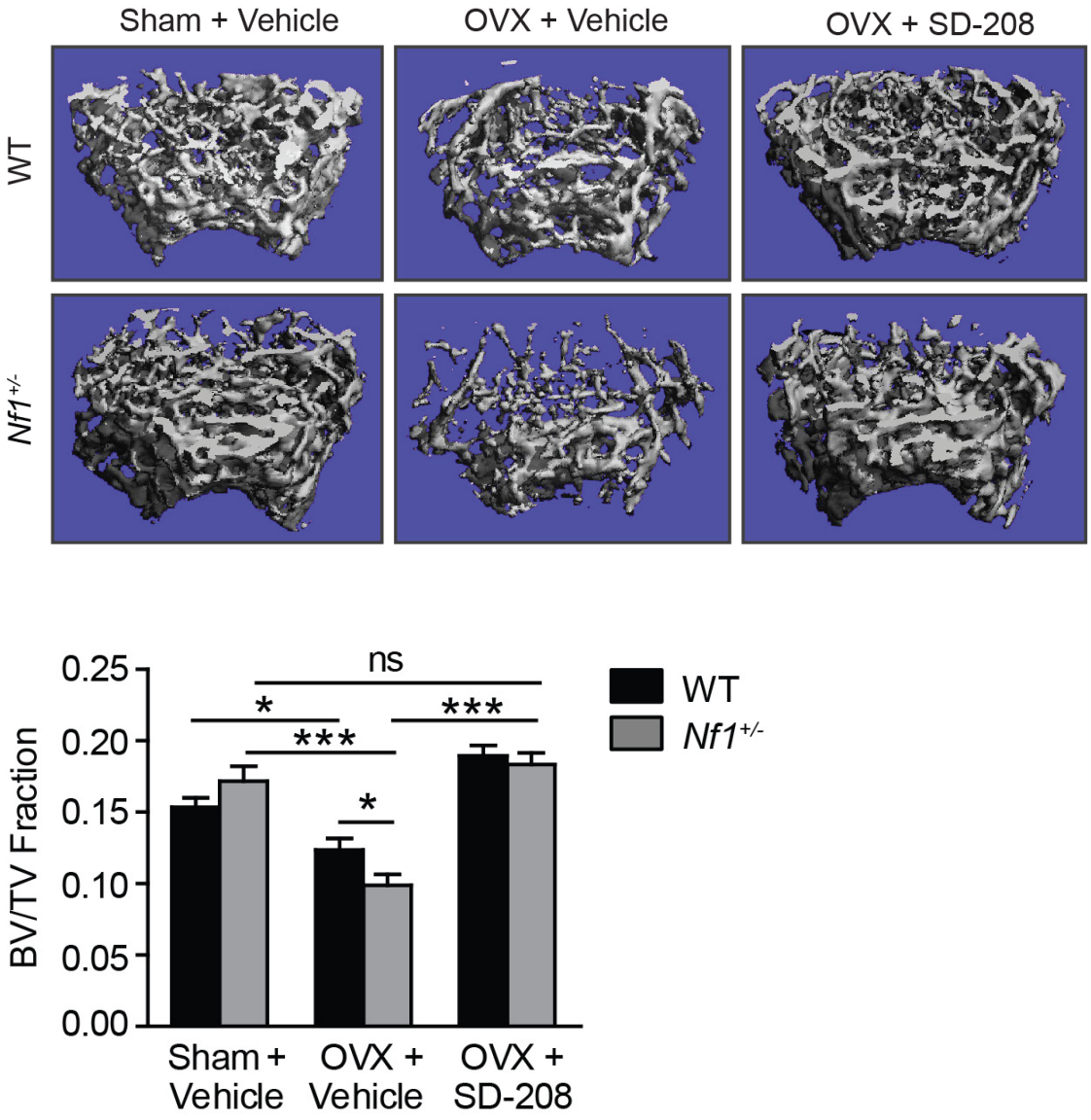
Sham + Vehicle
OVX + Vehicle
OVX + SD-208
WT
Nf1+/-
ns
*
***
***
*
BV/TV Fraction
0.25
0.20
0.15
0.10
0.05
0.00
WT
Nf1+/-
Sham + Vehicle
OVX + Vehicle
OVX + SD-208

Figure 28B

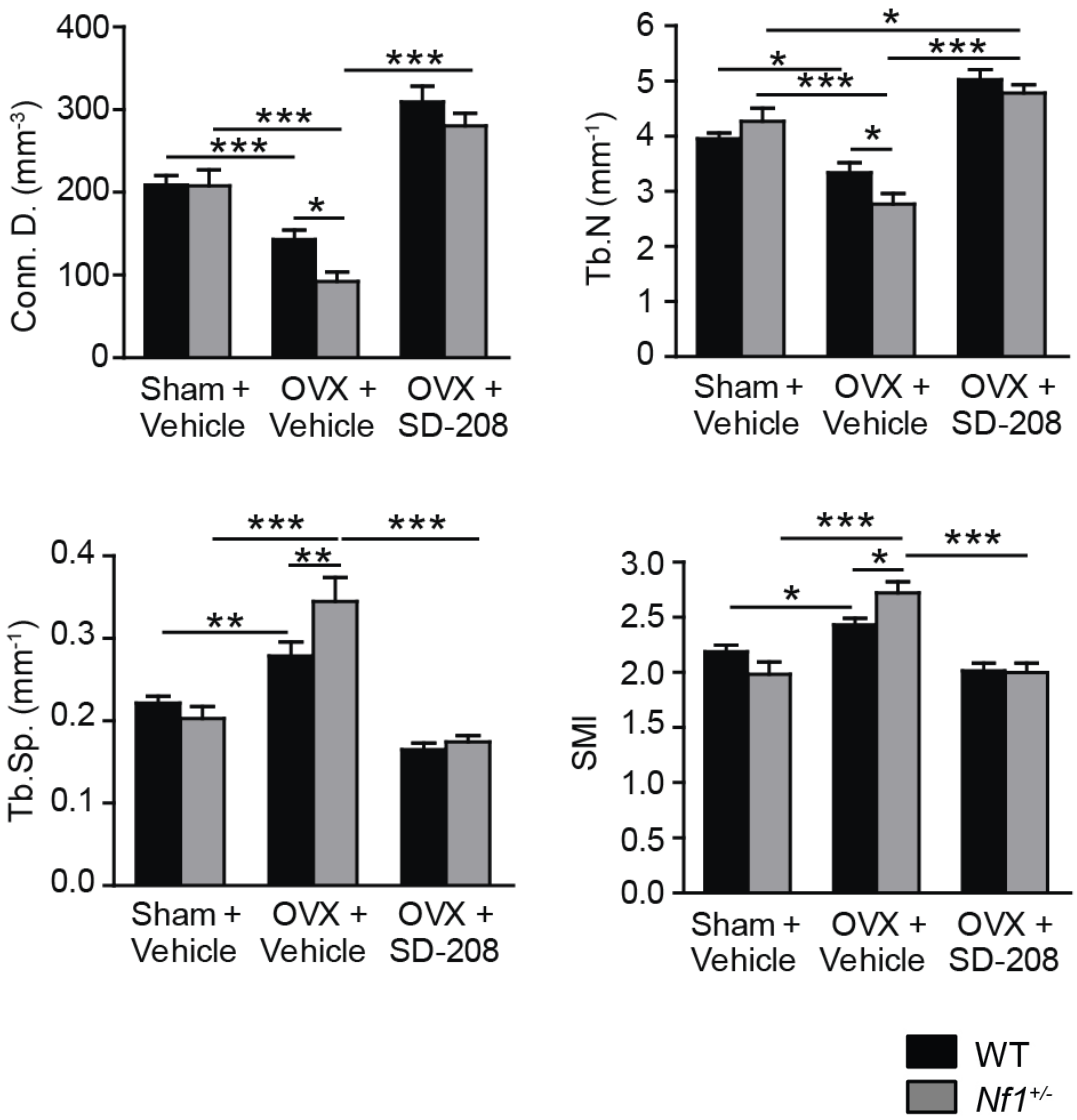
Conn. D. (mm-3)
400
300
200
100
0
***
***
***
*
Sham + Vehicle
OVX + Vehicle
OVX + SD-208
Tb.N (mm-1)
6
5
4
3
2
1
0
*
***
*
*
***
Sham + Vehicle
OVX + Vehicle
OVX + SD-208
Tb.Sp. (mm-1)
0.4
0.3
0.2
0.1
0.0
***
***
**
**
Sham + Vehicle
OVX + Vehicle
OVX + SD-208
SMI
3.0
2.5
2.0
1.5
1.0
0.5
0.0
***
***
*
*
Sham + Vehicle
OVX + Vehicle
OVX + SD-208
WT
Nf1+/-

Figure 28C

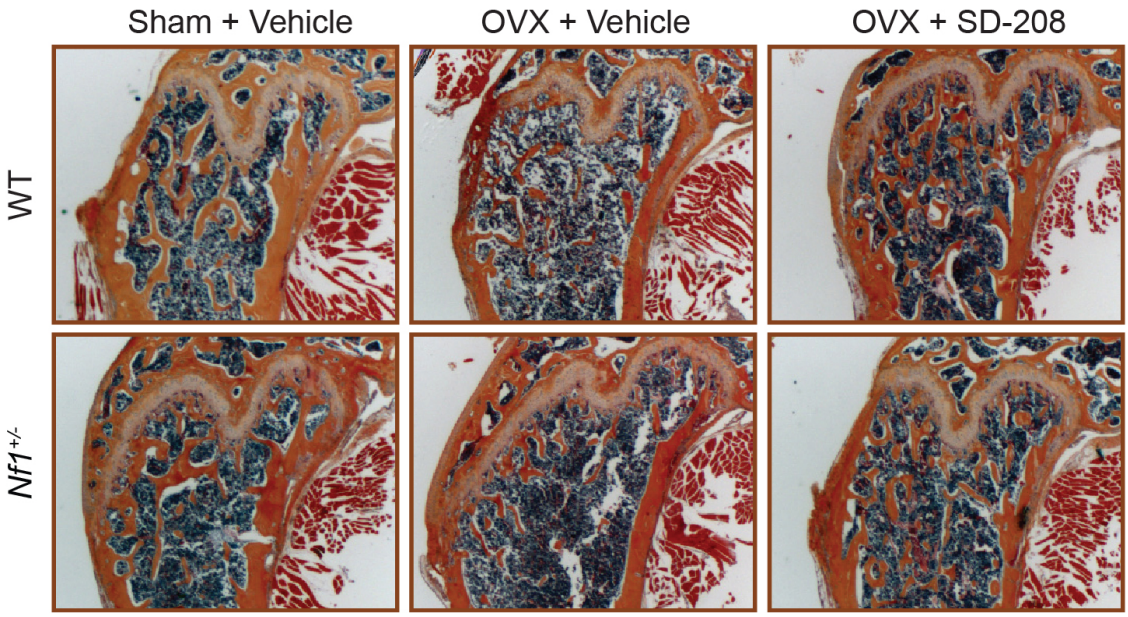


Figure 28D

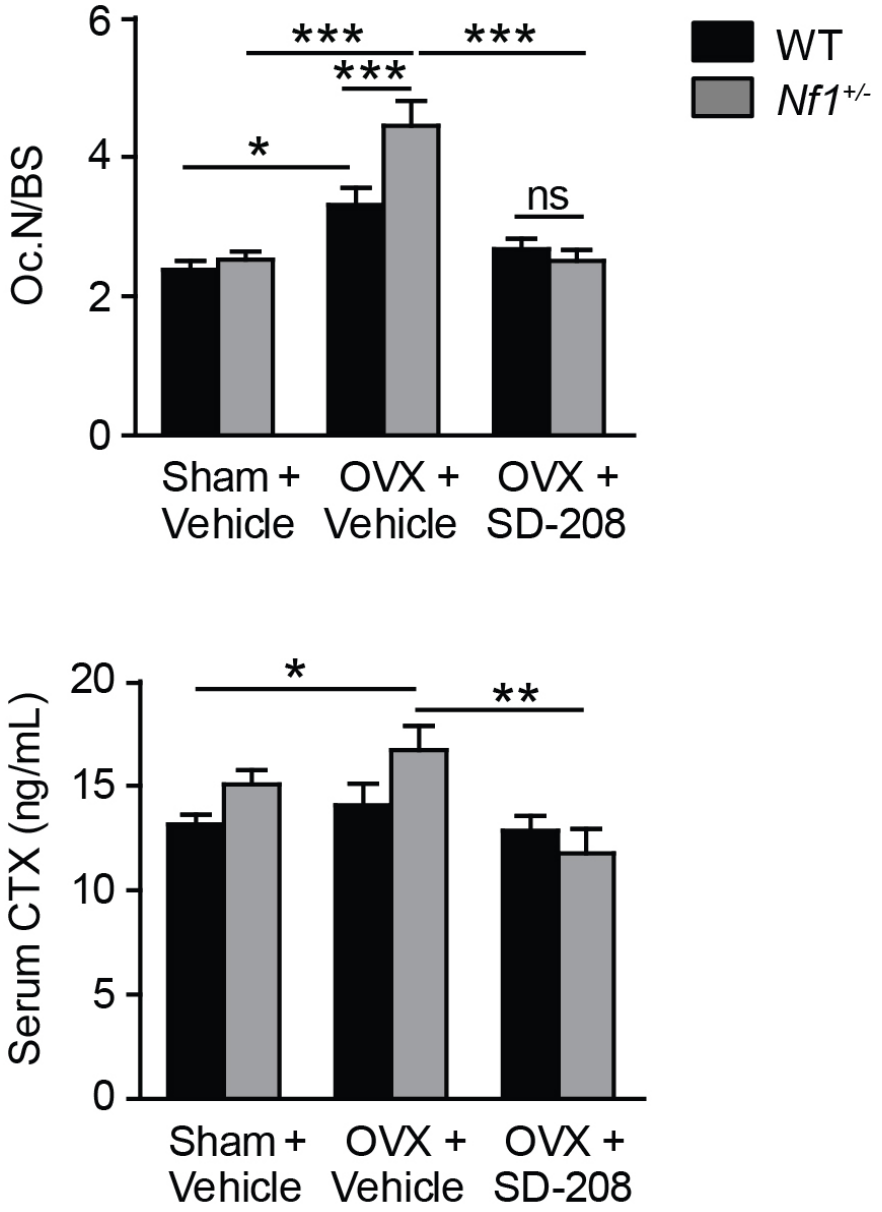
6
4
2
0
Oc.N/BS
***
***
***
*
ns
WT
Nf1+/-
Sham + Vehicle
OVX + Vehicle
OVX + SD-208
20
15
10
5
0
Serum CTX (ng/mL)
*
**
Sham + Vehicle
OVX + Vehicle
OVX + SD-208

Figure 28E

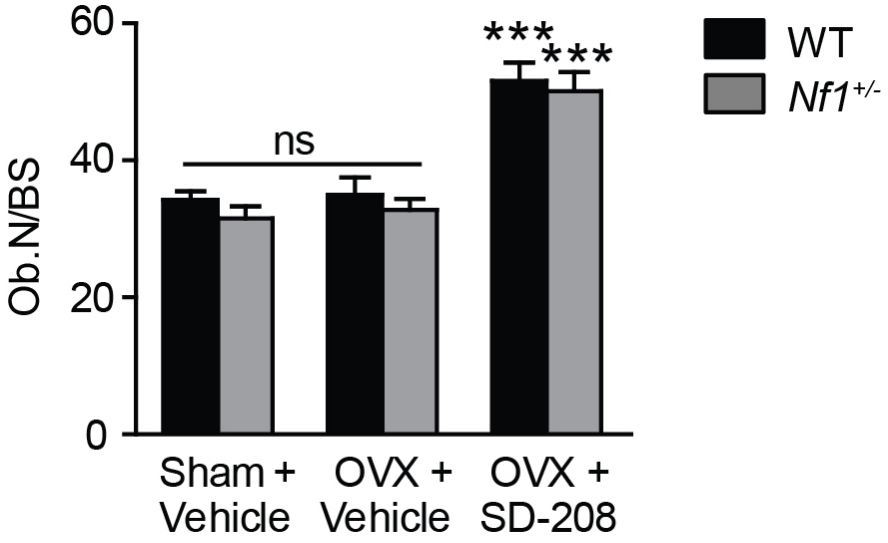


Figure 28F

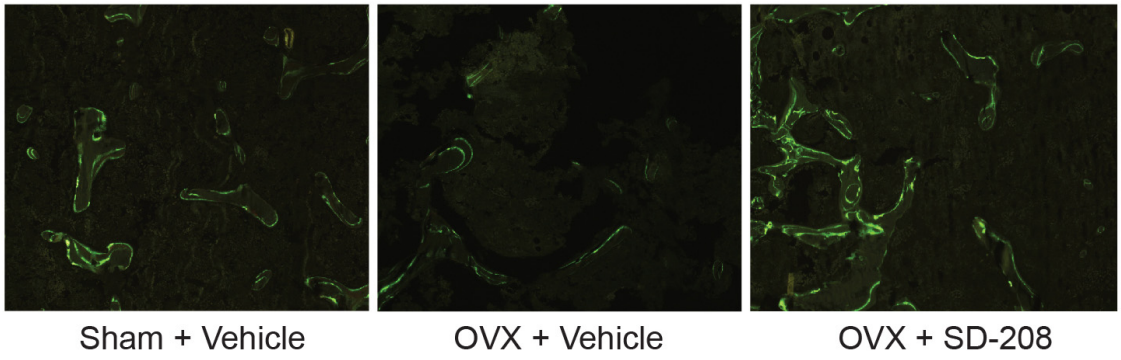
Sham + Vehicle
OVX + Vehicle
OVX + SD-208

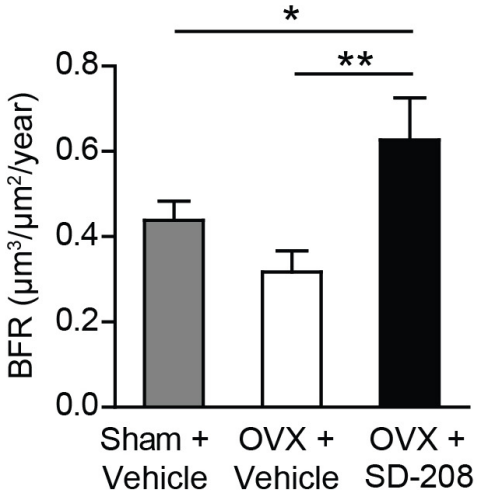
*
**
0.8
0.6
0.4
0.2
0.0
BFR (μm³/μm²/year)
Sham + Vehicle
OVX + Vehicle
OVX + SD-208

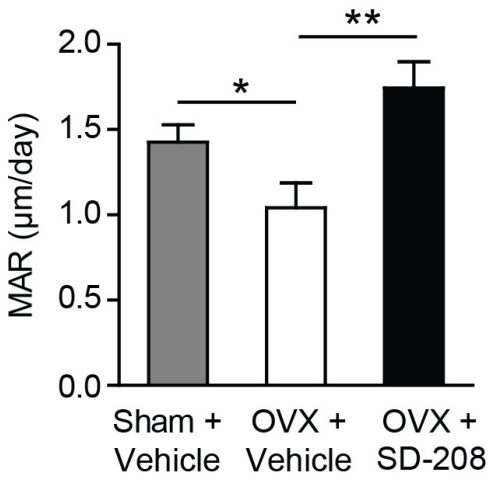
**
*
2.0
1.5
1.0
0.5
0.0
MAR (μm/day)
Sham + Vehicle
OVX + Vehicle
OVX + SD-208

Figure 28G

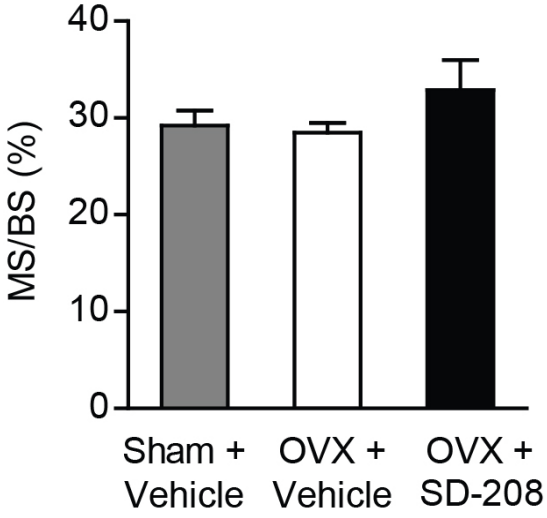


Figure 28H

**Figure 28. TGF-β signaling potentiates bone loss in *Nf1*$^{+/-}$ mice following OVX resorptive stress.** (A) The percent change in BMD was determined by pDEXA measurements before and six weeks after surgery plus treatment. *n* = 10-12. *P < 0.05, ****P* < 0.001. (B) Representative μCT (top panel) shows femoral trabecular bone in sham-operated and OVX mice following six weeks treatment with vehicle (1% methylcellulose) or TβRI inhibitor, SD-208 (60 mg/kg), administered by daily gavage. Trabecular bone volume fraction (BV/TV) was quantified in the distal femur by μCT. *n* = 10-12. **P* < 0.05, ****P* < 0.001 (bottom panel). (C) Trabecular microarchitecture parameters including connectivity density (Conn.D.), trabecular number (Tb.N), trabecular spacing (Tb.Sp), and structure model index (SMI) were quantified by μCT in OVX mice receiving SD-208 treatment as compared to controls. *n* = 10-12. **P* < 0.05, ***P* < 0.01, ****P* < 0.001. (D) Representative longitudinal sections of hematoxylin and eosin (H&E) stained femora (25x magnification) are shown. (E) Osteoclast numbers on the bone surface (Oc.N/BS) were counted manually on TRACP stained sections at 200x magnification. *n* = 10-12. **P* < 0.05, ****P* < 0.001 (top panel). Serum levels of the C-terminal cross-linking telopeptide of type I collagen (CTX) were measured by ELISA. *n* = 10-12. **P* < 0.05, ***P* < 0.01 (bottom panel). (F) Osteoblast numbers on the bone surface (Ob.N/BS) were counted manually on H&E stained sections at 200x magnification. *n* = 10-12. ****P* < 0.001. (G) Representative fluorescent micrographs demonstrate dual calcein labeling of the bone surface in *Nf1*$^{+/-}$ mice, 100x magnification. The bone formation rate (BFR) and mineral apposition rate (MAR) were quantified as shown. *n* = 3. **P* < 0.05,

**$P < 0.01$. (H) The Mineralizing surface (MS/BS) was quantified on dual calcein labeled sections. $n = 3$. ANOVA revealed no significant differences.

**TβRI inhibition rescues bone defects in *Nf1$^{flox/-}$;Col2.3Cre* mice**

Based on these findings, we reasoned that a cycle of uncoupled bone remodeling perpetuated by TGF-β1 overproduction and Smad-mediated hypersensitivity may pivotally underlie the pathogenesis of bone defects observed in the *Nf1$^{flox/-}$;Col2.3Cre* murine model. We therefore tested whether pharmacologic inhibition of TβRI kinase activity could rescue characteristic NF1 associated bone defects such as osteoporosis and tibial fracture non-union observed in *Nf1$^{flox/-}$;Col2.3Cre* mice [77, 78]. Cohorts of three- to four-month-old *Nf1$^{flox/-}$;Col2.3Cre* mice received treatment with either SD-208 (60 mg/kg/day) or the vehicle control (1% methylcellulose in sterile water) daily for four weeks. Bone mineral density (BMD) measurements were acquired both pre- and post-treatment to determine the percent change in BMD during the treatment period (Figure 29A). μCT (Figure 29B) and histological sections (Figure 29D and E) of the excised bones illustrate the low bone mass phenotype of vehicle treated *Nf1$^{flox/-}$;Col2.3Cre* mice as compared to WT controls. In contrast, dramatic increases in bone mineral density (Figure 29A) and trabecular bone volume fraction (Figure 29C) were observed in *Nf1$^{flox/-}$;Col2.3Cre* mice treated with SD-208. Although WT mice began treatment with nearly twice the bone mass of *Nf1$^{flox/-}$;Col2.3Cre* mice prior to therapy, we observed no significant differences in bone mass or trabecular architecture parameters (Figure 29C) between WT and *Nf1$^{flox/-}$;Col2.3Cre* mice following SD-208 treatment, indicating that pharmacologic TGF-β inhibition completely rescued bone mass defects in the *Nf1$^{flox/-}$;Col2.3Cre* mice. On the cellular level, osteoblast numbers, which were

diminished in vehicle treated *Nf1$^{flox/-}$;Col2.3Cre* mice, were significantly increased following SD-208 treatment (Figure 29F). In summary, the striking response of *Nf1$^{flox/-}$;Col2.3Cre* mice to TβRI kinase inhibition, even as compared to WT animals that were also receiving SD-208 treatment, substantiates the pivotal role of aberrant TGF-β signaling in the pathogenesis of NF1 associated osteopenia and osteoporosis in a mouse model that closely recapitulates the human disease.

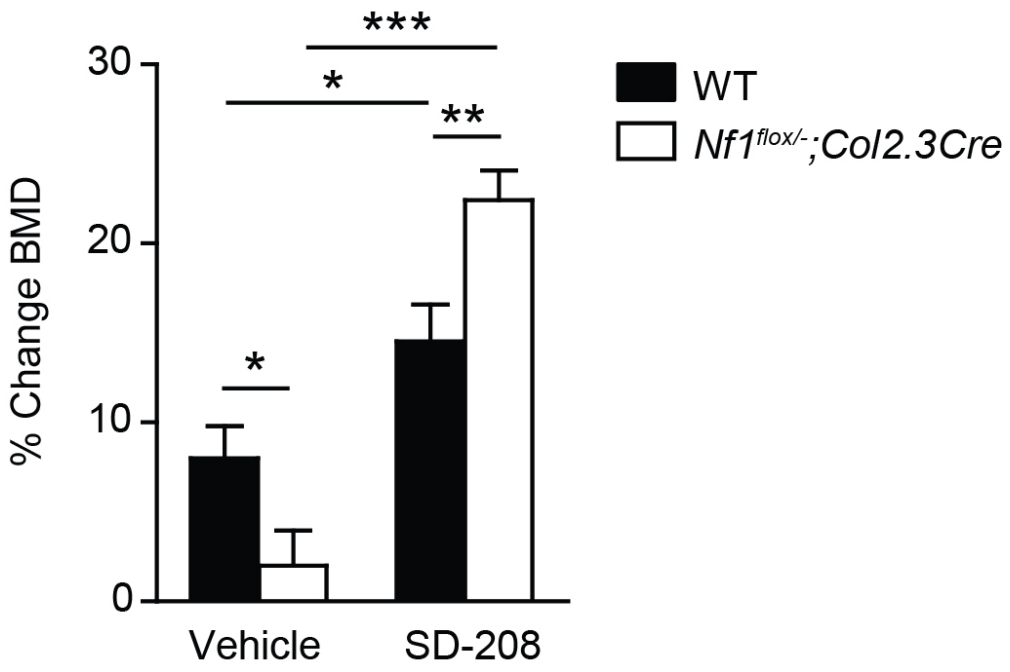


Figure 29A

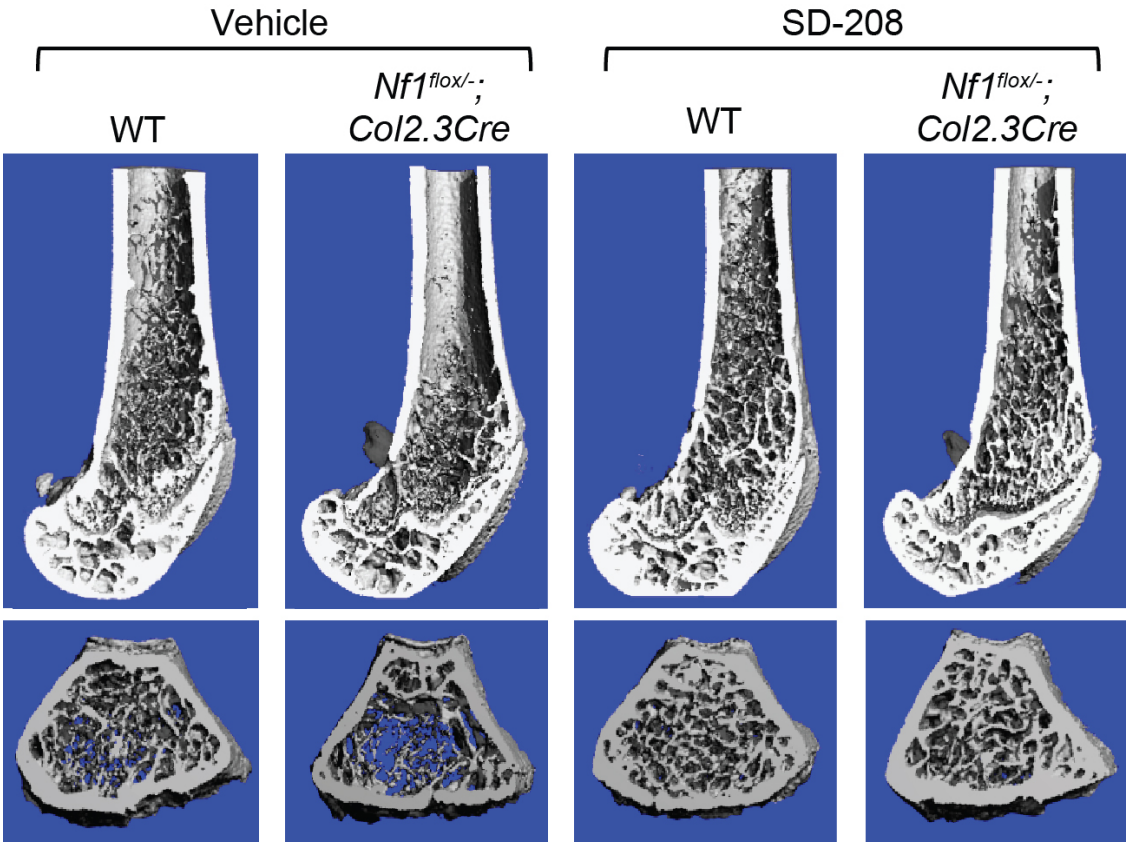


Figure 29B

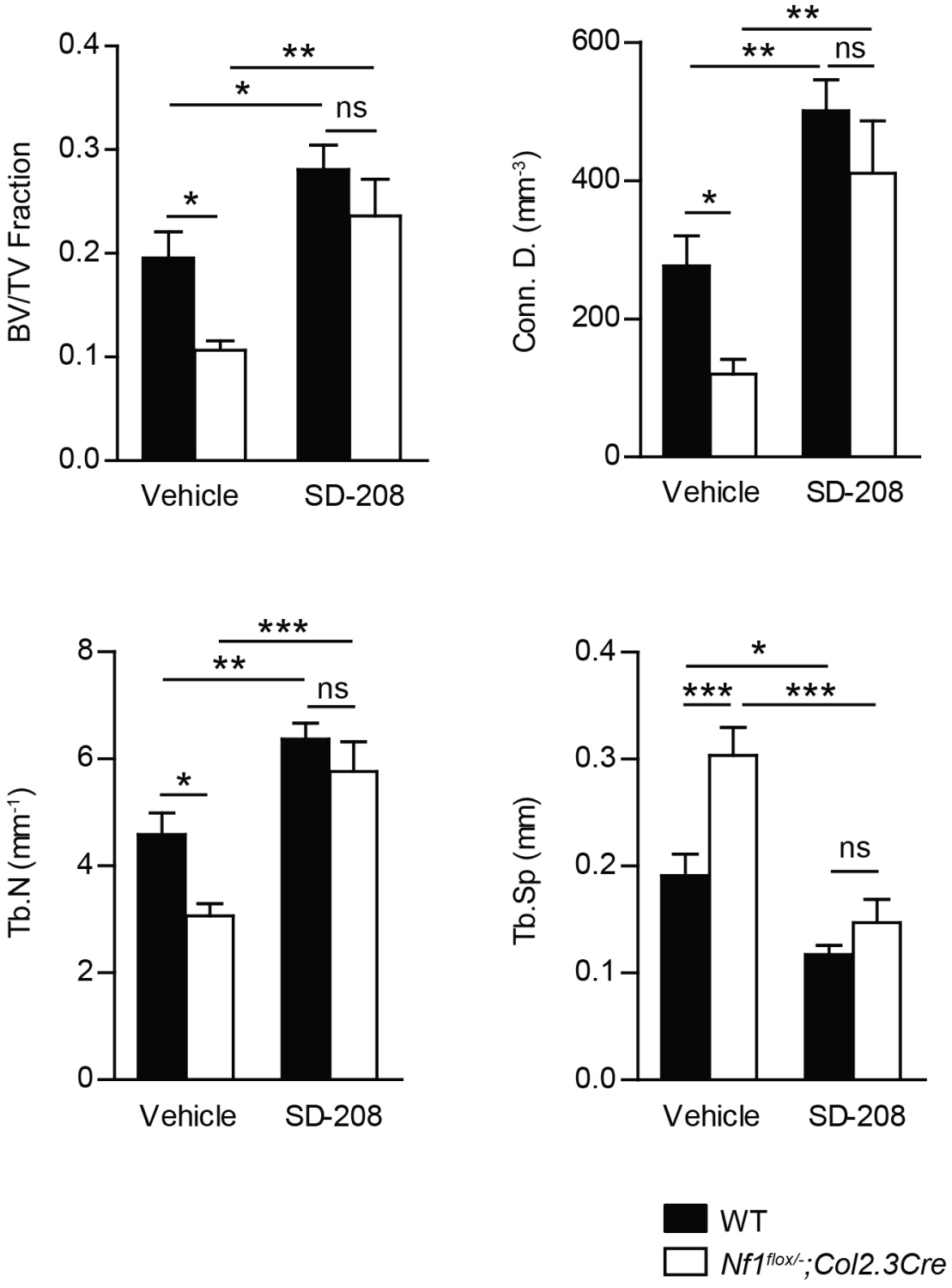
BV/TV Fraction
0.4
0.3
0.2
0.1
0.0
**
*
ns
*
Vehicle
SD-208
Conn. D. (mm-3)
600
400
200
0
**
**
ns
*
Vehicle
SD-208
Tb.N (mm-1)
8
6
4
2
0
***
**
ns
*
Vehicle
SD-208
Tb.Sp (mm)
0.4
0.3
0.2
0.1
0.0
*
***
***
ns
Vehicle
SD-208
WT
Nf1flox/-;Col2.3Cre

Figure 29C

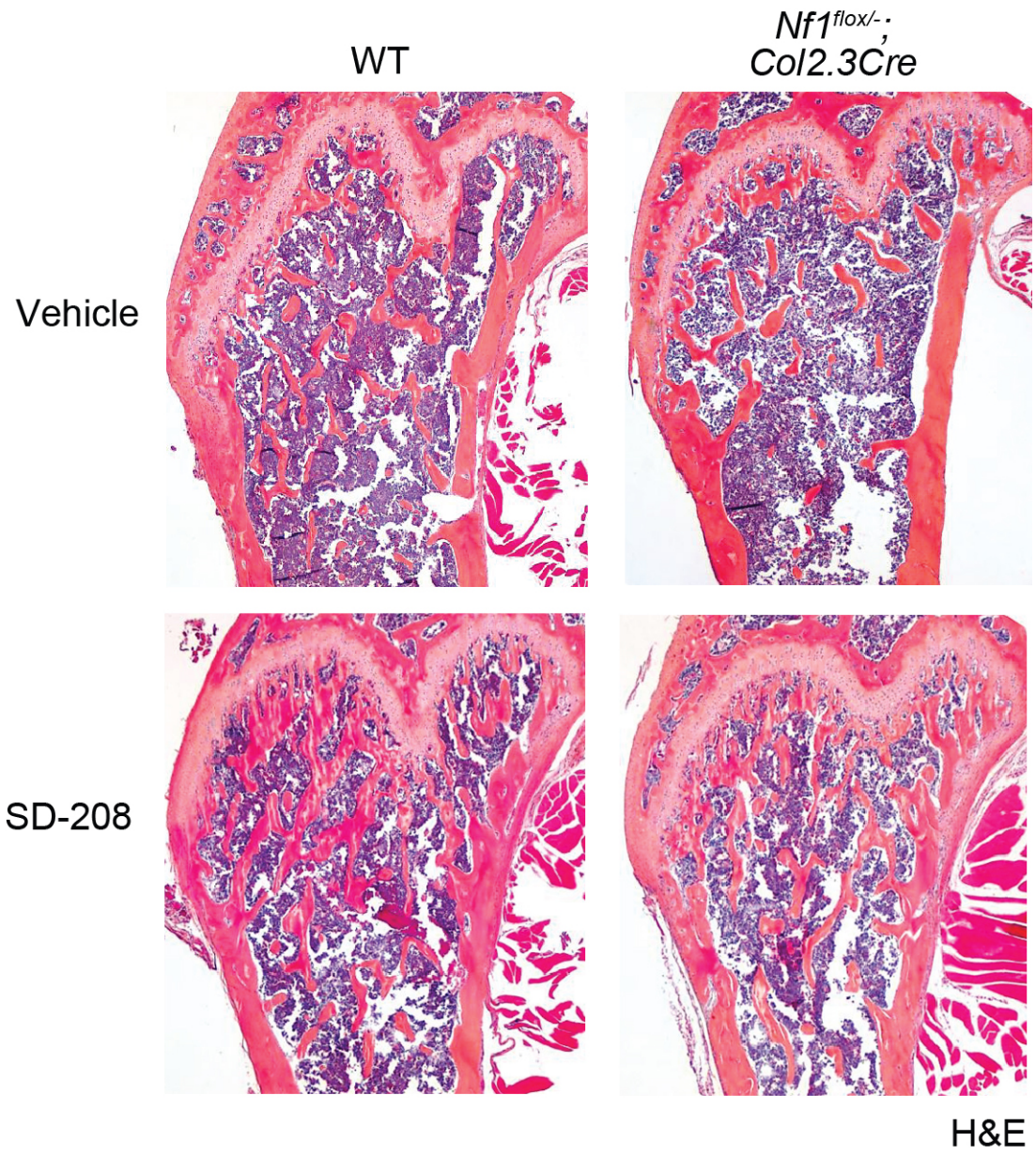


Figure 29D

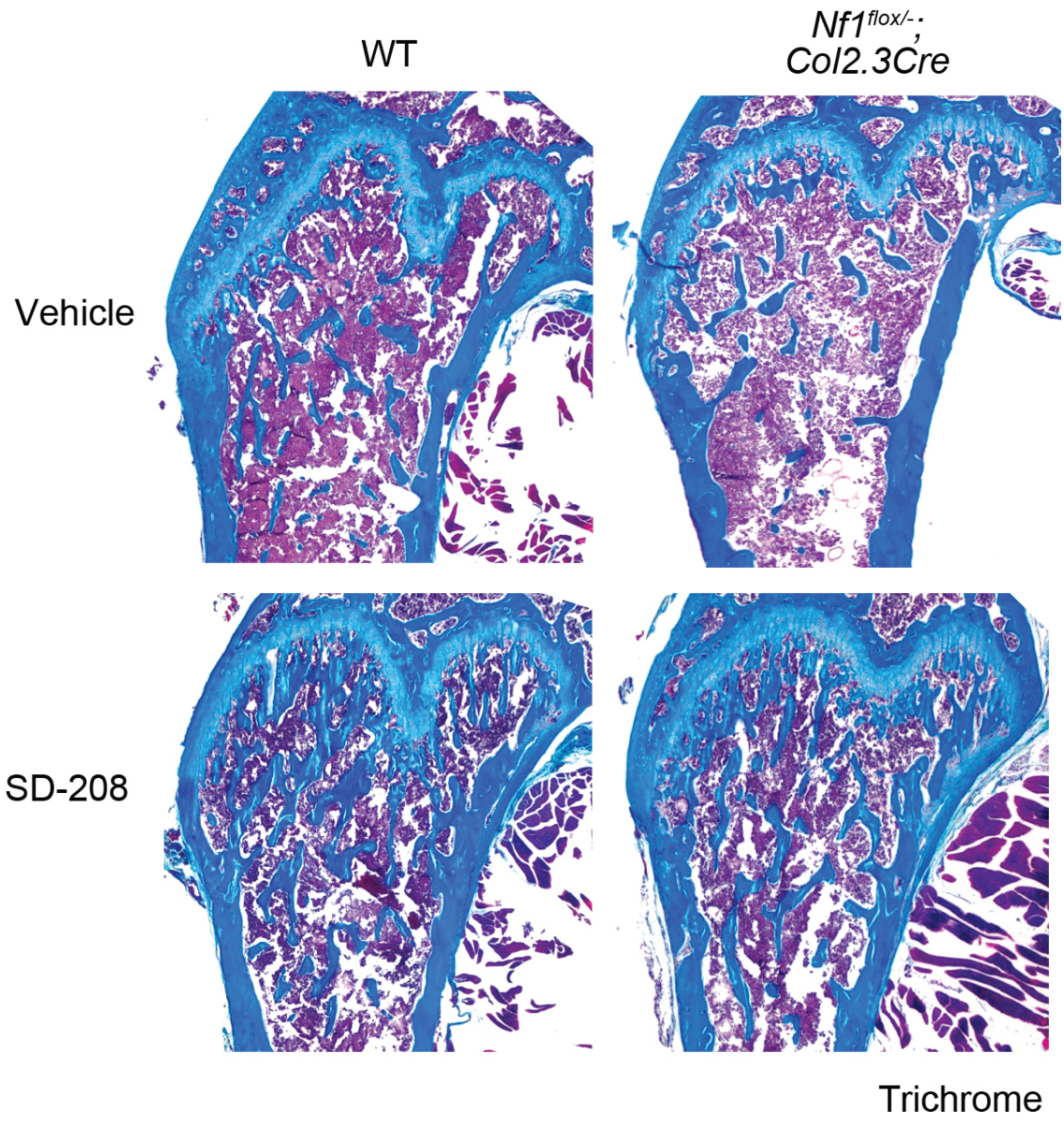


Figure 29E

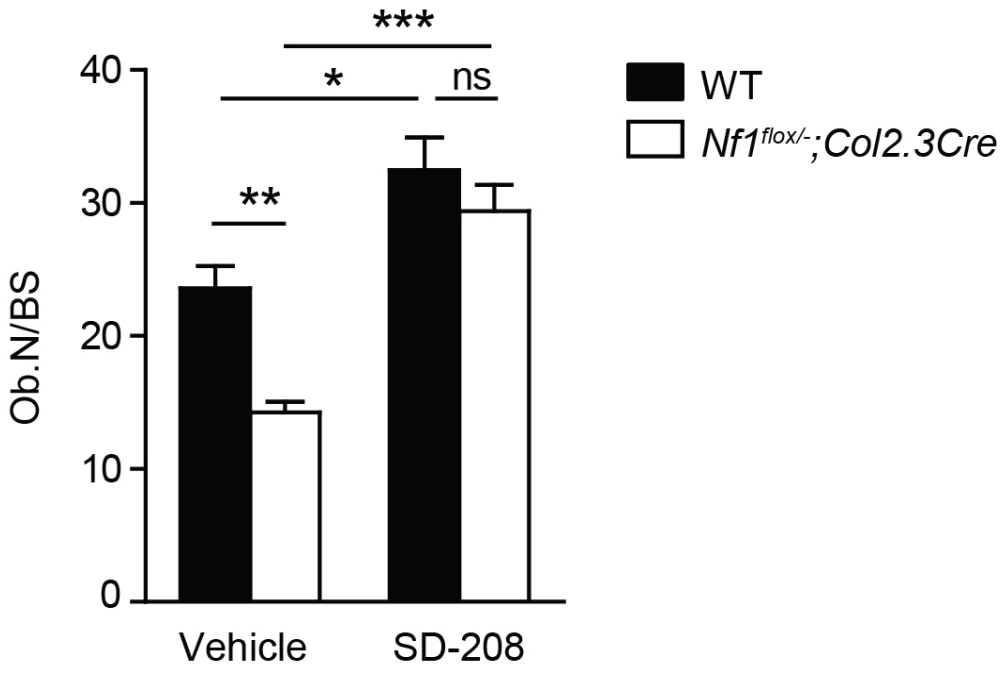


Figure 29F

**Figure 29. TβRI inhibition restores bone mass in *Nf1$^{flox/-}$;Col2.3Cre* mice.** (A) The percentage change in BMD of the distal femur was determined by pDEXA measurements before and after four weeks treatment with vehicle or SD-208. *n* = 7-12. **P* < 0.05, ***P* < 0.01, ****P* < 0.001. (B) Representative μCT reconstructed femora in longitudinal (top) and transverse (bottom) cross-sections following four weeks treatment with vehicle or SD-208 treatment. (C) Trabecular bone volume fraction (BV/TV), connectivity density (Conn. D.), trabecular number (Tb.N), and trabecular spacing (Tb.Sp) were quantified by μCT in femora following four weeks treatment with SD-208 (60 mg/kg/day) as compared to vehicle control. *n* = 7-12. **P* < 0.05, ***P* < 0.01, ****P* < 0.001. (D) Representative longitudinal sections of H&E stained femora (25x magnification) are shown. (E) Representative longitudinal sections of trichrome stained femora (25x magnification) are shown. (F) Osteoblast numbers on the bone surface (Ob.N/BS) were counted manually on H&E stained sections at 200x magnification. *n* = 7-12. **P* < 0.05, ***P* < 0.01 ****P* < 0.001.

Pseudarthrosis of the tibia is associated with significant morbidity in NF1 patients. This clinical feature is also recapitulated in *Nf1$^{flox/-}$;Col2.3Cre* mice [78]. Immunohistochemical analysis of *Nf1$^{flox/-}$;Col2.3Cre* mice with tibial fracture non-union revealed approximately three-fold increased levels of pSmad-2 within the fracture site as compared to WT controls (Figure 30A). If aberrant TGF-β signaling indeed underlies recalcitrant bone healing in NF1, we reasoned that pharmacologic TβRI blockade might prevent tibial fracture non-union in *Nf1$^{flox/-}$;Col2.3Cre* mice. To test this hypothesis, cohorts of *Nf1$^{flox/-}$;Col2.3Cre* mice were treated with SD-208 (60 mg/kg/day) or vehicle control for six weeks following tibial fracture. Compared to healthy WT mice, which exhibited robust callus formation, radiographic monitoring demonstrated persistent fracture non-union in *Nf1$^{flox/-}$;Col2.3Cre* mice treated with the vehicle control, with minimal or complete absence of callus formation at the fracture site (Figure 30B). Administration of SD-208 in *Nf1$^{flox/-}$;Col2.3Cre* mice substantially enhanced callus formation as compared to those receiving vehicle treatment. μCT evaluation of callus structural integrity further revealed a significant increase in the callus bone volume/tissue volume ratio (BV/TV) in *Nf1$^{flox/-}$;Col2.3Cre* mice undergoing SD-208 treatment (Figure 30C), suggesting that pharmacologic TβRI inhibition improved bone formation within the fracture site. Histological sectioning (Figure 30D) revealed fibrous tissue and an increased presence of TRACP positive staining osteoclasts within the fracture site of *Nf1$^{flox/-}$;Col2.3Cre* mice receiving vehicle treatment. SD-208 treatment significantly reduced osteoclast numbers (Figure 30E) and p-Smad2 levels (Figure 30F) within the fracture callus.

Collectively, these results provide the first direct evidence that pharmacologic TGF-β blockade is an effective therapeutic strategy to augment bone healing in a mouse model of NF1 tibial pseudarthrosis.

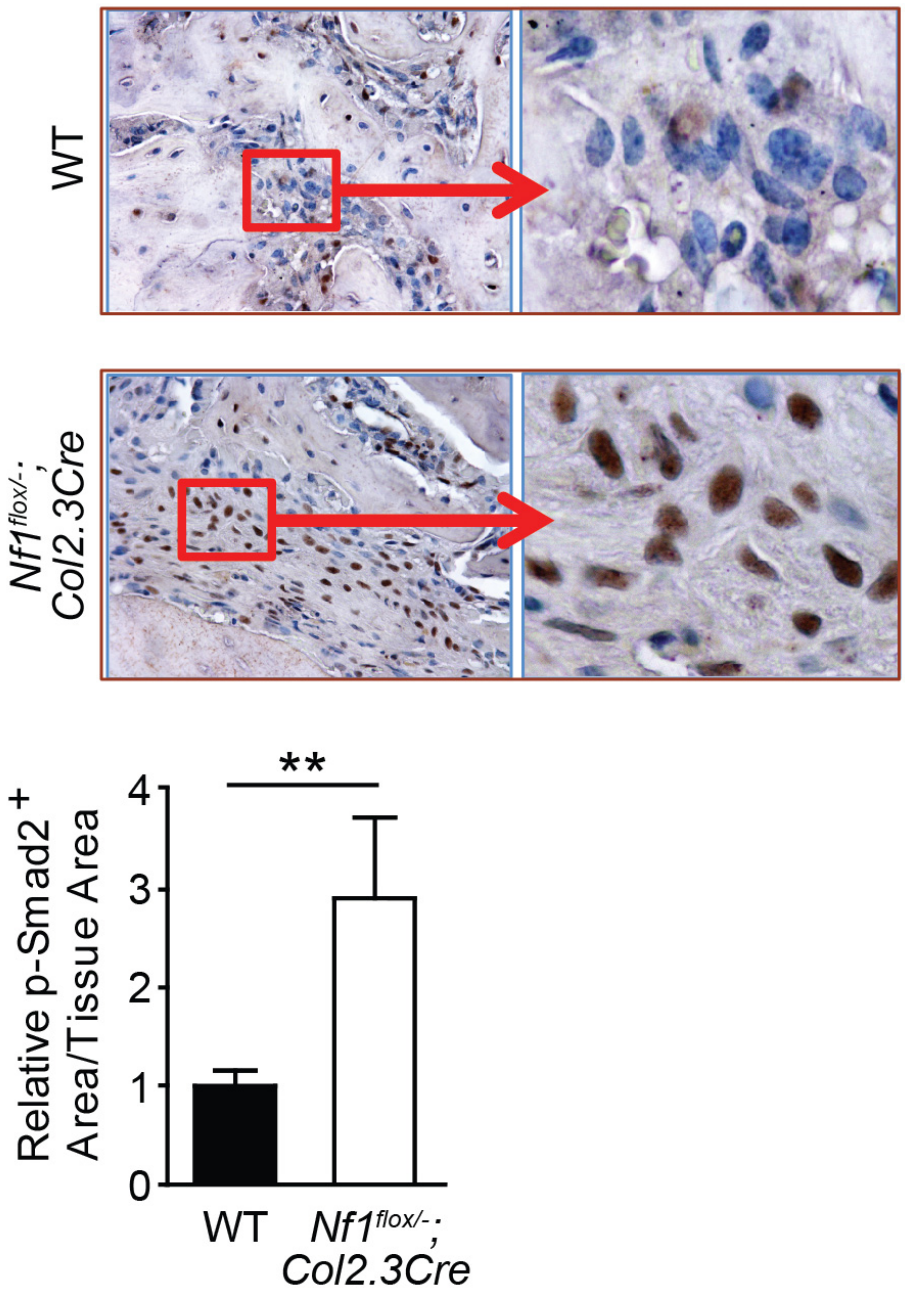
WT
Nf1flox/-; Col2.3Cre
**
Relative p-Smad2+ Area/Tissue Area
0
1
2
3
4
WT
Nf1flox/-; Col2.3Cre

Figure 30A

WT – Vehicle Treatment

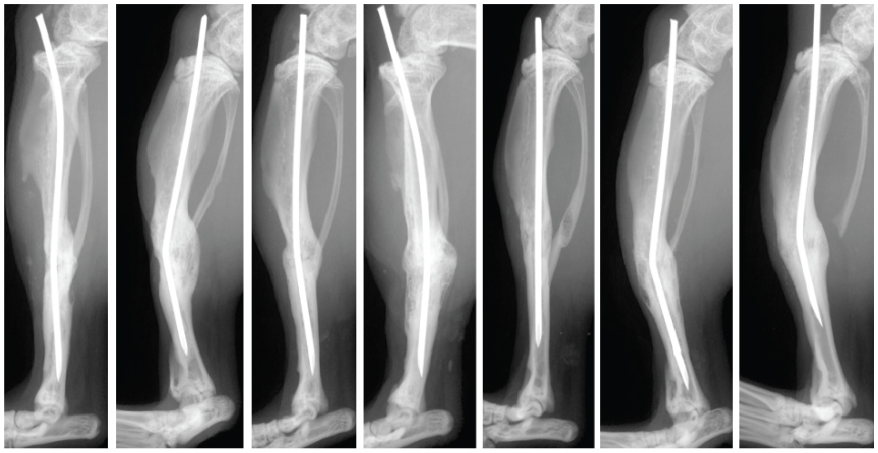

*Nf1*$^{flox/-}$*;Col2.3Cre* – Vehicle Treatment

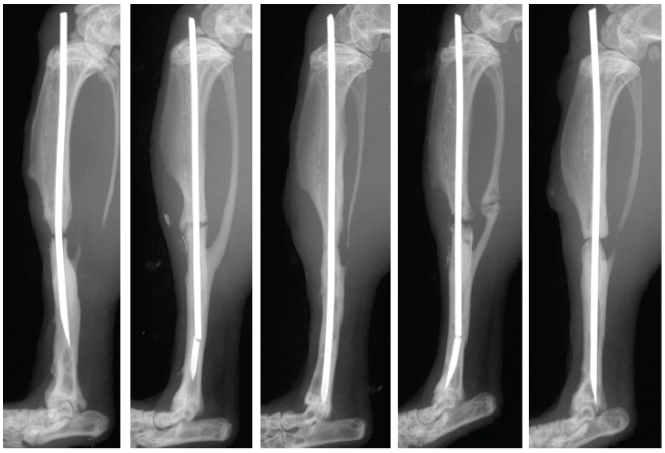

*Nf1*$^{flox/-}$*;Col2.3Cre* – SD208 Treatment

Figure 30B

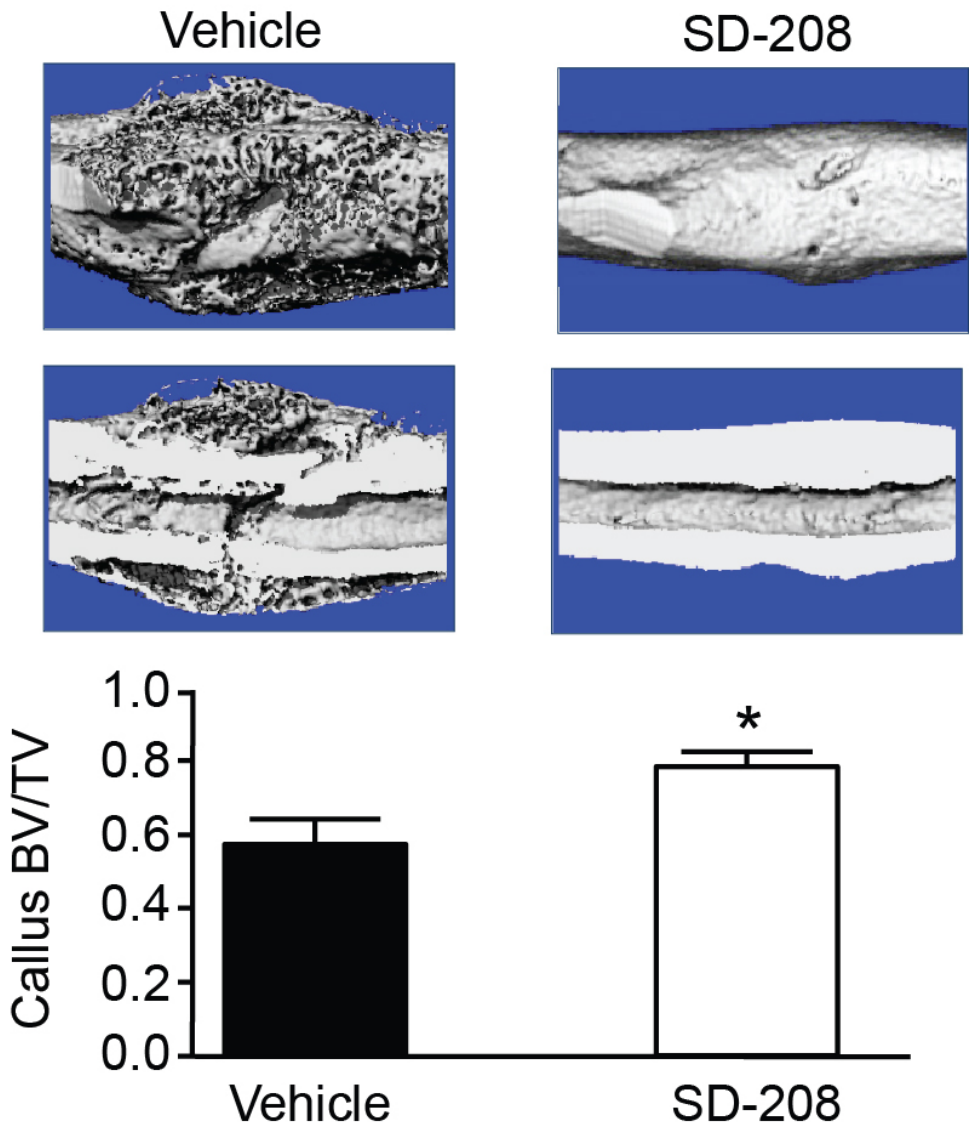


Figure 30C

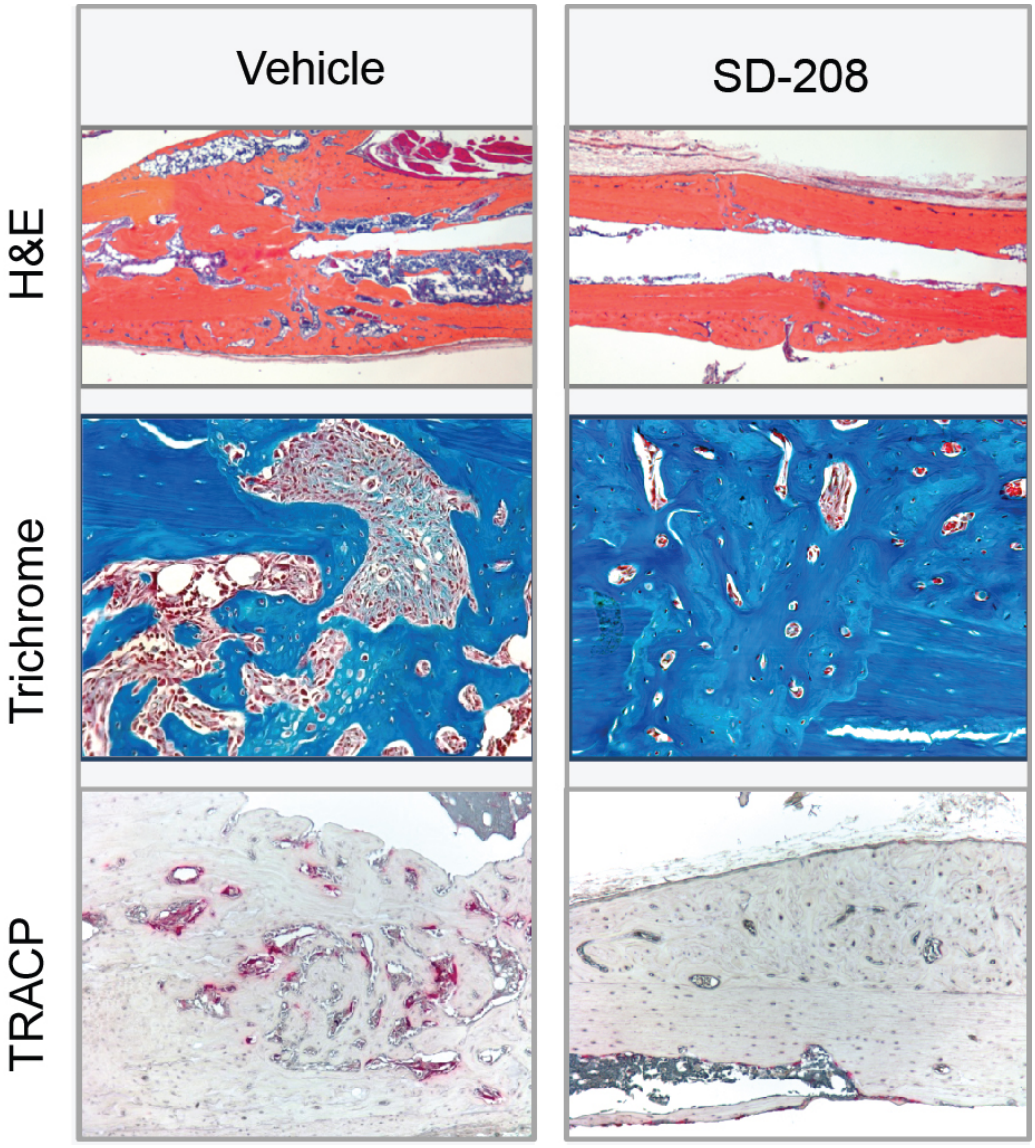


Figure 30D

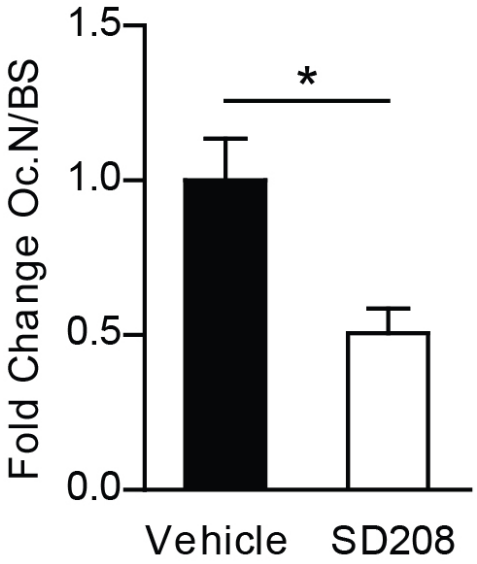


Figure 30E

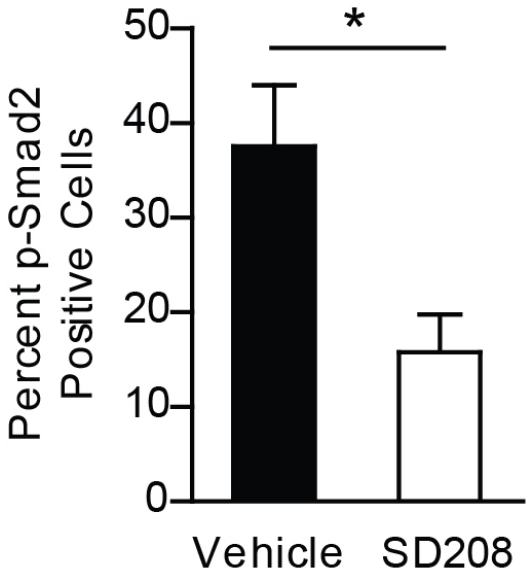


Figure 30F

**Figure 30. TβRI inhibition prevents tibial fracture non-union in *Nf1$^{flox/-}$;Col2.3Cre* mice.** (A) Immunohistochemical staining for p-Smad2 in fracture calluses of WT and *Nf1$^{flox/-}$;Col2.3Cre* mice. The p-Smad2 positive staining area was normalized to the tissue area and compared between genotypes. $n$ = 6. $^{**}P < 0.01$. (B) Radiographs showing tibial fracture healing in WT controls and *Nf1$^{flox/-}$;Col2.3Cre* mice treated with either vehicle or SD-208 (60mg/kg/day) for six weeks. (C) (Top panel) Representative μCT reconstructed whole callus and longitudinal cross-sections from *Nf1$^{flox/-}$;Col2.3Cre* mice treated with either vehicle or SD-208 for 4 wks following tibial fracture. (Bottom panel) Callus bone volume fraction (BV/TV) was quantified by μCT as shown in the bar graph. $n$ = 6-8. $^{*}P < 0.05$. (D) Representative tibial fractures in longitudinal cross-section stained with H&E (25x magnification), trichrome (100x, magnification), and TRACP (50x magnification). (E) The fold change in osteoclast number (Oc.N) per millimeter of bone surface (BS) was determined by manually counting multinucleated TRACP positive cells. $n$ = 6. $^{*}P < 0.05$. (F) Tibial fracture sections were immunostained for p-Smad2. The number of p-Smad2 positive cells was quantified as a percentage of the total cells per high power field. $n$ = 5-6. $^{*}P < 0.05$.

**Hypersecretion of MMP-2/9 potentiates latent TGF-β1 activation**

In order for TGF-β1 to bind to its receptors and exert its biological effects, it must first be cleaved from its latency associated peptide (LAP). When we measured the levels of latent, LAP-bound TGF-β1 versus active TGF-β1 in *Nf1$^{flox/-}$;Col2.3Cre* mice with tibial fracture non-union, we observed a dramatic increase in the ratio of active-to-latent TGF-β1 within the facture site as compared to WT controls (Figure 31A), implying that accelerated conversion of latent TGF-β1 to the active form may play an important role in upregulating the bioavailability of active TGF-β1. Cleavage of the TGF-β latency associated peptide (LAP) is known to occur through both acid and enzymatic mechanisms [139]. Among these, MMP-2 and MMP-9 have been shown to mediate the proteolysis of LAP and play an important role in bone remodeling and fracture healing in animal models [162-165]. We next measured the levels of active MMPs in the conditioned medium of *Nf1* haploinsufficient myeloid cells by gelatin zymography. In particular, the gelatinase activity of MMP-2/9 were significantly enhanced in *Nf1$^{+/-}$* myeloid conditioned medium versus WT controls (Figure 31B). We observed similar upregulation of active MMP-2/9 in the serum of a NF1 patient as compared to a matched, healthy control (Figure 31C). To demonstrate that only the active form of TGF-β1 can promote hyperactivation of the canonical Smad pathway, we transfected *Nf1* nullizygous osteoprogenitors with a Smad luciferase reporter construct and subsequently stimulated the transfected cells with either recombinant, active TGF-β1 (1 ng/mL) or 100 times the dose of latent, LAP-bound TGF-β1 (100 ng/mL). Expectedly, Smad luciferase reporter activity

was nearly 75% greater in *Nf1*$^{-/-}$ osteoprogenitors stimulated with recombinant active TGF-β1 as compared to WT controls, but not in cells stimulated with LAP-TGF-β1 (Figure 31D). Taken together, the results of this study suggest a working model (Figure 31E) in which genetic inactivation of *Nf1* results in systemically increased TGF-β1 levels. Excess quantities of latent, LAP-bound TGF-β1, sequestered in the bone matrix, are released by bone resorbing osteoclasts and excessively converted to the active form by MMP-2/9 mediated cleavage of LAP. Active TGF-β1 feeds back through p21-Ras-dependent hyperactivation of the canonical Smad pathway to perpetuate a cycle of accelerated osteoclast bone lytic activity, while simultaneously inhibiting osteoblast differentiation which would be required to initiate a compensatory anabolic response. Pharmacologic blockade of TβRI kinase activity (SD-208) disrupts this pathological circuitry, restoring bone mass and preventing tibial fracture non-union in *Nf1*$^{flox/-}$*;Col2.3Cre* mice recapitulating the human disease.

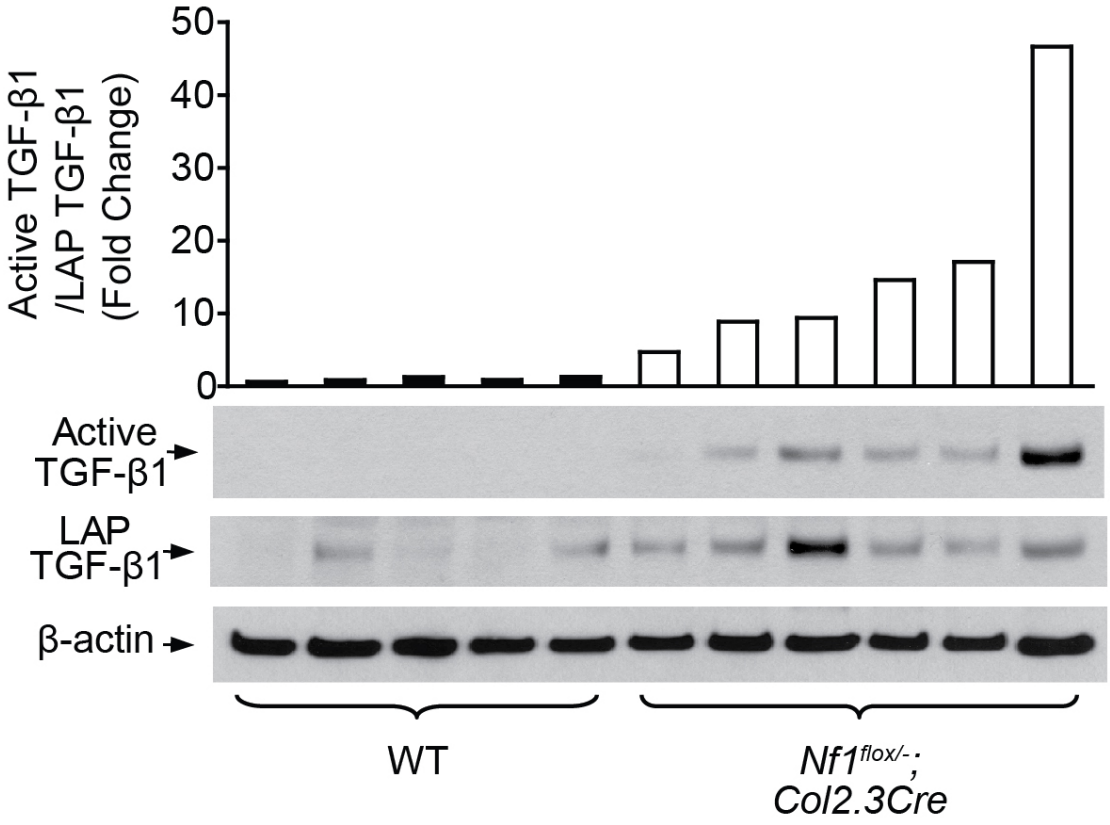
Active TGF-β1 /LAP TGF-β1 (Fold Change)
50
40
30
20
10
0
Active TGF-β1
LAP TGF-β1
β-actin
WT
Nf1flox/-; Col2.3Cre

Figure 31A

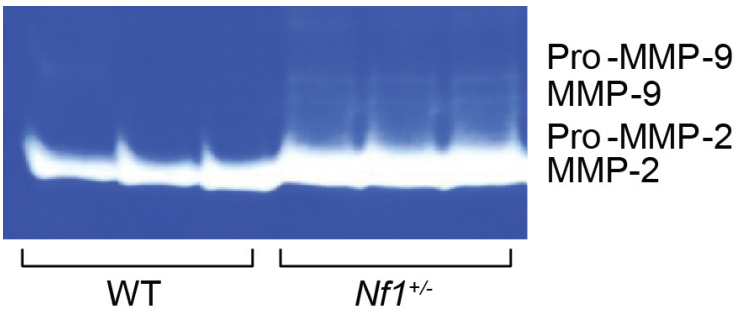


Figure 31B

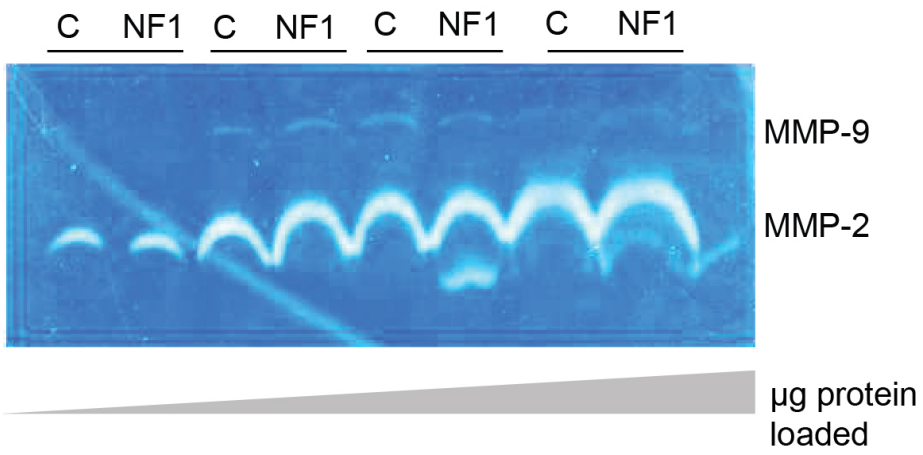


Figure 31C

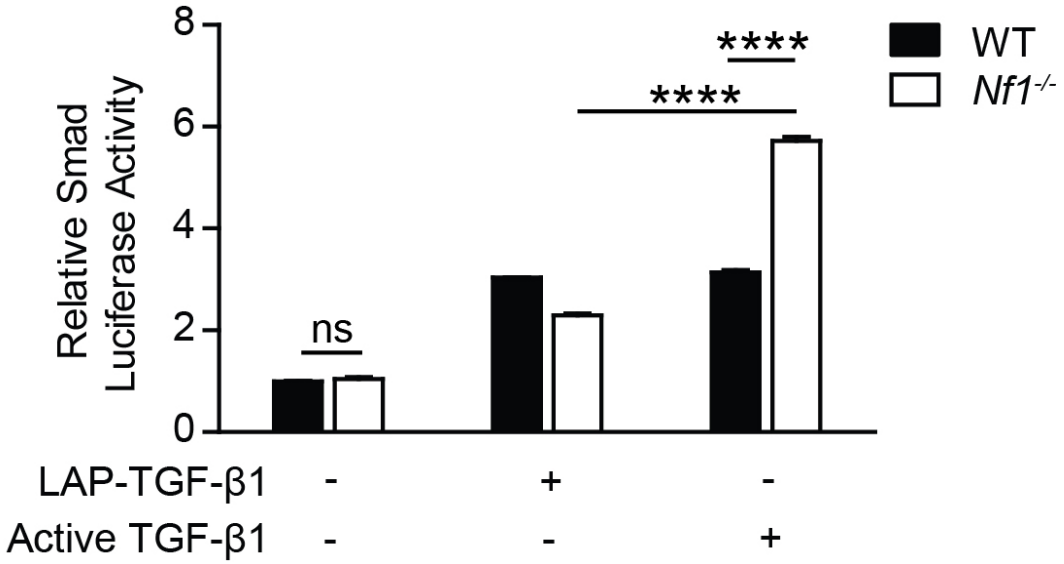
Relative Smad Luciferase Activity
8
6
4
2
0
ns
****
****
WT
Nf1-/-
LAP-TGF-β1 - + -
Active TGF-β1 - - +

Figure 31D

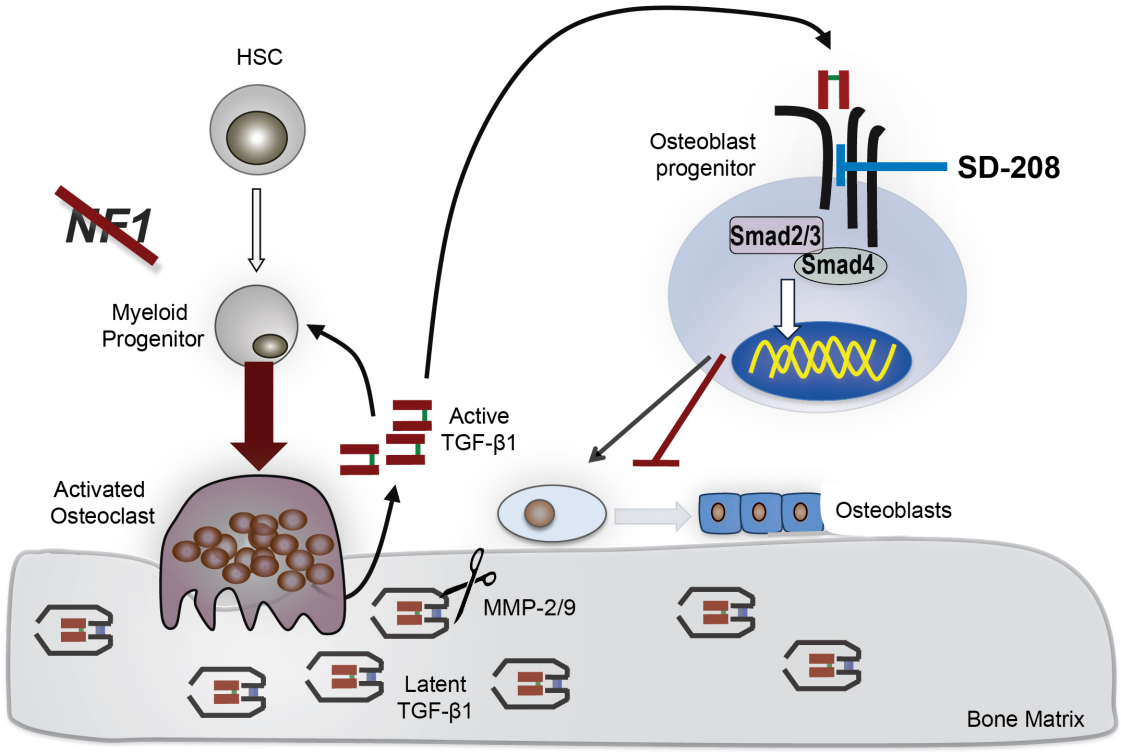
HSC
NF1
Myeloid
Progenitor
Activated
Osteoclast
Active
TGF-β1
Osteoblast
progenitor
SD-208
Smad2/3
Smad4
Osteoblasts
MMP-2/9
Latent
TGF-β1
Bone Matrix

Figure 31E

**Figure 31. Hypersecretion of MMP-2/9 promotes excessive latent TGF-β1 activation.** (A) Active TGF-β1, latency associated peptide (LAP)-bound TGF-β1, and β-actin were detected by western blot in protein extracts from the fracture site of *Nf1*$^{flox/-}$*;Col2.3Cre* mice with tibial fracture non-union and WT controls. The bar graph above represents the fold change in the active TGF-β1/LAP-TGF-β1 ratio. *n* = 5-6. (B) Activity levels of MMP-2/9 were measured in WT and *Nf1*$^{+/-}$ myeloid cell conditioned medium by zymography. *n* = 3. (C) Activity levels of MMP-2 and -9 were measured by zymography in the serum of a NF1 patient (NF1) and a matched, healthy control. (D) Osteoprogenitors transfected with a Smad luciferase reporter were stimulated with recombinant, active TGF-β1 (1 ng/mL) and latent, LAP-TGF-β1 (100 ng/mL) for 18 hours. *n* = 3. **P* < 0.05, ***P* < 0.01. (E) Working model of NF1 skeletal defects mediated by a pathological cycle of increased TGF-β1 expression, activation, and Smad signaling.

## Discussion

The precise role of TGF-β1 in regulating skeletal homeostasis has been historically difficult to define. Observations that exogenously administered TGF-β1 can stimulate bone formation [135, 140, 156] implicate TGF-β1 as an anabolic factor in bone metabolism. Conversely, recent genetic [95, 102] and pharmacologic [113, 114] data demonstrate that attenuation of endogenous TGF-β1 signaling may in fact augment bone mass and quality by simultaneously enhancing osteoblast differentiation while inhibiting osteoclast recruitment. Here, we demonstrate that hyperactive TGF-β1 signaling plays a pivotal role in the pathogenesis of fracture non-union and osteoporosis in a mouse model of the common autosomal dominant genetic disorder, neurofibromatosis type 1 (NF1).

Previous genetic studies suggest that either overabundance or deficiency of TGF-β1 can lead to poor bone quality. TGF-β1 knockout mice exhibit reduced bone mineral density, cortical thickness, and fracture toughness [98, 99]. By contrast, mice over-expressing TGF-β in osteoblasts show gene dosage dependent reductions in bone mineral concentration, elastic modulus, and hardness [95]. Tang and colleagues recently established a murine model that carries a Camurati-Engelmann disease (CED)-derived mutant TGF-β1 [94]. These TGF-β1 mutant mice demonstrate high levels of active TGF-β1 and exhibit progressive diaphyseal dysplasia similar to that seen in patients with CED [94]. Similarly, individuals with Loeys-Dietz and Marfan Syndrome, both of which involve altered TGF-β signaling, exhibit characteristic skeletal manifestations including osteopenia [116, 117, 120-122], scoliosis [115, 123, 166], and an

increased incidence of pseudarthrosis following orthopedic instrumentation [167, 168]. It has been hypothesized that chronically elevated serum TGF-β levels may also underlie bone loss in states such as hepatic and/or renal osteodystrophy [169].

Here, we show that *Nf1$^{flox/-}$;Col2.3Cre* mice exhibit five- to six-fold elevated serum TGF-β1 levels as compared to WT controls. Serum TGF-β1 levels were similarly increased in a cohort of human NF1 patients. Consistent with these data, we previously reported that *Nf1* haploinsufficient mast cells hypersecrete TGF-β, perpetuating excessive fibroblast proliferation and collagen synthesis within the neurofibroma microenvironment [89]. More recently, Wang and colleagues noted increased TGF-β mRNA levels in the fracture calluses of mice harboring conditional *Nf1* nullizygous osteoblasts [76].

Beyond merely overexpressing TGF-β1, *Nf1* mutant osteoblasts and osteoclasts pathologically differentiated and excessively resorbed bone in response to TGF-β1. These cellular dysfunctions were associated with increased activation of the canonical Smad pathway. Re-expression of the human, full-length *NF1* GRD in *Nf1* deficient osteoprogenitors attenuated TGF-β1 expression levels and inhibited Smad phosphorylation in response to TGF-β1 stimulation; thus, validating that TGF-β1 mediated biochemical gain-in-functions within neurofibromin deficient bone cells occur in a p21-Ras-dependent fashion.

The elevated ratio of active-to-latent TGF-β1 in *Nf1$^{flox/-}$;Col2.3Cre* mice with tibial fracture non-union further suggests that accelerated cleavage of the TGF-β1 latency associated peptide (LAP) may also play an important role in

upregulating the bioavailability of active TGF-β1 within the bone matrix. Several factors are known to activate latent TGF-β including integrins [170], thrombospondin-1[171], and MMP-2/9 [172]. In the present study, we found increased levels of active MMP-2 and MMP-9 in both the conditioned media of *Nf1* haploinsufficient myeloid cells and the serum of a human NF1 patient as compared to controls. Intriguingly, genetic ablation of MMP-2 and MMP-9 has been shown to alter bone remodeling [165] and fracture repair [162, 164]. Moreover, patient-derived hypertrophic non-union fracture tissue was also found to overexpress MMP-7 and MMP-12 in a recent clinical study [163]. Collectively, these findings suggest need for further investigation regarding the relationship between MMPs and TGF-β1 activation in normal and *Nf1*-deficient bone healing.

Recent clinical studies [70, 71, 80] and animal models [69, 76-79, 138, 141] suggest that cooperative interactions between local *Nf1*-nullizygous osteoprogenitors and *Nf1* haploinsufficient osteoclasts of the bone marrow play a critical role in modulating the disease process. By restoring the balance of coordinated osteoclast and osteoblast activity in NF1, attenuating TGF-β signaling may hold advantages over traditional monotherapies such as bisphosphonates, PTH, BMP, or vitamin D which selectively target either the osteoclast or the osteoblast alone. Furthermore, Heervä and colleagues recently demonstrated that osteoclasts derived from human NF1 patients were insensitive to bisphosphonate treatment versus healthy controls, reinforcing the need to develop novel targeted therapies designed specifically for the NF1 patient population [173]. Here, we show that suppression of hyperactive TGF-β signaling

can normalize the dysregulated functioning of *Nf1* deficient osteoblasts and osteoclasts, thereby restoring bone mass and preventing tibial fracture non-union in *Nf1$^{flox/-}$;Col2.3Cre* mice. These results underscore the need for next generation, highly selective TGF-β pharmacological inhibitors that could effectively treat the current therapy-resistant bone pathologies of NF1 patients.

In summary, this study provides direct pre-clinical evidence that dysregulated TGF-β signaling underlies osteoporosis and non-union fracture in a mouse model of NF1. These *in vivo* data also verify the regulatory role of TGF-β signaling in osteoclast and osteoblast biology – a complex topic that has been historically difficult to assess due to biphasic and dose-dependent effects of TGF-β on bone cells in *in vitro* culture. The marked response of *Nf1$^{flox/-}$;Col2.3Cre* mice to pharmacologic TGF-β inhibition , even as compared to WT controls also undergoing treatment , underscores the critical importance of the TGF-β pathway in the genesis of NF1-associated bone defects and as a target for therapeutic intervention. Given that current treatment outcomes for pseudarthrosis in NF1 remain poor, the potential application of pharmacologic TGF-β inhibitors to augment bone union warrants further pre-clinical and early phase clinical trials.

# CHAPTER 6. CONCLUSIONS AND FUTURE DIRECTIONS

## Conclusions

NF1 skeletal abnormalities such as osteoporosis, dystrophic scoliosis, and pseudarthrosis are associated with significant morbidity. To develop robust targeted therapies to effectively treat these deficits, it is necessary to expand our understanding of the cellular and molecular pathogenesis of NF1 associated osseous defects. To this end, we have shown that *Nf1*$^{flox/-}$*;Col2.3Cre* mice, harboring *Nf1* nullizygous osteoblasts on a *Nf1*$^{+/-}$ background, closely recapitulate multiple boney manifestations seen in the human disease including runting (short stature), bone mass deficits, spinal deformities, and tibial fracture non-union. As such, this model provides a valuable platform for investigating the consequences of *Nf1* gene dose in bone biology as well as for the preclinical testing of novel targeted therapeutics.

As compared to the overt osseous phenotypes observed in *Nf1*$^{flox/-}$*;Col2.3Cre* mice, the absence of similar findings in WT, *Nf1*$^{+/-}$, or even *Nf1*$^{flox/flox}$*;Col2.3Cre* mice further led us to reason that cooperative interactions between *Nf1* null osteoblasts and at least a subset of *Nf1*$^{+/-}$ lineages within the bone microenvironment are likely pivotal in the pathogenesis of these osseous features. Through a series of adoptive bone marrow transfer experiments, we have shown that *Nf1* haploinsufficiency in hematopoietic derived osteoclasts and myeloid progenitors is required for the genesis of tibial fracture non-union in *Nf1*$^{flox/-}$*;Col2.3Cre* mice. The paradigm that NF1 associated pseudarthrosis

involves the heterotypic interaction of multiple cell types with varying *NF1* gene dose is consistent with analogous observations in mouse models of at least two other NF1 related pathologies. (1) Optic nerve glioma formation in mice has been shown to require both *Nf1* nullizygosity in astrocytes together with *Nf1* haploinsufficiency in the microglia within the adjacent brain parenchyma [139, 140]. (2) Yang and colleagues demonstrated that *Nf1*-depedent plexiform neurofibroma genesis in *Nf1$^{flox/-}$;Krox20-Cre* mice requires the cooperative interaction of *Nf1$^{-/-}$* Schwann cell precursors and *Nf1* heterozygous mast cells in the tumor microenvironment [84].

Conditional ablation of a single *Nf1* allele in myeloid progenitors versus mature, terminally differentiated osteoclasts has also proven informative regarding the stage of myeloid/osteoclast development at which *Nf1* haploinsufficiency is permissive of increased osteolytic activity. While *Nf1$^{flox/+}$;LysMCre* mice exhibit increased osteoclast progenitor frequency (CFU-M), enhanced osteoclast formation, and accelerated bone loss following ovariectomy induced pro-resorptive challenge, *Nf1$^{flox/+}$;CtskCre* mice did not show signs of increased osteolytic activity as compared to WT controls in analogous experiments. Collectively, these data provide genetic evidence that haploinsufficiency of *Nf1* in myeloid progenitors, but not terminally differentiated osteoclasts alone, is required to expand the pool of osteoclast progenitors, thereby augmenting bone resorptive capacity *in vivo*.

Our studies indicate that the cellular mechanisms of *Nf1* osseous dysplasia are complex and may require the cooperative interaction of *Nf1* nullizygous osteoblasts and/or progenitors, as well as *Nf1* heterozygous osteoclasts and their myeloid precursors. These observations led us to consider cytokines such as TGF-β1, which function as master regulators in the spatiotemporal coupling of osteoblast and osteoclast activity [94], as potential molecular mediators of NF1 bone defects. We were alerted to this possibility by our previous observation that *Nf1* haploinsufficient myeloid cells potentiate neurofibroma phenotypes through secreted TGF-β signaling [89]. More intriguingly, characteristic NF1 osseous defects such as scoliosis, osteopenia, tibial dysplasia, and pseudarthrosis are frequently observed in a number of other clinical disorders associated with dysregulated TGF-β signaling, including Loeys-Dietz syndrome [115-118], Marfan syndrome [119-123], and Camurati-Engelmann disease [124].

Here, we provided genetic and pharmacologic evidence that hyperactive TGF-β1 signaling pivotally underpins osseous defects in *Nf1*$^{flox/-}$*;Col2.3Cre* mice. Compared to controls, serum TGF-β1 levels were five- to six- fold increased both in *Nf1*$^{flox/-}$*;Col2.3Cre* mice and in a cohort of NF1 patients. *Nf1* deficient osteoblasts, the principal source of TGF-β1 in bone, overexpressed TGF-β1 in a gene dosage dependent fashion. Moreover, *Nf1* deficient osteoblasts and osteoclasts were hyperresponsive to TGF-β1 stimulation, potentiating osteoclast bone resorptive activity while inhibiting osteoblast differentiation. These cellular phenotypes were further accompanied by p21-Ras-dependent hyperactivation of

the canonical TGF-β1-Smad pathway. Re-expression of the human, full-length neurofibromin GTPase-activating protein (GAP) related domain (*NF1* GRD) in primary *Nf1* deficient osteoblast progenitors, attenuated TGF-β1 expression levels and reduced Smad phosphorylation in response to TGF-β1 stimulation. As an *in vivo* proof of principle, we demonstrated that administration of the TβRI kinase inhibitor, SD-208, could rescue bone mass deficits and prevent tibial fracture non-union in *Nf1*$^{flox/-}$*;Col2.3Cre* mice. In sum, these data demonstrate a pivotal role for hyperactive TGF-β1 signaling in the pathogenesis of NF1 associated osteoporosis and pseudarthrosis. Importantly, they implicate the TGF-β signaling pathway as a potential therapeutic target in the treatment of NF1 osseous defects which are refractory to current therapies.

A number of pharmacologic TGF-β inhibitors are currently in early phase clinical trials for the treatment of idiopathic pulmonary fibrosis, focal segmental glomerulosclerosis, and various malignancies [174]. Despite promising responses, the ubiquitous role of TGF-β in regulating multiple physiological processes such as the immune system and cardiovascular development has raised concerns regarding the potential side effects of these drugs when administered systemically at high doses and for extended durations. Skin lesions, including eruptive non-malignant keratoacanthomas and squamous cell carcinoma, gingival bleeding, and fatigue were among the most commonly reported side-effects in metastatic melanoma patients receiving extended dosing at 10-15 mg/kg with the pan monoclonal TGF-β neutralizing antibody, GC-1008 [175]. In a dose escalation study of the small molecule TβRI kinase inhibitor,

LY2157299, for the treatment of refractory malignant glioma, pulmonary embolism and thrombocytopenia were dose-limiting toxicities observed during the second treatment cycle; however, no indications of cardiovascular toxicity were reported [176].

To circumvent adverse effects of systemic TGF-β inhibition, one potential strategy would be to utilize targeted drug delivery systems to limit drug bioavailability to the tissue of interest. Bisphosphonates [177, 178] and oligopeptides, such as repeating sequences of aspartate-serine-serine $(AspSerSer)_6$ [179], are two classes of stable bone-targeting moieties that have been utilized to deliver therapeutic agents to skeletal tissues. To achieve sustained drug release within a localized anatomical compartment, encapsulation of compounds in nanoparticles and/or polymeric scaffolds might serve as useful delivery vectors [180, 181]. Collagen sponges infused with recombinant BMPs are one particularly common application of this technology which has been used by orthopedic surgeons for the past decade to promote bone healing in spinal fusion, fracture non-union, and critical sized long-bone defects [182]. Ultimately, further testing of clinical grade pharmacologic TGF-β inhibitors optimized for targeted delivery to bone needs to be undertaken in NF1 murine pseudarthrosis models to facilitate clinical translation into patients.

**Future directions**

Although pharmacologic TGF-β inhibition successfully rescued bone mass deficits and prevented tibial fracture non-union in *Nf1$^{flox/-}$;Col2.3Cre* mice, its off-target effects on hematopoietic cells and other tissues remain a limiting factor for clinical translation in the treatment of NF1 patients with pseudarthrosis or osteoporosis. The characterization of specific downstream targets which are critical to modulating the physiological effects of TGF-β in osteoblasts and osteoclasts is now the primary focus of our ongoing research. We are currently working to identify transcription factors which selectively modulate aberrant cellular functions in *Nf1* mutant osteoclasts and osteoblasts induced by TGF-β1 stimulation. Ultimately, therapeutic modulation of such targets may provide novel treatment strategies for pseudarthrosis and other therapy resistant osseous manifestations of NF1.

## REFERENCES


1. Friedman, J.M., *Epidemiology of neurofibromatosis type 1.* Am J Med Genet, 1999. **89**(1): p. 1-6.

2. Viskochil, D., et al., *Deletions and a translocation interrupt a cloned gene at the neurofibromatosis type 1 locus.* Cell, 1990. **62**(1): p. 187-92.

3. Wallace, M.R., et al., *Type 1 neurofibromatosis gene: identification of a large transcript disrupted in three NF1 patients.* Science, 1990. **249**(4965): p. 181-6.

4. Leevers, S.J., H.F. Paterson, and C.J. Marshall, *Requirement for Ras in Raf activation is overcome by targeting Raf to the plasma membrane.* Nature, 1994. **369**(6479): p. 411-4.

5. Stokoe, D., et al., *Activation of Raf as a result of recruitment to the plasma membrane.* Science, 1994. **264**(5164): p. 1463-7.

6. Reynolds, R.M., et al., *Von Recklinghausen's neurofibromatosis: neurofibromatosis type 1.* Lancet, 2003. **361**(9368): p. 1552-4.

7. Riccardi, V.M., *Von Recklinghausen neurofibromatosis.* N Engl J Med, 1981. **305**(27): p. 1617-27.

8. Friedman, J.M. and P.H. Birch, *Type 1 neurofibromatosis: a descriptive analysis of the disorder in 1,728 patients.* Am J Med Genet, 1997. **70**(2): p. 138-43.

9. Listernick, R., et al., *Optic gliomas in children with neurofibromatosis type 1.* J Pediatr, 1989. **114**(5): p. 788-92.

10. Listernick, R., et al., *Natural history of optic pathway tumors in children with neurofibromatosis type 1: a longitudinal study.* J Pediatr, 1994. **125**(1): p. 63-6.

11. Lubs, M.L., et al., *Lisch nodules in neurofibromatosis type 1.* N Engl J Med, 1991. **324**(18): p. 1264-6.

12. Hyman, S.L., A. Shores, and K.N. North, *The nature and frequency of cognitive deficits in children with neurofibromatosis type 1.* Neurology, 2005. **65**(7): p. 1037-44.

13. Lin, A.E., et al., *Cardiovascular malformations and other cardiovascular abnormalities in neurofibromatosis 1.* Am J Med Genet, 2000. **95**(2): p. 108-17.

14. Fossali, E., et al., *Renovascular disease and hypertension in children with neurofibromatosis.* Pediatr Nephrol, 2000. **14**(8-9): p. 806-10.

15. Rasmussen, S.A., Q. Yang, and J.M. Friedman, *Mortality in neurofibromatosis 1: an analysis using U.S. death certificates.* Am J Hum Genet, 2001. **68**(5): p. 1110-8.

16. Friedman, J.M., et al., *Cardiovascular disease in neurofibromatosis 1: report of the NF1 Cardiovascular Task Force.* Genet Med, 2002. **4**(3): p. 105-11.

17. Lama, G., et al., *Blood pressure and cardiovascular involvement in children with neurofibromatosis type1.* Pediatr Nephrol, 2004. **19**(4): p. 413-8.

18. Rea, D., et al., *Cerebral arteriopathy in children with neurofibromatosis type 1.* Pediatrics, 2009. **124**(3): p. e476-83.

19. Brodeur, G.M., *The NF1 gene in myelopoiesis and childhood myelodysplastic syndromes.* N Engl J Med, 1994. **330**(9): p. 637-9.

20. Side, L., et al., *Homozygous inactivation of the NF1 gene in bone marrow cells from children with neurofibromatosis type 1 and malignant myeloid disorders.* N Engl J Med, 1997. **336**(24): p. 1713-20.

21. Emanuel, P.D., et al., *The role of monocyte-derived hemopoietic growth factors in the regulation of myeloproliferation in juvenile chronic myelogenous leukemia.* Exp Hematol, 1991. **19**(10): p. 1017-24.

22. Lammert, M., et al., *Decreased bone mineral density in patients with neurofibromatosis 1.* Osteoporos Int, 2005. **16**(9): p. 1161-6.

23. Kuorilehto, T., et al., *Decreased bone mineral density and content in neurofibromatosis type 1: lowest local values are located in the load-carrying parts of the body.* Osteoporos Int, 2005. **16**(8): p. 928-36.

24. Dulai, S., et al., *Decreased bone mineral density in neurofibromatosis type 1: results from a pediatric cohort.* J Pediatr Orthop, 2007. **27**(4): p. 472-5.

25. Yilmaz, K., et al., *Bone mineral density in children with neurofibromatosis 1.* Acta Paediatr, 2007. **96**(8): p. 1220-2.

26. Stevenson, D.A., et al., *Bone mineral density in children and adolescents with neurofibromatosis type 1.* J Pediatr, 2007. **150**(1): p. 83-8.

27. Tucker, T., et al., *Bone health and fracture rate in individuals with neurofibromatosis 1 (NF1).* J Med Genet, 2009. **46**(4): p. 259-65.

28. Crawford, A.H., *Pitfalls of spinal deformities associated with neurofibromatosis in children.* Clin Orthop Relat Res, 1989(245): p. 29-42.

29. Crawford, A.H., Jr. and N. Bagamery, *Osseous manifestations of neurofibromatosis in childhood.* J Pediatr Orthop, 1986. **6**(1): p. 72-88.

30. Illes, T., et al., *Decreased bone mineral density in neurofibromatosis-1 patients with spinal deformities.* Osteoporos Int, 2001. **12**(10): p. 823-7.

31. Clementi, M., et al., *Neurofibromatosis type 1 growth charts.* Am J Med Genet, 1999. **87**(4): p. 317-23.

32. Szudek, J., P. Birch, and J.M. Friedman, *Growth in North American white children with neurofibromatosis 1 (NF1).* J Med Genet, 2000. **37**(12): p. 933-8.

33. Virdis, R., et al., *Growth and pubertal disorders in neurofibromatosis type 1.* J Pediatr Endocrinol Metab, 2003. **16 Suppl 2**: p. 289-92.

34. Riccardi, V.M., *Neurofibromatosis : phenotype, natural history, and pathogenesis*. 2nd ed. 1992, Baltimore: Johns Hopkins University Press. ix, 498 p.

35. Alwan, S., S.J. Tredwell, and J.M. Friedman, *Is osseous dysplasia a primary feature of neurofibromatosis 1 (NF1)?* Clin Genet, 2005. **67**(5): p. 378-90.

36. Elefteriou, F., et al., *Skeletal abnormalities in neurofibromatosis type 1: approaches to therapeutic options.* Am J Med Genet A, 2009. **149A**(10): p. 2327-38.

37. Young, H., S. Hyman, and K. North, *Neurofibromatosis 1: clinical review and exceptions to the rules.* J Child Neurol, 2002. **17**(8): p. 613-21; discussion 627-9, 646-51.

38. Friedman, J.M., *Neurofibromatosis 1: clinical manifestations and diagnostic criteria.* J Child Neurol, 2002. **17**(8): p. 548-54; discussion 571-2, 646-51.

39. Stevenson, D.A., et al., *Descriptive analysis of tibial pseudarthrosis in patients with neurofibromatosis 1.* Am J Med Genet, 1999. **84**(5): p. 413-9.

40. Stevenson, D.A., et al., *Evidence of increased bone resorption in neurofibromatosis type 1 using urinary pyridinium crosslink analysis.* Pediatr Res, 2008. **63**(6): p. 697-701.

41. Rosen, H.N., et al., *Specificity of urinary excretion of cross-linked N-telopeptides of type I collagen as a marker of bone turnover.* Calcif Tissue Int, 1994. **54**(1): p. 26-9.

42. Delmas, P.D., et al., *Urinary excretion of pyridinoline crosslinks correlates with bone turnover measured on iliac crest biopsy in patients with vertebral osteoporosis.* J Bone Miner Res, 1991. **6**(6): p. 639-44.

43. Robins, S.P., et al., *Evaluation of urinary hydroxypyridinium crosslink measurements as resorption markers in metabolic bone diseases.* Eur J Clin Invest, 1991. **21**(3): p. 310-5.

44. Heerva, E., et al., *A controlled register based study of 460 neurofibromatosis 1 (NF1) patients: Increased fracture risk in children and adults over 41 years.* J Bone Miner Res, 2012. **27**(11): p. 2333-7.

45. Seitz, S., et al., *High bone turnover and accumulation of osteoid in patients with neurofibromatosis 1.* Osteoporos Int, 2010. **21**(1): p. 119-27.

46. Brunetti-Pierri, N., et al., *Generalized metabolic bone disease in Neurofibromatosis type I.* Mol Genet Metab, 2008. **94**(1): p. 105-11.

47. Gould, E., *The bone changes occuring in Von Recklinghausen's disease.* Q J Med, 1918. **11**: p. 221-228.

48. Weiss, R., *(A) Von Recklinghausen's disease in the Negro; (B) curvature of the spine in von Recklinghausen's disease.* Arch Dermatol Syphilol, 1921. **3**: p. 144-151.

49. Akbarnia, B.A., et al., *Prevalence of scoliosis in neurofibromatosis.* Spine (Phila Pa 1976), 1992. **17**(8 Suppl): p. S244-8.

50. Rezaian, S.M., *The incidence of scoliosis due to neurofibromatosis.* Acta Orthop Scand, 1976. **47**(5): p. 534-9.

51. Tsirikos, A.I., et al., *Assessment of vertebral scalloping in neurofibromatosis type 1 with plain radiography and MRI.* Clin Radiol, 2004. **59**(11): p. 1009-17.

52. Vitale, M.G., A. Guha, and D.L. Skaggs, *Orthopaedic manifestations of neurofibromatosis in children: an update.* Clin Orthop Relat Res, 2002(401): p. 107-18.

53. Durrani, A.A., et al., *Modulation of spinal deformities in patients with neurofibromatosis type 1.* Spine (Phila Pa 1976), 2000. **25**(1): p. 69-75.

54. Abdel-Wanis, M.E. and N. Kawahara, *The role of neurofibromin and melatonin in pathogenesis of pseudarthrosis after spinal fusion for neurofibromatous scoliosis.* Med Hypotheses, 2002. **58**(5): p. 395-8.

55. Crawford, A.H., et al., *The immature spine in type-1 neurofibromatosis.* J Bone Joint Surg Am, 2007. **89 Suppl 1**: p. 123-42.

56. Kim, H.W. and S.L. Weinstein, *Spine update. The management of scoliosis in neurofibromatosis.* Spine (Phila Pa 1976), 1997. **22**(23): p. 2770-6.

57. Peltier, L.F., *The classic. Ununited fractures in children. James Paget, 1891.* Clin Orthop Relat Res, 1982(166): p. 2-4.

58. Delgado-Martinez, A.D., E.C. Rodriguez-Merchan, and B. Olsen, *Congenital pseudarthrosis of the tibia.* Int Orthop, 1996. **20**(3): p. 192-9.

59. Sofield, H.A., *Congenital pseudarthrosis of the tibia.* Clin Orthop Relat Res, 1971. **76**: p. 33-42.

60. Morrissy, R.T., E.J. Riseborough, and J.E. Hall, *Congenital pseudarthrosis of the tibia.* J Bone Joint Surg Br, 1981. **63-B**(3): p. 367-75.

61. Gilbert, A. and R. Brockman, *Congenital pseudarthrosis of the tibia. Long-term followup of 29 cases treated by microvascular bone transfer.* Clin Orthop Relat Res, 1995(314): p. 37-44.

62. Ippolito, E., et al., *Pathology of bone lesions associated with congenital pseudarthrosis of the leg.* J Pediatr Orthop B, 2000. **9**(1): p. 3-10.

63. Cho, T.J., et al., *Biologic characteristics of fibrous hamartoma from congenital pseudarthrosis of the tibia associated with neurofibromatosis type 1.* J Bone Joint Surg Am, 2008. **90**(12): p. 2735-44.

64. Boyd, H.B., *Pathology and natural history of congenital pseudarthrosis of the tibia.* Clin Orthop Relat Res, 1982(166): p. 5-13.

65. Leskela, H.V., et al., *Congenital pseudarthrosis of neurofibromatosis type 1: impaired osteoblast differentiation and function and altered NF1 gene expression.* Bone, 2009. **44**(2): p. 243-50.

66. Lakkis, M.M. and J.A. Epstein, *Neurofibromin modulation of ras activity is required for normal endocardial-mesenchymal transformation in the developing heart.* Development, 1998. **125**(22): p. 4359-67.

67. Largaespada, D.A., et al., *Nf1 deficiency causes Ras-mediated granulocyte/macrophage colony stimulating factor hypersensitivity and chronic myeloid leukaemia.* Nat Genet, 1996. **12**(2): p. 137-43.

68. Zhang, Y.Y., et al., *Nf1 regulates hematopoietic progenitor cell growth and ras signaling in response to multiple cytokines.* J Exp Med, 1998. **187**(11): p. 1893-902.

69. Yang, F.C., et al., *Hyperactivation of p21ras and PI3K cooperate to alter murine and human neurofibromatosis type 1-haploinsufficient osteoclast functions.* J Clin Invest, 2006. **116**(11): p. 2880-91.

70. Heerva, E., et al., *Osteoclasts in neurofibromatosis type 1 display enhanced resorption capacity, aberrant morphology, and resistance to serum deprivation.* Bone, 2010. **47**(3): p. 583-90.

71. Stevenson, D.A., et al., *Multiple increased osteoclast functions in individuals with neurofibromatosis type 1.* Am J Med Genet A, 2011. **155A**(5): p. 1050-9.

72. Yan, J., et al., *Rac1 mediates the osteoclast gains-in-function induced by haploinsufficiency of Nf1.* Hum Mol Genet, 2008. **17**(7): p. 936-48.

73. Wu, X., et al., *Neurofibromin plays a critical role in modulating osteoblast differentiation of mesenchymal stem/progenitor cells.* Hum Mol Genet, 2006. **15**(19): p. 2837-45.

74. Yu, X., et al., *Neurofibromin and its inactivation of Ras are prerequisites for osteoblast functioning.* Bone, 2005. **36**(5): p. 793-802.

75. Elefteriou, F., et al., *ATF4 mediation of NF1 functions in osteoblast reveals a nutritional basis for congenital skeletal dysplasiae.* Cell Metab, 2006. **4**(6): p. 441-51.

76. Wang, W., et al., *Local low-dose lovastatin delivery improves the bone-healing defect caused by Nf1 loss of function in osteoblasts.* J Bone Miner Res, 2010. **25**(7): p. 1658-67.

77. Zhang, W., et al., *Primary osteopathy of vertebrae in a neurofibromatosis type 1 murine model.* Bone, 2011. **48**(6): p. 1378-87.

78. Wu, X., et al., *The haploinsufficient hematopoietic microenvironment is critical to the pathological fracture repair in murine models of neurofibromatosis type 1.* PLoS One, 2011. **6**(9): p. e24917.

79. Kolanczyk, M., et al., *Multiple roles for neurofibromin in skeletal development and growth.* Hum Mol Genet, 2007. **16**(8): p. 874-86.

80. Stevenson, D.A., et al., *Double inactivation of NF1 in tibial pseudarthrosis.* Am J Hum Genet, 2006. **79**(1): p. 143-8.

81. Lee, S.M., et al., *Is double inactivation of the Nf1 gene responsible for the development of congenital pseudarthrosis of the tibia associated with NF1?* J Orthop Res, 2012. **30**(10): p. 1535-40.

82. Friedman, J.M. and V.M. Riccardi, *Neurofibromatosis : phenotype, natural history, and pathogenesis*. 3rd ed. 1999, Baltimore: Johns Hopkins University Press. xiv, 381 p.

83. Hirota, S., et al., *Possible involvement of c-kit receptor and its ligand in increase of mast cells in neurofibroma tissues.* Arch Pathol Lab Med, 1993. **117**(10): p. 996-9.

84. Yang, F.C., et al., *Nf1-dependent tumors require a microenvironment containing Nf1+/-- and c-kit-dependent bone marrow.* Cell, 2008. **135**(3): p. 437-48.

85. Li, H., et al., *Ras dependent paracrine secretion of osteopontin by Nf1+/- osteoblasts promote osteoclast activation in a neurofibromatosis type I murine model.* Pediatr Res, 2009. **65**(6): p. 613-8.

86. Schindeler, A. and D.G. Little, *Recent insights into bone development, homeostasis, and repair in type 1 neurofibromatosis (NF1).* Bone, 2008. **42**(4): p. 616-22.

87. Janssens, K., et al., *Transforming growth factor-beta1 to the bone.* Endocr Rev, 2005. **26**(6): p. 743-74.

88. Juarez, P. and T.A. Guise, *TGF-beta in cancer and bone: implications for treatment of bone metastases.* Bone, 2011. **48**(1): p. 23-9.

89. Yang, F.C., et al., *Nf1+/- mast cells induce neurofibroma like phenotypes through secreted TGF-beta signaling.* Hum Mol Genet, 2006. **15**(16): p. 2421-37.

90. Gibbs, J.B., A. Oliff, and N.E. Kohl, *Farnesyltransferase inhibitors: Ras research yields a potential cancer therapeutic.* Cell, 1994. **77**(2): p. 175-8.

91. Sebti, S. and A.D. Hamilton, *Inhibitors of prenyl transferases.* Curr Opin Oncol, 1997. **9**(6): p. 557-61.

92. Massague, J., *TGF-beta signal transduction.* Annu Rev Biochem, 1998. **67**: p. 753-91.

93. Bismar, H., et al., *Transforming growth factor beta (TGF-beta) levels in the conditioned media of human bone cells: relationship to donor age, bone volume, and concentration of TGF-beta in human bone matrix in vivo.* Bone, 1999. **24**(6): p. 565-9.

94. Tang, Y., et al., *TGF-beta1-induced migration of bone mesenchymal stem cells couples bone resorption with formation.* Nat Med, 2009. **15**(7): p. 757-65.

95. Balooch, G., et al., *TGF-beta regulates the mechanical properties and composition of bone matrix.* Proc Natl Acad Sci U S A, 2005. **102**(52): p. 18813-8.

96. Derynck, R. and Y.E. Zhang, *Smad-dependent and Smad-independent pathways in TGF-beta family signalling.* Nature, 2003. **425**(6958): p. 577-84.

97. Massague, J., *How cells read TGF-beta signals.* Nat Rev Mol Cell Biol, 2000. **1**(3): p. 169-78.

98. Geiser, A.G., et al., *Decreased bone mass and bone elasticity in mice lacking the transforming growth factor-beta1 gene.* Bone, 1998. **23**(2): p. 87-93.

99. Atti, E., et al., *Effects of transforming growth factor-beta deficiency on bone development: a Fourier transform-infrared imaging analysis.* Bone, 2002. **31**(6): p. 675-84.

100. Alliston, T., et al., *TGF-beta-induced repression of CBFA1 by Smad3 decreases cbfa1 and osteocalcin expression and inhibits osteoblast differentiation.* EMBO J, 2001. **20**(9): p. 2254-72.

101. Maeda, S., et al., *Endogenous TGF-beta signaling suppresses maturation of osteoblastic mesenchymal cells.* EMBO J, 2004. **23**(3): p. 552-63.

102. Filvaroff, E., et al., *Inhibition of TGF-beta receptor signaling in osteoblasts leads to decreased bone remodeling and increased trabecular bone mass.* Development, 1999. **126**(19): p. 4267-79.

103. Qiu, T., et al., *TGF-beta type II receptor phosphorylates PTH receptor to integrate bone remodelling signalling.* Nat Cell Biol, 2010. **12**(3): p. 224-34.

104. Takai, H., et al., *Transforming growth factor-beta stimulates the production of osteoprotegerin/osteoclastogenesis inhibitory factor by bone marrow stromal cells.* J Biol Chem, 1998. **273**(42): p. 27091-6.

105. Murakami, T., et al., *Transforming growth factor-beta1 increases mRNA levels of osteoclastogenesis inhibitory factor in osteoblastic/stromal cells and inhibits the survival of murine osteoclast-like cells.* Biochem Biophys Res Commun, 1998. **252**(3): p. 747-52.

106. Quinn, J.M., et al., *Transforming growth factor beta affects osteoclast differentiation via direct and indirect actions.* J Bone Miner Res, 2001. **16**(10): p. 1787-94.

107. Sells Galvin, R.J., et al., *TGF-beta enhances osteoclast differentiation in hematopoietic cell cultures stimulated with RANKL and M-CSF.* Biochem Biophys Res Commun, 1999. **265**(1): p. 233-9.

108. Itonaga, I., et al., *Transforming growth factor-beta induces osteoclast formation in the absence of RANKL.* Bone, 2004. **34**(1): p. 57-64.

109. Fox, S.W., K.E. Evans, and A.C. Lovibond, *Transforming growth factor-beta enables NFATc1 expression during osteoclastogenesis.* Biochem Biophys Res Commun, 2008. **366**(1): p. 123-8.

110. Yasui, T., et al., *Regulation of RANKL-induced osteoclastogenesis by TGF-beta through molecular interaction between Smad3 and TRAF6.* J Bone Miner Res, 2011. **26**(7): p. 1447-56.

111. Gingery, A., et al., *TGF-beta coordinately activates TAK1/MEK/AKT/NFkB and SMAD pathways to promote osteoclast survival.* Exp Cell Res, 2008. **314**(15): p. 2725-38.

112. Futakuchi, M., et al., *Transforming growth factor-beta signaling at the tumor-bone interface promotes mammary tumor growth and osteoclast activation.* Cancer Sci, 2009. **100**(1): p. 71-81.

113. Mohammad, K.S., et al., *Pharmacologic inhibition of the TGF-beta type I receptor kinase has anabolic and anti-catabolic effects on bone.* PLoS One, 2009. **4**(4): p. e5275.

114. Edwards, J.R., et al., *Inhibition of TGF-beta signaling by 1D11 antibody treatment increases bone mass and quality in vivo.* J Bone Miner Res, 2010. **25**(11): p. 2419-26.

115. Loeys, B.L., et al., *A syndrome of altered cardiovascular, craniofacial, neurocognitive and skeletal development caused by mutations in TGFBR1 or TGFBR2.* Nat Genet, 2005. **37**(3): p. 275-81.

116. Kirmani, S., et al., *Germline TGF-beta receptor mutations and skeletal fragility: a report on two patients with Loeys-Dietz syndrome.* Am J Med Genet A, 2010. **152A**(4): p. 1016-9.

117. Ben Amor, I.M., et al., *Low bone mass and high material bone density in two patients with Loeys-Dietz syndrome caused by transforming growth factor receptor 2 mutations.* J Bone Miner Res, 2012. **27**(3): p. 713-8.

118. Sousa, S.B., et al., *Expanding the skeletal phenotype of Loeys-Dietz syndrome.* Am J Med Genet A, 2011. **155A**(5): p. 1178-83.

119. Wilner, H.I. and N. Finby, *Skeletal manifestations in the Marfan syndrome.* JAMA, 1964. **187**: p. 490-5.

120. Kohlmeier, L., et al., *The bone mineral status of patients with Marfan syndrome.* J Bone Miner Res, 1995. **10**(10): p. 1550-5.

121. Le Parc, J.M., et al., *Bone mineral density in sixty adult patients with Marfan syndrome.* Osteoporos Int, 1999. **10**(6): p. 475-9.

122. Moura, B., et al., *Bone mineral density in Marfan syndrome. A large case-control study.* Joint Bone Spine, 2006. **73**(6): p. 733-5.

123. Demetracopoulos, C.A. and P.D. Sponseller, *Spinal deformities in Marfan syndrome.* Orthop Clin North Am, 2007. **38**(4): p. 563-72, vii.

124. Janssens, K., et al., *Camurati-Engelmann disease: review of the clinical, radiological, and molecular data of 24 families and implications for diagnosis and treatment.* J Med Genet, 2006. **43**(1): p. 1-11.

125. Jacks, T., et al., *Tumour predisposition in mice heterozygous for a targeted mutation in Nf1.* Nat Genet, 1994. **7**(3): p. 353-61.

126. Zhu, Y., et al., *Ablation of NF1 function in neurons induces abnormal development of cerebral cortex and reactive gliosis in the brain.* Genes Dev, 2001. **15**(7): p. 859-76.

127. Dacquin, R., et al., *Mouse alpha1(I)-collagen promoter is the best known promoter to drive efficient Cre recombinase expression in osteoblast.* Dev Dyn, 2002. **224**(2): p. 245-51.

128. Clausen, B.E., et al., *Conditional gene targeting in macrophages and granulocytes using LysMcre mice.* Transgenic Res, 1999. **8**(4): p. 265-77.

129. Chiu, W.S., et al., *Transgenic mice that express Cre recombinase in osteoclasts.* Genesis, 2004. **39**(3): p. 178-85.

130. Milne, M., et al., *Thyroid hormone excess increases insulin-like growth factor I transcripts in bone marrow cell cultures: divergent effects on vertebral and femoral cell cultures.* Endocrinology, 1998. **139**(5): p. 2527-34.

131. Ishida, Y. and J.N. Heersche, *Progesterone- and dexamethasone-dependent osteoprogenitors in bone cell populations derived from rat vertebrae are different and distinct.* Endocrinology, 1999. **140**(7): p. 3210-8.

132. Hamamura, K. and H. Yokota, *Stress to endoplasmic reticulum of mouse osteoblasts induces apoptosis and transcriptional activation for bone remodeling.* FEBS Lett, 2007. **581**(9): p. 1769-74.

133. Pollari, S., et al., *Identification of microRNAs inhibiting TGF-beta-induced IL-11 production in bone metastatic breast cancer cells.* PLoS One, 2012. **7**(5): p. e37361.

134. Hiatt, K.K., et al., *Neurofibromin GTPase-activating protein-related domains restore normal growth in Nf1-/- cells.* J Biol Chem, 2001. **276**(10): p. 7240-5.

135. Xu, M., et al., *Constitutive mobilization of CD34+ cells into the peripheral blood in idiopathic myelofibrosis may be due to the action of a number of proteases.* Blood, 2005. **105**(11): p. 4508-15.

136. Staser, K., et al., *Normal hematopoiesis and neurofibromin-deficient myeloproliferative disease require Erk.* J Clin Invest, 2013. **123**(1): p. 329-34.

137. Bonnarens, F. and T.A. Einhorn, *Production of a standard closed fracture in laboratory animal bone.* J Orthop Res, 1984. **2**(1): p. 97-101.

138. Schindeler, A., et al., *Models of tibial fracture healing in normal and Nf1-deficient mice.* J Orthop Res, 2008. **26**(8): p. 1053-60.

139. Bajenaru, M.L., et al., *Optic nerve glioma in mice requires astrocyte Nf1 gene inactivation and Nf1 brain heterozygosity.* Cancer Res, 2003. **63**(24): p. 8573-7.

140. Daginakatte, G.C. and D.H. Gutmann, *Neurofibromatosis-1 (Nf1) heterozygous brain microglia elaborate paracrine factors that promote Nf1-deficient astrocyte and glioma growth.* Hum Mol Genet, 2007. **16**(9): p. 1098-112.

141. Wang, W., et al., *Mice lacking Nf1 in osteochondroprogenitor cells display skeletal dysplasia similar to patients with neurofibromatosis type I.* Hum Mol Genet, 2011. **20**(20): p. 3910-24.

142. Funasaki, H., et al., *Pathophysiology of spinal deformities in neurofibromatosis. An analysis of seventy-one patients who had curves associated with dystrophic changes.* J Bone Joint Surg Am, 1994. **76**(5): p. 692-700.

143. Casselman, E.S. and G.A. Mandell, *Vertebral scalloping in neurofibromatosis.* Radiology, 1979. **131**(1): p. 89-94.

144. Sartoris, D.J. and H. Jones, *Case report 343. Neurofibroma arising in sympathetic ganglion with probable associated spinal neuroarthropathy (presumptive diagnosis).* Skeletal Radiol, 1986. **15**(1): p. 60-4.

145. Goff, C.W. and W. Landmesser, *Bipedal rats and mice; laboratory animals for orthopaedic research.* J Bone Joint Surg Am, 1957. **39-A**(3): p. 616-22.

146. Machida, M., et al., *Pathogenesis of idiopathic scoliosis. Experimental study in rats.* Spine (Phila Pa 1976), 1999. **24**(19): p. 1985-9.

147. Birnbaum, R.A., et al., *Nf1 and Gmcsf interact in myeloid leukemogenesis.* Mol Cell, 2000. **5**(1): p. 189-95.

148. Vogel, K.S., et al., *Mouse tumor model for neurofibromatosis type 1.* Science, 1999. **286**(5447): p. 2176-9.

149. Cichowski, K., et al., *Mouse models of tumor development in neurofibromatosis type 1.* Science, 1999. **286**(5447): p. 2172-6.

150. Lasater, E.A., et al., *Genetic and cellular evidence of vascular inflammation in neurofibromin-deficient mice and humans.* J Clin Invest, 2010. **120**(3): p. 859-70.

151. Horowitz, M.C., J.A. Fretz, and J.A. Lorenzo, *How B cells influence bone biology in health and disease.* Bone, 2010. **47**(3): p. 472-9.

152. Pacifici, R., *T cells: critical bone regulators in health and disease.* Bone, 2010. **47**(3): p. 461-71.

153. Kacena, M.A., C.M. Gundberg, and M.C. Horowitz, *A reciprocal regulatory interaction between megakaryocytes, bone cells, and hematopoietic stem cells.* Bone, 2006. **39**(5): p. 978-84.

154. Kacena, M.A. and M.C. Horowitz, *The role of megakaryocytes in skeletal homeostasis and rheumatoid arthritis.* Curr Opin Rheumatol, 2006. **18**(4): p. 405-10.

155. Boyle, W.J., W.S. Simonet, and D.L. Lacey, *Osteoclast differentiation and activation.* Nature, 2003. **423**(6937): p. 337-42.

156. Heerva, E., et al., *A controlled register-based study of 460 neurofibromatosis 1 patients: Increased fracture risk in children and adults over 41 years of age.* J Bone Miner Res, 2012. **27**(11): p. 2333-7.

157. Alanne, M.H., et al., *Phenotypic characterization of transgenic mice harboring Nf1(+/-) or Nf1(-/-) osteoclasts in otherwise Nf1(+/+) background.* J Cell Biochem, 2012. **113**(6): p. 2136-46.

158. Bollag, G., et al., *Loss of NF1 results in activation of the Ras signaling pathway and leads to aberrant growth in haematopoietic cells.* Nat Genet, 1996. **12**(2): p. 144-8.

159. Zhang, Y., et al., *Quantitative effects of Nf1 inactivation on in vivo hematopoiesis.* J Clin Invest, 2001. **108**(5): p. 709-15.

160. Ingram, D.A., et al., *Leukemic potential of doubly mutant Nf1 and Wv hematopoietic cells.* Blood, 2003. **101**(5): p. 1984-6.

161. El-Hoss, J., et al., *A murine model of neurofibromatosis type 1 tibial pseudarthrosis featuring proliferative fibrous tissue and osteoclast-like cells.* J Bone Miner Res, 2012. **27**(1): p. 68-78.

162. Colnot, C., et al., *Altered fracture repair in the absence of MMP9.* Development, 2003. **130**(17): p. 4123-33.

163. Fajardo, M., et al., *Matrix metalloproteinases that associate with and cleave bone morphogenetic protein-2 in vitro are elevated in hypertrophic fracture nonunion tissue.* J Orthop Trauma, 2010. **24**(9): p. 557-63.

164. Lieu, S., et al., *Impaired remodeling phase of fracture repair in the absence of matrix metalloproteinase-2.* Dis Model Mech, 2011. **4**(2): p. 203-11.

165. Nyman, J.S., et al., *Differential effects between the loss of MMP-2 and MMP-9 on structural and tissue-level properties of bone.* J Bone Miner Res, 2011. **26**(6): p. 1252-60.

166. Avivi, E., et al., *Skeletal manifestations of Marfan syndrome.* Isr Med Assoc J, 2008. **10**(3): p. 186-8.

167. Birch, J.G. and J.A. Herring, *Spinal deformity in Marfan syndrome.* J Pediatr Orthop, 1987. **7**(5): p. 546-52.

168. Jones, K.B., et al., *Spine deformity correction in Marfan syndrome.* Spine (Phila Pa 1976), 2002. **27**(18): p. 2003-12.

169. Ehnert, S., et al., *TGF-beta1 as possible link between loss of bone mineral density and chronic inflammation.* PLoS One, 2010. **5**(11): p. e14073.

170. Munger, J.S., et al., *The integrin alpha v beta 6 binds and activates latent TGF beta 1: a mechanism for regulating pulmonary inflammation and fibrosis.* Cell, 1999. **96**(3): p. 319-28.

171. Schultz-Cherry, S. and J.E. Murphy-Ullrich, *Thrombospondin causes activation of latent transforming growth factor-beta secreted by endothelial cells by a novel mechanism.* J Cell Biol, 1993. **122**(4): p. 923-32.

172. Yu, Q. and I. Stamenkovic, *Cell surface-localized matrix metalloproteinase-9 proteolytically activates TGF-beta and promotes tumor invasion and angiogenesis.* Genes Dev, 2000. **14**(2): p. 163-76.

173. Heerva, E., et al., *Osteoclasts derived from patients with neurofibromatosis 1 (NF1) display insensitivity to bisphosphonates in vitro.* Bone, 2012. **50**(3): p. 798-803.

174. Connolly, E.C., J. Freimuth, and R.J. Akhurst, *Complexities of TGF-beta targeted cancer therapy.* Int J Biol Sci, 2012. **8**(7): p. 964-78.

175. Lonning, S., J. Mannick, and J.M. McPherson, *Antibody targeting of TGF-beta in cancer patients.* Curr Pharm Biotechnol, 2011. **12**(12): p. 2176-89.

176. Calvo-Aller, E., et al., *First human dose escalation study in patients with metastatic malignancies to determine safety and pharmacokinetics of LY2157299, a small molecule inhibitor of the transforming growth factor-beta receptor I kinase.* ASCO Annual Meeting. J Clin Oncol, 2008. **26**: p. (suppl):abstr14554.

177. Salerno, M., et al., *Bone-targeted doxorubicin-loaded nanoparticles as a tool for the treatment of skeletal metastases.* Curr Cancer Drug Targets, 2010. **10**(7): p. 649-59.

178. Yewle, J.N., D.A. Puleo, and L.G. Bachas, *Enhanced affinity bifunctional bisphosphonates for targeted delivery of therapeutic agents to bone.* Bioconjug Chem, 2011. **22**(12): p. 2496-506.

179. Zhang, G., et al., *A delivery system targeting bone formation surfaces to facilitate RNAi-based anabolic therapy.* Nat Med, 2012. **18**(2): p. 307-14.

180. Tautzenberger, A., A. Kovtun, and A. Ignatius, *Nanoparticles and their potential for application in bone.* Int J Nanomedicine, 2012. **7**: p. 4545-57.

181. Bose, S., M. Roy, and A. Bandyopadhyay, *Recent advances in bone tissue engineering scaffolds.* Trends Biotechnol, 2012. **30**(10): p. 546-54.

182. Geiger, M., R.H. Li, and W. Friess, *Collagen sponges for bone regeneration with rhBMP-2.* Adv Drug Deliv Rev, 2003. **55**(12): p. 1613-29.

# CURRICULUM VITAE

## Steven David Rhodes

## Education

Indiana University Medical Scientist Training Program (MSTP)
M.D., expected May 2015
Ph.D., Anatomy and Cell Biology, 2013

Wabash College, B.A., *Summa Cum Laude*, 2007
Major: Chemistry, Minor: Mathematics

## Research and Training Experience

M.D., Ph.D. Candidate, Indiana University Medical Scientist Training Program (MSTP), Indianapolis, IN — 2007

Research Fellow, Section of Nuclear Magnetic Resonance Laboratory of Membrane Biochemistry and Biophysics, NIH-NIAAA, Bethesda, MD — 2006

Research Fellow, Department of Biomedical Engineering, Cornell Center for Materials Research, Cornell University, Ithaca, NY — 2005

Camille & Henry Dreyfus Research Scholar, Department of Chemistry, Wabash College, Crawfordsville, IN — 2004

## Honors, Awards, and Fellowships

American Society of Hematology (ASH) Outstanding Abstract Achievement Award — 2012

Indiana University (IU) Simon Cancer Center Executive Committee Merylin Hester Scholarship — 2012

American Society for Bone and Mineral Research (ASBMR) Young Investigator Travel Grant — 2012

Children's Tumor Foundation (CTF) Young Investigator Award — 2011

American Society for Bone and Mineral Research (ASBMR) Young Investigator Award — 2011

2011 NIH/NCRR- Indiana Clinical and Translational Sciences Institute (CTSI) – TL1 Program Fellowship Award — 2011

| | |
|---|---|
| Indiana Clinical and Translational Sciences Institute (CTSI) Career Development Award | 2010 |
| *Summa Cum Laude*, Chemistry, Wabash College | 2007 |
| George Lewes Mackintosh Fellow, Wabash College | 2007 |
| Edgar C. Britton Memorial Award in Chemistry, Wabash College | 2007 |
| John Maurice Butler Prize for Scholarship and Character, Wabash College | 2007 |
| NIH/NIAAA Intramural Research Training Award (IRTA) | 2006 |
| Phi Lambda Upsilon Chemistry Honor Society | 2006 |
| Phi Beta Kappa | 2006 |
| Barry M. Goldwater Scholarship, Honorable Mention for Excellence in Mathematics, Science, and Engineering | 2006 |
| Junior Marshall, Wabash College | 2006 |
| Robert S. Harvey Award in Journalism, Wabash College | 2006 |
| Underwood Award in Chemistry, Wabash College | 2006 |
| Lewis Salter Memorial Award, Wabash College | 2006 |
| Howell Scholar in Chemistry, Wabash College | 2005 |
| Robert C. Byrd Honor Scholarship, Wabash College | 2005 |
| Camille & Henry Dreyfus Research Scholar, Wabash College | 2004 |

## **Teaching Experience**

| | |
|---|---|
| Instructor, DNA module, Molecular Medicine in Action (MMIA), Indiana University Cancer Research Institute, Indianapolis, IN | 2010-2013 |
| Peer tutor, Mathematics and Chemistry, Quantitative Skills Center, Wabash College, Crawfordsville, IN | 2004-2007 |

## Publications

1. Rhodes SD, Yang FC (in press). Single cell assays for mesenchymal stem cells. In: Dubitzky W, Wolkenhauer O, Cho K-H, Yokota H (editors) Encyclopedia of Systems Biology, 4 Vol., 3000 p. Springer New York, 2013.

2. Zhang W[1], Rhodes SD[1], Zhao L, He Y, Zhang Y, Shen Y, Yang D, Wu X, Li X, Yang X, Chen S, Turner C, Yang FC. Primary osteopathy of vertebrae in a neurofibromatosis type 1 murine model. *Bone*. 2011 Jun 1; 48(6):1378-87. [1]Co-first author.

3. Zhang W, Zhang Y, Li P, Rhodes SD, Wang Y, Xue X, Dong Y, Ding W, Shen Y, Zhang B. Administration of sodium ibandronate in the treatment of complicated giant cell tumor of the spine. *Spine* (Phila Pa 1976). 2011 Feb 1.

4. He Y, Staser K, Rhodes SD, Liu Y, Wu X, Park SJ, Yuan J, Yang X, Li X, Jiang L, Chen S, Yang FC. Erk1 positively regulates osteoclast differentiation and bone resorptive activity. *PLoS One*. 2011;6(9):e24780.

5. Wu X, Chen S, He Y, Rhodes SD, Mohammad KS, Li X, Yang X, Jiang L, Nalepa G, Snider P, Robling AG, Clapp DW, Conway SJ, Guise TA, Yang FC. The haploinsufficient hematopoietic microenvironment is critical to the pathological fracture repair in murine models of neurofibromatosis type 1. *PLoS One*. 2011;6(9):e24917.

6. Kimura T, Yeliseev AA, Vukoti K, Rhodes SD, Cheng K, Rice KC, Gawrisch K. Recombinant cannabinoid type 2 receptor in liposome model activates g protein in response to anionic lipid constituents. *J Biol Chem*. 2012 Feb 3;287(6):4076-87.

7. He Y, Rhodes SD, Chen S, Wu X, Yuan J, Yang X, Jiang L, Li X, Takahashi N, Xu M, Mohammad KS, Guise TA, Yang FC. c-Fms signaling mediates neurofibromatosis type-1 osteoclast gain-in-functions. *PLoS One*. 2012;7(11):e46900.

8. Staser K, Park SJ, Rhodes SD, Zeng Y, He YZ, Shew MA, Gehlhausen J, Cerabonna D, Chen S, Sun Z, Ingram DA, Nalepa G, Yang FC, Clapp DW. Normal hematopoiesis and neurofibromin-deficient myeloproliferative disease require Erk, *JCI.* Jan 2;123(1):329-34.

9. Albrecht DS, Lee JT, Mobly N, Rhodes SD, Minh D, Siegel JL, Porter LA. Functionalized porous silicon in a simulated gastrointestinal tract: modeling the biocompatibility of a monolayer protected nanostructured material. *Materials Research Society (MRS) Proceedings*. 2008, 1063-OO06-01.

## Abstracts and Presentations

1. Rhodes SD, He Y, Chen S, Yang H, Menon K, Staser KW, Yang X, Mohammad KS, Guise TA, Xu M, Yang FC. Haploinsufficiency of *Nf1* in myeloid lineages contributes to neurofibromatosis type 1 associated skeletal deficits. American Society of Hematology Annual Meeting, Atlanta, GA, December 8-11, 2012. Oral Presentation. ASH Outstanding Abstract Achievement Award.

2. Rhodes SD, He Y, Wu X, Zhang P, Chen S, Jiang C, Yokota H, Yang X, Peng X, Murthy S, Mohammad KS, Guise TA, Yang FC. Hyperactive transforming growth factor-beta1 signaling potentiates fracture non-union in neurofibromatosis type 1. American Society for Bone and Mineral Research (ASBMR) Annual Meeting, Minneapolis, MN, October 12-15, 2012. Oral Presentation. Young Investigator Travel Grant.

3. Rhodes SD, Menon K, He Y, Staser KW, Chen S, Mohammad KS, Guise TA, Yang FC. The role of osteoclasts in neurofibromatosis type 1 pseudarthrosis. ASBMR Annual Meeting. Minneapolis, MN, October 12-15, 2012. Oral Presentation.

4. Staser K, Park SJ, He YZ, Shew MA, Rhodes SD, Li Y, Nalepa G, Yang FC, Clapp DW. Normal hematopoiesis and *Nf1*-deficient myeloproliferative disease require Erk. International Society for Experimental Hematology (ISEH) Annual Meeting, Amsterdam, The Netherlands, August 23-26, 2012. Oral Presentation.

5. Rhodes SD, He Y, Staser KW, Menon K, Yang FC. The role of osteoclasts in neurofibromatosis type 1 pseudarthrosis. Children's Tumor Foundation NF Conference, New Orleans, LA, June 9-12, 2012. Oral Presentation.

6. He YZ, Staser K, Rhodes SD, Wu X, Zhang P, Chen S, Yang FC. Erk1 plays a critical role in macrophage development. American Society of Hematology Annual Meeting, December 10-13, 2011, San Diego, CA. Oral Presentation. Abstract Achievement Award.

7. Rhodes SD, He Y, Wu X, Hong LC, Zhang, P, Chen S, Jiang C, Yokota H, Peng X, Mohammad KS, Guise TA, Yang FC. Targeting the TGF-β/Smad pathway in neurofibromatosis skeletal defects. ASBMR Annual Meeting, San Diego, CA, September 16-20, 2011. Oral Presentation. Young Investigator Award.

8. Rhodes SD, He Y, Wu X, Hong LC, Zhang P, Chen S, Jiang C, Yokota H, Mohammad KS, Guise TA, Yang FC. Understanding the role of TGF-β in NF1 skeletal dysplasia. Developmental Biology and Neonatal Medicine Group Meeting, Herman B. Wells Center for Pediatric Research, Indiana University School of Medicine, Indianapolis, IN, January 5, 2010. Oral Presentation.

9. Staser KW, Park SJ, He Y, Shew MA, Gehlhausen JR, Rhodes SD, Li Y, Nalepa G, Yang FC, Clapp DW. Myelopoiesis requires Erk. Cancer Biology Training Consortium Annual Meeting, Tucson, AZ, November 5-7, 2010.

10. Staser KW, Park SJ, He YZ, Shew MA, Gehlhausen JR, Rhodes SD, Li Y, Nalepa G, Yang FC, Clapp DW. Marrow repopulation and stem cell expansion requires ERK. International Society for Experimental Hematology (ISEH) Annual Meeting, Melbourne, Australia, September 15-18, 2010. Oral Presentation. Travel Award.

11. Staser K, Park SJ, He YZ, Shew MA, Gehlhausen JR, Robinson MB, Li Y, Rhodes SD, Nalepa G, Yang FC, Clapp DW. Genetic evidence that myeloid proliferation requires ERK. American Society of Clinical Investigators (ASCI) Annual Meeting, Chicago, IL, April 23-25, 2010.

12. Rhodes SD, Kimura T, Yeliseev A, Gawrisch K. Functional reconstitution and 1H NMR study of recombinant peripheral cannabinoid receptor. 233rd American Chemical Society National Meeting, Chicago, IL, March 25-29, 2007. Poster Presentation.

13. Rhodes SD, Ahmed SM, Porter LA. Probing monolayer stability through chemical reactions on functionalized porous silicon. 231st American Chemical Society National Meeting, Atlanta, GA, March 26-30, 2006. Poster Presentation.

14. Rhodes SD, Porter LA. Organic synthesis on a chip: chemical reactions on functionalized porous silicon. 229th American Chemical Society National Meeting. San Diego, CA, March 13-17, 2005. Poster Presentation.

15. Thornberry DR, Fulmer GR, Rhodes SD, Porter LA. Degradation of functionalized porous silicon in simulated blood, gastric, and intestinal fluids. 229th ACS National Meeting, San Diego, CA, March 13-17, 2005. Poster Presentation.